

NORTHWESTERN UNIVERSITY

A Computational Materials-by-Design Approach for Cellulose-Based Nanocomposites

A DISSERTATION

SUBMITTED TO THE GRADUATE SCHOOL
IN PARTIAL FULFILMENT OF THE REQUIREMENTS

for the degree

DOCTOR OF PHILOSOPHY

Field of Mechanical Engineering

By

Robert Sinko

EVANSTON, ILLINOIS

September 2017

ABSTRACT

A Computational Materials-by-Design Approach for Cellulose-Based Nanocomposites

Robert Sinko

In recent times, there has been a transition away from traditional engineering materials to more advanced materials that are multi-functional and exhibit improved thermomechanical properties. Much of the inspiration for these advanced materials comes from natural biological systems that fulfill the needs of diverse organisms through clever material organization and mechanics. A better understanding of the underlying mechanics of natural systems that give rise to versatile mechanofunctionality provides insight into building new synthetic, bio-inspired materials. One specific approach to developing these new materials is to directly integrate biomolecules with impressive material properties into synthetic polymer materials to develop new polymer nanocomposites. Cellulose nanocrystals (CNCs) are one such biomolecule that exhibit impressive mechanical, thermal, and optical properties and are excellent candidates for inclusion in cellulose-polymer nanocomposites and all-cellulose thin films. CNCs serve as the key reinforcing component of wood, itself an all-natural nanocomposite, and offer advantages over comparable, synthetic materials such as aramid fibers due to their natural availability and reduced environmental impact.

The traditional approach to the development of new materials involves significant experimentation and iteration to determine design parameters that optimize material properties. For CNC-based nanocomposites, this approach has only been moderately successful and the properties of these new materials, specifically mechanical properties such as elastic modulus and failure strength, have not been optimized. In this work, we describe a new approach to the materials

design process termed computational materials-by-design. In this approach, computational tools are used to accelerate and improve the design process. For this specific system, this involves exploring the fundamental mechanics of CNCs (materials discovery), understanding how processing techniques can be used to change surface and interfacial properties (materials development), and describing how nanoscale simulation results can be used to predict macroscale material performance (property optimization). This computational approach offers numerous advantages over traditional materials design as it is iterative, scalable, cost effective, and applicable across multiple time and length scales. Specifically, our approach aims at probing and tuning the molecular level behavior of CNC-based nanocomposites to address current shortcomings in the materials and further suggest strategies for improving their thermomechanical properties.

To address these current shortcomings and further understand interfacial mechanics of these nanocrystals that are imperative to hierarchical material performance, here we present a computational materials-by-design approach to studying CNC-based nanocomposites. We begin with materials discovery where we aim to elucidate the natural behaviors and underlying mechanics of CNCs. We characterize and explain clear size dependence of the fracture energy of these materials that illuminates natural design principles. Further, we utilize nanoscale simulations to probe the interfacial traction-separation behavior of CNC interfaces and reveal key contributions of interfacial chemistry and hydrophobicity. We then shift to materials development where we utilize molecular simulation to characterize the effect of chemical surface modification on interfacial mechanics and water adsorption, and further demonstrate the effects of polymer grafting on polymer relaxation dynamics. Finally, our approach aims to optimize the properties of these new materials. To this effect, we first present multiscale models that allow us to predict bulk,

macroscale properties of polymer nanocomposites directly from nanoscale simulations. Second, we provide a molecular level explanation for a longstanding phenomenon for the drying creep behavior of nanoporous solids. All together, these studies shed light on the importance of nanoscale interfacial chemistry and mechanics, as well as natural design principles that provide guidance toward developing new high performance cellulosic materials using a computational materials-by-design approach.

Acknowledgements

I would first like to thank my advisor, Professor Sinan Keten, for his continued support and guidance throughout the entirety of my graduate research. I am inspired by his commitment to research and all the outstanding accomplishments that have come out of our group as a result since I joined. He has encouraged me to pursue this specific field of research but has also more generally instilled in me the idea of “materials-by-design”, an overall approach to studying and developing new materials that I hope to carry forward with me throughout my career. I would also like to express my gratitude to Professor Cate Brinson and Professor Randy Snurr for taking the time to serve as my M.S. and Ph.D. committee members. I greatly appreciate your interest in my research and the input you have provided me through teaching and collaborations to help shape my research.

I would like to thank my collaborators that have provided invaluable guidance, support, and discussion. I have had the opportunity to work with outstanding individuals within our own research group and would specifically like to mention Luis Ruiz, Wenjie Xia, Xin Qin, Zhaoxu Meng, Nitin Hansoge, Shawn Mishra, and Nick Brandis who I have been able to work with and learn from daily. Our daily conversations and collaborative effort have made my time as a graduate student an enjoyable experience and enhanced the quality of our work. Further, I have had the opportunity to work with outstanding experimental collaborators in Dr. Jeff Gilman (NIST) and Professor Doug Fox (American University), as well as colleagues within their groups. These collaborations have led to meaningful research and helped enhance the impact of our work by developing a symbiotic relationship between simulation and experiments. I also have had the opportunity to collaborate computationally with Professor Erik Luijten and Zonghui Wei. Their efforts have been greatly beneficial in enhancing our work related to water adsorption of cellulosic materials. Finally, I would like to acknowledge Professor Zdeněk P Bažant and Professor Matthieu

Vandamme whom I have had the opportunity to work with on the drying creep projects. They helped me apply my expertise in molecular simulation to a new problem and through this collaboration, we provided new insight into a longstanding phenomenon of nanoporous solids.

I would like to acknowledge support from the Department of Defense (DoD) through the National Defense Science and Engineering Graduate (NDSEG) Fellowship as well as the Department of Mechanical Engineering at Northwestern University. Additionally, I acknowledge funding through a supercomputing Grant from the Northwestern University High Performance Computing Center (Quest) as well as computing resources provided through the Department of Defense High Performance Computing Modernization Program (HPCMP).

Finally, I would like to acknowledge the love and continued support that has been provided by my parents (Ginny, Arnie, and Tammy) throughout my undergraduate and graduate education. They have continued to encourage me to pursue my goals and have made sacrifices along the way to get me to this point. I wouldn't be where I am today without them. Above all, I would like to acknowledge my wonderful wife Katie, who has stood by me throughout my entire time as a graduate student. She has supported me through all the late nights and early mornings needed to conduct my research, and I wouldn't be where I am without her support and encouragement. I'm excited for our life together and know she will be a constant source of support as I continue my academic career.

Table of Contents

Table of Figures.....	9
Table of Tables	11
Chapter 1 – Introduction	12
1.1 Cellulose Nanocrystals (CNCs) and Their Importance	14
1.2 Crystalline Structure of Cellulose	17
1.3 Recent Developments for CNC-Polymer Nanocomposites.....	20
1.4 Proposed Research: Computational Materials-by-Design	24
Chapter 2 – Simulation Methodology	27
2.1 Molecular Dynamics Simulations	27
2.2 CHARMM Force Field	31
2.3 CHARMM Force Field Parameters.....	33
2.4 Steered Molecular Dynamics Simulation Technique	36
2.5 Grand Canonical Monte Carlo (GCMC) Simulation Technique.....	41
2.6 Dissipative Particle Dynamics	43
Chapter 3 – Size Dependence of CNC Fracture Energy	45
3.1 Simulation Parameters.....	45
3.2 Mechanical Properties and Energetics of CNC Fracture	47
3.3 Width Size Dependence of Fracture Energy	51
3.4 Thickness Size Dependence of Fracture Energy.....	55
3.5 Predicting an Optimal CNC Size	61
Chapter 4 – Mechanics of CNC-CNC Interfaces	65
4.1 Simulation Parameters.....	65
4.2 Interfacial Separation Simulations	67
4.3 Interfacial Traction Simulations	71
4.4 Analytical Descriptions of Interfacial Traction-Separation Laws	77
4.5 Extension of Results to CNC Neat Films	85
Chapter 5 – Effects of Moisture on Interfacial Traction-Separation.....	91
5.1 Simulation Parameters.....	91
5.2 Moisture Effects on Interfacial Separation	93
5.3 Moisture Effects on Interfacial Traction.....	97
Chapter 6 – Tailoring of Water Adsorption and Interfacial Mechanics Through Ion Exchange Surface Modification.....	102
6.1 Simulation Parameters.....	103
6.2 Water Adsorption of Surface Modified CNCs.....	109
6.3 Separation of Surface Modified CNCs	113
6.4 Traction Behavior of Surface Modified CNCs	116
6.5 Comparison to Experimental Results	120
Chapter 7 – Relaxation Dynamics of Nanocomposites with Polymer-Grafted CNCs.....	122
7.1 Background and Simulation Parameters	122
7.2 Measuring Relaxation Dynamics of Polymers	127
7.3 Relaxation Dynamics of Polymer-Grafted CNCs.....	129

Chapter 8 – Predicting Macroscale Properties of Polymer Nanocomposites from Nanoscale Simulations	135
8.1 Simulation Parameters.....	136
8.2 Direct Energy Summation Method for Quantifying Interfacial Energies	141
8.3 Predicting Dispersion of CNCs in Nanocomposites	147
8.4 Predicting Nanocomposite Glass Transition Temperature from Interfacial Adhesion Energies	149
Chapter 9 – Nanoscale Origins of Drying Creep	156
9.1 The Pickett Effect	156
9.2 Coarse-Grained (CG) Model and Simulation Parameters	161
9.3 Behavior of Nanoconfined Water.....	165
9.4 Analytical Model for Drying Creep at the Nanoscale	173
9.5 Estimation of Underlying Energy Barriers to Shear Displacement	182
9.6 Comparison of Analytical Model and CGMD Simulations	185
9.7 Effect of Transverse Microprestress on Pure Creep Behavior	189
9.8 Modification of Analytical Model for Pure Creep and Calculation of Underlying Energy Barriers.....	192
9.9 Effect of Transverse Microprestress on Drying Creep Behavior	197
9.10 Modification of Analytical Model for Drying Creep.....	201
Chapter 10 – Conclusions and Outlook	206
Chapter 11 – References.....	209
Chapter 12 – Appendix: CHARMM Force Field Parameters.....	226
12.1 CHARMM Force Field for Carbohydrates	226
12.2 cgenff Force Field Parameters for Synthetic Polymers	227
12.3 FFTK Parameters for CNC Surface Modifications	236
12.3.A Methyltriphenylphosphonium (MePh ₃ P ⁺) Parameters.....	239
12.3.B 1-Hexyl-2,3-dimethyl imidazolium (HxMe ₂ Im ⁺) Parameters	241
12.3.C 1-Hexadecyl-2,3-dimethyl imidazolium (HdMe ₂ Im ⁺) Parameters.....	244
12.3.D 1,2,3-trimethylimidazolium (Me ₃ Im ⁺) Parameters.....	246
Chapter 13 – Appendix: Interfacial Mechanics Results for Additional CNC Lengths.....	248
Chapter 14 – Curriculum Vitae.....	252

Table of Figures

Figure 1-1: Nanocellulose in the hierarchical structure of wood.	15
Figure 1-2: Ashby plot of stiffness vs. failure strength of engineering materials.	17
Figure 1-3: CNC crystalline structure and relevant surfaces.	19
Figure 1-4: Mechanical properties of CNC-reinforced polymer nanocomposites.	22
Figure 2-1: Effect of SMD spring constant.	40
Figure 2-2: Rate dependence of SMD pulling velocity.	41
Figure 3-1: Atom assignments for SMD simulations of CNC fracture.	47
Figure 3-2: Free energy landscape and stress-strain curve for CNC failure.	48
Figure 3-3: CNC hydrogen bond occupancy.	50
Figure 3-4: Scaling of fracture energy with crystal width.	52
Figure 3-5: Average RMSD of CNCs as a function of width.	53
Figure 3-6: Scaling of fracture energy with crystal width: additional chain lengths.	55
Figure 3-7: Scaling of fracture energy with crystal thickness.	56
Figure 3-8: Interfacial vdW energy – 2 sheets per side.	58
Figure 3-9: Interfacial vdW energy - 3 sheets per side.	58
Figure 3-10: Comparison of closed-form expression to truncated sum.	60
Figure 3-11: Continuous approximation of numerical sum in Eq. (3-9).	61
Figure 3-12: CNC sizes in natural systems.	63
Figure 4-1: CNC-CNC interfacial simulation system setup.	66
Figure 4-2: Energy landscapes of CNC-CNC interfacial separation.	68
Figure 4-3: Relative non-bonded energy contributions to the adhesion energy.	71
Figure 4-4: Energy landscapes of CNC-CNC interfacial traction (width).	72
Figure 4-5: Force-displacement curves for CNC-CNC interfacial traction (width).	74
Figure 4-6: Hydrogen bond breaking/reformation mechanism for shearing of (110)–(110) interfaces.	76
Figure 4-7: Energy landscapes of CNC-CNC interfacial traction (length).	77
Figure 4-8: Analytical model to describe CNC interfacial shear failure.	82
Figure 4-9: Interfacial shear stress-strain curve and CNC neat film geometry.	87
Figure 4-10: Illustration of shear lag model geometry and CNC alignment.	88
Figure 5-1: Illustration of CNC-CNC wet interface.	92
Figure 5-2: Effect of moisture on interfacial separation and mechanical properties.	94
Figure 5-3: Illustration of interfacial separation mechanisms with water.	96
Figure 5-4: Effect of moisture on interfacial traction energy landscape.	98
Figure 5-5: Effect of moisture on energy barriers to interfacial shear deformation.	99
Figure 5-6: Moisture effects on interfacial shear modulus.	100
Figure 6-1: Surface modification from CNC extraction process.	103
Figure 6-2: Summary of FFTK parameterization of the MePh3P ⁺ cation.	105
Figure 6-3: Ion exchange surface modification of CNC surfaces.	107
Figure 6-4: Water adsorption on surface modified CNCs.	112
Figure 6-5: Effect of surface modification and moisture on interfacial adhesion energy of CNCs.	114
Figure 6-6: Hydrogen bond occupancy at surface-modified CNC interfaces.	116
Figure 6-7: Effect of surface modification and moisture on interfacial traction of CNCs.	118

Figure 6-8: Experimental measurements of CNC surface energy from inverse gas chromatography.....	121
Figure 7-1: Illustration of polymer grafting to CNCs.	124
Figure 7-2: Illustration of nanocomposite RVEs consisting of CNCs embedded in polymer matrix.....	126
Figure 7-3: Polymer grafting reduces solvent accessible surface area.....	127
Figure 7-4: Effect of grafting density on polymer relaxation dynamics.....	130
Figure 7-5: Local polymer relaxation dynamics.	132
Figure 7-6: Density profiles of polymer chains around CNCs.....	133
Figure 8-1: Illustration of ion exchange surface modifications.	137
Figure 8-2: Illustration of CNC-polymer interfaces and matrix polymers studied.....	139
Figure 8-3: Direct energy summation (DES) method for quantifying interfacial adhesion.	142
Figure 8-4: Interfacial adhesion energies for CNC-polymer and CNC-CNC interfaces. ..	144
Figure 8-5: Aligned and interdigitated conformation of CNC interfaces.....	145
Figure 8-6: Effect of partial ion exchange on interfacial filler adhesion.	147
Figure 8-7: Predicted dispersion factor of CNC-based nanocomposites.	149
Figure 8-8: Experimentally observed dispersion of CNCs in nanocomposites.	149
Figure 8-9: Multiscale modeling approach to predicting T_g in nanocomposites.	151
Figure 8-10: Effect of interfacial adhesion and dispersion on T_g of thin films and composites.	153
Figure 9-1: Illustration of the Pickett effect for nanoporous solids.	158
Figure 9-2: Coarse-grained model of water in nanopore and interatomic potentials.	162
Figure 9-3: Shear thinning behavior of nanoconfined water.....	168
Figure 9-4: Nanoconfinement of water near solid surfaces.	172
Figure 9-5: CGMD simulation methodology for analytical model of drying creep.....	176
Figure 9-6: Analytical predictions from Bell's model.....	180
Figure 9-7: Estimating energy barrier to shear from an Arrhenius model for the temperature dependence of viscosity.....	184
Figure 9-8: Comparison of simulation results with analytical model.	186
Figure 9-9: Effect of transverse microprestress on pure creep behavior.	191
Figure 9-10: Transverse microprestress changes the underlying energy barrier to shear displacement.	194
Figure 9-11: Modification of analytical model and comparison to CGMD simulations.	196
Figure 9-12: Effect of transverse microprestress on drying creep behavior.....	198
Figure 9-13: Differences in effects of transverse microprestress with increasing drying force for tension and compression.	199
Figure 9-14: Modification of existing analytical model of drying creep.....	203
Figure 9-15: Water interlayer velocity as a function of drying force.....	205
Figure 12-1: Cellulose repeat unit atom types.....	227
Figure 12-2: PMMA atom names, types, and partial charges.	228
Figure 12-3: PS atom names, types, and partial charges.	229
Figure 12-4: DGEBA atom names, types, and partial charges.....	231
Figure 12-5: PEDA (DP = 2) atom names, types, and partial charges.....	232
Figure 12-6: PEDA (DP = 3) atom names, types, and partial charges.....	233

Figure 12-7: CNC surface modification atom names, types, and partial charges.	237
Figure 12-8: MePh ₃ P ⁺ cation atom names.	239
Figure 12-9: HxMe ₂ Im ⁺ cation atom names.	241
Figure 12-10: HdMe ₂ Im ⁺ cation atom names.	244
Figure 12-11: Me ₃ Im ⁺ cation atom names.	246
Figure 13-1: Energy landscapes of CNC-CNC interfacial separation (10.38 nm length). .	248
Figure 13-2: Energy landscapes of CNC-CNC interfacial separation (15.57 nm length). .	248
Figure 13-3: Energy landscapes of (110)–(110) interfacial shear (additional lengths).	249
Figure 13-4: Energy landscapes of (200)–(200) interfacial shear (additional lengths).	250
Figure 13-5: Force-displacement curves for (110)–(110) interfacial shear (additional lengths).	251
Figure 13-6: Force-displacement curves for (200)–(200) interfacial shear (additional lengths).	251

Table of Tables

Table 4-1: Interfacial adhesion energies of CNC-CNC interfaces.	69
Table 4-2: Fitting parameters for the interfacial separation model.	80
Table 4-3: Fitting parameters for the interfacial traction model.	85
Table 4-4: Shear-lag model parameters.	89
Table 12-1: Bond parameters for epoxy systems.	233
Table 12-2: Angle parameters for epoxy systems.	234
Table 12-3: Dihedral parameters for epoxy systems.	234
Table 12-4: Sulfate group bond, angle and dihedral parameters.	237
Table 12-5: ATRP compound bond, angle and dihedral parameters.	238
Table 12-6: MePh ₃ P ⁺ atom types and partial charges.	240
Table 12-7: MePh ₃ P ⁺ bond, angle, and dihedral parameters.	241
Table 12-8: HxMe ₂ Im ⁺ atom types and partial charges.	242
Table 12-9: HxMe ₂ Im ⁺ bond, angle, and dihedral parameters.	243
Table 12-10: HdMe ₂ Im ⁺ atom types and partial charges.	245
Table 12-11: Me ₃ Im ⁺ atom types and partial charges.	246
Table 12-12: Me ₃ Im ⁺ bond, angle, and dihedral parameters.	247

Chapter 1 – Introduction

One of the major focus areas of current materials research is the investigation of new materials that improve upon the performance and characteristics of traditional engineering materials. Traditional engineering materials such as ceramics, metals, polymers, etc. still play an important role in society, but materials that are more versatile with improved mechanical properties and potential multifunctional behaviors have become increasingly more desirable. Examples of these advanced materials include composites¹⁻³, shape-memory alloys/polymers⁴⁻⁵, and bio-inspired materials⁶⁻¹². Much of the inspiration for new materials and material systems comes from natural systems that exhibit outstanding mechanical properties and multifunctionality. As such, three strategies have been identified for the development of these new bioinspired materials¹²: biomimicry (replicating what nature does well in terms of structure, chemistry, etc.), recombinant biosynthesis (rearranging biomolecules in a novel architecture), or a hybrid approach (combining biomolecules together with synthetic materials). Of these, the hybrid approach is of particular interest. For example, a biomolecule that exhibits outstanding material properties can be mixed with a synthetic polymer to form a new polymer nanocomposite structural component or thin film. In this work, cellulose nanocrystals (CNCs) are studied as one such biomolecule that can be included in new hierarchical materials for improved mechanical, thermal, and optical properties.

In addition to improving the overall properties of new materials, an important goal of current research (including this work) is to improve on the methodology of deploying these materials. The development of a new computational approach to materials design has been inspired by the Materials Genome Initiative, which aims to accelerate the materials design process while also increasing the number of new advanced materials brought to market¹³. Considering this initiative, this dissertation aims to emphasize a new materials design framework known as

computational materials-by-design. In this approach, we aim to primarily use computational tools, complemented by analytical theories and experiments, to accelerate the processes of materials discovery, development, and property optimization. Here, materials discovery entails identifying promising natural or synthetic materials and explaining their underlying mechanics and thermodynamics. This process provides a knowledge base for materials development, where we aim to design new hierarchical materials that leverage these findings. Finally, upon developing new materials systems, we utilize computational tools to optimize their properties by considering factors such as surface chemistry, hierarchical structure, and size dependence. Overall, this computational materials-by-design approach is a new methodology that leverages the inherent advantages of computation (iterative, scalable, cost) to suggest intentional design strategies that can improve materials performance beyond traditional engineering materials.

Throughout the entirety of this dissertation, we will highlight how we have applied this computational materials-by-design approach to better understand CNC-nanocomposites. We will highlight all facets of this approach (materials discovery, materials development, and property optimization) for this example material system where we hope to incorporate the outstanding mechanical, thermal, and optical properties of CNCs as filler particles in a synthetic polymer matrix. While we focus here on one specific material system, it is important to emphasize the generality of this approach and how it could be extended to any number of material systems in the future. In this introductory chapter, we focus on describing the properties of CNCs that make them attractive candidates for inclusion in new bioinspired materials, as well as recent developments in the field of CNC-polymer nanocomposites. We conclude the chapter with an overview of the entire dissertation and how we have utilized computational materials-by-design to develop strategies for improving the properties of this promising class of materials.

1.1 Cellulose Nanocrystals (CNCs) and Their Importance

Cellulose is the most abundant biopolymer on earth¹⁴ and is found in a number of organisms including bacteria, tunicates, and plants¹⁴⁻¹⁵. Within these diverse organisms, cellulose exhibits a wide range of functions that take advantage of its excellent optical, thermal, and mechanical properties. Within bacteria, cellulose is a component of protective gels that help protect these organisms from harmful ultraviolet light and radiation¹⁶. In plants, on the other hand, cellulose provides structural stability throughout the well-studied hierarchical structure shown in Figure 1-1. Within plants, and specifically the wood of trees, cellulose is found in both amorphous, semi-crystalline, and crystalline phases that together help provide impressive strength and stability to these organisms¹⁵. Further, the structurally anisotropic arrangement of cellulose fibrils (structures that are a combination of amorphous and crystalline regions) are responsible for many hygrothermal plant actuation mechanisms including seed opening and tree branch movement¹⁷⁻²⁰.

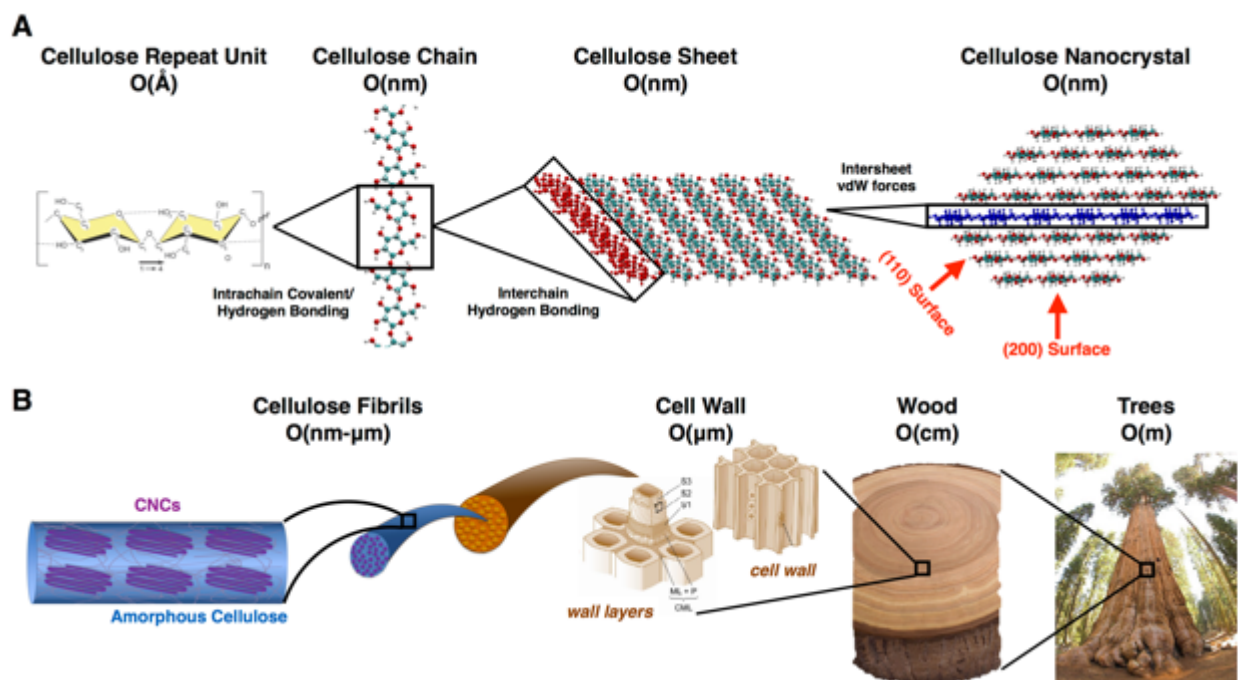


Figure 1-1: Nanocellulose in the hierarchical structure of wood. (A) Hierarchical structure of a cellulose nanocrystal (CNC) showing its formation from the basic cellulose repeat unit into the I β crystalline structure. Multiple cellulose repeat units (hundreds to tens of thousands) come together via covalent and hydrogen bonding to form long cellulose chains. These cellulose chains are stabilized into sheets by extensive interchain hydrogen bonding. (B) Hierarchical structure of cellulose in wood/trees starting with the basic building blocks of CNCs embedded within amorphous cellulose domains. Cellulose fibrils aggregate and order themselves across multiple length scales to provide structural stability and strength. Adapted from Sinko et. al, *MRS Bulletin* 2015²¹.

At the foundation of each of these diverse biological systems are highly crystalline cellulose nanocrystals (CNCs). These nanocrystals are the fundamental biological building block in several natural systems and most notably are at the foundation of the natural, hierarchical composite structure of wood as shown in Figure 1-1(B). Their high crystallinity, strong molecular interactions through hydrogen bonding and non-bonded van der Waals forces, and rigid chain structure give rise to impressive mechanical properties²²⁻²⁵ rivaling those of synthetic aramid fibers such as Kevlar²⁴. CNCs have been shown to have an elastic modulus ranging from 110 – 200 GPa

in the axial direction and 10 – 50 GPa in the transverse direction²⁶, which compares favorably to the elastic modulus of Kevlar that ranges from 75 – 150 GPa²⁷. Additionally, the low density of CNCs ($\sim 1.6 \text{ g/cm}^3$) provides them with one of the highest combinations of specific elastic modulus and specific failure strength as shown in Figure 1-2. Here the specific failure strength (σ_f/ρ) and elastic modulus (E/ρ) are simply the experimentally measured failure strength and elastic modulus normalized by the density. Further, CNCs offer even more advantages over comparable synthetic fibers in terms of their bioavailability, processing cost, and environmental sustainability. While at present the production and extraction of CNCs has yet to be fully optimized, it is estimated that the future production cost of CNCs could be as much as 5-30 times cheaper than the production of Kevlar. This is primarily attributed to the high bioavailability and processing capability of CNCs, coupled with their inherent sustainability where even the waste products from their extraction (amorphous cellulose, hemicellulose, lignin) can be utilized in other lignocellulosic applications.

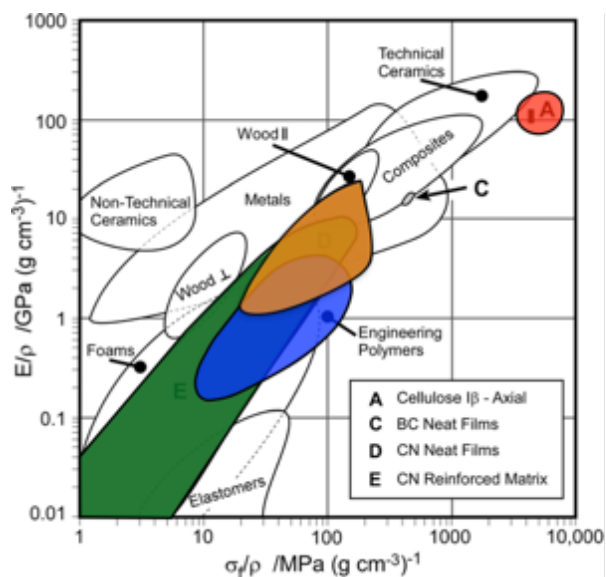


Figure 1-2: Ashby plot of stiffness vs. failure strength of engineering materials. Ashby plot showing the specific stiffness (elastic modulus divided by density, E/ρ) as a function of the specific failure strength (failure strength divided by density, σ_f/ρ) for several different materials as labeled in the plot. Of interest are the performance of CNCs (label A, red region), engineering polymers, (blue region), CNC neat films (label D, orange region), and CNC-polymer nanocomposites (label E, green region). Adapted from Moon et al., *Chem. Soc. Rev.* 2011¹⁵.

1.2 Crystalline Structure of Cellulose

Although CNCs and cellulose are typically discussed as a single class of materials, there are four unique forms of cellulose (Cellulose I, II, III, and IV) that exhibit unique mechanical properties and differences in their crystal structure²⁸⁻³⁰. Of these, Cellulose I (often referred to as the “natural” cellulose) is the most relevant and well-studied as it exhibits the best mechanical properties – specifically the highest elastic modulus^{15, 31-32}. For Cellulose I, there are two distinct crystalline polymorphs ($I\alpha$ and $I\beta$) that exhibit slightly different crystalline structures. $I\alpha$ CNCs have a triclinic crystal structure with a relative displacement of $c/4$ between adjacent crystalline planes (where c is a crystalline unit cell parameter). $I\beta$ CNCs, on the other hand, have a monoclinic crystal structure with an alternating relative displacement of $c/4$ and $-c/4$ between adjacent planes.

$I\beta$ CNCs are the most common polymorph of CNCs observed in natural systems and for the remainder of this study any reference to CNCs will also imply a reference to $I\beta$ CNCs.

The typical dimensions of CNCs observed in nature range from 3-50 nm in width/thickness and 50 – 500 nm in length depending on the extraction source. For example, wood CNCs have a cross-section of 3 – 5 nm and a length of 50 – 500 nm (aspect ratio of $\sim 10 - 150$) while tunicate CNCs have a cross-section of 8 – 20 nm and a length of 100 – 4000 nm (aspect ratio of $\sim 5 - 500$). Further, numerous cross-sectional shapes have been observed including squares, parallelograms, and circles, and is highly dependent on the source of extraction. One of the most commonly observed cross-sectional shapes is a hexagonal arrangement of 36 chains that is commonly referred to as an “elementary fibril”³¹ and is pictured in Figure 1-3(A). This elementary fibril structure exposes the two most common surfaces of CNCs: the (110) and (200) surfaces as indicated in Figure 1-3(A). The (110) surface is equivalent to the interchain direction within the crystal (Figure 1-1(A)) and has many exposed hydroxyl groups that make it prone to extensive hydrogen bonding. The (200) surface, on the other hand, is equivalent to the intersheet direction within the crystal (Figure 1-1(A)) and has an exposed flat ring structure with fewer hydroxyl groups^{28, 33}.

Beyond the hexagonal cross-section of an elementary fibril, rectangular cross-sections are also commonly observed and expose the (010) and (200) surfaces as pictured in Figure 1-3(B). The (010) surface exhibits nearly identical chemical characteristics to the (110) surface, but has a much higher surface roughness due to the recessed chains at the edges of the crystal. Independent of the CNC cross-section, CNCs have relatively high aspect ratios and are flat or ribbon-like with a small angle of twist of 1.5 degrees/nm³⁴⁻³⁵ that is a result of the hydrogen bonding and other intermolecular interactions between individual cellulose chains within the crystal.

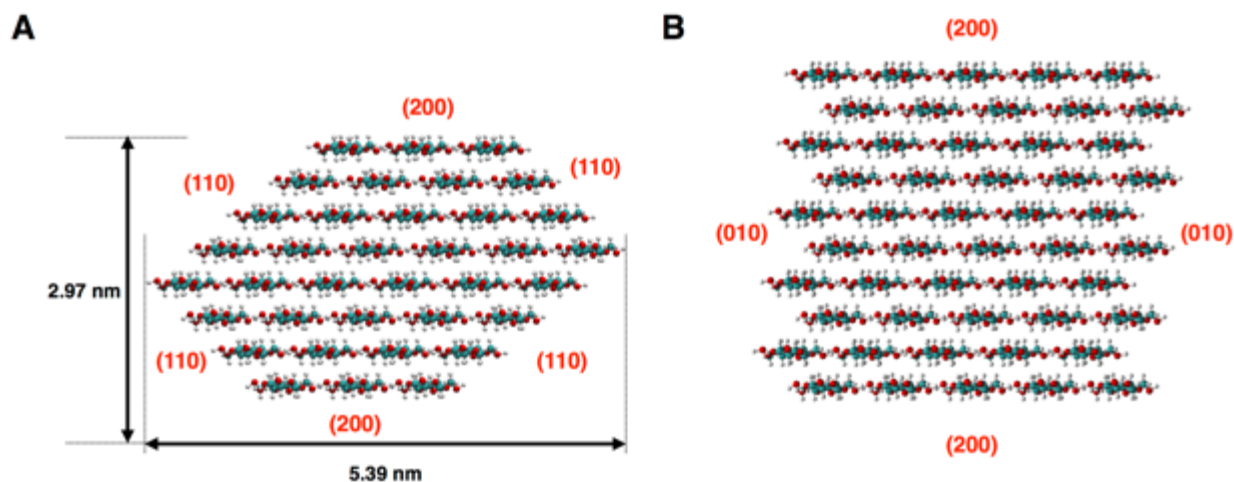


Figure 1-3: CNC crystalline structure and relevant surfaces. (A) Image of a β CNC "elementary fibril" consisting of 36 cellulose chains in a hexagonal arrangement with the (110) and (200) surfaces exposed. (B) Image of a monoclinic β CNC with the (200) and (010) surfaces exposed that illustrates the alternating crystalline planes having relative displacements of $+c/4$ and $-c/4$.

Although the crystalline structure and mechanical properties of CNCs have been well characterized and a general consensus has been reached, the extraction process³⁶ and further processing techniques³⁷⁻³⁸ are crucial to consider in studying these building blocks. Extraction processes can introduce defects along the surfaces of the crystal, while further processing, and in some case even the chemical nature of the extraction process, can lead to several different surface modifications of the free hydroxyl groups^{37, 39-43}. Specifically, the process of acid hydrolysis commonly used to extract CNCs from microfibrilated cellulose (MFC) or nanofibrilated cellulose (NFC) can replace the exposed hydroxyl groups on CNC surfaces with sulfate, phosphate, or carboxylic groups depending on the specific acid used for extraction.

These surface modification techniques present one strategy for altering the interfacial properties and compatibility of CNCs for specific applications including polymer nanocomposites. However, one of the key features of these surface modifications is that they can maintain the

crystalline morphology and integrity of CNCs as they do not change the internal chemistry or crystal stability. An example of one of these surface modification techniques is TEMPO (2,2,6,6-Tetramethylpiperidine-1-oxyl)-mediated oxidation⁴⁴⁻⁴⁶. This approach is used to functionalize hydroxyl groups on CNC surfaces to their corresponding carboxylic form without any change to the crystal's internal structure or mechanical properties. By effectively changing the surface chemistry without any crystal degradation, this allows for the intentional design of nanoscale interfaces that govern numerous macroscale thermomechanical properties.

1.3 Recent Developments for CNC-Polymer Nanocomposites.

Based on the impressive mechanical properties of CNCs as well as their material chemistry, there have been several important applications developed that utilize CNCs. First and foremost, engineering materials including ropes, paper, and timber for housing, are directly derived from cellulose in plants (CNCs included) and continue to be important raw materials for the worldwide paper, textile, and forest products industries⁴⁷. Beyond these materials, recent research has focused on applications aiming to scale up the properties of CNCs in a number of novel materials and applications including transparent films⁴⁸⁻⁴⁹, flexible displays⁵⁰⁻⁵⁴, components for drug delivery, templates for electronics, and batteries. However, despite all these promising applications, perhaps the application with the largest appeal to the scientific community is the development of new nanocomposites in which CNCs are used as a reinforcing filler phase. In the following section, progress in the development of these composites will be discussed, as well as current shortcomings that must be addressed to further advance their performance.

Nanocellulose offers advantages over other filler nanoparticles used in nanocomposites as CNCs are widely available and cheap to extract from industrial byproducts and waste using a variety of low-cost processing techniques. Thus far, significant research progress has been made

in hope of reengineering new nanocomposites with CNCs serving as reinforcing filler materials. For example, the presence of CNCs in these materials has served to enhance a number of material properties including elastic modulus^{39, 54-64} and glass transition temperature⁵⁹. Figure 1-4 compares several different polymers into which CNCs or nanofibrillated cellulose (NFC) (another primarily crystalline cellulosic material) have successfully been incorporated. Figure 1-4 demonstrates that cellulose serves to enhance nanocomposite mechanical properties, but also shows that the effect is significantly different depending on the host polymer. For example, in the case of NFC-PU (polyurethane) the stiffness is enhanced by nearly 3000% when cellulose is added but in the case of NFC-PLA (poly lactic acid) the enhancement is only 40%.

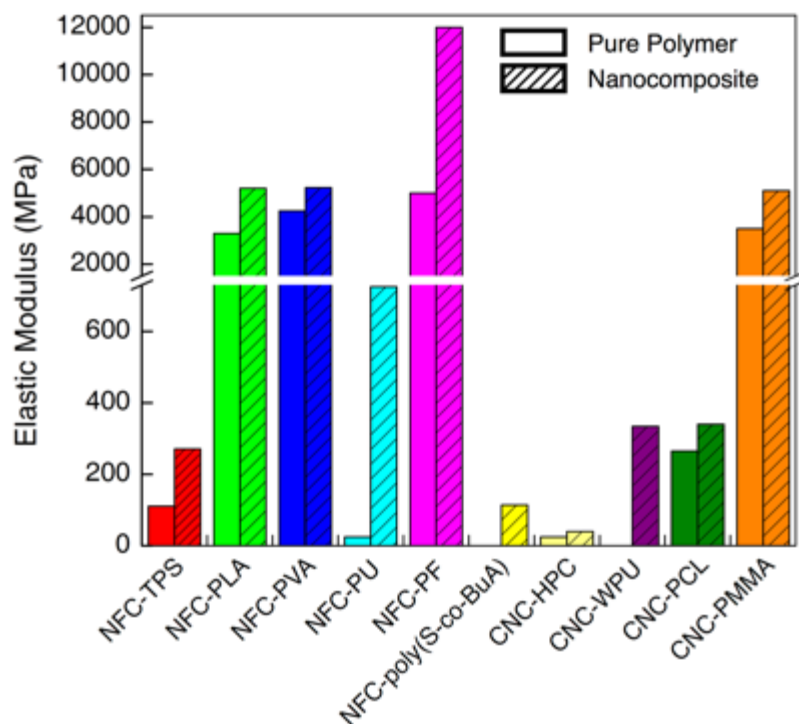


Figure 1-4: Mechanical properties of CNC-reinforced polymer nanocomposites. Elastic modulus of cellulose (cellulose nanocrystals (CNCs) and/or nanofibrillated cellulose (NFC)) reinforced nanocomposites: NFC-thermoplastic starch (TPS)⁵⁵, NFC-poly(lactic acid (PLA)^{61, 64}, NFC-poly(vinyl alcohol) (PVA)⁵⁸, NFC-polyurethane (PU)⁶², NFC-phenol formaldehyde (PF), NFC-poly(S-co-BuA)⁵⁴, CNC-Hydroxypropyl cellulose (HPC)³⁹, CNC-waterborne polyurethane (WPU)⁵⁷, CNC-polycaprolactone (PCL)^{60, 63}, and CNC-poly(methyl methacrylate) (PMMA)^{56, 59}. Adapted from Sinko et al., *MRS Bulletin* 2015⁶⁵.

These stark differences in the degree of elastic modulus enhancement of CNC-polymer nanocomposites provides some insight and motivation into what further research is needed. Although these materials have been shown to be experimentally feasible to manufacture and used in real-world applications for infrastructure, transportation, and renewable energy, there is still much room for improvement. When looking at the Ashby plot in Figure 1-2, we notice that although CNCs themselves (red region) exhibit outstanding mechanical properties in terms of specific stiffness and failure strength, the hierarchical materials into which they are incorporated

fall short of “ideal” performance. The specific strength and stiffness of both CNC neat films (orange region) and CNC-polymer nanocomposites (green region) fall well short of the optimal performance suggested by traditional composite theories (e.g. the rule of mixtures). In addition to underperforming traditional composites, these CNC-hierarchical materials also fall well short of the performance of traditional engineering materials including wood, metals, and ceramics. These experimental measurements suggest that these materials possess characteristics that cannot be explained completely by traditional theories and that their development thus far has not reached its full potential.

Based on these observations, we hypothesize that the central bottleneck to improving material performance lies at weak, nanoscale interfaces within materials that play a crucial role in dictating emergent, macroscale material properties. For example, nanoscale interfaces promote the formation of interphase regions of the matrix within nanocomposites that improve thermomechanical properties. Additionally, interfaces can help to promote the formation of percolated networks⁶⁶ among filler particles that distribute cracks³ and consequently improve material strength and toughness and can even help to instill shape-memory and stimuli-adaptive behavior into nanocomposites⁶⁷⁻⁷¹. Although it is apparent that these interfaces are important, it is difficult to generalize how a specific interface between two materials will behave without extensive characterization. Interfacial mechanics of CNCs are fundamental to the understanding of many different aspects of nanocellulose including CNC processing, surface modification of CNCs, self-assembly/organization of CNCs, and interactions with matrix materials in thin films and nanocomposites. To fully leverage the performance of CNCs in these hierarchical materials, it is therefore imperative to understand how interfacial behaviors and characteristics (e.g. adhesion, roughness, etc.) influence macroscopic properties. Not only are CNC-polymer interfaces important

to characterize in this context, but CNC-CNC interfaces are just as important as they also influence the performance of nanocomposites and neat films.

1.4 Proposed Research: Computational Materials-by-Design

Having identified a knowledge gap and opportunity for improvement in the development and optimization of CNC-based nanocomposites, my research has focused on the implementation of a computational materials-by-design approach for this class of materials. Here, we present the results of our molecular simulations that focus on materials discovery, materials development, and property optimization of these materials that are complemented by the development of analytical models, as well as experimental results. This work is part of a larger scale project within the Center for Hierarchical Materials Design (CHiMaD) that aims to emphasize the importance of nanoscale behavior in the design of new hierarchical materials and has provided experimental collaborations to both validate the results of simulation and provide inspiration for the development of new simulations. Throughout this work we will focus on the computational materials-by-design framework and how we have advanced through this materials design process for CNC-based nanocomposites. Before presenting our results, we summarize many of the simulation techniques used throughout this work in Chapter 2 (page 27), including an overview of molecular dynamics (MD), the CHARMM force field and system parameterization, steered molecular dynamics (SMD), grand canonical Monte Carlo (GCMC), and dissipative particle dynamics (DPD) using a coarse-grained model.

My research begins with the materials discovery process where we have aimed to understand the fundamental nanoscale mechanics of individual CNCs as well as their interfacial mechanics. In the first study presented in Chapter 3 (page 45), the fracture/failure behavior of an individual CNC is studied using SMD to explain the nanoscale interactions within the crystals that

give rise to their impressive mechanical properties. We also examine the size dependent fracture behavior of CNCs and use an analytical model to predict an optimal crystal size that reveals a natural design principle for these materials. In Chapter 4 (page 65), we then transition to studying the interfacial behavior between CNCs. This work again employs SMD to quantify the traction-separation behavior of nanocrystals and reveal interfacial mechanics that are highly dependent on surface chemistry – indicating the clear anisotropic nature of these materials. Our results are further extended to develop analytical models that describe the energetic interactions between two nanocrystals and we demonstrate how these results can be used to predict properties of CNC thin films. Finally, in Chapter 5 (page 91), we focus on understanding the effect of moisture on interfacial mechanics and describe nanoscale mechanisms that contribute to the degradation or appreciation of interfacial properties due to the presence of moisture.

Building upon these initial studies, we then shift our focus to materials development where we aim to understand how intentional nanoscale interface design can change mechanical properties. In Chapter 6 (page 102), we examine the effects of interfacial surface chemistry on traction-separation behavior as well as examine how surface chemistry can change the moisture adsorption behavior of CNCs using GCMC simulations. In Chapter 7 (page 122), we then shift our focus to polymer grafting of CNCs in which synthetic polymers are covalently linked to the CNC surface. Here we focus primarily on polymer-grafted CNCs embedded in a polymer matrix and examine how the CNC-polymer interface influences the relaxation dynamics of matrix polymer chains.

The final aspect of computational materials-by-design, property optimization, is highlighted in the final chapters of this work. First, in Chapter 8 (page 135), we develop a multiscale model that can link interfacial adhesion energies at the nanoscale between matrix and

fillers to the macroscale dispersion state of nanofillers. In this study, we also have established a protocol for populating materials design libraries to rapidly evaluate new chemical surface modifications that can guide experimentalists in their evaluation of new materials. Second, we propose a multiscale model that links the interfacial adhesion energy between CNCs and polymer to the glass-transition temperature of the resulting composite material. These multiscale models serve as prime examples of how nanoscale behaviors inform macroscale material properties and can be tuned to optimize desired material properties. Finally, in Chapter 9 (page 156), we shift our focus to using nanoscale CGMD simulations to explain the drying creep behavior of nanoporous solids (e.g. wood, concrete, etc.). We demonstrate for the first time how the macroscopically observed Pickett effect can be explained by the behavior of water confined in nanopores – a length scale that had previously not been considered. The dissertation and main findings are summarized in Chapter 10 (page 206) where we also provide some outlook to the future of cellulose-based materials and applications of computational materials-by-design.

Chapter 2 – Simulation Methodology

In this chapter, molecular simulation techniques used to study CNC-nanocomposites in the computational materials-by-design framework will be discussed. The first section provides an overview of theories behind molecular dynamics, as well as some practical considerations that are employed. The second section focuses on the CHARMM force field used in most of our simulations and discusses the specific reasons for choosing this force field, as well as presenting its analytical form. Next, we discuss parameterization techniques used for obtaining CHARMM force field parameters for chemistries that had not previously been studied in simulation. The final section discusses the simulation techniques employed throughout this work, including steered molecular dynamics (SMD), grand canonical Monte Carlo (GCMC), and dissipative particle dynamics (DPD). A brief discussion on coarse-graining methods (CG) is also included in this section. While certain simulation parameters are included in this chapter (such as simulation time, system constraints, etc.), more specific details can be found in the chapters for specific studies.

2.1 Molecular Dynamics Simulations

As alluded to in the previous sections, our primary method of investigating interfacial mechanics at the nanoscale will be to use computational simulations. Specifically, two types of molecular dynamics (MD) simulation are employed: all-atomistic molecular dynamics (AAMD) in which every atom is treated as a single particle, and coarse-grained molecular dynamics (CGMD) where multiple atoms are grouped into a single “superatom” or particle to improve computational efficiency and increase the size of systems we can study. Further information on the coarse-graining techniques employed are discussed in Section 2.4, with the discussion in this section being applicable to both types of simulation.

Molecular dynamics itself, first utilized in the 1950s⁷²⁻⁷³, is a simulation of the physical movements of particles within a given system, where these particles can represent atoms, molecules, or even some other coarse-grained entity. AAMD simulations have been previously used to study the behavior of CNCs^{65, 74-83}, and have proven to be a very versatile simulation method to probe material behavior at small length and time scales. The exact representation or meaning of the particles used in simulation is not crucial to the formulation of MD itself, but rather the most important component of an MD simulation is the effective interatomic potential energy between particles. This interatomic potential energy is where factors such as the specific chemistry, degree of coarse-graining, and any external force fields come into consideration. The main objective of MD is to simulate the evolution of a system over time in terms of particle positions, velocities, and accelerations and then use this information coupled with statistical mechanics principles to accumulate information about the structural, thermodynamic, and mechanical properties of the system.

At face value, an MD simulation is simple. One conducts an MD simulation by integrating Newton's equations of motion and updating the positions and velocities of each particle. For a system of N particles, the equation of motion that must be solved is given by Eq. (2-1)

$$m_i \vec{a}_i = -\nabla U(r_1, r_2, \dots, t) + \vec{f}_i, \quad i = 1, 2, \dots, N \quad (2-1)$$

where m_i is the mass of particle i , \vec{a}_i is the acceleration vector of particle i , U is the interatomic potential between particles that is a function of all atom positions and time, and \vec{f}_i is any constant force that is added to the system. By integrating these equations in time, the trajectory of the particles (i.e. their position and velocity) within the system can be traced and many key system properties can be extracted including temperature, pressure, bond energy, etc. However, unlike

continuum mechanics where analytical solutions to Newton's equations exist, no general solutions exist so a numerical integration technique must be implemented in these N-body systems.

There are several factors to consider when choosing the specific numerical algorithm to solve Eq. (2-1) numerically, including stability and accuracy of the method as well as practical considerations such as programming simplicity and computational memory requirements. One of the most popular algorithms that is used to obtain MD trajectories and update atom positions and velocities over time is the Velocity Verlet algorithm⁸⁴. Assuming the particle accelerations can be determined using Eq. (2-1) along with the specific interatomic potential, and we employ a time step of δt , the updated positions and velocities are given by Eq. (2-2) and (2-3), respectively.

$$\vec{r}(t + \delta t) = \vec{r}(t) + \delta t \vec{v}(t) + \frac{1}{2} \delta t^2 \vec{a}(t) \quad (2-2)$$

$$\vec{v}(t + \delta t) = \vec{v}(t) + \frac{1}{2} \delta t [\vec{a}(t) + \vec{a}(t + \delta t)] \quad (2-3)$$

These updated positions and velocities are determined by estimating the time derivatives of velocity and acceleration with a second-order Taylor series expansion around the point $t + \delta t$. Notably, this implicit integration method is inherently stable as it updates the particle velocity using information about the current force on the particle, at time t , as well as the force imparted on the particle at the next time step, time $t + \delta t$, that is obtained using the updated position in Eq. (2-2). While this method is inherently stable, one of the most important choices to make in an MD simulation is the time step to accurately capture all characteristics of the system. Because a numerical technique is employed, an appropriate time step must be chosen to ensure conservation of energy and physically correct motions of particles within the system. For example, if too large a time step is chosen then the algorithms might cause particles to overlap or polymer chains to pass through one another – motions that are not physically possible. Therefore, the time step must

be chosen such that it captures the fastest motion of the system that is relevant to the simulation. Typically, time steps are used that are 1/10 the time of the fastest period of relevant motion in the system. On the molecular scale, these time steps are typically on the order of femtoseconds (10^{-15} seconds) and in all our fully atomistic simulations a time step of 1 fs is employed. When utilizing coarse-graining techniques in which multiple atoms are mapped to a single particle, this allows for an increase in time step while still preserving information about the dynamics of the system.

In addition to understanding numerical integration techniques, molecular dynamics simulations also require the use of a statistical ensemble that describes the possible microstates of the system⁸⁵. In these ensembles, a partition function is used to describe the probability of each specific microstate and is dictated by the quantities that are held fixed in simulation. Four molecular ensembles of interest are the microcanonical ensemble (NVE), canonical ensemble (NVT), grand canonical ensemble (μ VT), and isothermal-isobaric ensemble (NPT). The abbreviations that follow the ensemble names indicate the quantities that are held fixed during simulation with N being the number of particles, V being the system volume, T being the system temperature, μ being the chemical potential of the system, and P being the system pressure. Depending on the properties of interest and the aim of a simulation, a different molecular ensemble may be employed. Information about the specific ensemble employed for a simulation is included in each specific chapter of the text.

Although it is entirely possible to create one's own MD code that utilizes numerical integration techniques to evolve the system in time, there are multiple readily available software packages that can be employed. These software packages, includes LAMMPS⁸⁶, NAMD⁸⁷, GROMACS⁸⁸, and AMBER⁸⁹, among numerous others, offer wide flexibility to simulate a number of different systems using a wide range of force fields. These packages have been developed

extensively over the past 20 or so years and offer a great amount of flexibility to simulate and analyze systems from several different perspectives. For the majority of our all-atomistic simulations, we chose to employ the NAMD molecular dynamics package for simulations as it was specifically designed for simulating the behavior of biomolecular systems. Further, it is capable of natively implementing the force field we use to model interactions of cellulose nanocrystals (Section 2.2) and has a strong steered molecular dynamics (Section 2.4) package built directly into the code. For our grand canonical Monte Carlo simulations (Section 2.5), we utilize the LAMMPS molecular dynamics package as it provides more versatility in performing this specific simulation technique. Additionally, the coarse-grained simulations also utilize LAMMPS as the interatomic potential and data output needs are more easily incorporated with the software.

2.2 CHARMM Force Field

One of the most important aspects of MD simulations is the choice of appropriate force-field parameters that describe the interatomic potential energy between atoms (U in Eq. (2-1)). The parameters used in these force fields directly influence the calculated macroscale properties and physical behavior of the system. In our simulations, we limit ourselves to the use of empirical force fields that reproduce structural and conformational changes within a system but do not consider chemical reactions. It is important to note that these chemical reactions can be considered using a reactive force field such as ReaxFF. Here, we discuss the force field employed in our fully atomistic modeling of CNCs, small molecules, and synthetic polymers. The force field used in our coarse-grained modeling efforts will be described in Chapter 9 (page 156).

Although the interatomic potential is generalized to a single variable in Eq. (2-1), this potential is really the sum of several different molecular level energy contributions including non-bonded van der Waals interactions, bond stretching, bending, and torsion, and electrostatic,

Coulombic interactions. Although there could be even more contributions to the total potential energy, such as improper terms or Urey-Bradley terms, we limit ourselves to the inclusion of the terms that are calculated by NAMD. Within NAMD, the total potential energy is the sum of the individual contributions and given by Eq. (2-4).

$$U = U_{non-bonded} + U_{Coulombic} + U_{bond} + U_{angle} + U_{dihedral} \quad (2-4)$$

The mathematical form of each of these contributions to the total potential energy is governed by the specific force field employed. In this research, we use the CHARMM force field⁹⁰⁻⁹³ that has the following analytical form for the total potential as given by Eq. (2-5).

$$U = \sum_{i,j} \varepsilon \left[\left(\frac{R_{min_{i,j}}}{r_{i,j}} \right)^{12} - 2 \left(\frac{R_{min_{i,j}}}{r_{i,j}} \right)^6 \right] + \frac{q_i q_j}{4\pi\varepsilon_0 r_{i,j}} + \sum_{bonds} k_b (r - r_0)^2 \quad (2-5)$$

$$+ \sum_{angles} k_\theta (\theta - \theta_0)^2 + \sum_{dihedrals} k_\phi [1 + \cos(n\phi - \delta)]$$

The first term in the equation represents the non-bonded interactions (both van der Waals and electrostatic) between beads summed over all pairs of particles. The van der Waals (vdW) energy is calculated using a standard 12-6 Lennard-Jones potential where ε is the depth of the potential energy well and $R_{min_{i,j}}$ is the location where the potential energy function reaches a minimum value. The electrostatic energy is calculated using the standard Coulombic potential between two point charges of values q_i and q_j , with $\varepsilon_0 = 8.85 \times 10^{-12}$ F/m being the permittivity of free space. The remaining terms in the force field correspond to bond stretching, bond bending, and bond torsion, respectively. For bond stretching and bending, a harmonic, linear spring potential is employed where a bond stiffness, k_b , and bond angular stiffness, k_θ , measure the energy deviations from the equilibrium bond length and angle (r_0 and θ_0 in Eq. (2-5), respectively). The bond torsion energy is a function of the dihedral angle ϕ , dihedral force constant k_ϕ , multiplicity

of the function n , and phase shift δ . As mentioned previously, the CHARMM force field may also contain energy contributions from improper (out of plane angles) and Urey-Bradley (distance between atoms 1 and 3 in an angle) terms, but they are omitted in this study as they are not important in the context of CNCs or other synthetic polymer materials. Here we have highlighted the force field used in our fully atomistic simulations, and the following section will further elaborate on the parameters employed for different materials in simulation.

2.3 CHARMM Force Field Parameters

The reason that the CHARMM force field was employed in our studies of CNCs is because CHARMM parameters for carbohydrates have been previously obtained and verified by other researchers⁹⁴. Optimization of parameters for a force field is one of the most challenging aspects of molecular simulation and often involves extensive quantum mechanical (QM) calculations. Extensive research has been conducted to parameterize force fields to match vibrational and conformational properties of atoms, molecules, and larger assemblies. Even with these well-established parameterization techniques, it is still challenging to match all physical properties with a single force field and set of parameters. A recent study examined the effect of different force fields on simulating the mechanical properties of CNCs and found that the force field used greatly influenced the calculated material properties⁹⁵. However, we aim to alleviate these parameterization concerns by utilizing a well-established parameter set that also shows good agreement with experimental measurements.

Here, we take advantage of previous parameterizations of a biomolecular force field for carbohydrate monosaccharides⁹⁶⁻⁹⁷. These parameterization studies focused on not only matching the free energies of these individual building blocks in the condensed phase, but also have shown that when put together they accurately match polysaccharide behavior. Because cellulose itself is

a polysaccharide (long chains of glucose units bound together), this force field is an excellent candidate to study the behavior of CNCs and will be employed in all simulations. Another advantage of choosing the CHARMM force field is that it has been parameterized for many other materials whose interactions with CNCs we are interested in studying in future research such as polymers, water, and numerous inorganic materials.

While parameters are readily available for cellulose, a key component of our work is to examine the molecular level interactions of CNCs and cellulosic materials with synthetic polymers, small molecules, and water. One of the advantages of using the CHARMM force field in simulation is the existence of the generalized CHARMM force field (cgenff)⁹⁸. This generalized force field contains a database of parameters that have been agglomerated from numerous prior studies. Using this generalized force field, CHARMM force field parameters for any arbitrary chemical structure based simply on the connectivity of the atoms within the molecule. In this parameterization method, force field parameters are obtained by analogy with other chemical structures that have been extensively parametrized and verified through quantum calculations and/or experiments. For example, if a new structure we wish to parameterize contains a carbon atom bonded to another carbon atom, an oxygen atom, and a hydrogen atom, we would search the generalized force field database to find similar chemical connectivity and assign parameters accordingly.

To obtain parameters using this method, one can simply upload the chemical structure to an online tool that performs atom typing and assignment of parameters. In addition to providing parameters, the cgenff program also provides a penalty value that indicates the “goodness of fit” of the parameters to the specific structure. If the penalty values are low (less than 10), then the parameters can be used immediately, however, if the penalty values are high then some additional

validation or recalibration of the parameters is needed. In this work, parameters for the synthetic polymers studied (polystyrene, poly(methyl methacrylate), and DGEBA-based epoxy) were all obtained using the cgenff program. The specific parameters obtained for these materials and used in our simulations are provided in Chapter 12 (page 226).

Despite the broad applicability of cgenff to a wide range of organic small molecules and synthetic polymers, there are some cases where the parameters obtained have high penalty values (> 50) associated with them. As an alternative, the partial charges and structural force field parameters can be determined using the Force Field Toolkit⁹⁹ (FFTK) package implemented in Visual Molecular Dynamics¹⁰⁰ (VMD). FFTK is a protocol that allows for rapid parameterization of small molecules using optimization methods that minimize differences between quantum-mechanical (QM) calculations and molecular mechanics (MM) calculations with the CHARMM force field. Specifics of the methodology are included in the original reference, but the overall technique will be briefly summarized here. First, the molecule's geometry is optimized using QM calculations performed using Gaussian09¹⁰¹ with second-order Møller–Plesset perturbation theory (MP2) and the 6-31G(d) basis set. Using this optimized geometry, the partial charges are then determined by performing QM calculations of the interactions of the molecule with single water molecules at hydrogen bond donor and acceptor sites within the molecule. These results are used to estimate the partial charges through an optimization procedure that aims to match the interaction energy with water molecules and the molecule's electric dipole moment μ defined by Eq. (2-6)

$$\mu = \sum_i q_i \mathbf{r}_i \quad (2-6)$$

where q_i is the partial charge of atom i and \mathbf{r}_i is the distance of each atom from the geometric center of the molecule. Next, QM simulations are performed to calculate the Hessian matrix for the system and determine the potential energy surface (PES) for the molecule. These results are

then used in an iterative optimization procedure where bond and angle parameters (i.e. stiffness and equilibrium position) are determined by matching QM and MM results. Finally, the dihedral parameters are obtained by performing dihedral perturbations in QM calculations to map the dihedral energy landscape. Again, the MM parameters are determined using an optimization routine to match the QM and MM results. In this work, the FTK protocol was used to determine force field parameters for the surface modifications studied in Chapter 6 (page 102) and Chapter 8 (page 135).

2.4 Steered Molecular Dynamics Simulation Technique

Although molecular dynamics at its core involves solving Newton's equations of motion for a set of particles using pre-defined force fields, there have been several additional techniques developed that can be used to manipulate these systems. Steered molecular dynamics (SMD) is a simulation technique¹⁰² that can be used to replicate experimental nanomanipulation procedures such as atomic force microscopy (AFM). In AFM experiments, molecules or other nanoscale structures are pulled via their attachment to a cantilevered tip and the forces/motions of this tip are recorded and used for analysis. These experimental procedures are often used to probe interfacial and mechanical properties of nanoscale materials¹⁰³⁻¹⁰⁵, but difficulty remains in precisely controlling parameters such as pulling direction and making accurate measurements.

However, when replicating this process in simulation using SMD techniques, one can more easily control the failure of the system with the added benefit of atomic resolution. SMD is a non-equilibrium computational technique where a force is applied to the system (or a subset of it) to enhance the sampling of a certain configurational space. To apply this force to the system, the steered/pulled atoms are tethered to a virtual atom through a harmonic spring. This virtual atom is moved with either a constant velocity or a constant force, and consequently through this motion

and attachment of the virtual harmonic spring, all the steered particles in the system move as well. It is important to note that in all our simulations we employ constant velocity SMD conditions. The harmonic spring potential that links the virtual atom to the steered atom is defined by a spring constant k and pulling velocity v . As the virtual particle moves, the force F_{smd} applied to the steered particles is given by Eq. (2-7)

$$F_{smd} = k(vt - x(t)) \quad (2-7)$$

where t is the elapsed simulation time and $x(t)$ is the distance of the center of mass of the steered atoms from its initial position. It should be noted that Eq. (2-7) represents the case in which the steered atoms are moved along a straight-line path (i.e. atoms are pulled in a single direction), but the SMD technique is also applicable to any generalized set of directions. Selecting which atoms should be steered, fixed, or further constrained is important to accurately simulate the intended mechanical deformation. The selection of these groups of atoms will be discussed for each individual study in Chapters 3 (page 45) and 4 (page 65).

The output of SMD simulations is the displacement of the steered atoms and the force applied to these atoms. From these quantities, we calculate the non-equilibrium work done on the system by the SMD potential along the reaction coordinate of interest as given by Eq. (2-8)

$$W = \int_A^B F_{smd} \cdot dx \quad (2-8)$$

where A and B are the initial and final states of the system. In order to recreate the free-energy landscape (or equivalently the potential of mean force (PMF)) of some failure process, the non-equilibrium work must be linked with the reversible work. However, this is often challenging in non-equilibrium simulations because of the short time scale of MD simulations and the high variability between the work calculated using different initial conditions/trajectories.

In order to address these challenges and link the non-equilibrium process to the equilibrium, reversible work, we employ Jarzynski's equality¹⁰⁶. This equality is founded in thermodynamic principles and takes advantage of the fact that the average work performed on a system is always greater than or equal to the free energy difference between two specified states as stated by Eq. (2-9).

$$\langle W \rangle \geq \Delta F \quad (2-9)$$

The inequality of Eq. (2-9) is only valid in the case of a quasi-static process in which the system transitions between two equilibrium states infinitely slowly. However, Jarzynski derived the following equality that relates the free energy between equilibrium states and the non-equilibrium work of a process (as measured during SMD simulations) as given by Eq. (2-10)

$$\langle e^{-\beta W} \rangle = e^{-\beta \Delta F} \quad (2-10)$$

where $\beta = 1/k_b T$ is the inverse of the thermal energy and k_b is Boltzmann's constant. From this equation, one can obtain an exponential average of the free energy as given by Eq. (2-11)

$$\Delta F_{exp} = -\frac{1}{\beta} \log \langle e^{-\beta W} \rangle \quad (2-11)$$

Despite the validity of this equality and averaging scheme, it has been noted that the exponential average is not always the most desirable as it requires many samples to produce accurate results. Instead, an averaging scheme that is more accurate using fewer samples is desirable as this requires fewer simulations to be conducted and has a lower computational cost associated with it. Park et al.¹⁰² examined a number of different averaging schemes, and determined that the second cumulant expansion, given by Eq. (2-12) is an appropriate averaging scheme that typically requires between 5-10 samples to give an accurate representation of the energy landscape.

$$\Delta F_{2nd} = \langle W \rangle - \frac{1}{2} \beta [\langle W^2 \rangle - \langle W \rangle^2] \quad (2-12)$$

Beyond methods for analyzing multiple SMD trajectories, another important consideration for this technique is the selection of appropriate SMD parameters; namely the pulling velocity and virtual spring constant. As discussed rigorously in the paper by Park et al.¹⁰², a high spring constant is necessary in order to reduce mechanical vibrations of the pulled atoms and ensure realistic failure. Figure 2-1 shows the dependence of the calculated energy landscape on the SMD spring constant for shear failure of a CNC-CNC interface. For low values of the spring constant, one observes severe oscillations in the energy landscape that lead to unrealistic behavior of the system. However, as the spring constant is increased, system vibrations during pulling are decreased and there are no observable effects of this parameter on the energy landscape. Therefore, in line with previous observations of Park et al.¹⁰², a high spring constant is appropriate and for all simulations outlined in this paper a spring constant of 4000 kcal/mol-Å² is used in order to reduce vibrations between the virtual and steered atoms.

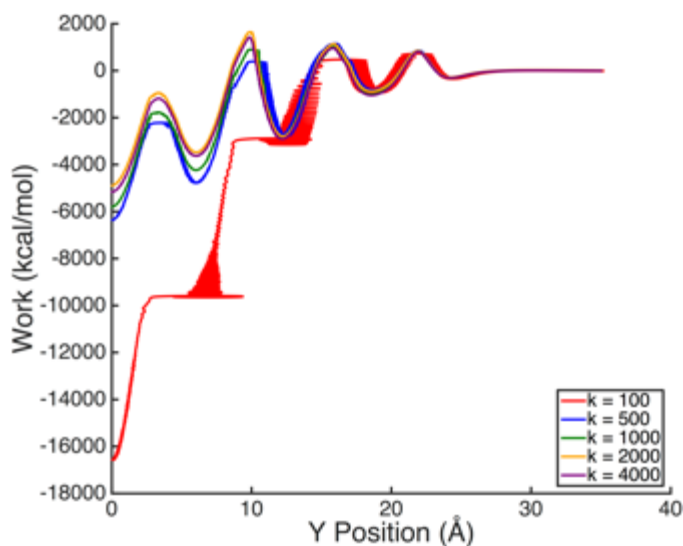


Figure 2-1: Effect of SMD spring constant. Comparison of the energy landscapes obtained from SMD simulations of CNC-CNC interfacial shear failure using spring constants ranging from 100 kcal/mol-Å² to 4000 kcal/mol-Å². The results indicate that as the spring constant is increased, the oscillations exhibited by the steered atoms decrease and the failure modes become more realistic as they are dominated by intermolecular interactions instead of external system oscillations. These results support the choice of a high spring constant in order to maintain the stiff spring approximation explained by Park et al.¹⁰² in their paper.

Additionally, it is important to choose a pulling velocity low enough such that the system does not show any rate dependence. For fast pulling rates, the free energy shows strong rate dependence and leads to unrealistic energetics and calculated mechanical properties. However, it is also important to consider pulling rates that are computationally reasonable as selecting rates that are too low will lead to incredibly long and computationally expensive simulation times with minimal gains in simulation accuracy. To choose an appropriate rate, rate dependence studies were conducted for the systems studied here. The results of shearing a CNC-CNC interface at different pulling rates are shown in Figure 2-2. Here, we see that changing the SMD pulling velocity from 0.005 Å/ps to 0.1 Å/ps (0.5 m/s to 10.0 m/s) does not appreciably change the system behavior nor the energy landscape. Therefore, any pulling velocity below 0.1 Å/ps would be an appropriate

choice for our simulations as there is no rate dependence below this value. Therefore, in all simulations we employ a pulling velocity of 0.02 \AA/ps (2 m/s) as a feasible experimental pulling rate that is computationally efficient to simulate. In this section, we have illustrated the importance of SMD parameter selection for one specific system. Similar studies on rate dependence have been conducted for each study within this work and SMD parameters have been carefully chosen as discussed in the following chapters.

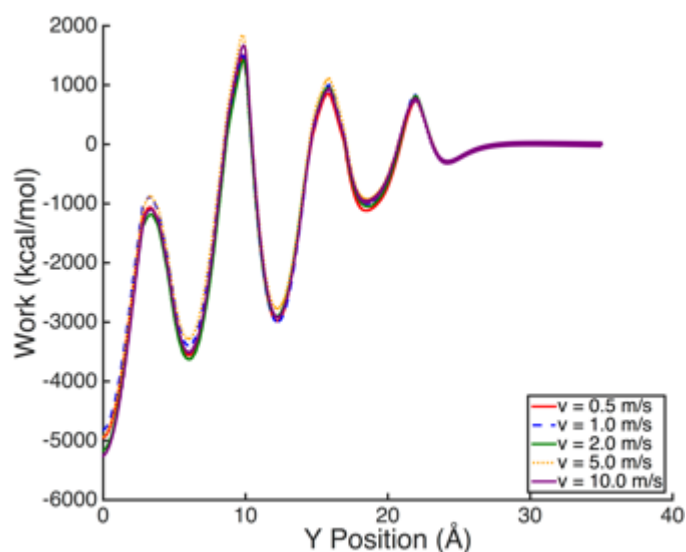


Figure 2-2: Rate dependence of SMD pulling velocity. Comparison of the energy landscapes obtained from SMD simulations of CNC-CNC interfacial shear failure using pulling velocities ranging from 0.5 m/s to 10.0 m/s . The results indicate that these pulling velocities are below the critical velocity above which there is rate dependence of the energy landscape.

2.5 Grand Canonical Monte Carlo (GCMC) Simulation Technique

While SMD focuses on probing the mechanical properties of systems, there are other molecular simulation techniques that focus on aspects such as mapping potential energy surfaces, quantifying relaxation behavior, and measuring water adsorption. Measuring water adsorption is of particular interest for CNCs and their associated nanocomposites as it can greatly influence mechanical properties. To study this behavior in simulation, a technique known as grand canonical

Monte Carlo (GCMC) is utilized. GCMC simulations are conducted under the grand canonical (μVT) ensemble in which the chemical potential, volume, and temperature of the system are held constant. Notably, in this ensemble the number of particles is not held constant and therefore allows for the insertion or deletion of particles over the course of the simulation. This key feature provides versatility in that molecules can be added or deleted throughout the simulation while preserving key system parameters. This process has been previously utilized to study the adsorption characteristic of other cellulosic materials^{75, 107} and has shown good agreement with experiments.

After a system has reached equilibrium, GCMC simulations are used to perform exchanges (i.e. insertions or deletions) of water molecules with an imaginary ideal gas reservoir at a fixed temperature and chemical potential. At each GCMC step, insertions and deletions are attempted in a Monte Carlo framework in which the acceptance probability of such a move is governed by the change in the potential energy of the system resulting from the insertion or deletion. One important factor in these simulations is that insertions and deletions must be attempted using equal probability, and the acceptance rate is governed by the Metropolis criterion¹⁰⁸. In addition to performing the insertions and deletions, traditional MD simulations (using an NVT ensemble) are performed in between these GCMC steps in order to re-equilibrate the system with the newly inserted or deleted water molecules accounted for. These combined GCMC-MD simulations are run until an equilibrium number of water molecules is reached and allow for the adsorption of water in the system to be quantified. This method is primarily utilized in Chapter 6 (page 102), where specific simulation parameters are further discussed.

2.6 Dissipative Particle Dynamics

The final simulation technique/approach that is discussed here and later employed in Chapter 9 (page 156) is dissipative particle dynamics (DPD)¹⁰⁹⁻¹¹⁰. DPD is a thermostating method used in systems where preservation of accurate hydrodynamics is important (e.g. the flow of water in a nanochannel). With traditional MD thermostats, such as the Langevin thermostat employed in most of our simulations, temperature is conserved in the system by rescaling particle velocities. This approach is usually adequate, however, one of the negative consequences¹¹¹ is that by rescaling velocities, momentum of the system is not conserved. While this is not a problem for quasi-static, equilibrium simulations, it causes issues where momentum plays an important role in governing system properties and behavior, such as the flow of fluids. Instead, DPD thermostats aim to preserve momentum and system temperature by simulating the interaction of soft spheres with three forces: a conservative force F^C , a dissipative force F^D , and a random force F^R . The method will be briefly described in the following paragraph, but for a further explanation and derivation the reader is encouraged to examine the following references¹⁰⁹⁻¹¹⁰.

The DPD force contains three components (conservative, dissipative, and random) that are summed over all pairs of molecules i and j and is given by Eq. (2-13).

$$f_i = \sum_{ij, i \neq j} F_{ij}^C + F_{ij}^D + F_{ij}^R \quad (2-13)$$

Additionally, we note that this formulation includes a cut-off radius of $r_c = 12 \text{ \AA}$ for the calculation of these forces to improve computational efficiency in our simulations. The conservative force F_{ij}^C is a soft repulsion between particles given by Eq. (2-14) where \mathbf{r}_{ij} is the vector between the positions of particles i and j and a_{ij} indicates the strength of the repulsion.

$$\mathbf{F}_{ij}^C = \begin{cases} a_{ij}(1 - r_{ij})\widehat{\mathbf{r}}_{ij} & (r_{ij} < r_c) \\ 0 & r_{ij} \geq r_c \end{cases} \quad (2-14)$$

Second, we consider the dissipative or drag force between particles given by Eq. (2-15) where γ is the damping parameter, \mathbf{v}_{ij} is the relative velocity of particles i and j , and w^D is some weighting function. This is the force that is specifically incorporated in order to preserve momentum of the system while also maintaining the system temperature.

$$\mathbf{F}_{ij}^D = -\gamma w^D(r_{ij})(\mathbf{r}_{ij} \cdot \mathbf{v}_{ij})\widehat{\mathbf{r}}_{ij} \quad (2-15)$$

Finally, the random force is given by Eq. (2-16) where σ is some scaling factor, w^R is some weighting function, and θ_{ij} is a randomly fluctuating Gaussian variable.

$$\mathbf{F}_{ij}^R = \sigma w^R(r_{ij})\theta_{ij}\widehat{\mathbf{r}}_{ij} \quad (2-16)$$

All forces act along the line of centers between pairs of atoms and have been shown to conserve both linear and angular momentum. This thermostat is implemented directly in LAMMPS⁸⁶, where it simply requires the selection of the damping parameter which determines the degree to which energy is dissipated to control system temperature. Further, we note here that other references have shown that if certain relationships between the random force and dissipative force are satisfied, the system will have the canonical (NVT) ensemble¹⁰⁹⁻¹¹⁰. This technique has been used to study a wide range of systems including confined water¹¹², blood cells¹¹³, and polymer nanoparticles¹¹⁴ and will be used in this work to examine the behavior of water flow within a nanopore in Chapter 9 (page 156).

Chapter 3 – Size Dependence of CNC Fracture Energy

This chapter focuses on the materials discovery aspect of computational materials-by-design and aims to understand the underlying chemistry and mechanics of CNCs that give rise to their impressive mechanical properties. This study aims to further elucidate size dependence of CNC mechanical properties when fractured along their weakest crystalline plane. Using SMD techniques, we cause failure of an individual CNC and characterize the energy landscape of this failure process, as well as quantify fracture properties of CNCs. We examine the dependence of the fracture energy on both CNC thickness and CNC width and provide explanations for the observed size effects. Using these size dependent scaling laws, we predict an optimal size for CNCs from a fracture perspective and demonstrate that this size is in line with the observed size of CNCs in nature's toughest materials – thereby shedding light on a natural design principle. Portions of the text and figures within this chapter are reprinted or adapted with permission from Sinko et al., *ACS Macro Letters* 2014⁶⁵. Copyright 2014 American Chemical Society.

3.1 Simulation Parameters

In this set of simulations, we aim to study the fracture behavior of an individual monoclinic CNC along the (200) plane. Sonication experiments have shown cellulose microfibrils to peel along the (200) plane while maintaining all intrasheet interactions, suggesting this to be the weakest plane under isotropic loading conditions^{33, 115}. In order to simulate the fracture of CNCs, we utilize the SMD techniques discussed in Chapter 2 (page 27). All simulations are conducted using NAMD⁸⁷ and the parameters from the CHARMM 37 force field for carbohydrates^{94, 96}. The CNC structures were generated using the cellulose-builder toolkit¹¹⁶ that allows one to generate a wide range of cellulose crystal polymorphs, shapes, and sizes. Simulations employ periodic boundary conditions in an NVT ensemble (constant number of particles, volume, and temperature)

with full electrostatics calculated using a particle mesh Ewald having a resolution of approximately 1 Å. Although we are using periodic boundary conditions, the structures being studied are finite crystals and therefore we employ vacuum padding in each dimension to prevent the CNC from interacting with its periodic image across boundaries. Vacuum is created in the simulation box 15 Å in each direction normal the (100) and (010) surfaces and 30 Å normal to the (200) surface to accommodate the deformation of the crystal during simulation and ensure no periodic interactions.

The monoclinic CNC, pictured in Figure 3-1, is equilibrated for 2 nanoseconds at a temperature of 300K with no constraints applied. After equilibration, 10 snapshots of the system are taken at 100 picosecond intervals to be used as the initial equilibrated conformations for the SMD simulations. During these SMD simulations, the carbon atoms in the cellulose chains in the lower half of the crystal (blue atoms in Figure 3-1) are fixed in space. Fixing these atoms ensure that the CNC will fail/cleave along the middle plane within the crystal. The SMD force is applied to all atoms (carbon, oxygen, and hydrogen) in the top half of the crystal (orange atoms in Figure 3-1). All of the steered atoms are constrained to move only in the pulling direction to cause pure interfacial failure and prevent peeling along the failure plane. SMD simulations are conducted until the two crystal halves are completely separated with this process taking approximately 1 nanosecond of simulation time.

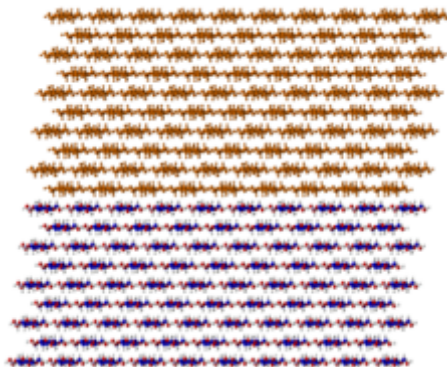


Figure 3-1: Atom assignments for SMD simulations of CNC fracture. This VMD snapshot shows a monoclinic CNC that is used to study failure of the (200) plane within the crystal. During SMD simulations, the carbon atoms in the bottom half of crystal (blue atoms) are fixed to their initial position while all atoms in the top half of the crystal (orange atoms) are pulled by the SMD force. Additionally, the steered atoms are also constrained to move only in the pulling direction to prevent peeling along the failure plane.

3.2 Mechanical Properties and Energetics of CNC Fracture

The first simulation conducted was the fracture of a single monoclinic CNC having crystalline dimensions of 7x10x10, with these units corresponding to the number of crystalline repeat units. The energy landscape for the failure process is shown in Figure 3-2(A) with the corresponding stress-strain plot shown in Figure 3-2(B). From the energy landscape, or alternatively the potential of mean force (PMF) obtained from multiple SMD simulations, we can directly obtain the fracture energy of the crystal which is simply the difference in the energy between the equilibrium and separated state. The free energy difference for this crystal is calculated to be $\sim 14,560$ kcal/mol. To quantitatively compare this value to other materials, it is necessary to normalize this quantity by the cross-sectional area of the crystal (8511 \AA^2) which results in a measured fracture energy of $1.71 \text{ kcal/mol-\AA}^2$ (1.19 J/m^2). This value is comparable to that of many brittle materials such as silica glass that have an experimentally measured fracture

energy ranging from 1–5 J/m²¹¹⁷. Our analyses presented here suggest that even though CNCs exhibit relatively weak molecular interactions, they have a high work required to fracture.

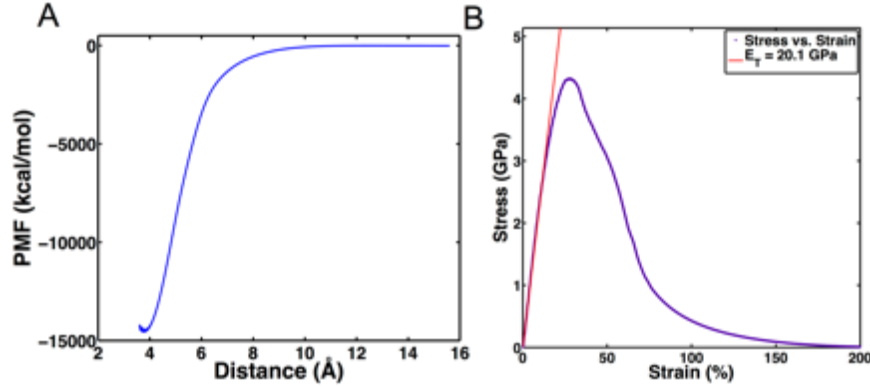


Figure 3-2: Free energy landscape and stress-strain curve for CNC failure. (A) Free energy landscape or potential of mean force (PMF) for the failure of an individual 7x10x10 CNC (units indicate number of crystalline repeat units). The fracture energy of the crystal is measured as the difference in energy between the equilibrium and separated states and is approximately 14,560 kcal/mol. (B) Using thermodynamic principles, the stress-strain curve can be obtained directly by differentiating the energy landscape. From this plot, the transverse modulus of the CNC is measured to be 20.1 GPa, which is in good agreement with recent experimental measurements.

In addition to the fracture energy, our simulations allow us to examine mechanical properties of CNCs from the stress-strain curve presented in Figure 3-2(B). The calculation of this stress-strain curve from the energy landscape is not trivial, but is rather based on thermodynamic principles as outlined below¹¹⁸. The PMF profile shown in Figure 3-2(A) is analogous to the Helmholtz free energy profile, with the differential of this profile given by Eq. (3-1)

$$dF = -SdT + V_0 \sum_{ij} \sigma_{ij} \varepsilon_{ij} \quad (3-1)$$

where S is the entropy, T is the temperature, V_0 is the equilibrium volume of the system, and σ_{ij} and ε_{ij} are the stress and strain tensors respectively. In one dimension $\sigma_{ij} = \sigma$ and $\varepsilon_{ij} = \varepsilon$ and the stress can be written as shown in Eq. (3-2).

$$\sigma(\varepsilon) = \left(\frac{\partial(F/V_0)}{\partial\varepsilon} \right)_T \quad (3-2)$$

Applying basic continuum mechanics concepts, the Young's modulus E (i.e. the elastic stiffness of the system along the reaction coordinate) is given by Eq. (3-3).

$$E = \left(\frac{\partial\sigma}{\partial\varepsilon} \right)_T \quad (3-3)$$

For a non-linear, elastic material the Young's modulus would depend on the level of strain, $E = E(\varepsilon)$. The Young's modulus corresponding to zero strain $E(\varepsilon = 0) = 20.1$ GPa is measured from the stress-strain plot in Figure 3-2(B) and is a reasonable approximation up to levels of strain of ~20% (i.e. the stress-strain curve is approximately linear below 20% strain). This modulus value falls into the range predicted from previous simulations as well as atomic force microscopy experiments of 11–57 GPa¹¹⁹. This value is lower than the elastic modulus along the chain direction of 110–200 GPa since the intersheet plane is stabilized by weaker molecular interactions compared to the covalent and hydrogen bonds that exist in the chain direction^{29-30, 120-124}.

Although there is extensive experimental evidence for the specific molecular interactions that are dominant in each specific crystalline direction, one can use MD simulations to further clarify their dynamics. Whereas covalent bonding stabilizes the chain direction in addition to hydrogen bonds between repeat units, stability of the cellulose sheets can be attributed to (i) the large number of hydroxyl groups that facilitate hydrogen bonding^{120, 125} or (ii) out-of-plane van der Waals interactions between the backbone rings¹²⁶⁻¹²⁷. To demonstrate these dominant interactions within our simulations, we conduct hydrogen bond occupancy analyses with the results presented in Figure 3-3. Hydrogen bond occupancy, defined as the percentage of time that a hydrogen bond is considered “on” during simulation, provides a simple numerical measure for the strength of cohesion along a plane, where longer lifetimes (i.e. higher occupancy) lead to

greater fracture strength according to many stochastic theories of fracture¹²⁸⁻¹²⁹. In all of our analyses, hydrogen bonds are measured using distance and angle criteria with a distance cutoff of 4 Å and angle cutoff of 50°, that corresponds to the upper limits of hydrogen bond formation¹³⁰. Our results show that hydrogen bonds stabilize the intrasheet direction (i.e. between individual chains) and have high occupancies greater than 90% or even up to 200% which indicates double hydrogen bond occupancy of a specific atom. On the contrary, intersheet hydrogen bonds are transient (less than 10% occupancy on average) due to unfavorable donor-hydrogen-acceptor angle of hydroxyls along this plane. Instead, the strong interaction between cellulose sheets is attributed to hydrophobic ring-ring interactions and hydrophilic ribbons within the sheets that is in line with studies supporting the amphiphilic nature of cellulose sheets^{126-127, 131}.

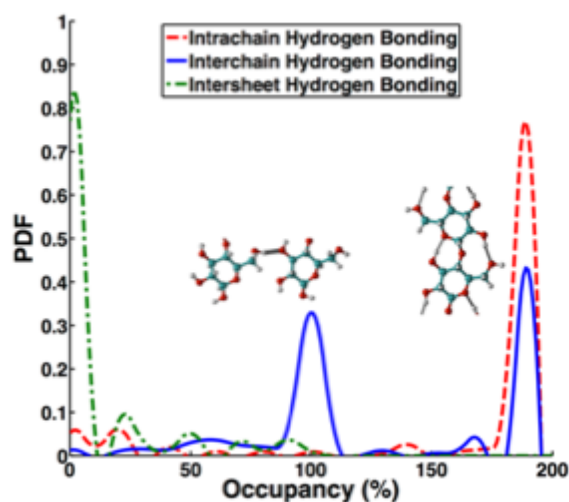


Figure 3-3: CNC hydrogen bond occupancy. This plot shows the occupancy of hydrogen bonds within a CNC during MD simulations in the intrachain, interchain, and intersheet dimensions. Hydrogen bond occupancy is defined as the percentage of time a hydrogen bond is “on” during simulation, with a value of 200% indicating that an atom can form 2 unique hydrogen bonds. Within individual chains, hydrogen bond occupancy is high in addition to covalent bonding between repeat units. In the interchain direction, the hydroxyl groups between adjacent chains promote high hydrogen bonding and stabilize the sheets. On the other hand, in the intersheet direction, hydrogen bond occupancy is low and indicates that this crystalline direction is stabilized instead by non-bonded, van der Waals interactions.

3.3 Width Size Dependence of Fracture Energy

After examining the fracture of a single CNC and understanding the underlying molecular interactions, it was determined that a size-dependence study was appropriate to conduct in line with other nanostructures observed in biology including silk nanocrystals and beta-sheets¹³²⁻¹³³. The objective of these studies was to understand how the fracture energy scales with molecular dimensions and if smaller or larger crystalline dimensions are preferred in promoting greater fracture strength. Scaling of the fracture energy with crystal size is an especially relevant aspect of both cellulose neat films and nanocomposites, as CNCs commonly act as physical cross-links that resist failure and must be appropriately sized in order to optimally serve this function.

The first size dependence study focused on varying the width of the crystal while maintaining a constant crystal thickness and cellulose chain length. The crystal width was varied from 3 chains per sheet to 15 chains per sheet, and the associated fracture energy as a function of crystal width is shown in Figure 3-4 for a chain length of 20 repeat units and a thickness of 12 cellulose sheets. The fracture energy shows a clear dependence on the crystal width with the fracture energy increasing initially with crystal width, but also exhibiting saturation to approximately 5 kcal/mol-Å² for larger widths. Upon observing this effect, our focus shifted towards understanding what factors govern this scaling relationship – specifically understanding the saturation in the fracture energy with increasing crystal width.

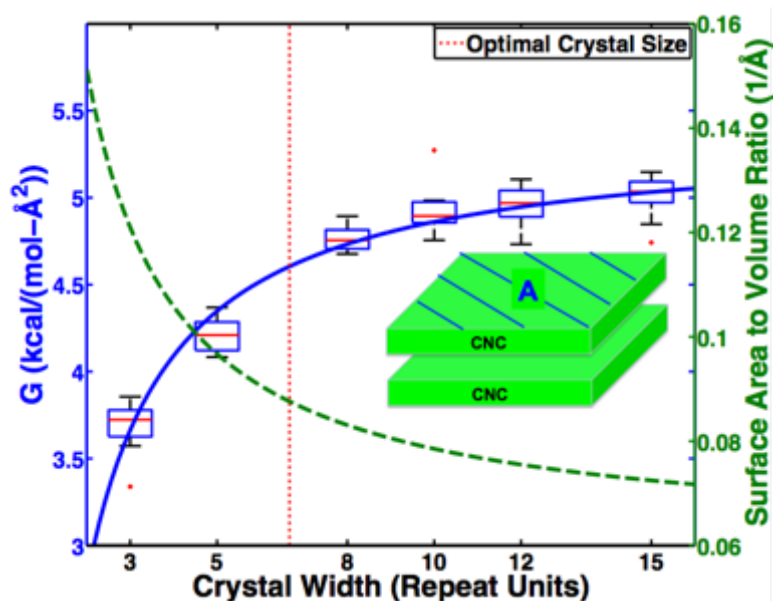


Figure 3-4: Scaling of fracture energy with crystal width. The fracture energy for CNCs ranging from a width of 3 chains per sheet to 15 chains per sheet is plotted as a function of the crystal width. The crystal width is given in terms of number of repeat units, where a repeat unit is equivalent to a single cellulose chain. These crystals have a chain length of 20 repeat units and a thickness of 12 cellulose sheets. The fracture energy initially increases with increasing crystal width but then saturates to a value of approximately 5 kcal/mol-Å² for larger widths. The proposed scaling relationship (blue curve) states that the fracture energy is proportional to the inverse of the crystal width and agrees well with simulation data. Additionally, using fracture energy and surface area to volume considerations, the optimal crystal width is between 7 and 8 chains.

Since we are changing the crystal width in this size dependence study, it is hypothesized that the scaling relationship can be attributed to some sort of edge effect. Due to the geometry of CNCs and the discrete stacking arrangement of chains, chains at the edge of the crystal overhang freely and have no chains to stabilize them in the immediately adjacent layers above or below. These chains are therefore subject to higher thermal fluctuations and their instability causes them to serve as pseudo-defects that become crack nucleation points in the crystal. To quantify these fluctuations and their instability, we measure the average root mean square deviation (RMSD) of

atomic position across the width of the system in Figure 3-5. The RMSD for an individual atom is a measure of the variation of the atomic position over time and is given analytically by Eq. (3-4)

where x_i is the position of atom i and T is the total simulation time.

$$RMSD = \sqrt{\frac{1}{T} \sum_{t_j=1}^T (x_i(t_j) - x_i(0))^2} \quad (3-4)$$

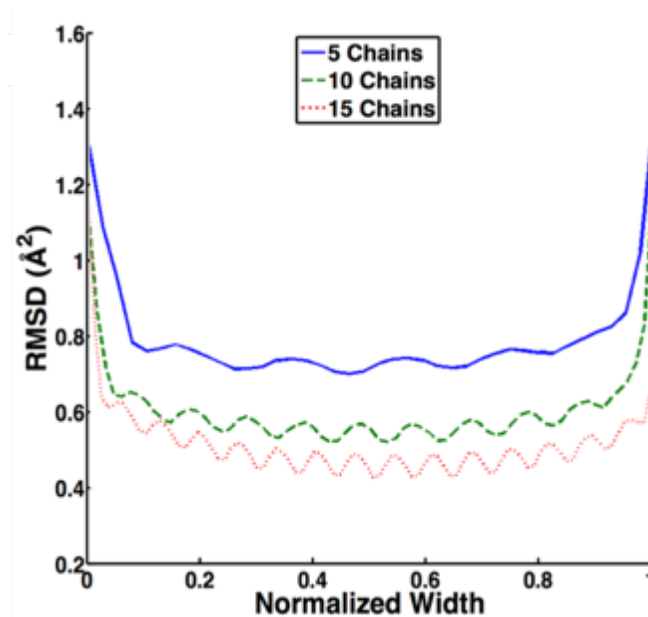


Figure 3-5: Average RMSD of CNCs as a function of width. RMSD data shows that fluctuations in atom positions are significantly greater near the edges of the crystal indicating higher thermal fluctuations and reduced stability of edge chains. For increasing crystal width, the magnitude of fluctuations decreases and the percentage of the crystal influenced by edge defects also decreases. This influence of edge defects on crystal stability helps to explain the scaling behavior of the fracture energy observed in Figure 3-4.

Upon examining the RMSD data presented in Figure 3-5, we see a change in the RMSD data along the width of the crystals and as a function of the number of CNC chains along the width. Near the edges of the crystal, the RMSD has higher values that support the notion of higher thermal

fluctuations due to decreased stability of the CNC crystalline structure. More importantly, however, are the trends observed for changing CNC crystal width. Higher overall RMSD values are observed for smaller crystals and are particularly amplified near the edges, indicating greater thermal fluctuations of the atoms and thus lower stability. These unstable regions constitute a greater portion of the overall width, thereby lowering CNC stability. For instance, CNCs with a width of 5 chains have edge regions/defects that account for nearly 20% of the overall crystal width while CNCs with a width of 15 chains have edge regions that account for only about 5% of the total width. This implies that the ideal width of a CNC inclusion must be large enough such that the edge defects play a lesser role and further that larger CNCs have greater fracture energy as they minimize the impact of the edge defect region.

Assuming that the number of edge chains that have lower binding strength and stability is more or less constant across all systems (having a width w), the fracture energy should scale inversely with the crystal width, w . This scaling relationship, given by Eq. (3-5), shows that the fracture energy, G , depends on the size of the defect region, t , and the width of the crystal, w .

$$G \sim \frac{w - t}{w} \quad (3-5)$$

Using this inverse scaling relationship, the blue curve in Figure 3-4 is obtained and is shown to fit relatively well with the simulation data. Additionally, to demonstrate that this effect is independent of the chain length, simulations were conducted for chain lengths of 5 and 10 repeat units with the results shown in Figure 3-6 below. Again, the proposed scaling relationship of the fracture energy given by Eq. (3-5) holds and fits well with the simulation data. This indicates that the scaling relationship is independent of chain length and that edge defects in the width dimension are responsible for the observed fracture energy scaling with crystal width and, more generally, cross-sectional area.

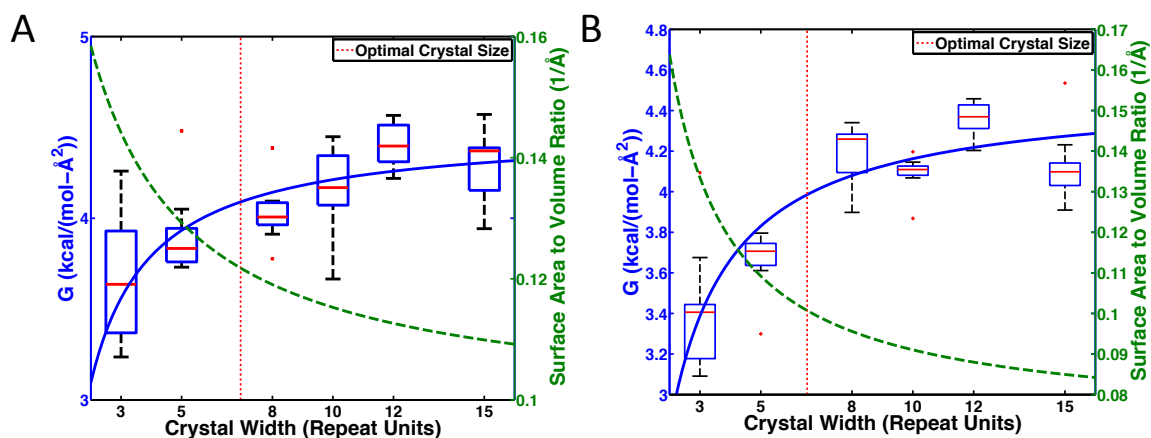


Figure 3-6: Scaling of fracture energy with crystal width: additional chain lengths. Fracture energy as a function of crystal width for a chain length of (A) 5 repeat units and (B) 10 repeat units showing an inverse width scaling relationship of the fracture energy (blue curves). These plots demonstrate that the fracture energy scaling relationship with the crystal width is independent of the chain length. Further, for all chain lengths the fracture energy saturates to a constant value of approximately 4 – 5 kcal/mol-Å² indicating that there is no observable size dependence of the fracture energy on chain length for the lengths studied here.

3.4 Thickness Size Dependence of Fracture Energy

In addition to examining the fracture energy scaling with crystal width, we examined the scaling as a function of crystal thickness. Fracture energies for CNCs ranging from 2 to 20 repeat units in the thickness dimension are presented in Figure 3-7. In these cases, the crystal width is held constant at 10 chains and the chain length is held constant at 10 repeat units. It is also important to note that each repeat unit in the thickness dimension is composed of two cellulose sheets, so the systems studied range from 4 to 40 total cellulose sheets in the thickness dimension.

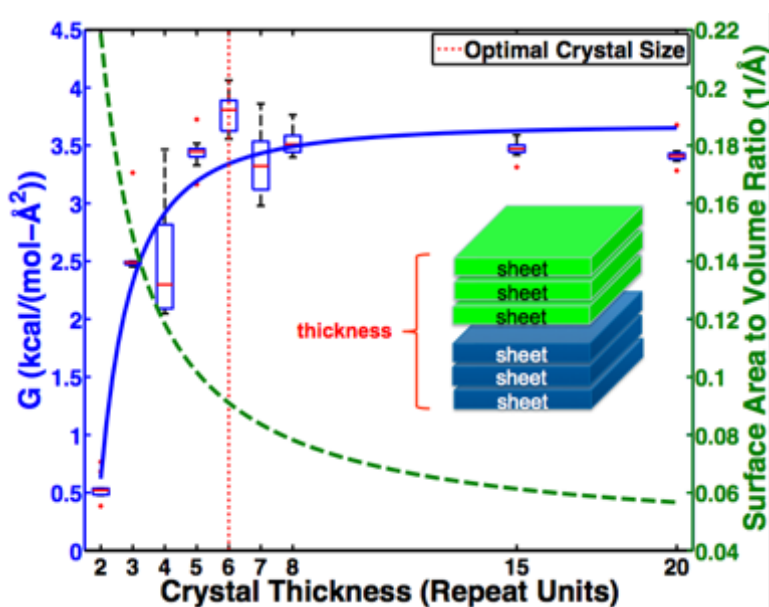


Figure 3-7: Scaling of fracture energy with crystal thickness. The fracture energy for CNCs is plotted as a function of the crystal thickness (in terms of the number of repeat units). These crystals have a constant chain length of 10 repeat units and width of 10 cellulose chains per sheet. The fracture energy initially increases with increasing crystal thickness, but then quickly saturates to a value of approximately $3.5 \text{ kcal/mol-}\text{\AA}^2$ for larger thicknesses. The scaling relationship (blue curve), shows that the fracture energy is proportional to the inverse number of sheets squared as explained by collective effects of sheet stacking. Additionally, using fracture energy and surface area to volume considerations, the optimal crystal thickness is predicted to be 6 repeat units (12 total sheets).

Figure 3-7 shows that the fracture energy exhibits a similar asymptotic scaling relationship as was observed with the width scaling. After an initial, substantial increase in the fracture energy with crystal thickness, the fracture energy saturates to a constant value of $\sim 3.5\text{-}4 \text{ kcal/mol-}\text{\AA}^2$ for larger crystal thicknesses. However, unlike the width dependence of the fracture energy this scaling cannot be explained by edge defects as the influence of edge defects is held constant for all system sizes. Instead, this scaling relationship can be explained by considering that van der Waals interactions are dominant in the sheet stacking direction and examining the collective effects

of sheet stacking. An expression for the van der Waals interaction energy E_v between two infinite plates separated by a distance a is given by Eq. (3-6)¹³⁴

$$E_v(a) = -\frac{H}{12\pi a^2} \quad (3-6)$$

where H is the Hamaker coefficient – a material constant defined for materials interacting across a specific medium. This constant has been measured for cellulose thin films separated by vacuum between the surfaces to be $\sim 5.8 \times 10^{-20} \text{ J}$ ¹³⁵.

Here we derive an expression for how the van der Waals interaction energy between two stacks of plates (i.e. CNC sheets) depends on the number of layers in each stack to explain how the fracture energy scales with CNC thickness. To derive an expression for the total interfacial energy, the energy contributions of individual sheets separated by varying distances must be computed. Given that the CNC has a well-defined crystal structure in the equilibrium state, the distances between pairs of sheets can be assumed to be discrete multiples of the equilibrium spacing, a , between individual sheets. The equilibrium spacing between cellulose sheets within the crystal is taken to be $a = 3.8 \text{ \AA}$. In our derivation, we utilize the key assumption that the Hamaker coefficient is constant in our system regardless of the medium separating the sheets. That is, we assume that the Hamaker coefficient for two cellulose sheets separated by vacuum is the same as that for two cellulose sheets separated by a combination of vacuum and any number of additional cellulose sheets.

In this case, the total energy can be derived by summing over all possible pairwise sheet-sheet interactions within the crystal. A few simple illustrations provide insight into the scaling relationship developed. The first case, illustrated in Figure 3-8, consists of two cellulose sheets on each side of the fracture interface, with the resulting interfacial energy given by Eq. (3-7).

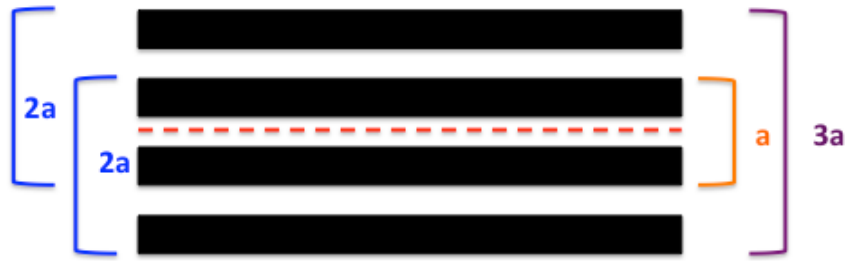


Figure 3-8: Interfacial vdW energy – 2 sheets per side. Illustration showing the individual pairwise interactions between sheets that contribute to the total interfacial energy at the fracture surface for a system consisting of 4 total sheets (2 sheets per side).

$$E_v(a) = -\frac{H}{12\pi a^2} - \frac{2H}{48\pi a^2} - \frac{H}{108\pi a^2} = -\frac{H}{12\pi a^2} \left(\frac{1}{1} + \frac{2}{4} + \frac{1}{9} \right) \quad (3-7)$$

Similarly, for three sheets on each side of the fracture interface, as illustrated in Figure 3-9, the resulting energy is given by Eq. (3-8).

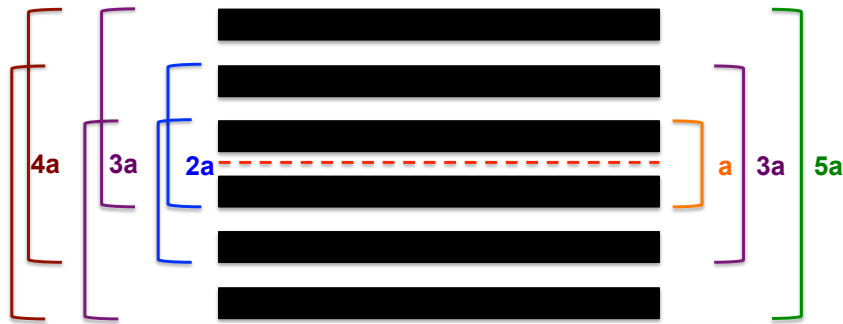


Figure 3-9: Interfacial vdW energy - 3 sheets per side. Illustration showing the individual pairwise interactions between sheets that contribute to the total interfacial energy at the fracture surface for a system consisting of 6 total sheets (3 sheets per side).

$$\begin{aligned} E_v(a) &= -\frac{H}{12\pi a^2} - \frac{2H}{48\pi a^2} - \frac{3H}{108\pi a^2} - \frac{2H}{192\pi a^2} - \frac{H}{300\pi a^2} \\ &= -\frac{H}{12\pi a^2} \left(\frac{1}{1} + \frac{2}{4} + \frac{3}{9} + \frac{2}{16} + \frac{1}{25} \right) \end{aligned} \quad (3-8)$$

Based on these simple illustrations, we can then generalize the interfacial energy along the fracture plane of the crystal in a closed form expression given by Eq. (3-9) where n is the number of sheets on each side of the fracture surface.

$$E_v(a) = \frac{H}{12\pi a^2} \sum_{i=-n+1}^{n-1} \frac{(n - |i|)}{(i + n)^2} \quad (3-9)$$

While this discrete summation is exact for the total surface energy of stacks of infinite plates based on the assumptions presented earlier, it might not accurately describe the scaling behavior observed in CNCs for several possible reasons. Deviations from the exact scaling relationship can be expected due to (i) finite size of the crystals¹³⁶, which may effectively change the distance scaling of the sheets and (ii) faster decay due to screening effects and a reduction in the Hamaker coefficient as more layers are added¹³⁷⁻¹³⁸. For example, the Hamaker coefficient between the outer-most sheets in Figure 3-8 (separated by distance $3a$) may be slightly different because there are two cellulose sheets in between that change the effective medium of long-range interactions. Based on these considerations and also considering that numerical simulations often involve cutoffs for van der Waals interactions, we assume that van der Waals interactions for any pair of sheets separated by eight or more sheets result in a negligible contribution to the total interfacial energy.

In order to illustrate how this assumption changes the numerical sum given by Eq. (3-9), we plot the exact summation and the summation with numerical cutoff in Figure 3-10. This plot demonstrates that the difference between the exact summation and the truncated sum is at most 20% for the relevant range of crystal thicknesses studied here. Although the truncated sum and exact expression would deviate more for larger crystal thicknesses, those crystal sizes are beyond CNC sizes found in natural systems, so we can confidently use this cutoff criterion.

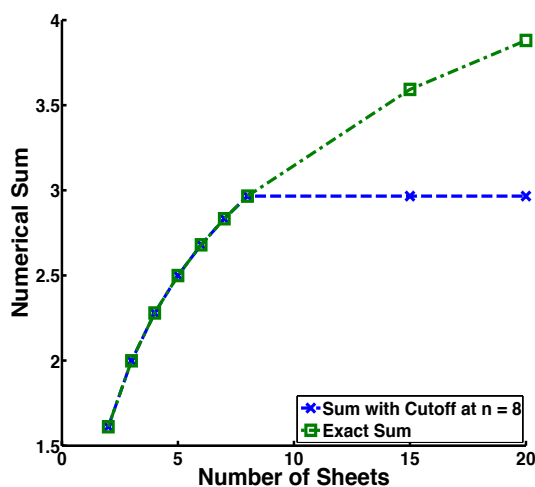


Figure 3-10: Comparison of closed-form expression to truncated sum. Numerical sum given by Eq. (3-9) that is derived by considering pairwise sheet-sheet vdW interactions as both an exact summation (green curve) and with a cutoff correcting for long range interactions at $n = 8$ sheets on each side of the interface (blue curve). The difference between the exact summation and the sum with cutoff is at most 20% for the relevant range of CNC sizes.

Additionally, since there is no analytical closed form for the summation in Eq. (3-9) and to simplify the fitting process to numerical simulations, we approximate the summation by a continuous function involving a term that decays with the inverse square of the number of sheets, $1/n^2$, where n is the number of sheets on each side of the fracture interface. This continuous function of the form $A - k/n^2$ is fit to the discrete numerical sum (with cutoff), as shown in Figure 3-11 below with an r^2 (goodness of fit) value for the continuous approximation of 0.9062. This continuous function allows us to easily fit a scaling relationship to the SMD data in a simple, compact form, while maintaining a physical basis for the inverse square power relationship for the thickness dependence of the fracture energy of CNCs. This fit is shown as the blue curve in Figure 3-7 and shows good agreement with the simulation data. The fitting parameters also yield a prediction for the Hamaker coefficient of $H = 3.9 \times 10^{-20}$ J, which is in good agreement with experimental measurements of a cellulose thin film, $H = 5.8 \times 10^{-20}$ J. These findings provide a

physical basis for why there is nearly a 4-fold increase in the fracture energy of CNCs as the thickness is increased and explain why this increase saturates quickly beyond only a few stacked sheets. Specifically, the collective effects of stacked cellulose sheets initially contribute greatly to fracture strength but become negligible beyond a critical length scale due to the decay scaling of van der Waals interactions, which we have shown to be the dominant forces along the (200) plane of CNCs in Section 3.2.

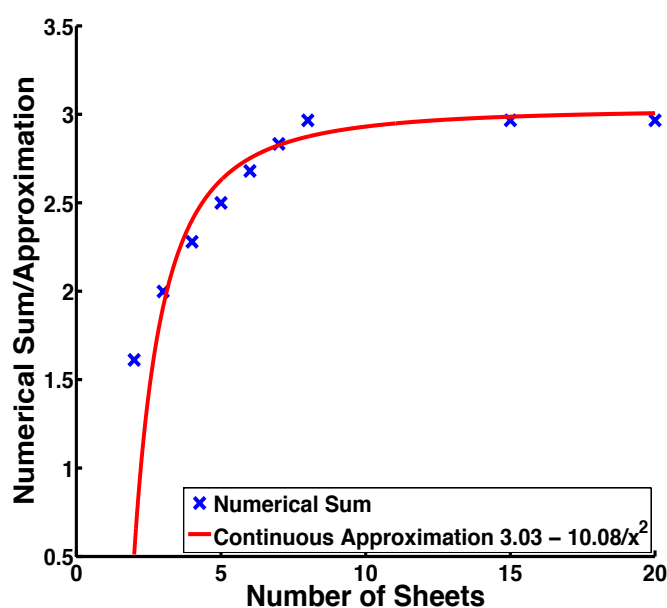


Figure 3-11: Continuous approximation of numerical sum in Eq. (3-9). In order to more easily and compactly fit the simulation data to the proposed model, and because there is no closed-form simplification of the summation given by Eq. (3-9), we use an inverse square relationship between the numerical sum with cutoff and the number of sheets on each side of the interface. The goodness of fit statistic for this continuous approximation is $r^2 = 0.9062$, indicating it is appropriate to use when fitting to the SMD data.

3.5 Predicting an Optimal CNC Size

In the previous two sections, we have shown clear scaling relationships for the fracture energy with both crystal width (Section 3.3) and crystal thickness (Section 3.4). The scaling of the fracture energy with crystal width can be explained by the presence of edge defects, while the

scaling with crystal thickness can be explained by collective effects of sheet stacking and non-bonded van der Waals interactions. Based on these scaling relationships presented in Figure 3-4 and Figure 3-7, it is now possible to determine the smallest width and thickness of a CNC that maximizes the fracture energy. The fracture energy of CNCs alone is not enough to predict an “optimal” size of CNCs for inclusion in neat films or as nanocomposite fillers. Instead, the ideal nanofiller should also maximize its surface area to volume ratio to avoid interfacial failure of these hierarchical materials which means that nanocrystals that have the same fracture energy but with smaller width and thickness will mechanically outperform larger crystals. Therefore, our criteria for choosing an optimal sized nanocrystal should involve maximizing the fracture energy and maximizing surface area to volume ratio.

However, when looking at the fracture energy and surface area to volume ratio scaling in Figure 3-4 and Figure 3-7, it is apparent that the fracture energy scales inversely with surface area to volume ratio. Therefore, an objective approach to defining the “optimal” crystal size is needed. Here, we utilize the difference between the fracture energy and surface to volume ratio where both quantities are normalized. These normalized quantities are such that the largest crystal has a normalized fracture energy of 1 and the normalized surface area to volume ratio has a value of 0. Considering the overlap point as the minimum value, the 80-20 Pareto rule¹³⁹ suggests that the optimum dimensions lie at 20% of the maximum difference between the normalized fracture energy and normalized surface area to volume ratio. Based on this concept and using our simulation data as presented in Figure 3-4 and Figure 3-7, we predict that the ideal dimensions of CNCs should be 6-7 chains in width (regardless of chain length) and 12-14 layers thick, which corresponds to 6.2 – 7.3 nm in width and 4.8 – 5.6 nm in thickness. Red dashed lines in Figure 3-4, Figure 3-6, and Figure 3-7 indicate these “optimal” sizes.

Although these results are important on their own for choosing the ideal size of CNCs when incorporating them into new hierarchical cellulose materials, they are even more interesting in the context of cellulose-based biological materials. Upon compiling experimental data for the geometric size of CNCs within a number of different systems in Figure 3-12^{15, 31}, it is clear that CNCs embedded in amorphous domains in biological structural materials often have a width and height around a few nanometers, rarely exceeding 10 nm. Considering that CNCs often provide structural support, especially in trees and other plants, it is conceivable that the small size of CNCs follows a natural design principle that maximizes fracture energy while also maximizing surface area to volume ratio. This notion is supported by our study as our predicted “optimal” CNC size (red diamond in Figure 3-12) that considers these two criteria falls directly in line with the size of CNCs observed in natural systems.

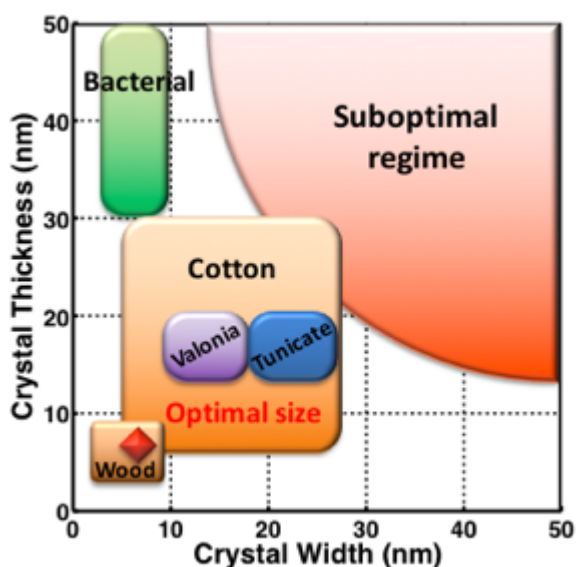


Figure 3-12: CNC sizes in natural systems. Comparison of CNC width and thickness for a number of natural CNC sources including wood, bacteria, tunicates, and a number of other materials. The optimal size predicted by our simulations (red diamond) is in good agreement with the experimentally measured sizes, indicating that nature’s evolutionary design principles promote CNCs that both maximize fracture energy and surface area to volume ratio.

This study builds on earlier works that suggest nanoconfinement and flaw tolerance as important natural design principles for creating strong and tough materials, although illustrating different mechanisms in the case of CNCs. The optimal dimensions of CNCs arise directly from sheet geometry and the scaling nature of van der Waals molecular interactions along the (200) plane – two key bottom-up design parameters in nature. Our methodology for computing fracture energies and examining size dependence in nanostructures paves the way for understanding collective fracture energy scaling in other systems, such as peptide assemblies and functionalized graphene sheets. Additionally, our studies build upon earlier works that suggest flaw tolerance and nanoconfinement are important natural design principles for creating strong and tough materials¹⁴⁰⁻¹⁴². As a next step towards further understanding the interfacial behaviors of CNCs to incorporate them into next-generation functional materials that utilize nature's own evolutionary design principles, we will next look at the mechanics of CNC-CNC interfaces in Chapter 4 (page 65).

Chapter 4 – Mechanics of CNC-CNC Interfaces

In this chapter, we aim to build upon our findings discussed in Chapter 3 (page 45) by examining interfacial failure between multiple CNCs and characterize their traction-separation laws. Using SMD techniques, we examine the interfacial failure of interfaces between two (110) CNC surfaces and two (200) CNC surfaces. We make key comparisons between the two most common interfaces between CNC elementary fibrils in two primary modes of failure: (i) normal to the interface, i.e. tension or separation and (ii) parallel to the interface, i.e. shear or traction. Using the results of our simulations, we develop analytical traction-separation potentials that describe the intercolloidal interactions between individual CNCs. Using these potentials and a previously developed shear lag model, we can make predictions for the elastic properties of aligned, CNC neat films that are in good agreement with recent experiments. Portions of the text and figures within this chapter are reprinted or adapted with permission from Sinko and Keten, *J. Mech. Phys. Solids* 2015⁷⁹ Copyright 2015 Elsevier.

4.1 Simulation Parameters

The focus of this study is to characterize the two prominent interfaces, the (110)–(110) and (200)–(200), as pictured in Figure 4-1(A) and Figure 4-1(B). These interfaces are believed to be the most common interfaces between CNCs aligned along their length based on the experimentally observed self-assembly behavior of CNCs in the liquid crystalline state that form chiral nematic structures^{31, 143}. Although mixed contact between surfaces is possible, it is unlikely in aligned systems due to differences in geometry and chemistry of the (110) and (200) surfaces. For this study, we utilize the CNC elementary fibril cross-section (5.39 nm in width and 2.97 nm in height) as this is a commonly observed cross-section observed upon extraction from plants and is close to the optimal size predicted by our size dependence study⁶⁵ presented in Chapter 3 (page 45).

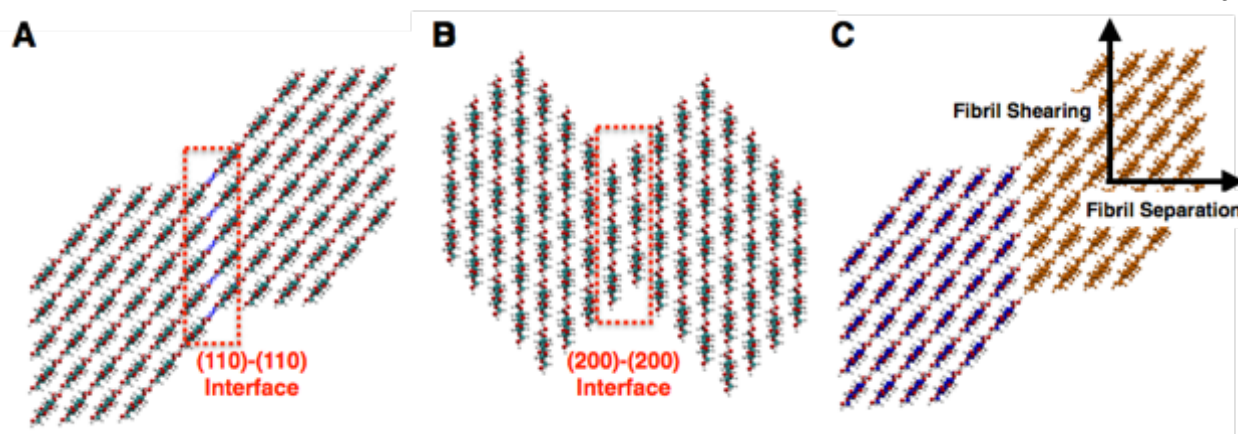


Figure 4-1: CNC-CNC interfacial simulation system setup. (A) VMD snapshot of the (110)–(110) interface between two CNC elementary fibrils. (B) VMD snapshot of the (200)–(200) interface between two CNC elementary fibrils. (C) Schematic showing the directions of interfacial separation and interfacial shearing (traction). The blue atoms in the left CNC are the carbon atoms that are fixed during SMD simulations and the orange in the right CNC are the atoms (carbon, oxygen, and hydrogen) that are pulled using the SMD force during simulation.

All simulations are again conducted using the NAMD⁸⁷ molecular dynamics package and the CHARMM 37 force field for carbohydrates^{94, 96}. Since our goal is to develop traction-separation potentials¹⁴⁴ of interfacial failure, our SMD simulations focuses on separating the fibrils in two directions: (i) normal to the interface and (ii) parallel to the interface with the specific pulling directions indicated in Figure 4-1(C). It should be noted that in the case of fibril shearing we examine failure both along the width of the fibrils (direction indicated in Figure 4-1(C)) and the length of the fibrils (direction into the page). The molecular structures were generated using a combination of the cellulose-builder toolkit¹¹⁶ to generate the individual crystals and the psfgen tool in VMD¹⁴⁵ to merge the two CNCs into a single system, with the CNCs oriented such that the x-direction is normal to the interface. After generating the system structures, systems are equilibrated for 1.0 nanoseconds under an NVT ensemble at a temperature of $T = 298$ K. The systems studied here are again finite, so sufficient vacuum padding is added to the simulation box

around the fibrils in order to prevent it from interacting with the opposite side of the other fibril. During equilibration, the carbon atoms in both fibrils are constrained to move only in the y -direction to prevent twisting of the fibrils (typically observed to be approximately $1.5^\circ/\text{nm}^{34-35}$) in order to decouple twisting effects from the inherent traction-separation behavior.

After the system was equilibrated, SMD simulations were conducted to cause interfacial separation and interfacial shear failure. Depending on the mode of failure, 5 (interfacial separation) or 10 (interfacial shear) snapshots of the system are taken at 100 picosecond intervals to be used as the initial equilibrated conformations for the SMD simulations. The carbon atoms in the leftmost CNC (blue atoms in Figure 4-1(C)) are fixed in space, while all atoms in the rightmost CNC (orange atoms in Figure 4-1(C)) are subject to the steering force used to cause interfacial failure. All the steered atoms are constrained to move only in the pulling direction via a harmonic constraint in order to prevent peeling and ensure pure interfacial separation or shear failure. SMD simulations were conducted until the interfaces experienced a complete loss of interfacial contact (as assessed by observing saturation in the energy landscape to a constant value), with simulations lasting between 0.6 – 8.0 nanoseconds depending on the specific interface and failure mode. It should be noted that all the results presented in this chapter correspond to CNCs having a fibril length of 5 repeat units, with results for fibrils having lengths of 10 and 15 repeat units included in Chapter 13 (page 248). Multiple CNC lengths were studied to determine if there was any size dependence of CNC-CNC interfacial properties as a function of the chain length.

4.2 Interfacial Separation Simulations

The first set of simulations conducted were interfacial separation simulations to measure the interfacial adhesion energy of the (110)–(110) and (200)–(200) interfaces. The energy landscapes (i.e. work-displacement curves) for the interfacial separation are shown in Figure 4-2.

Based on previous experimental work and our findings presented in Figure 3-3, it is hypothesized that the (110)–(110) interface should be dominated by hydrogen bonding^{122, 146} while the (200)–(200) interface should be stabilized primarily by van der Waals interactions^{65, 76}. Because electrostatic hydrogen bonds are stronger than weak secondary interactions, it is anticipated that the (110)–(110) interface should have a higher interfacial adhesion energy than the (200)–(200) interface. The results shown in Figure 4-2 support this hypothesis, indicating that the energy required to separate the (110)–(110) interface is nearly twice that for the (200)–(200) interface.

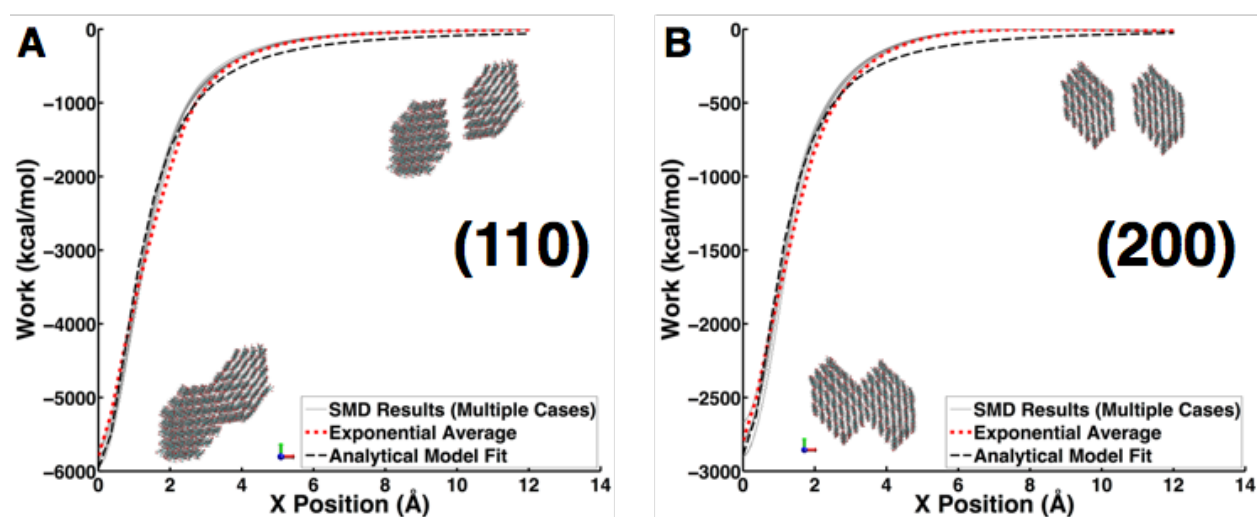


Figure 4-2: Energy landscapes of CNC-CNC interfacial separation. Work vs displacement curves obtained from SMD simulations of separating the (A) (110)–(110) interface and (B) (200)–(200) interface. In both plots, the gray, solid curves represent energy landscapes for 5 individual simulations, the red, dotted curves represent the exponential average of these different cases, and the black, dashed curves represent the analytical model used to describe these energy landscapes as discussed in Section 4.4.

The free energy landscapes for interfacial separation in Figure 4-2 show how the interfacial energy changes as a function of separation distance. However, it is also useful to simply look at the free energy difference, ΔF , between the equilibrated and separated states, as this provides a single numerical value to describe the interfacial strength/adhesion. Because the total interfacial

area influences the free energy difference, the work of separation per unit area (i.e. fracture surface energy or interfacial adhesion energy), G , is a more useful metric and is simply the free energy difference normalized by the interfacial area ($\Delta F/A$). The interfacial adhesion energy and interfacial areas for all of the interfaces studied here (including all three chain lengths) are provided in Table 4-1. Our results show that the fracture surface energy of the (110)–(110) interface is nearly twice that of the (200)–(200) interface with $G = 5.0\text{--}5.5 \text{ kcal/mol-}\text{\AA}^2$ ($3\text{--}4 \text{ J/m}^2$) for the (110)–(110) compared to $G = 2.0\text{--}2.3 \text{ kcal/mol-}\text{\AA}^2$ ($1.5\text{--}1.8 \text{ J/m}^2$) for the (200)–(200). The results in Table 4-1 indicate that there is little to no size dependence as the interfacial adhesion energy is approximately constant for all chain lengths. This suggests that the system sizes studied here are beyond the critical length scale^{132, 147} below which chain length would play a role on the computed energies. However, it is important to note that there still may be some interfacial size dependence in terms of crystal width/thickness, but those aspects are not explored within this study.

Table 4-1: Interfacial adhesion energies of CNC-CNC interfaces. Comparison of the interfacial adhesion energies and hydrogen bond densities for the (110)–(110) and (200)–(200) interfaces. The adhesion energy of the (110)–(110) interface is nearly double that for the (200)–(200) interface and can be explained by the significantly higher number and area density of hydrogen bonds that are developed across the interface.

Interface	Fibril Length, Repeat Units (nm)	Interfacial Surface Area, \AA^2	Interfacial Adhesion Energy, kcal/mol- \AA^2 (J/m^2)	Average Number of Hydrogen Bonds at Interface	Area Density of Hydrogen Bonds (\AA^{-2})
(110)–(110)	5 (5.19)	1219	4.75 (3.30)	45	0.0369
	10(10.38)	2437	5.61 (3.90)	103	0.0423
	15 (15.57)	3656	5.48 (3.81)	170	0.0465
(200)–(200)	5 (5.19)	1064	2.62 (1.82)	8	0.00752
	10(10.38)	2128	2.64 (1.83)	15	0.00705
	15 (15.57)	3192	2.38 (1.65)	24	0.00752

As mentioned previously, the drastic difference in adhesion energies for the two interfaces is hypothesized to be the result of a disparity in the dominant molecular interactions along the specific surfaces; most notably, hydrogen bonding. In order to verify this hypothesis, two approaches are taken. First, the average number of hydrogen bonds at the interface is calculated during system equilibration. The results are shown in Table 4-1 and indicate that the total number of hydrogen bonds is greater for the (110)–(110) interface compared to the (200)–(200) interface. However, since the interfaces are of different size, an area density of hydrogen bonds for each interface is also calculated. These values indicate that the area density of hydrogen bonds is nearly an order of magnitude larger for the (110)–(110) interface. Given the stronger nature of electrostatic hydrogen bonds compared to van der Waals interactions, this difference likely governs the larger adhesion energy of the (110)–(110) interface.

The second approach to explain these differences is to examine the relative contributions to the interfacial adhesion energy from non-bonded, electrostatic interactions and non-bonded, van der Waals interactions across the interface. Figure 4-3 show the relative contributions from these two components for each surface. For the (110)–(110) interface in Figure 4-3(A), electrostatic contributions, which are directly correlated with the number of hydrogen bonds developed across the interface, account for roughly 54% of the total adhesion energy. However, for the (200)–(200) interface in Figure 4-3(B), these electrostatic contributions account for only 33% of the total adhesion energy and are much smaller in their absolute magnitude (0.58 J/m^2) compared to the (110)–(110) interface (1.99 J/m^2). These results again support the notion that increased electrostatic interactions (i.e. hydrogen bonds) for the (110)–(110) interface give rise to higher adhesion energy compared to the (200)–(200) interface.

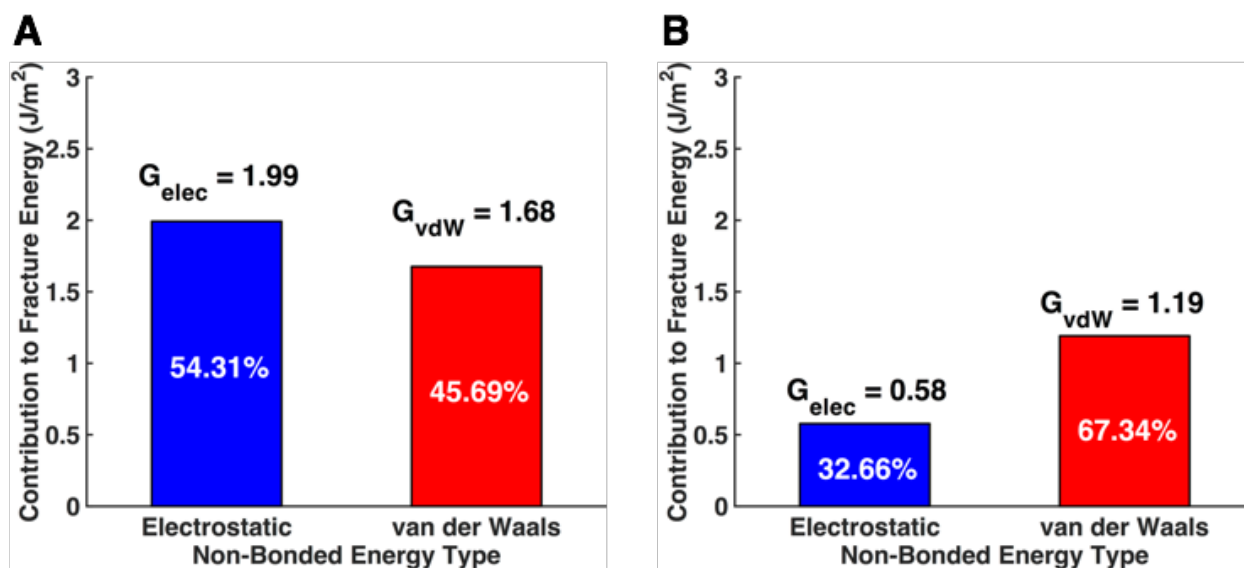


Figure 4-3: Relative non-bonded energy contributions to the adhesion energy. These bar plots show the energetic contributions of non-bonded electrostatic interactions (blue bars) and non-bonded van der Waals interactions (red bars) for (A) the (110)–(110) interface and (B) the (200)–(200) interface averaged over all CNC chain lengths studied (5, 10, and 15 repeat units). Contributions to the total fracture energy for the (110)–(110) interface are dominated by non-bonded, electrostatic interactions (i.e. hydrogen bonding). On the other hand, the (200)–(200) interface is dominated by contributions from non-bonded, van der Waals interactions. The relative differences in the electrostatic energy contributions, both in magnitude and percentage of the total energy, help to explain the observed differences in the adhesion energy between the two interfaces.

4.3 Interfacial Traction Simulations

Although the separation behavior in itself is interesting, it alone is not adequate to capture the entire mechanical behavior of macroscale cellulose assemblies. Specifically, in bacterial cellulose films¹⁶, nanocomposites^{15, 122}, and other materials that contain CNCs, the strong interactions between CNCs lead to the formation of larger-scale networks where load is transferred primarily by the shear resistance between crystals. Improved mechanical properties are obtained when contact between CNCs is increased by shear-alignment¹⁴⁸, but a quantitative model for describing resistance to sliding at these crucial interfaces remains to be established. For this

purpose, we investigate the traction behavior and associated energy landscapes of CNC interfaces by performing shearing simulations along the width and length of CNC fibrils. Our discussions will initially focus on interfacial shearing simulations along the width, whereas interfacial shearing simulations along the length are used to further support the initial conclusions we make. The results for the (110)–(110) interfacial shear simulations along the width dimension are presented in Figure 4-4(A) and the results for the (200)–(200) interface are shown in Figure 4-4(B). The shear mechanisms at play and energy landscapes for both interfaces are similar and exhibit a periodic form that combines local energy minima and maxima with an overall saturation of the energy. The behavior exhibited here is similar to stick-slip friction that is observed for the interactions between many materials and merits a detailed examination in the context of polysaccharide nanocrystals.

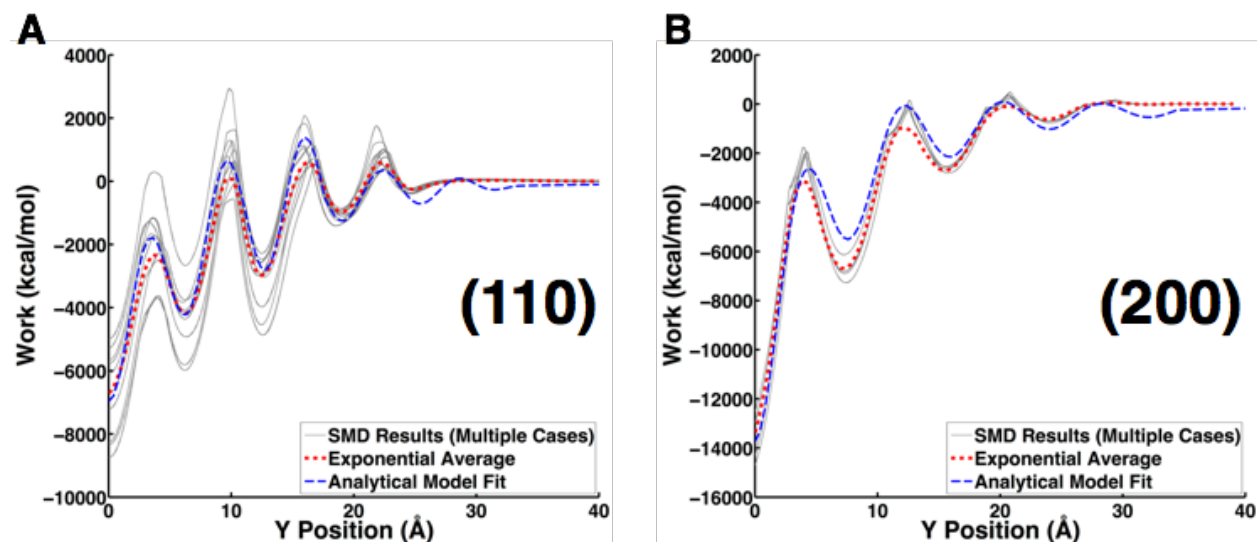


Figure 4-4: Energy landscapes of CNC-CNC interfacial traction (width). Work vs displacement curves obtained for SMD simulations of shearing the (A) (110)–(110) interface and (B) (200)–(200) interface along the width dimension. In both plots, the gray, solid curves represent energy landscapes for 10 individual simulations, the red, dotted curves represent the exponential average of these different cases, and the blue, dashed curves represent the analytical model used to describe these energy landscapes as discussed in Section 4.4.

When examining the energy landscapes pictured in Figure 4-4, there are a number of key observations that can be made. First, we observe that the periodicity of the shear energy landscapes can be directly related to the molecular dimensions/geometry of the corresponding CNC surfaces. In Figure 4-4(A) for the (110)–(110) interface, there are five energy minima/maxima that correspond to each of the five chains at the interface as pictured in Figure 4-1(A). Along the (110) surface, chains have a spacing of 5.85 \AA ¹⁴⁹ and therefore should become aligned across the interface every 5.85 \AA during the shearing process. The average distance between these energy minima and maxima in the energy landscape is found to be approximately 6 \AA and indicates that the positions of these energy peaks/valleys are directly related to the surface geometry. This observation also holds true for the (200)–(200) interface as the energy minima/maxima are located approximately 8.3 \AA apart, which is nearly identical to the crystal dimension for interchain spacing along the (200) surface of 8.2 \AA ¹⁴⁹. These observations are in good agreement with a recent study⁷⁷ where similar periodicity corresponding to molecular dimensions was observed in the force-displacement profile for sliding between a finite CNC and infinite cellulose substrate.

Beyond the energy landscape being directly correlated with surface geometry, Figure 4-4 also demonstrates that the energy barriers to shear are significantly higher for the (200)–(200) interface compared to the (110)–(110) interface. In addition to the magnitude of the energy barriers differing between the two interfaces, there are also some differences in the shape of the energy barriers. For the (110)–(110) interface, there is a smooth transition between energy minima and maxima while the (200)–(200) interface exhibits a sharper transition consistent with stick-slip friction mechanisms observed for granular materials¹⁵⁰⁻¹⁵². These differences are even more pronounced when looking at the force-displacement curves for the SMD simulations pictured in Figure 4-5. For the (110)–(110) interface, the average force (red curve in Figure 4-5) exhibits a

smooth, sinusoidal profile as the fibrils are sheared, whereas the (200)–(200) interface exhibits a zigzag shape for the force vs. displacement profile. Our findings indicate a transition from so-called “continuous sliding” for the (110)–(110) interface to clear stick-slip shearing mechanisms for the (200)–(200) interface. Describing this interfacial shear failure as “continuous sliding” may seem somewhat counter-intuitive at first, considering the clear energy maxima that must be overcome as pictured in Figure 4-4(A). However, “continuous sliding” simply refers to the fact that the two surfaces are constantly moving past one another and do not become stuck and/or caught up on each other during shearing.

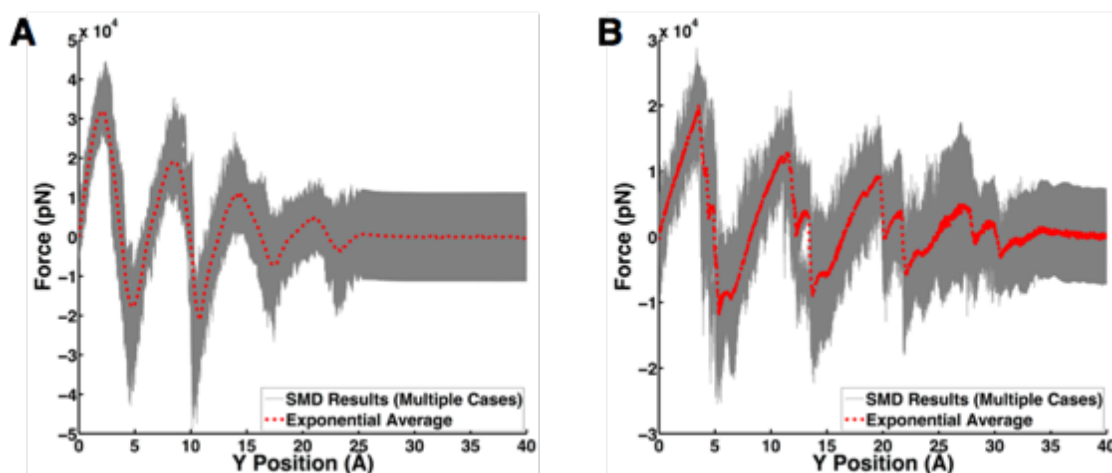


Figure 4-5: Force-displacement curves for CNC-CNC interfacial traction (width). The force-displacement curves for shearing of the (A) (110)–(110) interface and (B) (200)–(200) interface along the width dimension. The gray curves represent force-displacement curves from all of the individual SMD simulations while the red, dashed lines represent the exponential average of these simulations. The (110)–(110) interface exhibits a smooth, sinusoidal shape in the force-displacement curve indicative of continuous interfacial sliding while the (200)–(200) interface exhibits a sharp, zigzag shape indicative of stick-slip interfacial friction.

A recent experimental study on NaCl crystals¹⁵³ demonstrated a similar transition from continuous sliding to stick-slip as the shear energy barrier (also known as the corrugation energy) increases from 0.1 eV to 0.5 eV. This transition is predicted by an order parameter, η , that is a

function of the shear energy barriers, distance between energy barriers, and elastic modulus of the material. Specifically, assuming the modulus and distance between barriers are approximately equal, the order parameter scales directly with the magnitude of the energy barriers. For large values of this parameter (high energy barriers), stick–slip behavior is observed while low values of this parameter (low energy barriers) are indicative of continuous sliding. Shearing behaviors of the (110)–(110) and (200)–(200) interfaces fit well qualitatively within this framework as the order parameter for the (200)–(200) interface is much higher than the (110)–(110) interface due to significantly higher energy barriers.

The continuous sliding behavior exhibited by the (110)–(110) interface is particularly interesting when examining the dynamics of hydrogen bonding across the interface. Figure 4-6(A) shows the number of hydrogen bonds developed between the two CNCs during shear failure. This profile demonstrates that there are clear increases and decreases in the number of hydrogen bonds developed across the interface during shear simulations. This breaking and reformation of hydrogen bonds is a direct result of misalignment and subsequent realignment of cellulose sheets, specifically the hydroxyl groups, across the interface as the two CNCs move past one another, as illustrated in Figure 4-6(B). The location of local maxima in the number of hydrogen bonds corresponds to the locations of energy minima in Figure 4-4(A) and similarly local minima in the number of hydrogen bonds correspond to energy maxima in the energy landscape. On the other hand, the (200)–(200) stick-slip behavior cannot be attributed to similar hydrogen bond breaking/reformation events as there are very few (see Table 4-1) across the interface. Instead, molecular friction, arising from sterical contacts between hydrogen and hydroxyl groups, causes the sharper, more distinct stick-slip events. Further, the increased energy barriers observed in

Figure 4-4(B) are attributed to polar/non-polar patches along the interface that are more energetically expensive to overcome than the all-hydrophilic (110) surface.

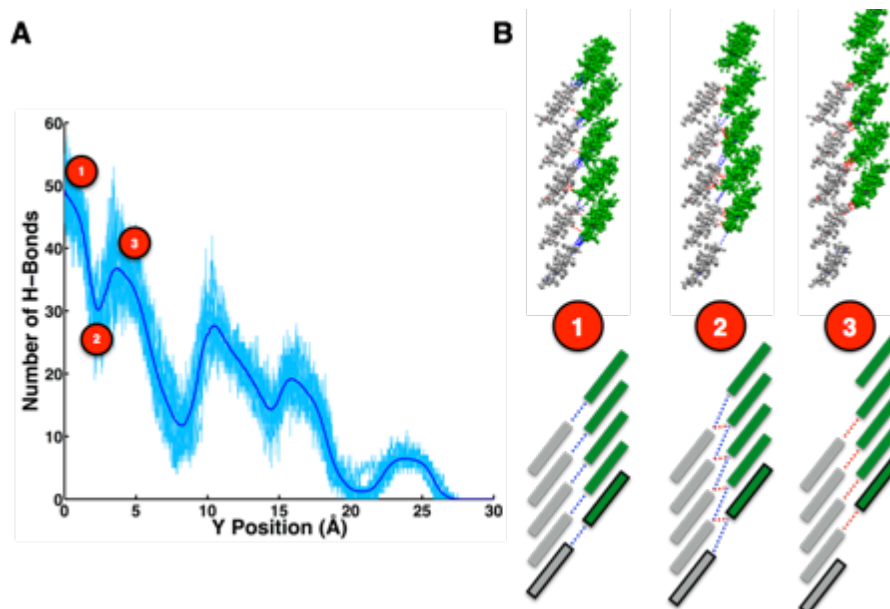


Figure 4-6: Hydrogen bond breaking/reformation mechanism for shearing of (110)–(110) interfaces. (A) Number of hydrogen bonds along the (110)–(110) interface as a function of the shearing displacement in simulation. The minima/maxima in this plot correspond to maxima/minima in the energy landscape shown in Figure 4-4(A), indicating they are the cause of the observed continuous sliding mechanism. (B) VMD snapshots and illustrations of the shearing mechanism that is responsible for the shape of the energy landscape. During shearing of the (110)–(110) interface, hydrogen bonds break/reform and can be directly related to the corresponding energy landscape. Here, blue hydrogen bonds exist between chains that are aligned at equilibrium (i.e. beginning of the shear simulations and indicated by location 1) and red hydrogen bonds exist between adjacent chains that are misaligned at equilibrium. As the system moves from location 1 to 2, blue hydrogen bonds break and red hydrogen bonds begin to form, resulting in a local minimum in the total number of hydrogen bonds. Moving from location 2 to 3, more red hydrogen bonds form due to CNC chains becoming aligned and there is a local maximum in the number of hydrogen bonds.

In addition to shearing the interface along the width dimension, SMD simulations were conducted where the interfaces were sheared along their length (axial direction). The results for these simulations are shown in Figure 4-7 and demonstrate similar trends to those observed for

shearing along the width dimension. The periodicity of the energy landscapes is again dictated by the geometry of the surface with the energy minima/maxima spaced approximately 10.4 \AA apart, which is in good agreement with the CNC crystalline dimension along the length of the chain of 10.38 \AA ¹⁴⁹. Additionally, the difference between continuous sliding for the (110)–(110) interface and stick–slip behavior for the (200)–(200) interface is still observed. This finding ascertains that this behavior is indeed dictated by the underlying interaction mechanisms across the interface, and not the particular shearing direction.

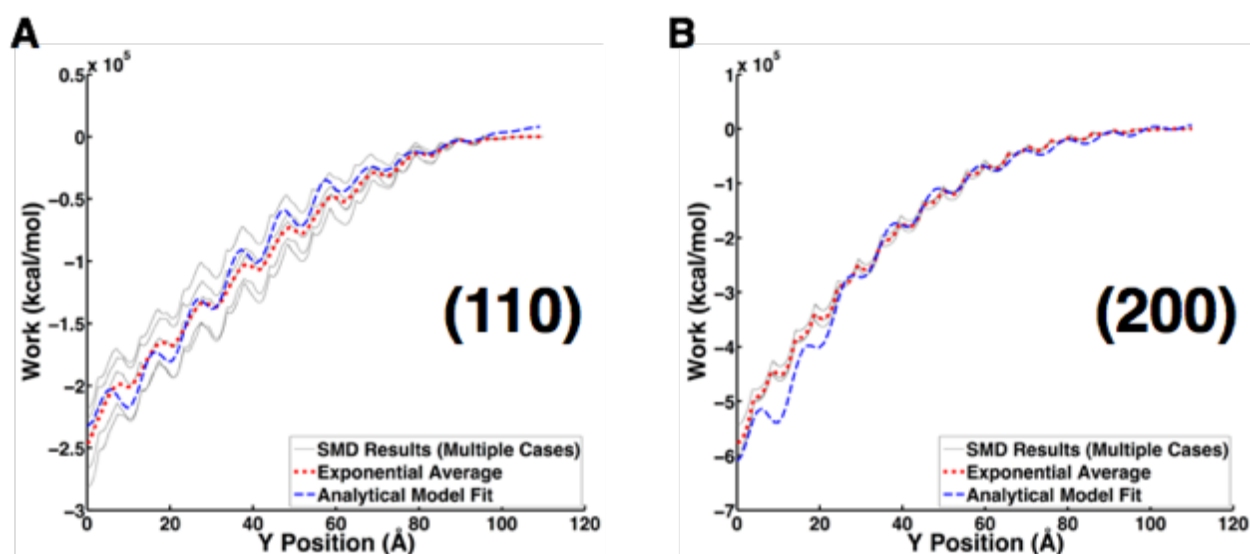


Figure 4-7: Energy landscapes of CNC-CNC interfacial traction (length). Work vs displacement curves obtained for SMD simulations of shearing the (A) (110)–(110) interface and (B) (200)–(200) interface along the length dimension. In both plots, the gray, solid curves represent energy landscapes for 10 individual simulations, the red, dotted curves represent the exponential average of these different cases, and the blue, dashed curves represent the analytical model used to describe these energy landscapes as discussed in Section 4.4.

4.4 Analytical Descriptions of Interfacial Traction-Separation Laws

In the previous two sections, we have examined the results of SMD simulations to describe the interfacial separation and shear behavior of the two most prominent CNC-CNC interfaces. Although these analyses have quantified key mechanical properties of the interfaces that are

important for understanding the behavior of macroscale materials (interfacial adhesion energy, shear energy barriers, etc.), they neglect to consider the exact shapes of the energy landscapes, or in other words the exact characteristics of the so-called traction separation laws. In this section, we focus on developing analytical models that describe the colloidal interaction between two fibrils in both separation and shear failure modes. In other words, we develop analytical functions that describe the energy landscapes presented in Sections 4.2 and 4.3.

First, we focus on developing an analytical model that describes the separation behavior of CNCs as shown in Figure 4-2. Although different molecular interaction mechanisms are dominant for the two interfaces, based on the knowledge gained from our initial study in Chapter 3 (page 45) and the hydrogen bond densities shown in Table 4-1, Figure 4-2 indicates that the distance scaling of the free energy for the separation process is similar for both interfaces. This similarity suggests that despite clear differences between the interfacial chemistries, the interfacial separation for both surfaces can be described using the same analytical function. Considering that van der Waals interactions are an underlying interaction for both interfaces, we can simplify the modeling of this interface if we treat the two surfaces as flat parallel plates. Similar to the thickness scaling analysis presented in Chapter 3 (page 45), we utilize the fact that the van der Waals interaction energy E_v between two parallel, flat plates separated by a distance x is given by Eq. (4-1)¹³⁴

$$E_v(x) = -\frac{H}{12\pi x^2} \quad (4-1)$$

where H is the Hamaker coefficient that defines the attraction between two surfaces in a specific medium. Eq. (4-1) indicates that the van der Waals interaction energy is proportional to the inverse square distance between the two plates. Considering only the attractive part of the potential, and assuming that the energy goes to $-\Delta F$ at the point $x = 0$, one can rewrite this as Eq. (4-2)

$$E_v(x) = \frac{-\Delta F}{1 + ax^2} \quad (4-2)$$

where ΔF is the difference in the free energy between the equilibrium and separated states and $x = 0$ is the equilibrium distance between surfaces. The fitting parameter a in Eq. (4-2) depends on the interfacial geometry and the Hamaker coefficient of the material. However, we must also include the repulsive part of the potential when CNC surfaces are separated by less than their equilibrium distance and will push away from one another. By changing the equilibrium position of the surfaces to be at $x = r_0$ and assuming the repulsive and attractive potentials are of a similar analytical form, the separation potential can be written as Eq. (4-3).

$$E_v(x) = \frac{-\Delta F}{1 + a(x - r_0)^2} \quad (4-3)$$

In order to validate this model for the interfacial separation, Eq. (4-3) is fit to the SMD simulation results for both interfaces. Specific parameter values obtained using a least-squares regression technique are included in Table 4-2. The best-fit curve for the (200)–(200) interface captures the simulation results well, as shown in Figure 4-2(B), with a goodness of fit statistic of $r^2 = 0.992$. The model in Eq. (4-3) was derived for surfaces interacting with purely van der Waals interactions and does not take into account the significant interfacial hydrogen bonding energetics of the (110)–(110) interface that may exhibit a different distance scaling relationship. However, since van der Waals interactions still contribute significantly to the overall fracture energy (see Figure 4-3(A)), this model was used for the (110)–(110) interface. Figure 4-2(A) shows that the model fits remarkably well with a goodness of fit statistic of $r^2 = 0.994$. This indicates that hydrogen bonding does not change the distance scaling of the energy landscape appreciably, but solely serves as a strengthening mechanism for the interface at short distances. This notion is supported by the fact that the fitting parameter a is approximately constant for both interfaces and

all lengths with an average value of $a = 1.38$. These similarities are somewhat expected since hydrogen bonds are implicit in the CHARMM force field, but still interesting in the sense that adding additional electrostatic interactions, which exhibit different distance scaling than vdW interactions, does not change the overall distance scaling of the energy landscape. Finally, when comparing fitting parameters for different chain lengths, we notice that the value of ΔF when normalized by the length is approximately constant and has a value of ~ 1790 kcal/mol-nm for the (110)–(110) interface and ~ 730 kcal/mol-nm for the (200)–(200) interface. This finding again suggests no size dependence of the interfacial adhesion energy as a function of CNC chain length.

Table 4-2: Fitting parameters for the interfacial separation model.

Interface	Length, nm	a	ΔF	Coefficient of Determination, r^2
(110)–(110)	5.19	1.489	8874	0.9942
	10.38	1.406	19720	0.9944
	15.57	1.335	27380	0.9943
(200)–(200)	5.19	1.329	3842	0.9918
	10.38	1.328	7718	0.9924
	15.57	1.419	11050	0.9920

While an analytical model describing CNC interfacial separation was rather straightforward, a model to describe the interfacial shear behavior is somewhat more complicated. These traction potentials are extremely important for describing the failure of cellulose neat films and nanocomposites across different interfacial planes. Here, we attempt to provide a comprehensive model that reflects the interfacial behavior in our simulations, but is also generalized enough that it could be extended to similar crystalline interfaces in other material systems. In order to develop an adequate model, a few simple assumptions were made. First, it is assumed that the local energy minima/maxima in the energy landscapes are equally spaced. This

enables the use of a periodic function to describe peak spacing but may neglect contributions of strains within the crystal that cause unequal spacing between extrema. Second, it is assumed that the magnitude of the energy barriers decays according to a well-defined analytical function. For example, it is observed from our simulations that energy barriers decay linearly for the (110)–(110) interface and exponentially for the (200)–(200) interface. Although a more complicated, exact description of the energy barrier decay could be implemented if the trends are not well defined, an analytical function is preferred for simplicity. Overall, these simplifications allow for the development of a simple, physically informed model that is capable of describing the shear landscape of an arbitrary finite, rough surface with well-defined local maxima and minima based on the surface geometry and chemistry.

When examining the shear energy landscapes in Figure 4-4 and Figure 4-7, we observe two clear components to the overall shear behavior. The first component is an overall saturation in the energy landscape similar to the separation potential described previously and illustrated for interfacial shearing in Figure 4-8(A). For this overall saturation behavior, we will utilize the formula for the van der Waals interaction energy for two flat, parallel surfaces presented in Eq. (4-1). That formula assumes that the surfaces are separated in a direction normal to the interface (x-direction in our simulations), but in shearing simulations their centers are moved apart parallel to the interface (y-direction in our simulations). We propose that the van der Waals interaction energy between two surfaces should not only scale with separation distance, but more generally with the radial distance between the geometric centers of the surfaces. In this case, the interaction energy E_v between the two surfaces would be given by Eq. (4-4) where r is the radial distance between the centers of mass (COM) of the two surfaces.

$$E_v(r) = E_v(x, y) = -\frac{H}{12\pi r^2} = -\frac{H}{12\pi x^2 + 12\pi y^2} \quad (4-4)$$

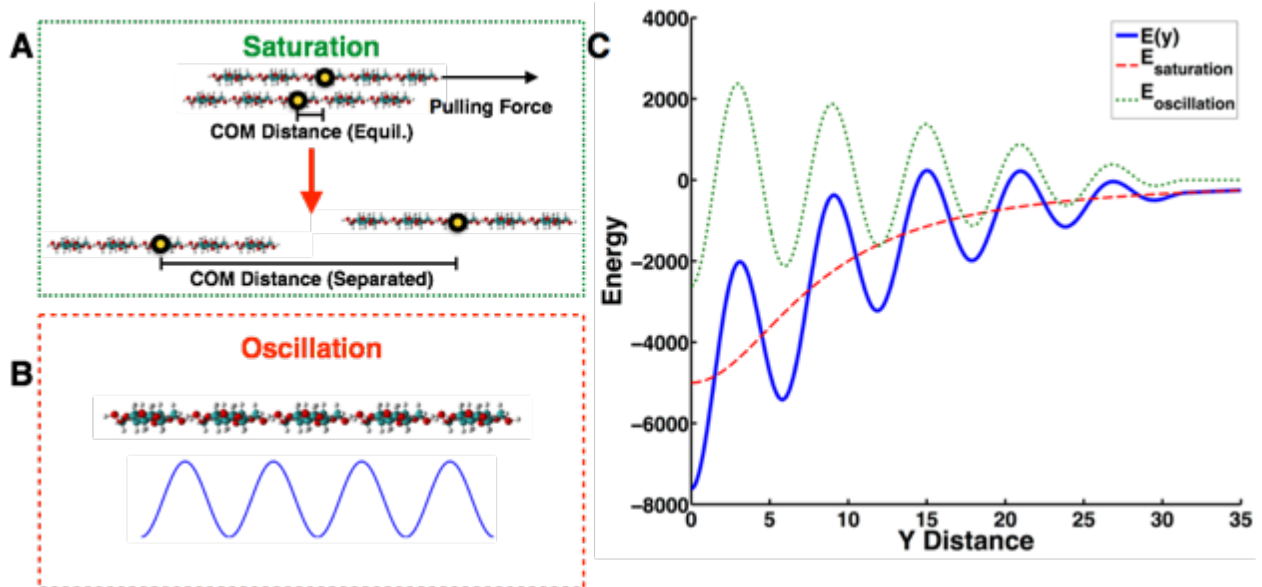


Figure 4-8: Analytical model to describe CNC interfacial shear failure. (A) The saturation in the energy landscape is due to the transition from equilibrium to a state of complete loss of interfacial contact between the finite surfaces that make up the CNC–CNC interfaces. This saturation can be approximated using a $1/y^2$ power law. (B) The oscillation term is governed by the atomic roughness of the CNC surfaces and molecular interactions across the interfaces. These oscillations in the energy can be described by the Prandtl–Tomlinson model for atomic friction when modified for a finite interface. (C) The superposition of these two energy components results in a general, analytical model that can describe the shearing of any finite surface with periodic roughness.

Therefore, since the separation distance between the two surfaces is constant throughout the shearing process (i.e. constant value of the variable x), then the interaction energy of the two surfaces is simply a function of the shear displacement y . Then, Eq. (4-4) can be rewritten as Eq. (4-5) by introducing fitting constants a and ΔF_s , the change in free energy between the equilibrium state and the separated state after shearing.

$$E_{v,sat} = \frac{-\Delta F_s}{1 + ay^2} \quad (4-5)$$

The second component of the shear energy landscape is the periodic nature of the energy minima and maxima governed by the surface chemistry and geometry of the CNCs. Previous studies have shown that friction between atomically rough surfaces can be described by the Tomlinson model, and we use this model as the basis for the periodic component of our traction potential. The Tomlinson model¹⁵⁴⁻¹⁵⁵ utilizes a sinusoidal potential function, as illustrated in Figure 4-8(B), to capture periodicity, which is the general shape of the energy landscapes suggested by our SMD simulations. The limitation of utilizing the traditional Tomlinson model in our potential is that it was developed for sliding of either an infinite surface past another infinite surface or a finite surface sliding along an infinite substrate. Therefore, it does not take into account the finiteness of the interfaces used in our simulations and relevant to any system in which interfacial contact is lost during deformation. In order to accurately implement this periodic description of the energy landscape into our potential, we must include some sort of decay function that accounts for a change in the magnitude of the energy barriers as interfacial contact is lost. This periodic, oscillatory component of the energy landscape (i.e. the modified Tomlinson potential) can be written analytically in Eq. (4-6).

$$E_{v,per}(y) = -f_{decay}(y)E_{set} \cos\left(\frac{2\pi y}{d}\right) \quad (4-6)$$

In Eq. (4-6), d is the distance between energy minima or maxima (as governed by the surface geometry), E_{set} is the energy required to break one set of molecular interactions, and $f_{decay}(y)$ is the decay function that controls the decay in the magnitude of the energy barriers as the interfacial contact changes. As mentioned previously, it is observed that a linear decay function best captures the change in energy barriers for the (110)–(110) interfaces while an exponential

decay function best describes the (200)–(200) energy barrier decay. The decay functions for these respective interfaces are given by Eq. (4-7) and (4-8).

$$f_{decay^{(110)}}(y) = -\left[\frac{4n+1}{8} - \frac{|y|}{2d}\right] \quad |y| \leq d\left(n + \frac{1}{4}\right) \quad (4-7)$$

$$f_{decay^{(200)}}(y) = -e^{-c|y|} \quad |y| \leq d\left(n + \frac{1}{4}\right) \quad (4-8)$$

In Eq. (4-7), n is the total number of energy minima in the landscape (as governed by the surface geometry and shear direction), and in Eq. (4-8) c is a constant that controls the rate of decay of the energy barriers. All of the other variables have the same values/meaning as mentioned previously. It is important to note that we include the $|y|$ term such that the function represents shearing in either the positive or negative y -direction as the energy profile should be symmetric about the equilibrium configuration at $y = 0$. Knowing both the periodic and saturation components of the energy landscape, we can develop the total traction potential as a superposition of these two individual components as illustrated in Figure 4-8(C). The final form of the traction potentials for the (110)–(110) and (200)–(200) interfaces are given by Eq. (4-9) and Eq. (4-10), respectively.

$$E_{v^{(110)}}(y) = -\frac{\Delta F_s}{1+ay^2} - E_{set} \left[\frac{4n+1}{8} - \frac{|y|}{2d}\right] \cos\left(\frac{2\pi y}{d}\right) \quad |y| \leq d\left(n + \frac{1}{4}\right) \quad (4-9)$$

$$E_{v^{(200)}}(y) = -\frac{\Delta F_s}{1+ay^2} - E_{set} e^{-c|y|} \cos\left(\frac{2\pi y}{d}\right) \quad |y| \leq d\left(n + \frac{1}{4}\right) \quad (4-10)$$

The analytical models for the traction potential given above in Eq. (4-9) and (4-10) were fit to the SMD data shown in Figure 4-4 and Figure 4-7 using a combination of known physical parameters for the surfaces and a least squares regression technique. Upon first glance, it appears there are a large number of parameters in the model, however, many of these quantities are simply obtained from the geometry of the surfaces that make up the interface, specifically the values of n

and d . For (110)–(110) interfacial shearing along the width, $n = 5$ and $d = 6.0 \text{ \AA}$, while for (200)–(200) interfacial shearing, $n = 4$ and $d = 8.3 \text{ \AA}$. For fibrils sheared along their length, n is equal to the number of repeat units in the fibril and $d = 10.4 \text{ \AA}$. The parameter E_{set} can be obtained directly from simulation by estimating the energy contribution of a single set of molecular interactions from the final energy barrier in the energy landscape (i.e. when there is only one set of bonds/interactions left to broken). Therefore, the only true fitting parameters are a , which controls the rate of saturation of the energy landscape, and c , which controls the rate of decay of energy barriers for the (200)–(200) interface. These fitting parameters are included below in Table 4-3. The goodness of fit statistics for this model (shown as blue, dashed curves in Figure 4-4 and Figure 4-7) to the SMD shear energy landscapes (both along the width and length for all fibril lengths) range from $r^2 = 0.80 - 0.99$, thereby indicating good agreement between the model and simulation results.

Table 4-3: Fitting parameters for the interfacial traction model.

Interface	Length, (nm)	n	d	E_{set}	ΔE_s	a	c	r^2
(110)–(110) Width	5.19	5	6.0	750	5000	0.03	-	0.9539
	10.38	5	6.0	1500	10000	0.03	-	0.9364
	15.57	5	6.0	2250	25000	0.03	-	0.9316
(110)–(110) Axial	5.19	5	10.4	1250	50000	0.0015	-	0.9826
	10.38	10	10.4	2500	260000	0.0006	-	0.9857
	15.57	15	10.4	3750	1.07e6	0.0002	-	0.8972
(200)–(200) Width	5.19	4	8.1	9500	9000	0.03	0.09	0.8834
	10.38	4	8.1	19000	18000	0.03	0.09	0.8333
	15.57	4	8.1	28500	27000	0.03	0.09	0.9001
(200)–(200) Axial	5.19	5	10.6	40000	140000	0.004	0.04	0.9764
	10.38	10	10.6	80000	620000	0.001	0.02	0.9805
	15.57	15	10.6	1.2e5	1.38e6	0.0005	0.01	0.9503

4.5 Extension of Results to CNC Neat Films

The analytical potentials described in Section 4.4 provide some unique insight into the traction-separation laws of CNCs and provide the basis for developing coarse-grained models of

CNC-CNC interactions. Additionally, these potentials allow us to provide new insight into previous experimental observations of hierarchical cellulosic materials at the macroscale. For example, a unique property of bacterial cellulose films is that they dissipate large amounts of energy while maintaining a high elastic modulus, making them intriguing materials for applications such as acoustics in which deadening of sound is desirable¹⁵⁶. Insight from our model suggests that the slip events along the interface can give rise to large energy dissipation similar to that observed in silk and other biological materials¹⁶, and also explains the observed experimental behavior of cellulose neat films.

In addition to providing qualitative support of recent experiments, the traction and separation models can be used to estimate mechanical properties for the interfaces including the interlayer shear modulus and Young's modulus. The models developed for the traction potentials are particularly useful as they can be used to directly estimate the interlayer shear modulus, G , that would be difficult to obtain experimentally. To obtain the interlayer shear modulus, one can obtain the stress-strain plot for shear failure of the interface, as shown in Figure 4-9(A) by differentiating Eq. (4-9) or (4-10) with respect to the interfacial shear strain. Although this mechanical property by itself is important for comparing interfacial characteristics of CNCs to other materials, we can further use it to predict the mechanical properties of macroscale, hierarchical CNC materials.

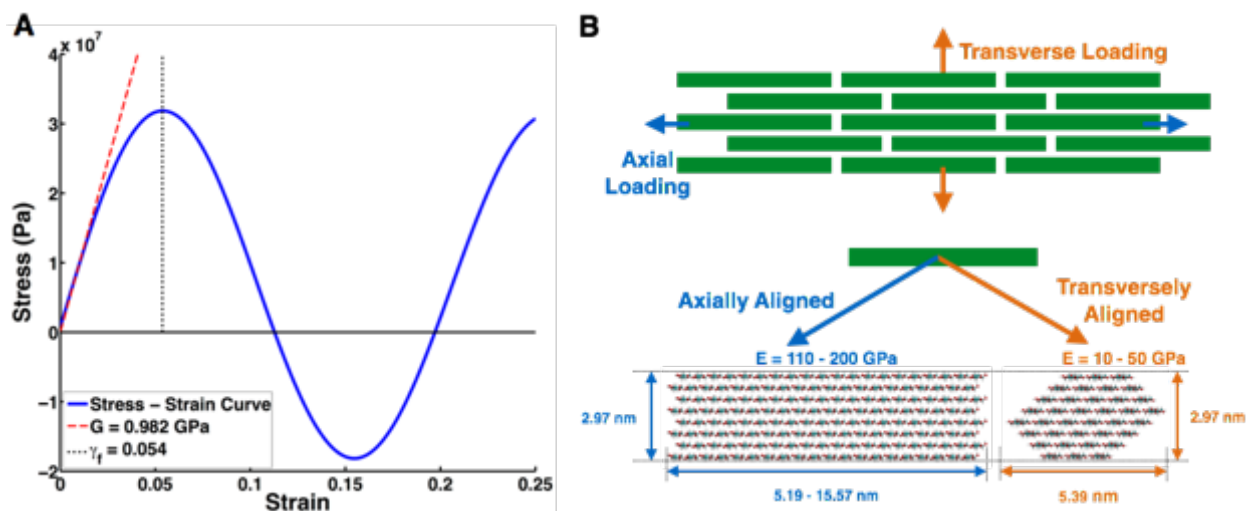


Figure 4-9: Interfacial shear stress-strain curve and CNC neat film geometry. (A) Stress–strain plot for the shearing of two CNC crystals based on the traction potentials developed in Eq. (4-9) and (4-10). This plot represents the shearing of the (110)-(110) interface along the width. The interlayer shear modulus is estimated by taking the initial slope of the stress–strain curve and the strain at failure initiation is taken as the strain at the maximum stress. (B) Illustration of a CNC neat film where each of the rectangles represents a single CNC. A shear-lag model is used to predict the overall performance of this system based on the CNC dimensions, mechanical properties of individual CNCs, and the interfacial shear properties obtained from stress–strain plot shown in panel (A).

Aligned, CNC neat films (illustrated schematically in Figure 4-9(B)) are one example of a hierarchical cellulose material whose material properties are greatly influenced by nanoscale CNC interfaces. There are a number of continuum mechanics models that relate interfacial mechanical properties to macroscale properties such as failure strain and effective elastic modulus. In order to validate the results of our computational study, here we employ a shear-lag model to estimate the performance of a CNC neat film. This particular shear-lag model¹⁵⁷⁻¹⁵⁹ has been used to study stacks of graphene sheets as well as other biological composites, wherein it demonstrates that the interlayer shear properties of these systems are crucial to the macroscale material performance. Specifically, this model can be used to reliably predict the effective elastic modulus, E_{eff} , of a film as a function of CNC mechanical properties and geometry.

As derived in the original references¹⁵⁷⁻¹⁵⁹, the effective modulus of the film is given by

Eq. (4-11)

$$E_{eff} = \frac{2E\lambda hL}{(2h + b) \left[\lambda L + 2 \coth\left(\frac{\lambda L}{2}\right) \right]} \quad (4-11)$$

where E is the elastic modulus of the constituent material, G is the interlayer shear modulus, h is the CNC thickness, b is the spacing between CNCs, and L is the chain length. The relevant dimensions of CNCs used in the model are shown in Figure 4-10(A). Additionally, this model uses a parameter λ , given in Eq. (4-12), that is a ratio of the shear modulus to the elastic modulus.

$$\lambda = \left(\frac{2G}{Ehb} \right)^{1/2} \quad (4-12)$$

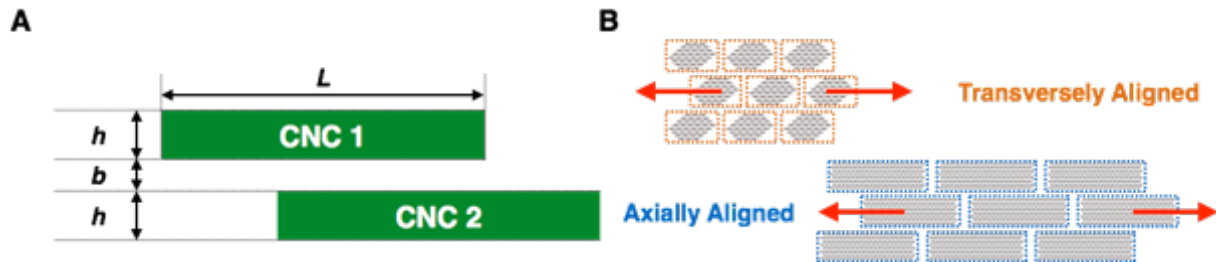


Figure 4-10: Illustration of shear lag model geometry and CNC alignment. (A) Illustration of two CNCs within an aligned thin film showing the height, h , and length, L , of the crystals as well as the distance between them, b , that are parameters used in the shear-lag model. (B) Illustration of the difference between a transversely and axially aligned CNC thin film that exhibit different mechanical properties.

The results of our simulations provide an estimate of the interlayer shear modulus that has not previously been characterized for CNC-CNC interfaces. The remaining parameters for this shear-lag model can be obtained from the crystalline structure of CNCs and experimental measurements of CNC mechanical properties. Depending on the orientation of CNCs and the pulling direction of the film, the mechanical properties (elastic modulus of CNC fibrils and interlayer shear stiffness) and relevant dimensions of the aligned fibrils will change, thereby

leading to a range of predicted values for the effective elastic modulus of the film. The predictions for the moduli of these varying CNC neat films are provided in

Table 4-4 for both CNC-CNC interfaces studied here and two orientations – the first where the CNCs are aligned axially in the pulling direction and the second where the CNCs are aligned transversely in the pulling direction (see Figure 4-10(B)). In the case of axial alignment, we also examine the effect of changing the parameter L since multiple CNC lengths were studied in our simulations.

Table 4-4: Shear-lag model parameters. This table contains values measured from simulation (interlayer shear modulus, G , and shear strain at failure, γ_c) and taken from experiment (CNC elastic modulus, E , and relevant CNC dimensions) that were input into the shear lag model to predict an effective elastic modulus, E_{eff} , for CNC neat films.

System	Simulation Values		Literature Values			Model Results
	G (GPa)	γ_c	E (GPa)	h (nm)	L (nm)	E_{eff} (GPa)
(110)–(110) Pulled Axially	2.04	0.086	110	3.23	5.19- 15.57	8.61-40.3
(200)–(200) Pulled Axially	7.4	0.087	110	2.72	5.19- 15.57	26.3-62.9
(110)–(110) Pulled Transversely	0.982	0.052	10	3.23	2.32	0.823
(200)–(200) Pulled Transversely	1.94	0.063	10	2.72	4.92	3.95

Depending on the orientation of the CNCs (axial or transverse) and dominate interface ((110) or (200)), this shear-lag model estimates the effective modulus of CNC neat films to range from 0.8–63 GPa. When comparing these values to those reported in literature for bacterial

cellulose¹⁶ (10–20 GPa) and aligned, wood-based (7–30 GPa) CNC films¹⁴⁸, we can conclude that the predictions are in good agreement with experimentally obtained values. It is important to note that the shear-lag model assumes perfect CNC alignment within the thin film and interfaces with identical, isotropic characteristics. Within the experimental samples, however, factors such as crystal misalignment, surface defects, and the presence of amorphous domains are major factors—all of which reduce the effective modulus. These factors are important in developing more accurate predictions for the performance of CNC films using our traction potentials. However, this simple model illustrates that CNC interfacial behavior coupled with knowledge of failure planes within the crystals⁶⁵ is central to developing an enhanced understanding of CNC neat films.

Chapter 5 – Effects of Moisture on Interfacial Traction-Separation

This chapter builds upon the work discussed in Chapter 4 (page 65), by again focusing on interfacial traction-separation behavior of two CNCs. However, here we are primarily interested in assessing how the presence of moisture at these interfaces plays a role in changing the interfacial mechanical properties. This work again falls under the materials discovery aspect of computational materials-by-design as we are focused on gaining a molecular level perspective of CNC interfaces in the presence of moisture. Using SMD techniques, we examine the interfacial failure between two CNC surfaces with a single atomic layer of water molecules placed in between. We find that molecular water at the interface between hydrophilic (110) CNC surfaces has a negligible effect on the tensile separation adhesion energy. However, when water cannot hydrogen bond easily to the surface (i.e., (200) hydrophobic surfaces), it tends to maintain hydrogen bonds with other water molecules across the interface and form a capillary bridge that effectively increases the energy required to separate the crystals. Under shear loading, water lowers the energy barrier to sliding by reducing the atomic friction and consequently the interlayer shear modulus between crystals, independent of the hydrophobicity of the surface. Our simulations indicate that these nanoscale interfaces and physical phenomena such as interfacial adhesion, interlayer shear properties, and stick-slip friction behavior can be drastically altered by the presence of water. Portions of the text and figures within this chapter are reprinted or adapted with permission from Sinko and Keten, *Appl. Phys. Lett.* 2014⁷⁹. Copyright 2014 AIP Publishing LLC.

5.1 Simulation Parameters

This study focuses on understanding how small molecule solvents, specifically water, can serve to disrupt molecular interactions between CNCs and change the underlying interfacial mechanical properties. Specifically, we are interested in whether the changes to the mechanical

properties are beneficial or harmful in nature. This work focuses on comparing the traction-separation behavior of CNCs interfaces for the cases of no water at the interface (dry condition – results reused from Chapter 4 (page 65)) and the in the case of a single, atomic layer of water placed at the interface (wet condition). Again, we focus on comparing the two most common interfaces for I β cellulose – the (110) interface and the (200) interface as indicated in Figure 5-1.

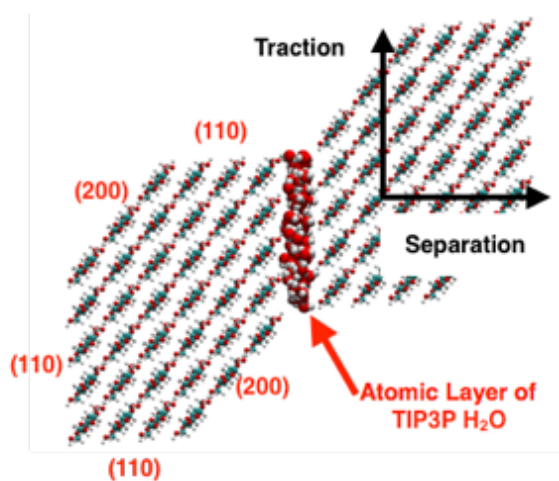


Figure 5-1: Illustration of CNC-CNC wet interface. Illustration of a CNC-CNC interface showing the (110) wet interface with an atomic layer of TIP3P water molecules between two CNCs. The pulling directions for traction and separation are indicated, as well as the two CNC surfaces ((110) and (200)) studied here.

Rather than repeat the SMD methodology used to probe the interfacial traction-separation behavior here, we refer the reader to Chapter 4, Section 4.1 (page 65). We utilize the same simulation technique for the case of a wet interface, with the primary difference being the atomic layer of water added at the interface as illustrated in Figure 5-1 for the (110)–(110) interface. To create these wet interfaces, the two crystals were moved apart normal to the interface by 5 Å and an atomic layer of TIP3P water was placed in between the crystals with a density of 1.00 g/cm³ (the bulk density of water) using the solvate tool in VMD. The TIP3P water molecule is a 3-site

water molecule (i.e. each of the three atoms is represented explicitly) and is well integrated with the CHARMM force field. We again study the elementary fibril geometry and examine finite crystals having chain lengths of 5, 10, and 15 repeat units (5.2 – 15.6 nm) to assess any possible size dependence. Equilibration and SMD simulations are conducted using the method described in Chapter 4, Section 4.1 (page 65) and we consider 5 unique starting conformations for the subsequent analysis.

5.2 Moisture Effects on Interfacial Separation

The first set of simulations examined interfacial separation with a focus on two metrics: the fracture or adhesion energy and peak force, with the fracture energy, G , defined as the energy required to separate interfaces from their equilibrium conformation to a completely separated state. These two quantities provide insight into the strength and toughness of the interface and the values are compared for the two different interfaces with and without water in Figure 5-2. Figure 5-2(A) shows there is no size dependence for different length CNCs and that the fracture energy is significantly higher for the (110) interface with values of 3.3-3.9 J/m² compared to 1.6-1.9 J/m² for the (200) interface. This trend can be directly attributed to the increased hydrogen bonding of (110) surfaces compared to (200) surfaces as observed in previous experiments¹⁴⁶ and simulations⁶⁵.

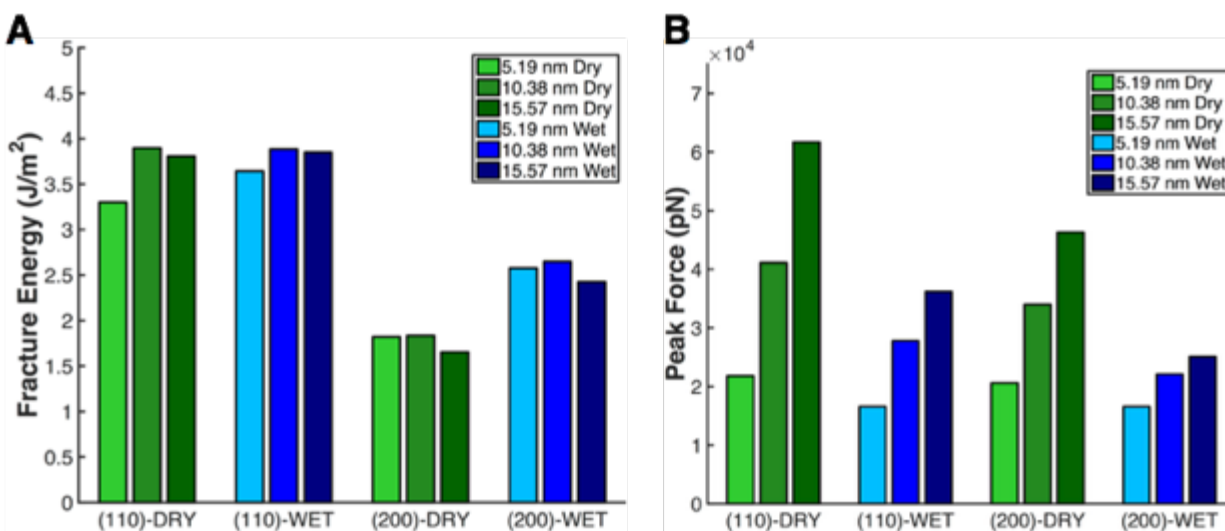


Figure 5-2: Effect of moisture on interfacial separation and mechanical properties. (A) Comparison of the work required to separate interfaces (i.e. fracture or adhesion energy) for dry interfaces (green bars) and wet interfaces (blue bars). Results are shown for both the (110) interface and (200) interfaces. (B) Comparison of the peak force experienced during interfacial separation for each of the different interfaces studied here.

When comparing fracture energies for interfaces with and without water in Figure 5-2(A), the trends are dependent on the specific CNC surface chemistry. For (110) interfaces, there is no appreciable change in the fracture energy when water is added, as the range for both cases is 3.3-3.9 J/m². However, fracture energies increase for (200) interfaces from 1.6-1.9 J/m² to 2.4-2.7 J/m² when water is present – an increase of nearly 50%. To understand these trends, a more detailed examination of the molecular level behavior of water molecules at the interface is required. Based on our previous work⁶⁵, we know that the surfaces are distinctly different in terms of their chemistry and molecular interactions. Specifically, the (110) surface has a much higher hydrogen bonding capacity compared to the (200) surface that is dominated by secondary, van der Waals interactions. Therefore, due to differences in the dominant interaction mechanism across each interface, we suspect that the interaction of water molecules with these surfaces will also differ as

hydrogen bonds are a dominant force in the ordering and conformation of water molecules in the liquid state¹⁶⁰.

Simulation trajectories for the separation process support this notion. Figure 5-3 shows snapshots from separation simulations at time $t = 0$, $t = 0.60$ ns, and $t = 1.2$ ns and illustrates the key differences between the interfaces. For the (110) interface, we observe that water tends to stick to the (110) surfaces during separation and any physical contact between the surfaces is eliminated as shown in Figure 5-3(A). However, for the (200) interface, trajectories show that water molecules prefer to maintain their interactions with one another and form a so-called capillary bridge¹⁶¹ between surfaces (Figure 5-3(B)). These capillary bridges have been observed in experiments between silica spheres having radii of 20-50 μm ¹⁶² and between a 25 nm AFM tip and silicon wafer¹⁶³. In this case, the capillary-bridge between the CNC surfaces leads to an increase in the fracture energy of this interface compared to the dry condition as it allows for increased extension of the interface before failure.

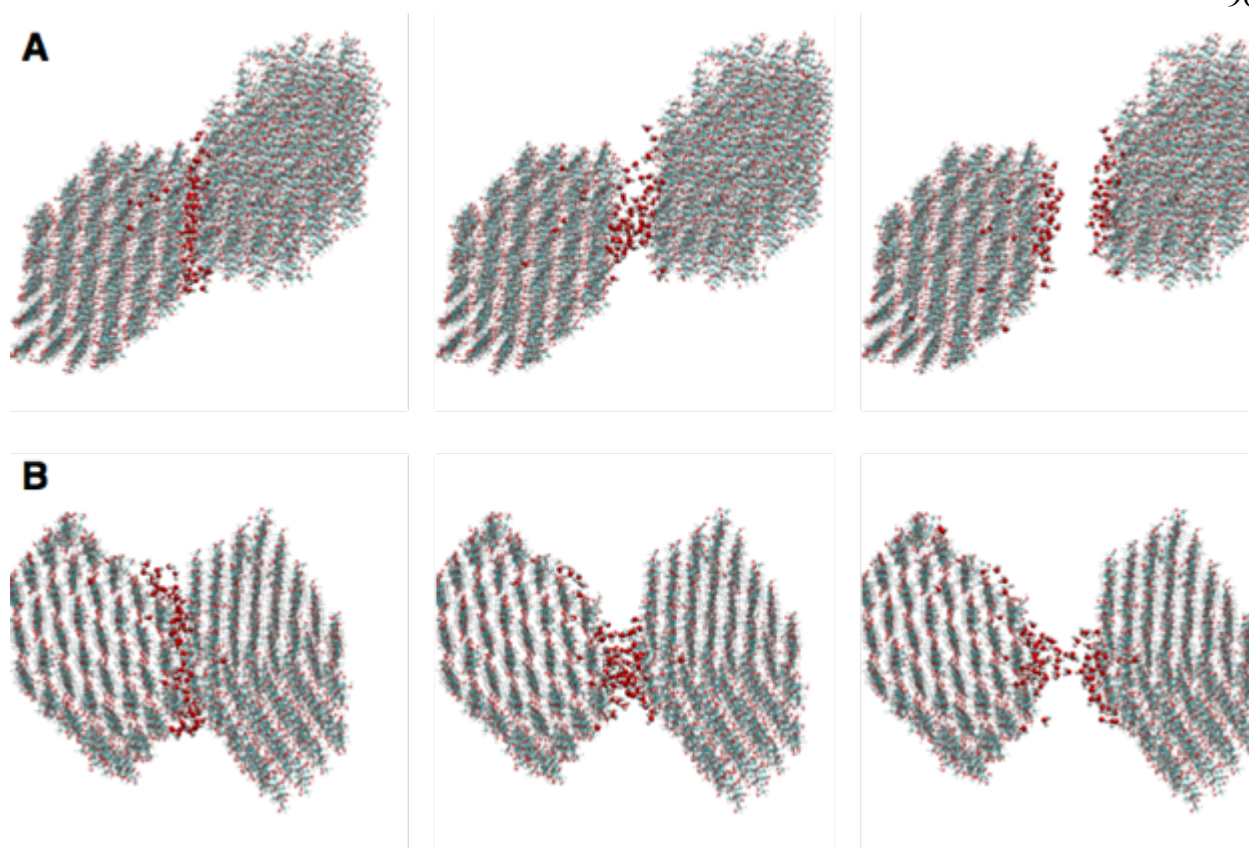


Figure 5-3: Illustration of interfacial separation mechanisms with water. VMD snapshots of the separation of the (A) (110) CNC interface and (B) (200) interface during SMD simulations. The first image corresponds to the systems after the initial equilibration run, the second image corresponds to time $t = 0.75$ ns, and the third image corresponds to time $t = 1.5$ ns. For the (110) interface, there is clean interfacial separation, while for the (200) interface there an interfacial capillary water bridge develops that provides an increase in the adhesion between CNCs.

The development of this capillary bridge also provides some additional insight into hydrophobicity of CNCs. Although CNCs are generally assumed to be largely hydrophilic^{61, 70}, as they can be dispersed in water and agglomerate upon drying⁷¹, the results of these simulations suggest distinct hydrophobic and hydrophilic patches. The (110) surface exhibits hydrophilic characteristics, as water molecules tend to stick to this surface during separation coupled with little to no change in the fracture energy compared to the dry state. However, the (200) surface exhibits hydrophobic characteristics, as water molecules prefer to maintain contact (i.e. hydrogen bonds)

with one another in lieu of non-bonded, van der Waals interactions with the (200) surface. This ordering of water molecules near the hydrophobic surface and weak hydrogen bonding has been observed for other hydrocarbon systems¹⁶⁴ and is desirable here as the formation of capillary bridges leads to an increased interfacial adhesion energy. This dual-natured hydrophilic/hydrophobic behavior of CNCs is also important in thinking of these materials as natural Janus particles that could be utilized in future interfacial applications¹⁶⁵⁻¹⁶⁶.

The peak force data presented in Figure 5-2(B) suggests similar trends between both interfaces in the presence of water. When water is added, the peak force (equivalently the peak stress) is reduced, for both interfaces, by 20-50%. Water reduces the peak force necessary to separate the interfaces from one another, thereby making these interfaces weaker. Although this lower peak force would also suggest a lower adhesion energy, when examining the energy landscapes¹⁶⁷ for dry and wet cases it is clear that the presence of water increases the extension of the interface to failure from approximately 6 Å in the dry case to 10 – 12 Å in the wet case. Further, because of these decreased peak forces with interfacial water, the elastic modulus of separation is decreased from 19.2 GPa to 13.3 GPa for the (110) interface and from 10.5 GPa to 9.5 GPa for the (200) interface – a difference of 10-30%.

5.3 Moisture Effects on Interfacial Traction

In addition to the separation behavior, the traction/shear behavior is of interest as interfacial shear properties greatly influence the properties of hierarchical materials¹⁵⁹. When comparing energy landscapes for dry and wet interfaces shown in Figure 5-4, there are clear differences. In the dry state, local energy minima and maxima are present in the energy landscapes that correspond to stick-slip events or the breaking and reformation of hydrogen bonds. However, in the hydrated state, these local energy minima and maxima are significantly reduced and almost eliminated as

no distinct “hopping” events can be discerned from the energy landscapes. Although not traditionally considered a “good” lubricant, water is at the foundation of a number of biological lubricants including saliva¹⁶⁸ that effectively reduce atomic friction between materials. Here, water serves as an effective lubricant as it reduces the energy barrier to induce shearing by up to 3-4 times as shown in Figure 5-5(A).

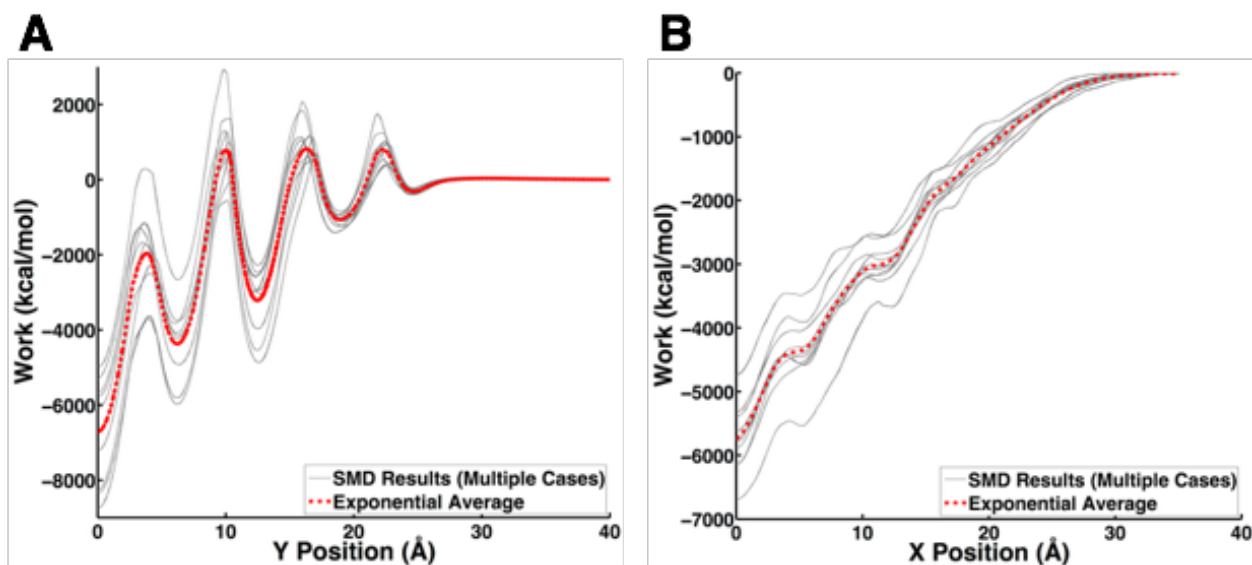


Figure 5-4: Effect of moisture on interfacial traction energy landscape. Interfacial energy landscapes of the interfacial traction process for the (110) interface for the (A) dry interface and (B) wet interface. For the dry interface, the energy barriers to shear deformation are large and well-pronounced, while moisture at the interface serves to significantly decrease energy barriers to shear and results in a “smoother” energy landscape.

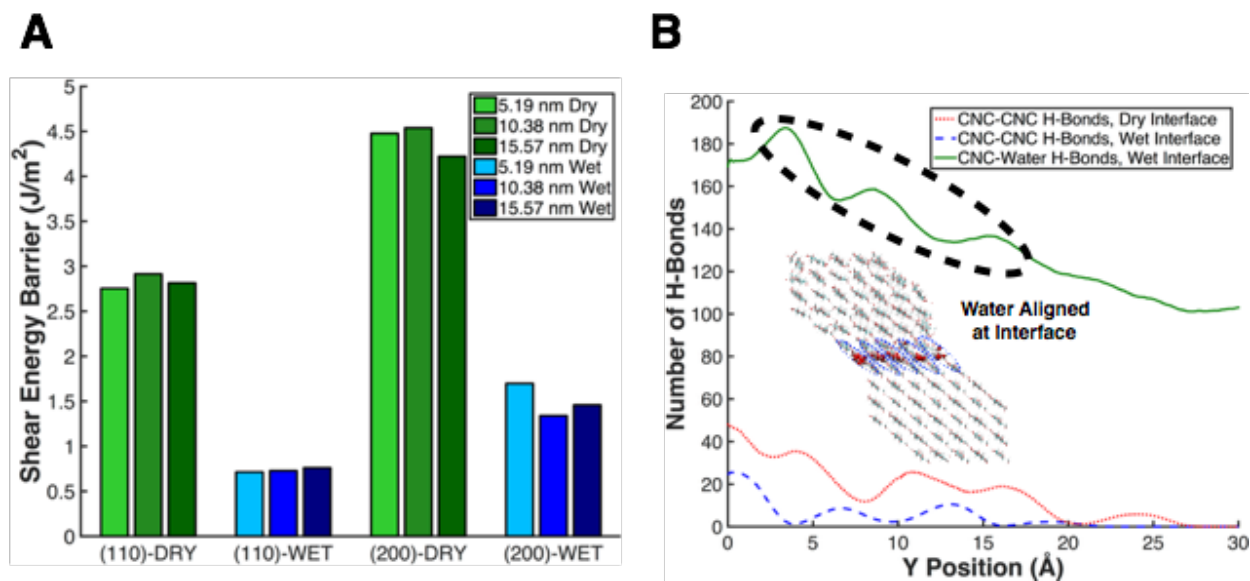


Figure 5-5: Effect of moisture on energy barriers to interfacial shear deformation. (A) Comparison of the shear energy barriers for dry interfaces (green bars) and wet interfaces (blue bars) for both the (110) and (200) interfaces. (B) The decreases in the shear energy barrier can be attributed to a disruption of interfacial hydrogen bonds for the (110) interface. Here the number of hydrogen bonds are plotted as a function of the interfacial shear displacement for the dry interface (red curve showing CNC-CNC hydrogen bonds) and wet interface (blue and green curves showing CNC-CNC and CNC-water hydrogen bonds, respectively).

In order to better quantify the interfacial effects of water under shear loading, the interlayer shear modulus, an important quantity in shear-lag models for hierarchical materials¹⁵⁹, is calculated by taking the second derivative of the initial portion of the energy landscape. The results, shown in Figure 5-6, indicate that water drastically reduces the interlayer shear modulus by two orders of magnitude from, on average, 1940 MPa to 20.4 MPa for the (200) interface and from 982 MPa to 10.5 MPa for the (110) interface. This indicates that the water layer significantly disrupts the shear resistance to sliding due to disrupted interfacial hydrogen bonds (Figure 5-5(B)) for (110) interfaces or reduced steric hindrances between surfaces for the (200) interfaces. As shown in Figure 5-5(B), the number of CNC-CNC hydrogen bonds (calculated using distance cut-off of 4 Å and angle cut-off of 50°) for the wet interface is approximately 50% lower than for the

dry interface. This decrease and associated reduction in energy barriers can be directly attributed to CNC-CNC contacts being disrupted or replaced by CNC-water hydrogen bonds that do not offer significant shear resistance. Interfacial shear properties are crucial to composite performance¹⁵⁹ and the significant effect water has on them helps to explain the drastic stiffness changes observed in cellulose-based nanocomposites upon wetting^{68, 70-71}. Our simulation results suggest that water can indeed be used as a quick way to disrupt percolated networks of CNCs and promote stimuli-responsive behavior in composites.

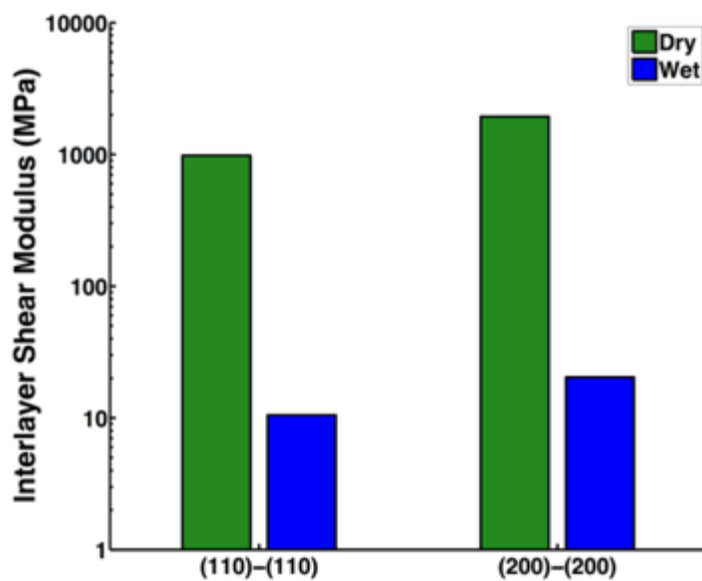


Figure 5-6: Moisture effects on interfacial shear modulus. Interfacial shear modulus (calculated by taking the first derivative of the initial portion of the shear energy landscape in Figure 4-4) for the dry interfaces (green bars) and wet interfaces (blue bars). Moisture at the interfaces significantly reduces the interlayer shear modulus by almost two orders of magnitude for both interfaces studied.

Results of traction-separation SMD simulations have been presented for CNC interfaces to study the effects of water on interfacial properties. Separation simulations revealed that water could either have a negligible effect or, surprisingly, increase the work required to separate crystals depending on the hydrophobicity of the interfacial surfaces. Our results suggest that there are clear hydrophobic and hydrophilic patches on CNCs, making them ideal candidates for applications that

require dual-natured, Janus particles as they offer benefits of being naturally available¹⁵ at a low cost compared to traditional synthetic techniques¹⁶⁶. Although our simulations were conducted using ideal CNC surface chemistries, advances in chemistry that allow for more complex, tailored surface modifications¹⁶⁹⁻¹⁷⁰ can enhance the capabilities of CNCs in this capacity with future applications ranging from molecular self-assembly to selectivity. The effects of surface chemistry on interfacial mechanics and moisture responsiveness will be discussed in Chapter 6 (page 102).

Traction simulations demonstrated the capability of water to act as a lubricant between surfaces and drastically change interfacial shear properties. A single atomic layer of water can reduce the amount of friction between these atomically rough surfaces that make up the interface, albeit at the cost of reducing the interlayer shear modulus between crystals. These interlayer shear properties are especially important in the context of hierarchical cellulose materials such as aligned neat films¹⁷¹ in which the emergent macroscale behavior is dictated by nanoscale interactions. On one hand, our simulations reveal that the presence of water between crystals, and possibly other solvents or polymers, could be detrimental to the overall performance of these materials. On the other hand, drastic change in the shear modulus at the CNC interfaces corroborates earlier findings that percolated networks of nanocrystals or nanowhiskers can have stimuli-responsive mechanical properties arising from moisture effects at interfaces. Not only does the type of interface govern several interfacial properties, but processing and environmental conditions play an important role in dictating the performance of these hierarchical cellulose materials.

Chapter 6 – Tailoring of Water Adsorption and Interfacial Mechanics Through Ion Exchange Surface Modification

In the previous three chapters (Chapters 3–5), we focused on the materials discovery aspect of computational materials-by-design and aimed to understand fundamental, underlying mechanics of CNCs and interfaces they form with one another. With these results in mind, we now shift our focus to the materials development aspect where we aim to identify how intentional nanoscale interface design can be used to alter the properties of CNC-based nanocomposites. In this chapter, we begin by examining the effects of surface modification on the water adsorption and interfacial mechanical properties of CNCs. Specifically, we study a surface modification technique known as ion exchange in which sodium ions on the surface of sulfated CNCs are replaced with methyltriphenylphosphonium (MePh_3P^+) cations. We utilize a combination of GCMC simulations and SMD simulations to understand changes in the surface behaviors that impact water adsorption and interfacial mechanical properties. Notably, we find that this specific surface modification can be used to reduce water adsorption. Further, we find that the surface modification decreases adhesion and shear resistance for dry interfaces, while offering improved response to the presence of interfacial moisture. Portions of the text and figures within this chapter are reprinted or adapted with permission from Fox et al., *ACS Appl. Mater. Interfaces* 2016. Copyright 2016 American Chemical Society. GCMC simulations were conducted in collaboration with Zonghui Wei and Dr. Erik Luijten, Northwestern University, and experimental results included are provided courtesy of Dr. Doug Fox, American University, and Dr. Jeff Gilman, National Institute of Standards and Technology.

6.1 Simulation Parameters

To simulate the effects of water adsorption and interfacial traction-separation of surface modified CNCs, there are several preliminary steps we need to take to generate these systems. While initially we had considered the ideal CNC surface chemistry, here we consider the effect of the chemical extraction process on the surface chemistry of CNCs. When CNCs are prepared from oxyanionic acids such as H_2SO_4 or H_3PO_4 , in addition to the acid hydrolysis at the disordered regions of the fiber, a side esterification reaction occurs on the surface of the nanocrystals¹⁷²⁻¹⁷³. This leads to incorporation of anionic sites periodically along the CNCs in which hydroxyl groups are replaced by other chemical compounds. In this study, we consider the case of sulfuric acid being used as the extraction acid, which results in hydroxyl groups at the surface being replaced by sulfate groups as shown in Figure 6-1.

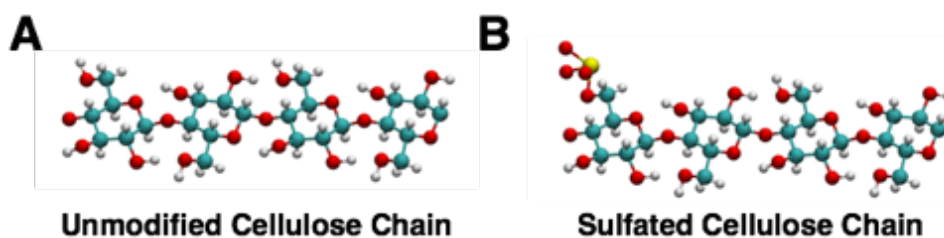


Figure 6-1: Surface modification from CNC extraction process. When CNCs are extracted using acid hydrolysis, the acid not only removes the crystalline region from the disordered amorphous region, but also produces a side esterification reaction at the surface. This reaction causes hydroxyl groups at the surface to be replaced by other chemical groups. For example, in this study we consider the case of using sulfuric acid as the extraction agent in which the unmodified surface (panel A) has some of the hydroxyl groups replaced by sulfate groups (panel B).

In simulation, there are several considerations that must be made when replacing hydroxyl groups with sulfate groups. First, appropriate parameters must be obtained for this specific modification. Using *cgenff*⁹⁸ of the modified glucose subunit of cellulose, we find the parameters for the sulfate group to have low penalty values (as indicated in Chapter 12 (page 226)) and are

acceptable for simulation. Second, we need to consider the percentage of hydroxyl groups that are replaced by sulfate groups on the CNC surface. In all simulations performed here, 1 out of every 10 hydroxyl groups on the surface of the CNC are replaced with sulfate groups. This is in good agreement with experimental values¹⁷⁴ which have measured the density of sulfate groups ranging from 1 out of every 10 hydroxyl groups to 1 out of every 30 hydroxyl groups. Finally, we also note that the sulfate groups that replace hydroxyl groups at the surface have a net negative charge and must be neutralized by some associated cation. Experiments have shown that the sulfate groups are most often neutralized by a single sodium cation (Na^+). The presence of these sodium cations creates severable obstacles to optimal CNC performance including high levels of water absorption, low thermal stability, poor miscibility with nonpolar polymers, and irreversible aggregation of dried CNCs.

A general approach to changing the interactions between CNCs is via surface modification¹⁷⁵. Recently, Fox *et al.* developed a novel ion exchange method to further modify sulfated CNC surfaces¹⁷⁶. In this ion exchange technique, the sodium cation can be exchanged for larger, more non-polar cations such as methyl(triphenyl)phosphonium (MePh_3P^+), pictured in Figure 6-2(A). Experiments have shown that replacing the sodium cation with MePh_3P^+ reduces water adsorption and improves thermal stability of the nanocrystals. Further, these modified CNCs improve filler dispersion when incorporated in polystyrene–CNC nanocomposites¹⁷⁶. These experimental results demonstrate the tremendous potential of using ion-exchanged CNCs in CNC-reinforced nanocomposites to overcome current shortcomings in this class of materials. Despite the promising experimental results, a molecular-level understanding and explanation of the effects of surface modification is still limited. Computational approaches can be utilized to obtain direct insight into the properties of chemically modified CNC surfaces. With the advent of generalized

all-atomistic force fields¹⁷⁷, these novel chemical modifications can be rapidly parameterized⁹⁹ and further characterized using existing simulation techniques. In this study, we investigate the surface and interfacial behaviors of ion-exchanged CNCs using grand-canonical Monte Carlo (GCMC) to measure water adsorption and steered molecular dynamics (SMD) to quantify interfacial mechanical properties.

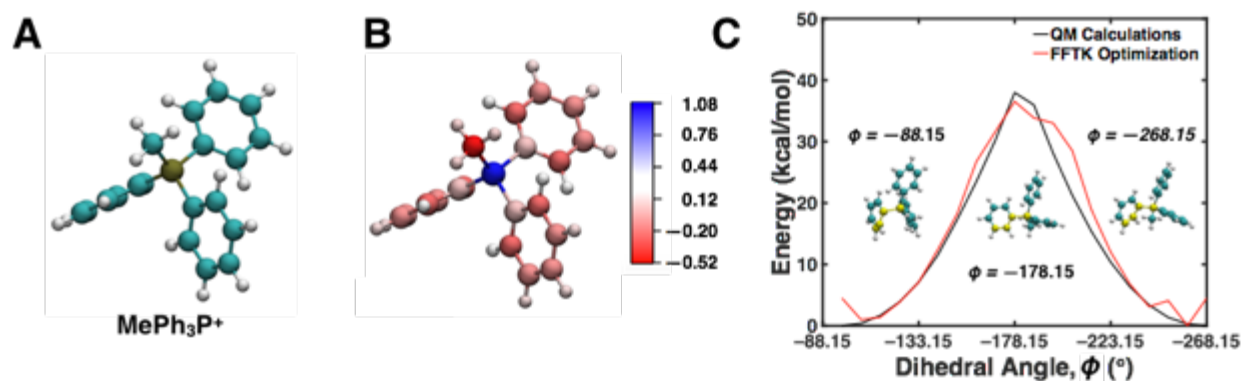


Figure 6-2: Summary of FFTK parameterization of the MePh₃P⁺ cation. (A) Illustration of the MePh₃P⁺ ionic surface modification that is exchanged for sodium cations on sulfated CNCs. Color codes: cyan–carbon, white–hydrogen, brown–phosphorus. (B) Illustration of the cation colored by the atoms’ partial charges calculated using the FFTK protocol. Electronegative atoms are shaded red, electropositive atoms are shaded blue, and aliphatic hydrogen atoms are shaded white with a fixed charge of +0.09e. The net dipole moment of the ion is found to be 1.1 D (1.1×10^{-18} statC·cm) (C) Comparison of the energy landscape of the C–C–C–P dihedral (yellow atoms) within MePh₃P⁺ ranging from a dihedral angle of $\phi = -88.15^\circ$ to $\phi = -268.15^\circ$ in steps of 15° . A cut-off of 10 kcal/mol is used in optimization and root-mean-square error (RMSE) calculations. The plot shows good agreement between the energy landscapes computed using QM calculations (black) and the optimized CHARMM dihedral parameters obtained from FFTK (red line) resulting in an RMSE of 2.343.

In our simulations of surface-modified CNCs, we utilized the CHARMM force field⁹¹ and employed parameters from the generalized CHARMM force field¹⁷⁷ and CHARMM force field for carbohydrates¹⁷⁸⁻¹⁸⁰ for the sulfated CNCs. For the MePh₃P⁺ ionic surface modification, illustrated in Figure 6-2(A), we initially intended to use the generalized CHARMM force field, but

upon parameterizing the molecule with the cgenff program¹⁷⁷ (version 3.0.1), we noticed extremely high penalty values (greater than 50) for partial charges as well as bond, angle, and dihedral parameters. As an alternative, we determined the partial charges and structural parameters with high penalty scores using the Force Field Toolkit⁹⁹ (FFTK) package implemented in Visual Molecular Dynamics¹⁰⁰ (VMD) as discussed in Chapter 2 (page 27). Figure 6-2(B) illustrates the partial charges calculated using this technique. The magnitude of the dipole moment for the MePh_3P^+ cation is found to be ~ 1.1 D, which is much lower than the dipole moment of 1.85 D calculated for a water molecule. To demonstrate the accuracy of this parameterization technique, Figure 6-2(C) shows a comparison between the energy landscapes of the C–C–C–P dihedral calculated using QM relaxed potential-energy surface scans and the optimized dihedral parameters from FFTK. The full set of parameters used to simulate the MePh_3P^+ are provided in Chapter 12 (page 226).

To study the water adsorption on CNC surfaces, GCMC simulations were conducted using the LAMMPS package⁸⁶. It should be noted that although CHARMM interfaces very well with NAMD, we can easily convert our structure and parameter files to be compatible with LAMMPS. CNCs with two (110) surfaces exposed and dimensions of 10.38 nm along the length of the chain (10 repeat units), 3.31 nm along the width of the crystal (6 chains), and 1.19 nm along the thickness of the crystal (2 layers) were generated using the cellulose-builder tool¹⁸¹ and psfgen tool in VMD. On each surface, we exchanged 1 out of every 10 hydroxyl groups with sulfate groups and placed the sodium or MePh_3P^+ cations adjacent to these groups. The sulfate groups were equally spaced on the surfaces as pictured in Figure 6-3(B). The CNC was put in a simulation box with dimensions of 10.38 nm \times 3.31 nm \times 8 nm with periodic boundary conditions in three dimensions. The CNC was first equilibrated in vacuum at $T = 300$ K for 2 ns using an NVT ensemble and a Langevin

thermostat with a damping parameter of 100 fs. Spring forces with a spring constant of 10 kcal/mol-Å² were applied to the backbone carbon atoms of the cellulose chains to tether them to their initial positions within the CNC surface plane. After the system was equilibrated, GCMC simulations were performed with insertions and deletions attempted every 100 fs, with the system equilibrated using grand canonical MD simulations between GCMC steps.

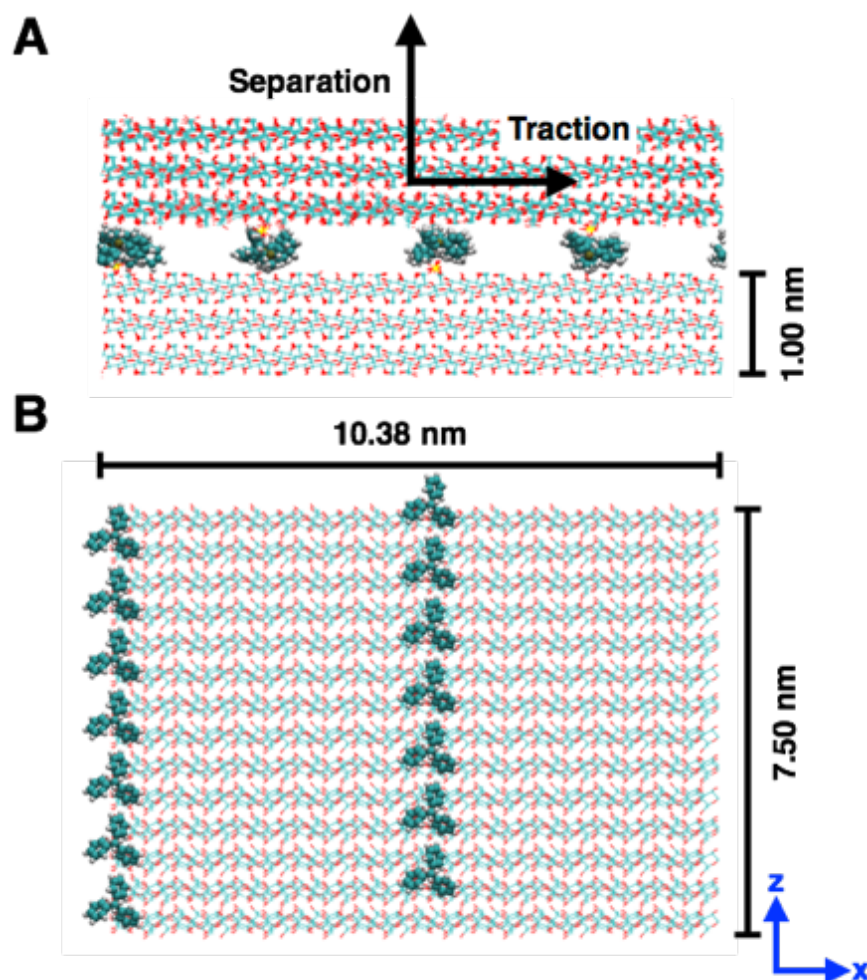


Figure 6-3: Ion exchange surface modification of CNC surfaces. (A) Illustration of the CNC–CNC interface studied using SMD simulations and indicating the direction of the SMD pulling force used to induce traction and separation failure of the interface. (B) Illustration of one of the surface-modified CNCs surfaces showing the distribution of cations as well as the dimensions of the CNC.

To understand how surface modifications influence the traction-separation behavior of surface-modified CNC interfaces, SMD simulations were conducted using NAMD software⁸⁷. CNC interfaces, with the (110) surface exposed, were generated using the same tools mentioned in the previous section and are illustrated in Figure 6-3(A). For our SMD simulations, CNCs have dimensions of 10.38 nm along the length of the chain (10 repeat units), 7.50 nm along the width of the crystal (14 chains), and 1.79 nm along the thickness of the crystal (3 layers). To create interfaces, two CNCs were placed in a simulation box together such that the sulfate groups from opposing surfaces were in an interdigitated conformation as shown in Figure 6-3(A). Periodic boundary conditions were used along the length and width of the crystals with a non-periodic boundary employed along the thickness of the crystal. The number of hydroxyl groups replaced with sulfate groups was also 10% with a sulfate group distribution pictured in Figure 6-3(B).

Before conducting traction-separation simulations, CNC–CNC interfaces were equilibrated under an NVT ensemble at $T = 300$ K for 1.5 ns. During this equilibration, the backbone carbon atoms of the lower crystal were fixed in place while the upper crystal was free to move into contact with the lower crystal to develop the interface. As measured from simulations, the distance between the center of mass of the top crystal and the center of mass of the bottom crystal at equilibrium is ~ 18.91 Å for Na-CNCs and ~ 25.39 Å for MePh₃P-CNCs. For the cases with water at the interface, a single atomic layer of rigid TIP3P water molecules was inserted between the two CNCs prior to equilibration using packmol¹⁸². Past experiments¹⁷⁶, as well as the GCMC simulations conducted in this study, revealed that MePh₃P⁺-modified CNCs adsorb less water than those with a sodium cation. We aimed to reflect this in our interfacial simulations by placing fewer water molecules at interfaces with MePh₃P⁺ cations (616 water molecules at 90%

relative humidity according to GCMC simulations) than those with sodium cations (707 water molecules at 90% relative humidity).

Once the systems were equilibrated, SMD simulations were conducted to determine the traction-separation behavior of both “dry” and “wet” interfaces. In these simulations, the bottom crystal was again fixed and the SMD force was applied to the center of mass of backbone carbon atoms in the top crystal to simulate interfacial traction and separation, as indicated in Figure 6-3(A). SMD simulations employed a constant pulling velocity of 0.00002 Å/fs and a relatively high SMD spring constant of 4000 kcal/mol-Å² to reduce oscillations of the pulled atoms. These SMD parameters are consistent with our previous studies^{78, 183} and are appropriate for avoiding any issues associated with rate dependence. Five simulations with independent starting configurations were conducted for each case to appropriately determine the mechanical properties and changes in free energy^{102, 106} associated with these interfacial modes of failure.

6.2 Water Adsorption of Surface Modified CNCs

GCMC simulations were conducted to determine the effect of surface modification on water adsorption and potentially improve the material response that is considered a negative aspect of Na-CNCs. While we can directly control the chemical potential μ in simulation, experiments focus instead on controlling the relative humidity (RH) of the environment. Therefore, we must relate the chemical potential to the relative humidity using the Widom method under the NPT ensemble given by Eq. (6-1)

$$\mu = k_b T \ln \left(\frac{P \Lambda^3 \phi}{k_B T q} \right) \quad (6-1)$$

where k_B is Boltzmann’s constant, T is the temperature, Λ is the de Broglie wavelength, q represents the single-molecule partition function (excluding the translational component) and ϕ is

the fugacity coefficient. For the TIP3P water molecule used in our simulation, the saturated fugacity coefficient is found to be ~ 1 at $T = 300 \text{ K}$ ¹⁸⁴. This indicates water can be treated as an ideal gas in this case. Therefore, we can relate the chemical potential to the relative humidity through Eq. (6-2) where μ_{sat} is the chemical potential of saturated vapor which is determined to be -10.96 kcal/mol for water.

$$\mu - \mu_{sat} = k_b T \ln RH \quad (6-2)$$

Figure 6-4 summarizes the results of our water adsorption simulations. Figure 6-4(A) shows the number of water molecules adsorbed per unit area for each of the different surface modifications as a function of the relative humidity. Notably, we find that replacing sodium with MePh_3P^+ can reduce the water adsorption by as much as $\sim 15\text{-}20\%$ which is qualitatively consistent with experiments. The qualitative agreement indicates the accurate prediction ability of simulations in terms of relative water uptake ability, which can facilitate future design of CNC surface modifications. Further, simulations also provide insight into the molecular-level structure, ordering, and dynamics of water molecules near CNC surfaces. As shown in Figure 6-4(B), adsorbed molecules tend to aggregate near the cations and sulfate groups on CNC surfaces as they have stronger interactions with the highly electronegative sulfate groups. To provide a detailed view of the interactions between the water molecules and the cations, we calculate the radial distribution functions (RDFs) of the oxygen atoms of the water molecules around the different cations as shown in Figure 6-4(C). The RDF central points are chosen as the sodium atom itself for Na-CNCs and the central phosphorus atoms in MePh_3P^+ for the MePh_3P -CNCs. For the Na-CNC surfaces, the RDFs show short-distance peaks at $\sim 2.3 \text{ \AA}$, demonstrating the strong electrostatic interactions between water molecules and sodium cations. There are also secondary peaks at $\sim 4.4 \text{ \AA}$, which arise from the intermolecular hydrogen bonding of water molecules with

the first layer of water surrounding the sodium cations. For the MePh₃P-CNC surfaces, the RDFs also display a two-peak profile but with closer peak locations that can be attributed to the bulky ionic structure of MePh₃P⁺ disrupting interactions between the water molecules and the positively charged phosphorous atom. Compared to the water distribution near Na-CNC surfaces, where the first layer of water is distributed within 3 Å from the sodium atom, water molecules appear at least 3 Å away from the phosphorus atom on MePh₃P-CNC surfaces. The disruption from the bulky ion structure and the effective non-polar nature of MePh₃P⁺ shown in Figure 6-2(B) are the primary reasons that these surface-modified CNCs exhibit reduced water uptake compared to Na-CNCs.

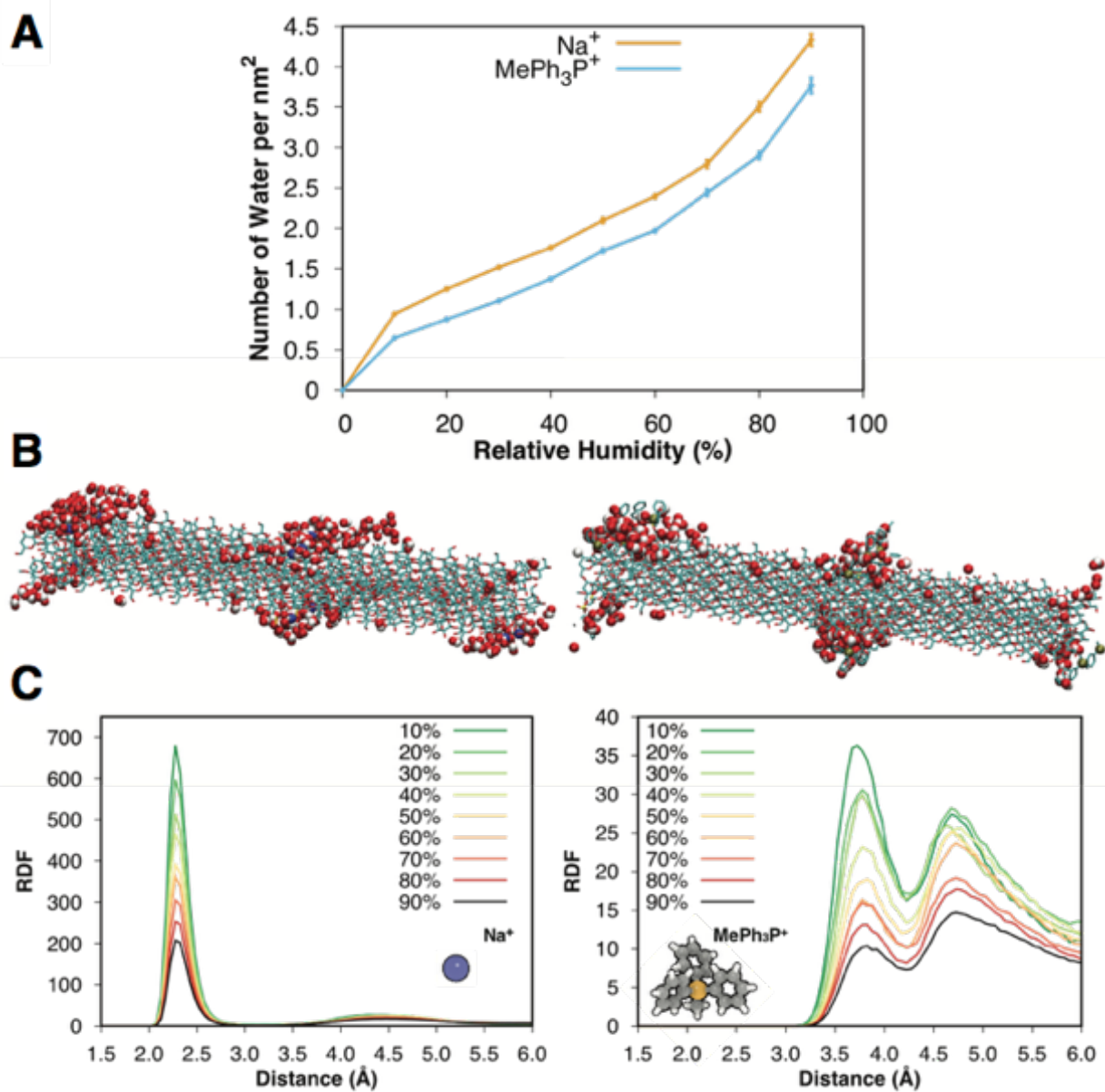


Figure 6-4: Water adsorption on surface modified CNCs. (A) Number of adsorbed water molecules per nm² as a function of RH for Na-CNC and MePh₃P-CNC surfaces, obtained from GCMC simulations. (B) Representative simulation configurations of adsorbed water on Na-CNC (left) and MePh₃P-CNC surfaces (right) at RH = 60%. Color codes: cyan–carbon, red–oxygen, white–hydrogen, yellow–sulfur, blue–sodium, brown–phosphorus. (C) RDFs of water oxygen atoms around the sodium atoms (left) and the phosphorus atoms in MePh₃P⁺ (right).

6.3 Separation of Surface Modified CNCs

Separation simulations are used to determine several important interfacial mechanical properties including interfacial adhesion energy as well as interfacial stiffness and strength. First, we calculate the interfacial adhesion energy by integrating the force–displacement curves and taking an exponential average of five independent trajectories^{102, 106}. These force–displacement curves and the interfacial adhesion energies for dry and wet interfaces are shown for Na-CNCs in Figure 6-5(A) and for MePh₃P-CNCs in Figure 6-5(B). For the force-displacement curves, a separation distance of zero corresponds to the equilibrium configuration of the two CNC surfaces. There are several interesting trends we observe in the interfacial adhesion energy calculations. First, we note that in the dry case the adhesion energy is significantly decreased when sodium cations are replaced with the larger MePh₃P⁺ cations. As discussed in our previous study¹⁷⁶, the larger cation decreases interfacial adhesion by physically increasing the distance between the two CNCs, which prevents hydrogen-bonding formation across the interface and at the same time reduces van der Waals interactions.

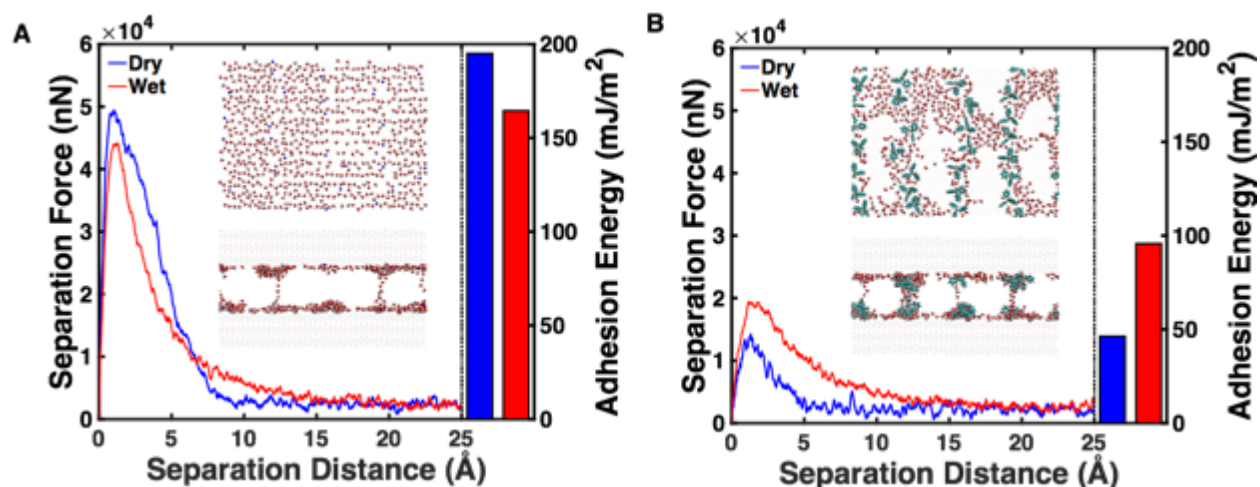


Figure 6-5: Effect of surface modification and moisture on interfacial adhesion energy of CNCs. Force–displacement curves and interfacial adhesion energies for the separation of CNC–CNC interfaces averaged over five independent starting configurations for (A) Na-CNCs and (B) MePh₃P-CNCs. Blue plots/bars correspond to the dry interface and red plots/bars correspond to the wet interface. The adhesion energy is calculated by integrating the individual SMD force–displacement curves and taking the exponential average to get the energy difference between the equilibrated state and fully separated state corresponding to a separation distance of 3 nm. Insets are top and side views of the water distribution at CNC–CNC interfaces. The aggregation of water molecules around MePh₃P⁺ modifications leads to the formation of more numerous capillary bridges between CNC surfaces.

Beyond comparing the two surface chemistries directly, it is interesting that when water is introduced at the interface there are opposing trends. For the interface with MePh₃P⁺ cations, the interfacial adhesion energy increases by ~106% when water is introduced while for the interface with sodium cations the interfacial adhesion energy decreases by ~16%. As the interfaces are separated, water molecules can either stay in close contact to the individual surfaces or maintain contact with other water molecules to form so-called capillary bridges¹⁸⁵⁻¹⁸⁶ between the surfaces. The simulation snapshots in Figure 6-5(A) and (B) show that with the same distance (~4 nm) between the center of masses of the upper and lower crystals, the MePh₃P⁺ interface exhibits capillary bridges that are larger in number (6 total bridges) than the sodium interface (3 total

bridges). The existence of more numerous capillary bridges can be attributed to the higher concentration of water molecules around the MePh_3P^+ cations at the interface as illustrated in the top view of the interfaces at equilibrium separation distances in Figure 6-5(A) and (B). Additionally, formation of these bridges is encouraged because of the chemical nature of the MePh_3P^+ cation. The three non-polar phenyl groups on this cation encourage the formation of capillary bridges as water-water interactions are more thermodynamically favorable than water-phenyl interactions. As discussed in our previous study¹⁸⁷ and illustrated in the force-displacement plots for MePh_3P^+ in Figure 6-5(B), these capillary bridges serve to increase the adhesive force between surfaces as well as the interfacial failure strain.

The decrease in adhesion energy observed for sodium interfaces can be explained by water molecules disrupting hydrogen bonds between CNC surfaces. In other words, hydrogen bonds between hydroxyl groups on CNC surfaces are replaced by water-hydroxyl hydrogen bonds that are relatively weaker due to their decreased occupancy shown in Figure 6-6. The occupancy is defined as the percentage of time a hydrogen bond is within the cut-off criteria over the course of a canonical simulation. Occupancy values greater than 100% indicate a donor/acceptor forms more than one hydrogen bond. Hydrogen bonds are calculated in VMD using a donor-acceptor distance cut-off of 4 Å and an angle cut-off of 50° where the angle ϕ is defined as $\phi = 180^\circ - \phi_{\text{O-H-O}}$ ¹⁸⁸. Our simulation results parallel recent experimental findings that measure the surface energies of surface-modified CNCs. In those experiments¹⁷⁶, compared to the dry samples, the surface energy of Na-CNCs decreases at RH = 50% while the surface energy of MePh_3P -CNCs increases.

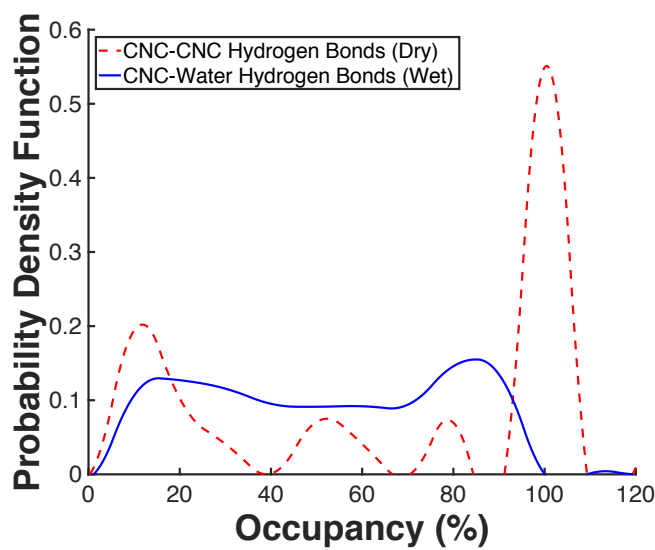


Figure 6-6: Hydrogen bond occupancy at surface-modified CNC interfaces. The occupancy is defined as the percentage of time a hydrogen bond is “on” (i.e. within the specified distance and angle cut-off) during simulation. Here, hydrogen bond occupancy is computed between CNCs in the dry case and between CNCs and water in the wet case. We find that occupancy is on average higher between two CNCs, allowing us to consider them a more stable and stronger molecular level interaction.

6.4 Traction Behavior of Surface Modified CNCs

Traction simulations also reveal some interesting behavior in how the different interfacial chemistries respond to the presence of water under shear deformation. The force–displacement plots are shown for these traction simulations in Figure 6-7. For the dry interface with sodium cations, a sinusoidal, periodic shape is observed for the shear force–displacement curves. Here the force peaks have a periodicity of ~ 5.2 Å, which corresponds to the size of one glucose unit along the cellulose chain backbone. We also observe two distinct shearing events that can be explained by examining the hydrogen bonds and alignment of glucose units across the interface. The first event, corresponding to a force barrier (i.e. the difference between force minimum and maximum) of 20–30 nN, is consistent with the breaking of many hydrogen bonds across the interface. We verify this mechanism by tracking the number of hydrogen bonds formed between cellulose chains

across the interface as shown in Figure 6-7(A). The locations of the large force barriers slightly lag behind the maximum values in the number of hydrogen bonds when C6 hydroxyls (yellow atoms in Figure 6-7(B)) are aligned with C2 hydroxyls (blue atoms in Figure 6-7(B)) on the opposing CNC surface. In contrast, the second shearing event has a lower force barrier of 10–15 nN and corresponds to the positions where there is a minimum number of hydrogen bonds. Here, C2 and C6 hydroxyls interact with the identical hydroxyls across the interface and form fewer hydrogen bonds, resulting in significantly lower force barriers to shear displacement.

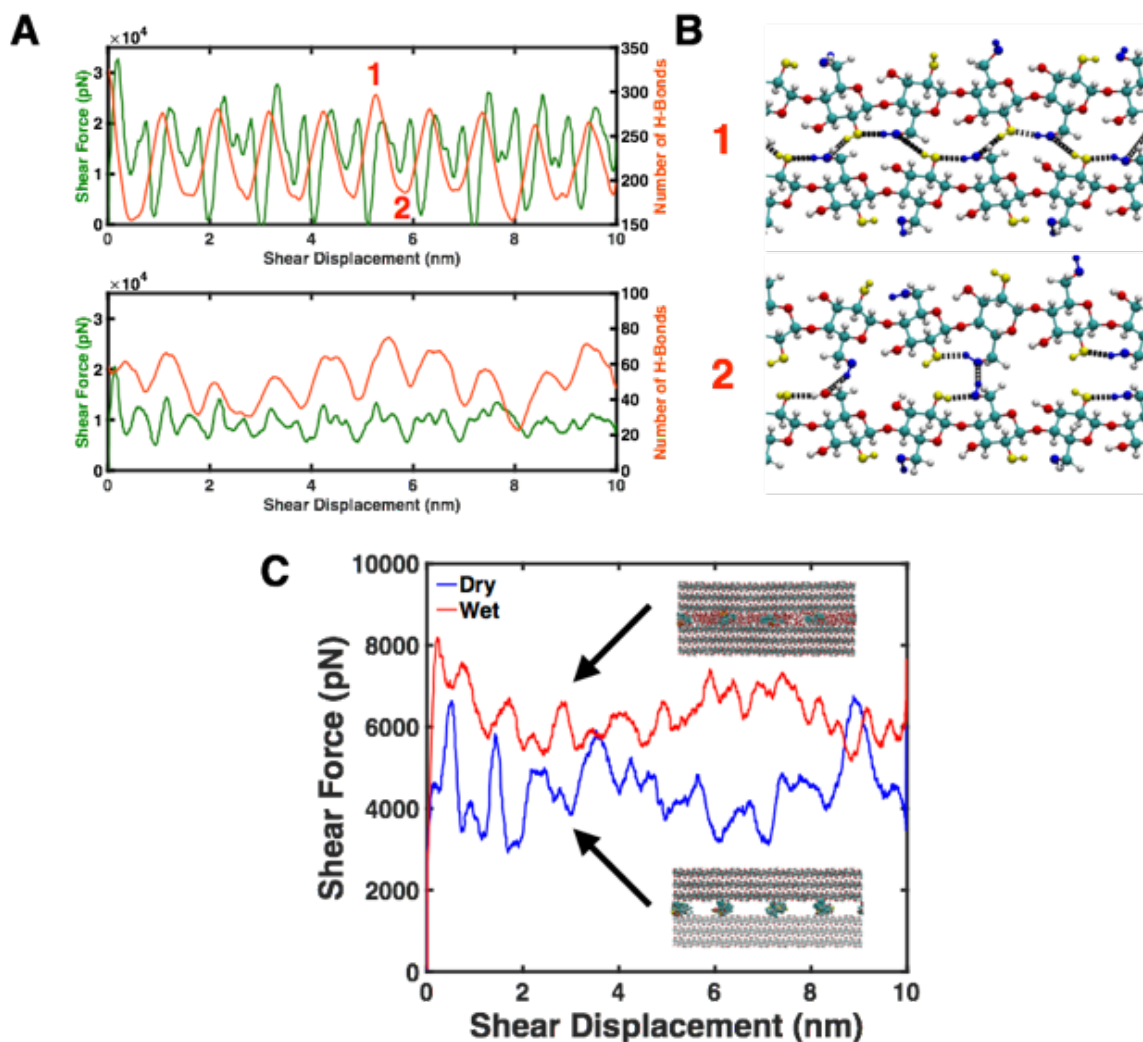


Figure 6-7: Effect of surface modification and moisture on interfacial traction of CNCs. (A) Force–displacement curves (green lines) for the CNC–CNC interface with sodium cations under shear deformation both in the absence (top) and presence (bottom) of moisture. The number of CNC–CNC hydrogen bonds formed across the interface (orange lines) are overlaid on these curves to demonstrate how the force–displacement behavior is governed by breaking and reformation of hydrogen bonds. (B) Illustration of the hydrogen bond network formed across the interface. A maximum number of hydrogen bonds (marker 1 in Figure 5A) is formed when C6 hydroxyls (yellow atoms) interact with C2 hydroxyls (blue atoms) across the interface and a minimum is observed (marker 2 in Figure 5A) when these hydroxyls interact with the identical hydroxyls across the interface. (C) Force–displacement curves for the CNC–CNC interface with MePh_3P^+ cations under shear deformation both in the absence (blue line) and presence (red line) of moisture.

While this overall shape and periodicity is mostly preserved when water is added at the interface, the shear force barrier is significantly decreased to 5–10 nN. These results suggest that water serves as a lubricating agent and reduces interfacial friction to sliding between the two surfaces. The near-sinusoidal shape suggests that a hydrogen bond network is maintained across the interface as shown in Figure 6-7(B), although the number of CNC–CNC hydrogen bonds decreases significantly compared to the dry interface. The decrease in CNC–CNC hydrogen bonding is accompanied by the development of a CNC–water–CNC hydrogen bonding network across the interface. This network also contributes to some amount of interfacial shear strength, but is significantly weaker than the network formed at the dry interface due to the lower stability and lifetime of CNC–water hydrogen bonds discussed in the previous section.

The behavior of the MePh_3P^+ interface is quite different as shown in Figure 6-7(C). While there is still some indication of periodicity, the force barriers are significantly smaller in magnitude compared to Na-CNCs. This is expected for such an interface with no hydrogen bonds due to the large physical distance between CNC hydroxyl groups. During shear deformation, these hydroxyl groups interact through relatively weaker non-bonded interactions with cations from the opposing surface¹⁷⁶. When water is added at this interface, the interfacial shear force is increased. These results can be explained by the amphiphilic nature of the surfaces that couple hydrophilic patches of the hydroxyl-rich bare CNC surface with effectively hydrophobic patches at the locations of the MePh_3P^+ . We consider the locations of the cations to be effectively hydrophobic due to the presence of the non-polar phenyl groups that do not interact favorably with water molecules. The results of our previous study⁷⁸ suggest that water serves as a lubricating agent for purely hydrophilic or hydrophobic surfaces. Rather than acting as a lubricating agent, water here serves to bridge the hydrophilic patches on opposing surfaces and leaves the cation-CNC interactions

unchanged. In the dry case, these hydrophilic regions are physically separated, but when water is introduced, it fills the empty space as shown in Figure 6-7(C). In doing so, the interface exhibits increased resistance to shear deformation through a newly developed water-mediated hydrogen bonding network across the interface.

6.5 Comparison to Experimental Results

While the results of these simulations provide some insight into molecular level behavior of surface modified CNCs, we are also interested in determining if this behavior is exhibited experimentally. While a direct experimental comparison is unobtainable due to the difficulty of conducting traction-separation simulations between individual CNCs, we can validate our results using other experiments. Here, we utilize the results of inverse gas chromatography (IGC) experiments that measure the surface energy of surface modified CNCs⁸⁶. In this experimental method¹⁸⁹, a series of gases are flown past a column containing CNCs and by measuring the amount of gas adsorbed, the surface energy can be computed. Here, the surface energy is similar to the interfacial adhesion energy calculated in our simulation.

The experimental results are shown in Figure 6-8. First, we consider the results presented in Figure 6-8(A) for several different surface modifications. We see that the surface energy is lowered by replacing sodium ions with MePh_3P^+ cations, which agrees with the simulation results that show that the adhesion energy is lowered when replacing sodium ions and disrupting CNC-CNC interactions (i.e. hydrogen bonding). Second, the results presented in Figure 6-8(B) show how the surface energy changes in response to moisture. For the sodium cation, there is a decrease in the surface energy at 50% RH, while for the MePh_3P^+ cation there is a slight increase in the surface energy. This falls in line with the simulation results that show similar trends for systems at 100% humidity. Overall, it is promising to see good agreement between simulation and

experiments and suggests that nanoscale simulations can be used in the future to rapidly evaluate the performance of many different types of surface modifications to further accelerate the materials development process.

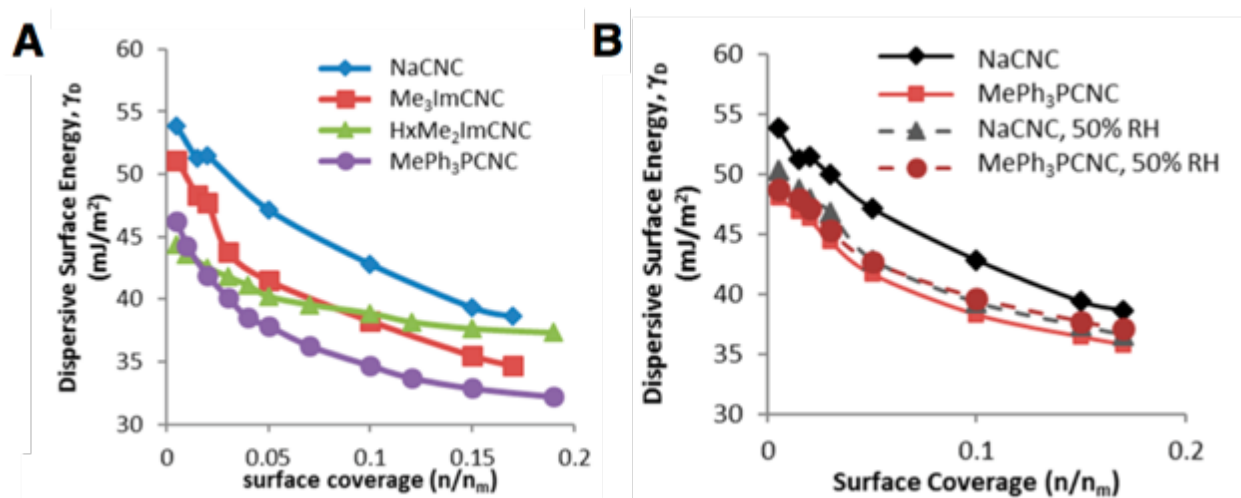


Figure 6-8: Experimental measurements of CNC surface energy from inverse gas chromatography. (A) Surface energy for several different CNC surface modifications as a function of overall surface coverage. Of interest are the blue curve (Na-CNCs) and purple curve ($\text{MePh}_3\text{P-CNCs}$). (B) Surface energy for the two surface modifications of interest for both dry environments (dark curves) and at 50% RH humidity (light curves). These experimental results are in good agreement with nanoscale simulations of interfacial mechanics.

Chapter 7 – Relaxation Dynamics of Nanocomposites with Polymer-Grafted CNCs

In the previous chapter, we focused on how ion exchange can be used to chemically modify the surfaces of CNCs and greatly influence their water adsorption and interfacial mechanics. In the spirit of continuing the process of materials development, here we consider the effects of direct grafting of synthetic polymers to the surface of CNCs. While this most likely has some direct implications on the interfacial mechanics and water adsorption, here we present results related to how the presence of polymer grafts alters relaxation dynamics of polymers chains when these polymer-grafted CNCs are embedded in a synthetic polymer matrix. Polymer relaxation provides an initial understanding of the degree of nanoconfinement developed within the system and provides insight into how polymer grafts can be used to effectively change polymer nanocomposite thermomechanical properties. Using polymer relaxation measurements, we directly compare traditional non-grafted particles to polymer-grafted nanoparticles and explain how polymer grafts can accelerate relaxation dynamics and reduce the effects of nanoconfinement.

7.1 Background and Simulation Parameters

The development of polymer-grafted nanoparticles has traditionally been proposed for improving the properties of nanocomposites¹⁹⁰. In these materials, miscibility of inorganic filler particles (e.g. silica) with an organic host phase (e.g. amorphous polymers such as polystyrene (PS) or poly(methyl-methacrylate) (PMMA)) is often low and these weak filler-matrix interfaces lead to poor particle dispersion and thermomechanical properties¹⁹¹. To mitigate these issues, polymers can be grafted directly to the surface of the nanoparticle in order to form a compatibilizing, shielding layer between the nanoparticle and host polymer matrix that ultimately improves the material performance¹⁹². Based on these observations for inorganic nanoparticles, a

wide range of synthesis techniques were developed for CNCs to improve their compatibility with the host polymer matrix in new nanocomposites³⁷. These nanocomposites with polymer grafted CNCs have shown improvements in thermomechanical properties including elastic modulus¹⁹³ and glass transition temperature¹⁹⁴, while the nanoparticles themselves have shown interesting behavior in terms of their water and pollutant adsorption¹⁹⁵. Despite these improvements, a comprehensive explanation has not been provided as to why these enhancements are observed. As a first step towards fully understanding polymer-grafted nanoparticles, here we provide insight into how polymer grafts influence polymer relaxation dynamics.

To study the relaxation of polymer-grafted CNCs embedded in a polymer matrix, we must first generate the polymer-grafted CNCs. Due to the wide range of synthesis techniques available, we chose to study polymers grafted directly to the surface of CNCs through atom transfer radical polymerization (ATRP)¹⁹⁶⁻¹⁹⁸. In this process, an initiator compound is mixed with CNCs and initiates polymerization of the grafted chains directly on the surface of the CNCs. Based on a recent experimental study¹⁹⁹, the initiator compound chosen to simulate CNCs grafted with PMMA chains is 2-bromoisobutyryl as illustrated in Figure 7-1(A). In simulation, the hydroxyl groups on the CNC surface are covalently bonded to the backbone carbon of the initiator compound, which in turn is covalently bonded to the PMMA graft. The parameters for the CNC, ATRP initiator compound, and PMMA chains are provided in Chapter 12 (page 226). In this study, 20-mer PMMA chains are utilized in all simulations for both grafted and free polymer chains.

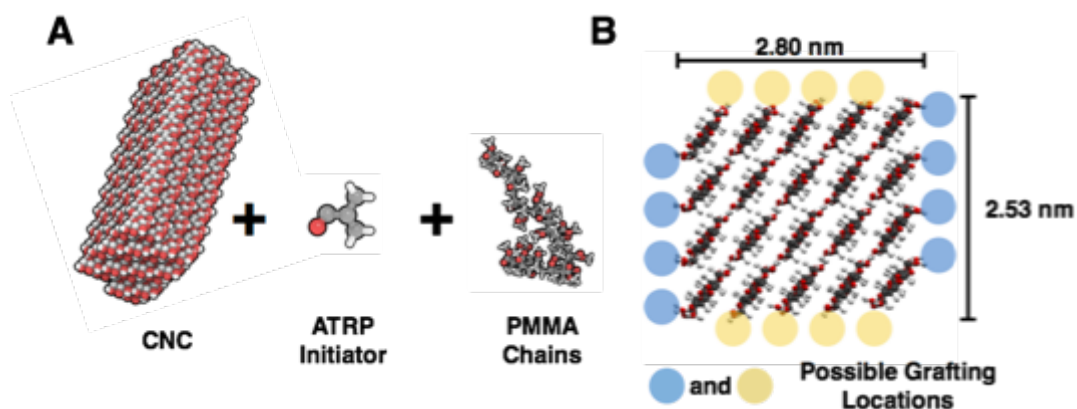


Figure 7-1: Illustration of polymer grafting to CNCs. (A) Illustration of the process of polymer grafting in which unmodified CNCs, an atom transfer radical polymerization (ATRP) initiator compound, and polymer (PMMA) chains are mixed together to form polymer grafted CNCs. The exact chemistry of the ATRP initiator is provided in Chapter 12 (page 226). (B) Illustration of the CNC rectangular cross-section used in simulation containing 20 total cellulose chains. The hydroxyl groups that are available as grafting sites are indicated by blue or yellow circles. For this specific CNC cross-section and 10 repeat units along the length of the CNC, there are 160 possible grafting sites.

In these simulations, we employ a CNC containing 20 total chains containing 10 repeat units in a rectangular arrangement as pictured in Figure 7-1(B), which also highlights each of the possible grafting sites (exposed hydroxyl groups from the (110) surface) for this crystal geometry. In generating the polymer-grafted CNCs, we specify the grafting density of polymer grafts. In this work, we generate systems with a grafting density of 20% (32 total grafts) and 50% (80 total grafts), which correspond to 0.29 nm^{-2} and 0.72 nm^{-2} in terms of number of grafts per unit surface area. Once the polymer-grafted CNCs have been generated, they are placed into a simulation box without any matrix polymer to conduct an initial equilibration and relaxation of the polymer grafts. It is important to note here that we employ periodic boundary conditions along the length of the CNC such that the CNC chains are covalently bonded to their periodic image. These equilibration simulations are conducted in NAMD⁸⁷ under an NVT ensemble and an annealing process is used

to relax the polymer grafts. During this annealing, the backbone carbon atoms of the CNC chains are tethered to their initial positions to preserve the CNC crystalline structure. The annealing process consists of an initial temperature ramp from 300 K to 750 K at an effective heating rate of 1 K/ps. The system is then held at 800 K for 5 ns before undergoing a similar temperature ramp down from 800 K to 300 K at an equivalent cooling rate. This annealing process is repeated three times to ensure a relaxed conformation of the grafted polymer chains.

Once the polymer-grafted CNCs have been equilibrated, we then must embed these materials into a polymer matrix to generate a representative volume element for a nanocomposite. For these simulations, we consider three cases: 1) a CNC without any polymer grafts used as the baseline representation of a nanocomposite, 2) a polymer-grafted CNC with 20% grafting density, and 3) a polymer-grafted CNC with 50% grafting density. The relaxed filler particles are initially placed in the center of the simulation box and packmol²⁰⁰ is then used to pack free PMMA matrix chains around the filler structure. For each of the cases studied, the total number of polymer chains (i.e. grafted chains + free chains) is held constant at 340. The number of free chains for the three cases studied are therefore 340, 308, and 260, respectively, and these chains are packed into a simulation box with initial dimensions of 10 nm x 10 nm x 10.38 nm. The three systems are illustrated in Figure 7-2.

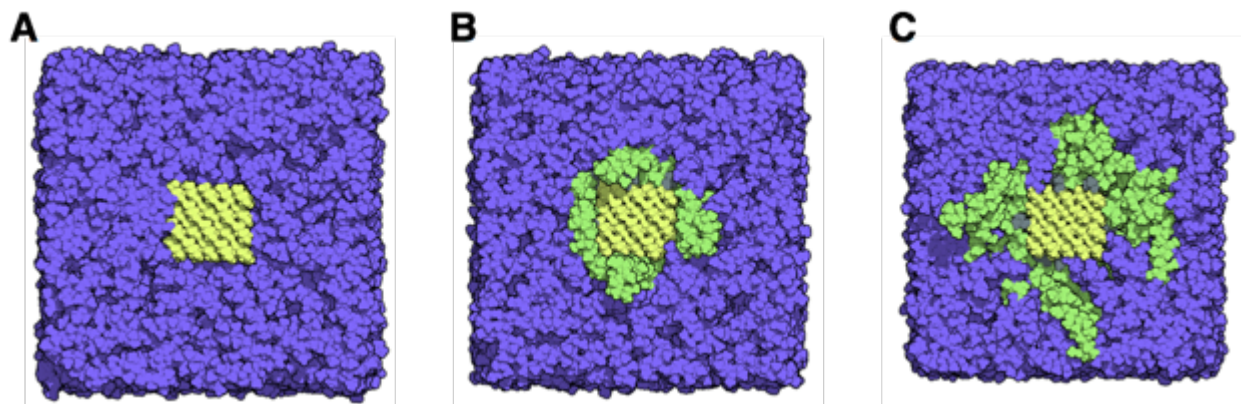


Figure 7-2: Illustration of nanocomposite RVEs consisting of CNCs embedded in polymer matrix. Simulation snapshot of the equilibrated systems containing an (A) unmodified CNC, (B) 20% polymer-grafted CNC (CNC-g-PMMA), or (C) 50% CNC-g-PMMA embedded in a PMMA matrix. Yellow atoms represent the CNC, green atoms represent the polymer grafts, and purple atoms represent the PMMA matrix.

Once the systems have been generated, an initial annealing process is simulated in NAMD under an NPT ensemble to allow for initial relaxation of the polymer chains. During this process, the CNC is again tethered to its initial position. Three heating and cooling cycles are conducted between 300 K and 750 K at an effective rate of 1 K/ps. The system is held at these high and low temperatures for 1 ns each. An NPT ensemble is used here to hold the system pressure at 0 during simulation and ensure that all possible prestress is relaxed. NVT equilibration simulations are used to measure the polymer relaxation dynamics upon the completion of the NPT simulations that determine the equilibrium box size. Since we are interested in how this relaxation changes with temperature, we conduct simulations for each system at temperatures ranging from 400 K to 800 K, all of which are above the computational glass transition temperature of PMMA²⁰¹⁻²⁰². The equilibration simulations are all run for 15 ns, with an output frequency of 5 ps, to ensure that we are capturing the necessary changes in system structure needed to accurately evaluate the polymer relaxation dynamics.

7.2 Measuring Relaxation Dynamics of Polymers

Upon generating the polymer-grafted CNCS, a few unique properties were observed. Specifically, we noticed a clear effect of grafting density on the isolated polymer-grafted CNCS, specifically in terms of the solvent accessible surface area (SASA). One of the main reasons for including these polymer grafts is to shield the CNC surface from interacting directly with the host polymer matrix. These interactions are generally unfavorable, and by shielding these interactions one can increase filler-matrix compatibility. For the isolated CNCS, we find that increasing the grafting density greatly reduces the SASA of these materials as shown in Figure 7-3. For an unmodified CNC, the SASA is calculated in VMD using a 1.4 Å probe to be 10,581 Å². When adding polymer grafts, this value decreases by ~22% for 20% grafting density and by ~53% for 50% grafting density, suggesting an approximate linear relationship between grafting density and the exposed CNC surface area.

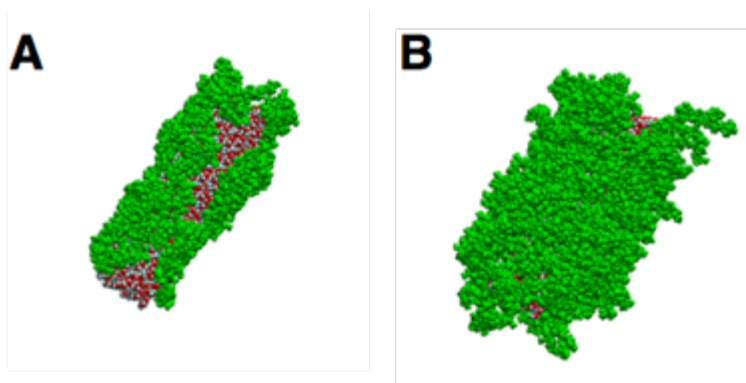


Figure 7-3: Polymer grafting reduces solvent accessible surface area. Simulation snapshots of the (A) 20% CNC-g-PMMA and (B) 50% CNC-g-PMMA. The green atoms are the PMMA grafted directly to the CNC, which is represented by the red (oxygen), white (hydrogen), and cyan (carbon atoms). Introducing polymer grafts decreases the solvent accessible surface area (SASA) and increasing the grafting density further decreases this quantity.

While measuring the SASA of isolated CNCs provides some initial insight into how polymer grafts influence CNC-polymer interfaces in nanocomposites, we are more interested here in quantifying the relaxation dynamics of the polymer chains themselves. To quantify the relaxation of the polymer chains, we calculate the P_2 bond autocorrelation function, given by Eq. (7-1) for the alpha carbon atoms in the backbone of the PMMA chains.

$$P_2(t) = \frac{3}{2} \langle (\vec{b}(0) \cdot \vec{b}(t))^2 \rangle - \frac{1}{2} \quad (7-1)$$

Here, the bond autocorrelation function at time t is the time average dot product of the bond vector at the initial time, $\vec{b}(0)$, with the bond vector at the current time, $\vec{b}(t)$, over all bonds within the system. This order parameter provides a measure of correlation between the initial conformation of the polymer chains and the current conformation that governs relaxation. The relaxation time is further related to this correlation function by fitting the simulation data with a Kohlrausch-Williams-Watts (KWW) stretched exponential function²⁰³ given by Eq. (7-2)

$$P_2(t) = A \exp \left[- \left(\frac{t}{\tau_{KWW}} \right)^\beta \right] \quad (7-2)$$

where A is an exponential pre-factor that considers relaxation at short times (bond vibrations, angle bending, etc.), τ_{KWW} is the KWW relaxation time, and β is the exponential stretch factor. This stretch factor indicates the broadness of the distribution of relaxation times within the system. While the KWW relaxation time provides some measure of relaxation, we are more specifically interested in the segmental relaxation time, τ_{seg} . This value is often estimated by the time at which the bond autocorrelation function reaches a value of 0.2, but can be more exactly given by Eq. (7-3) where Γ is the statistical gamma function.

$$\tau_{seg} = \frac{\tau_{KWW}}{\beta} \Gamma\left(\frac{1}{\beta}\right) \quad (7-3)$$

Finally, we can determine the temperature dependence of the segmental relaxation time. The temperature dependence of this quantity can be fit with the Vogel-Fulcher-Tammann (VFT) equation²⁰⁴ given by Eq. (7-4) where τ_0 , D , and T_0 are physically informed fitting parameters.

$$\tau_{seg}(T) = \tau_0 \exp\left[\frac{DT_0}{T - T_0}\right] \quad (7-4)$$

7.3 Relaxation Dynamics of Polymer-Grafted CNCs

Using the above simulation methodology and relaxation analyses, we present results here for the relaxation of polymer-grafted CNCs and unmodified CNCs embedded within a synthetic polymer matrix. Figure 7-4(A) presents an example of the bond-autocorrelation function calculated for the 20% grafting density system over the first 3 ns of simulation. We calculate this value for simulations ranging in temperature from 200 K to 800 K, with the bond-autocorrelation curves moving down and to the left with each increase in temperature. These results are presented for calculations involving all chains – both grafted and free chains. We notice that initially the bond-autocorrelation function is high, but as the simulation progresses and polymer chains move and relax throughout the system due to thermal fluctuations, bonds become less correlated to their initial position and the value of the function decreases. Also, we note that with increasing temperature the decay of the bond autocorrelation is accelerated as increased thermal energy causes increased motion of the chains.

The bond-autocorrelation data presented in Figure 7-4(A) is then used to calculate the segmental relaxation time using the method described in the previous section. The segmental relaxation time as a function of system temperature is presented in Figure 7-4(B) for the three

systems studied. The solid lines in this figure represent the VFT fit given by Eq. (7-4) and indicate that each of the systems is exhibiting the expected temperature-dependent relaxation behavior. Most interesting, however, is the relative values of the relaxation times for the different systems. Notably, we find that the main effect of introducing polymer grafts on the surface of the CNC is to accelerate relaxation dynamics – in other words the segmental relaxation time is decreased. This result suggests that introducing polymer grafts introduces some effect that allows for increased mobility of polymer chains – thereby allowing them to reach a relaxed conformation more quickly. Additionally, we find that increasing the grafting density from 20% to 50% serves to further accelerate the relaxation behavior. This relaxation behavior has also been observed experimentally for polymer grafted silica nanoparticles²⁰⁵ and supports the observations from our simulations.

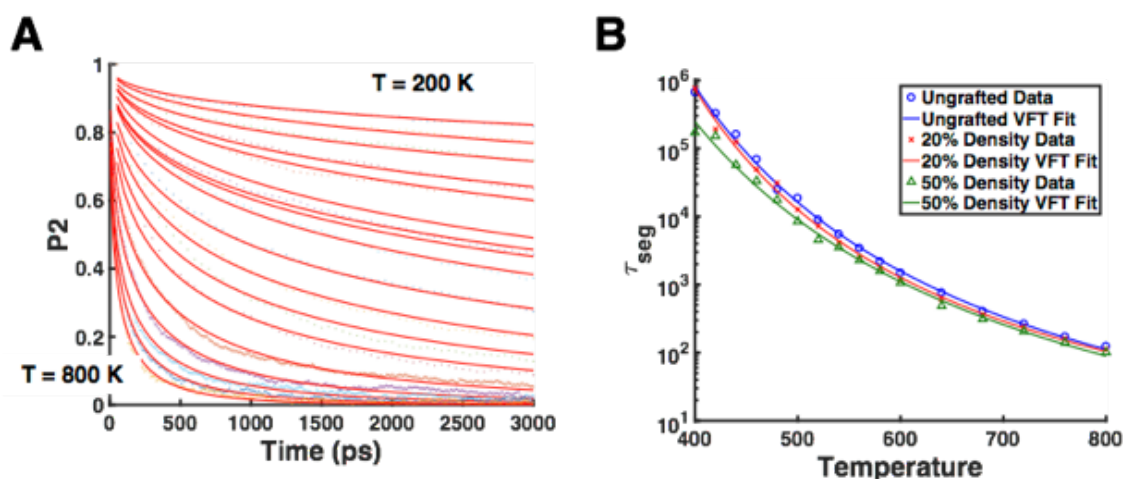


Figure 7-4: Effect of grafting density on polymer relaxation dynamics. (A) $P_2(t)$ bond-autocorrelation function as a function of simulation time for the 20% grafting density system. Each of the individual data sets and fit curves represent a simulation at a single temperature ranging from 200 K to 800 K. Each subsequent curve that is lower and to the left represents an increase in temperature. Data points are obtained directly from simulation and the red curves are fit using a KWW stretched exponential. (B) Segmental relaxation time as a function of temperature for the unmodified CNC (blue points and curve), 20% CNC-g-PMMA (red lines and curve), and 50% CNC-g-PMMA (green points and curve). Data points represent simulation data and the solid curves represent the VFT fit for each data set.

We hypothesize that the relaxation behavior of polymer chains within the systems is due to the development of an increased amount of free volume within the system caused by the polymer grafts. To verify this hypothesis, we begin by looking at the local relaxation dynamics of polymer chains within the systems. The local polymer relaxation is calculated by dividing the system into rectangular bins as illustrated in Figure 7-5(A). Each bond is assigned to a specific bin by taking the midpoint of that bond at each time step so that the motion of bonds from one bin to another is accounted for. Results of these local relaxation calculations are shown in Figure 7-5(B). For the unmodified CNC, we find that the relaxation time is significantly higher near the surface of the nanocrystal, thereby indicating some effect of nanoconfinement that has been previously described for polymer thin films^{201-202, 206-207}. Upon introducing polymer grafts on the CNC surface, we find that this effect of nanoconfinement is substantially decreased, such that the polymer almost behaves as if in the bulk state. This suggests that the grafted polymers themselves have a much faster relaxation compared to the free, matrix chains and effectively decrease the overall and local relaxation times of the nanocomposite system.

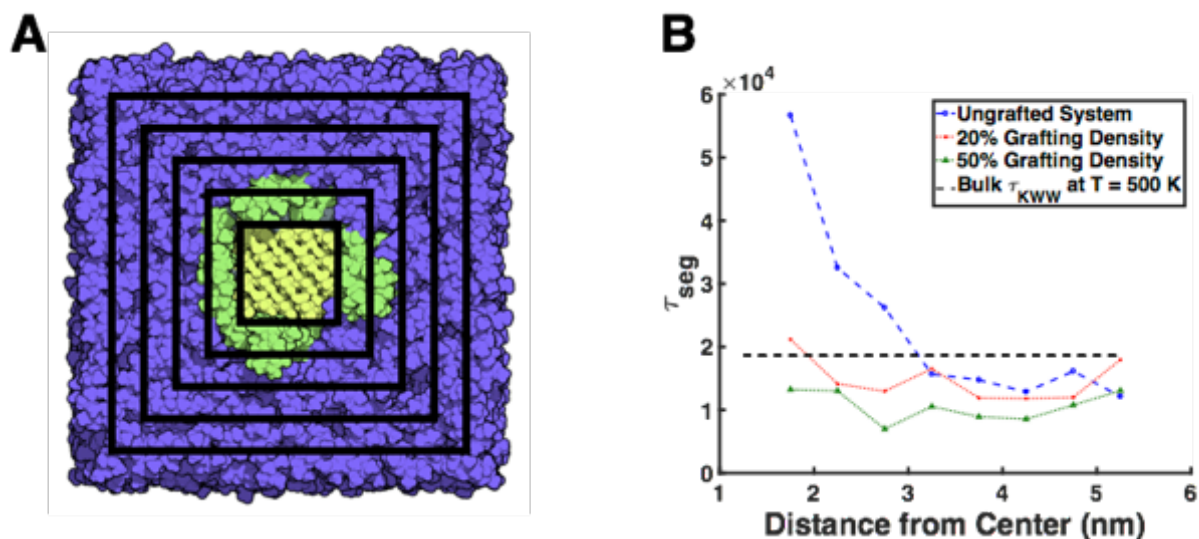


Figure 7-5: Local polymer relaxation dynamics. (A) Illustration of the rectangular bins used to calculate the local polymer dynamics as well as the density profile of the simulated systems. (B) Segmental relaxation time as a function of the distance from the center of the simulation box for the unmodified CNC (blue points and curve), 20% CNC-g-PMMA (red points and curve), 50% CNC-g-PMMA (green points and curves). All calculations are performed for a system temperature of 500K.

A further explanation for the accelerated relaxation dynamics as well as the local relaxation behavior is provided by measuring the polymer density profile. Figure 7-6 presents the density profile for all chains (panel A) and the free chains (panel B) calculated using the binning procedure illustrated in Figure 7-5(A). Here, the density is simply defined as the density of alpha carbons since these are the only atoms used to quantify relaxation. However, similar trends should be observed if considering all atoms. We notice that compared to the bulk PMMA density, all the systems with an embedded CNC exhibit increased polymer density directly adjacent to the CNC surface. This can be attributed to relatively strong interactions between PMMA chains and the CNC surface due to the development of hydrogen bonds. Additionally, we find that introducing polymer grafts at the CNC-matrix interface decreases the local packing of matrix chains near the interface. This indicates that polymer grafts provide a larger amount of accessible free volume for

the matrix chains near the CNC-PMMA interface that allows for accelerated relaxation dynamics. This further supports the idea that polymer grafts form a compatibilizing layer between the matrix and nanofiller that can aid in the dispersion of nanoparticles. In Figure 7-6(B), we directly see the effect of this compatibilizing polymer layer (i.e. the corona formed of polymer grafts around the CNC) as it effectively pushes matrix chains away from the CNC and instead promotes interactions between the grafted and matrix chains that improves compatibility and accelerates relaxation.

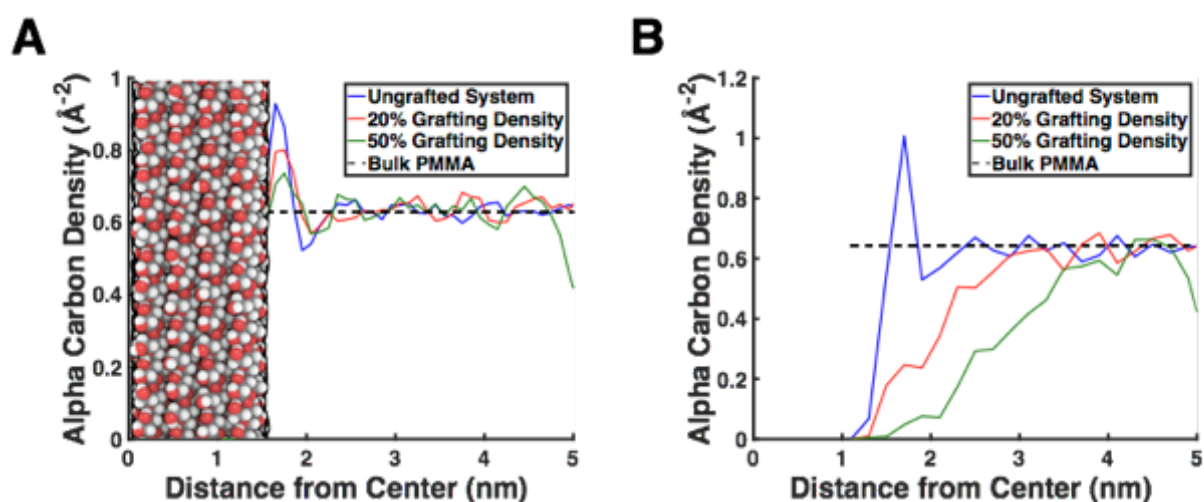


Figure 7-6: Density profiles of polymer chains around CNCs. (A) Density profile of all polymer chains (grafted and free) within the system and (B) density profile of just the free chains within the system. The density profile is calculated using only the positions of the backbone alpha carbons averaged over the length of the simulation. In both plots, calculations are performed for a system temperature of 500 K and blue curves correspond to the unmodified CNC, red curves correspond to the 20% CNC-g-PMMA, and green curves correspond to 50% CNC-g-PMMA.

In this chapter, we have conducted an initial investigation into the effects of polymer-grafted CNCs on nanocomposite properties. We have found, in agreement with recent experimental studies²⁰⁵, that polymer grafts serve to accelerate relaxation dynamics by increasing the amount of free volume at the interface. Interestingly, this accelerated relaxation is accompanied by a decrease in nanoconfinement effects. Nanoconfinement effects have generally been

considered a positive aspect of nanoscale filler particles as they serve to appreciate the thermomechanical properties of the polymer near the nanoparticle. However, the trade-off here is that incorporating polymer-grafted CNCs should improve matrix-filler compatibility. This increased compatibility should lead to increased dispersion which in turn should lead to improved mechanical properties of the bulk material. Future work that can provide a molecular level explanation for the mechanical enhancements provided by polymer grafts will be useful in fully leveraging these materials in new nanocomposites. Understanding how to optimize design parameters for these materials (i.e. graft length, density, polymer species, etc.) is an important first step in the materials development process and in the future will greatly assist in optimizing CNC-polymer nanocomposite properties.

Chapter 8 – Predicting Macroscale Properties of Polymer Nanocomposites from Nanoscale Simulations

Prior to this chapter, the computational materials-by-design approach to CNC-based nanocomposites has focused on materials discovery and development. We have studied the fundamental molecular structure and mechanics that are important for CNCs and examined how we can further tailor these behaviors through surface modification and polymer grafting. In this chapter, we switch our focus to the concept of property optimization. Specifically, we focus here on the development of multiscale models that allow us to utilize the results of nanoscale simulations in a predictive fashion to determine macroscale material properties. We present the results of two studies. The first describes how we can use interfacial energies to predict the dispersion state of nanoparticles in nanocomposites. In this section, we also touch on techniques that could be used to create materials design libraries that will help accelerate the process of property optimization. The second study focuses on utilizing nanoscale interfacial energies to predict changes in the glass-transition temperature (T_g) of a polymer nanocomposite. Portions of the text and figures within this chapter pertaining to the dispersion predictions are reprinted or adapted with permission from Fox et al., *ACS Appl. Mater. Interfaces* 2016. Copyright 2016 American Chemical Society. Portions of the text and figures within this chapter pertaining to the glass transition temperature predictions are reprinted or adapted with permission from Qin et al., *ACS Nano Lett.* 2015. Copyright 2015 American Chemical Society. The author would like to acknowledge Xin Qin and Wenjie Xia who made significant contributions to the results presented in Section 8.4.

8.1 Simulation Parameters

In this study, we focus on quantifying interfacial energies of nanoscale interfaces using fully atomistic molecular dynamics simulations. We are primarily interested in calculating two types of interfacial energies. The first is the interfacial energy between two CNCs which is a measure of filler-filler cohesion in polymer nanocomposites. These calculations have previously been performed for unmodified CNCs in Chapter 3 (page 45) and for modified CNCs in Chapter 6 (page 102). The second is the interfacial adhesion between CNCs and polymer films that describes the adhesive strength of filler-matrix interfaces in polymer nanocomposites. In this introductory section, we will discuss the different CNC surface modifications and polymers that are considered in our studies.

When quantifying the interfacial energy of CNC-CNC interfaces, we are primarily interested in determining the influence of surface modification on this interfacial energy. Rather than examine unmodified CNC surfaces as was done in previous chapters, here we consider CNC surfaces that have been chemically modified due to their extraction from cellulosic materials such as wood pulp. As discussed in Chapter 6 (page 102), we focus on CNCs that have been extracted through acid hydrolysis with sulfuric acid and have consequently had some of the hydroxyl groups on the surface replaced by sulfate groups as illustrated in Figure 8-1(A). Expanding upon the ion exchange technique initially discussed in Chapter 6, here we focus on replacing the sodium cation that neutralizes the sulfate group with four larger cations: methyltriphenylphosphonium (MePh^3P^+), 1-Hexyl-2,3dimethyl imidazolium (HxMe_2Im^+), 1-Hexadecyl-2,3-dimethyl imidazolium (HdMe_2Im^+), and 1,2,3-trimethylimidazolium (Me_3Im^+). These cations are illustrated in Figure 8-1(B) with the parameters used in simulation provided in Chapter 12 (page 226). To create surface modified CNCs, we generate a CNC using the cellulose-builder toolkit having the

dimensions shown in Figure 8-1(C). We then replace 1 out of every 10 hydroxyl groups with sulfate groups (i.e. one per cellulose chain in our system) and place the appropriate cation near this group. We chose an arrangement of surface modifications as illustrated in Figure 8-1(C). In addition to studying the cases of full exchange (i.e. all sodium cations replaced with the larger cation), we consider the effects of partial exchange in which some sodium is retained in addition to the replacement by the larger cations.

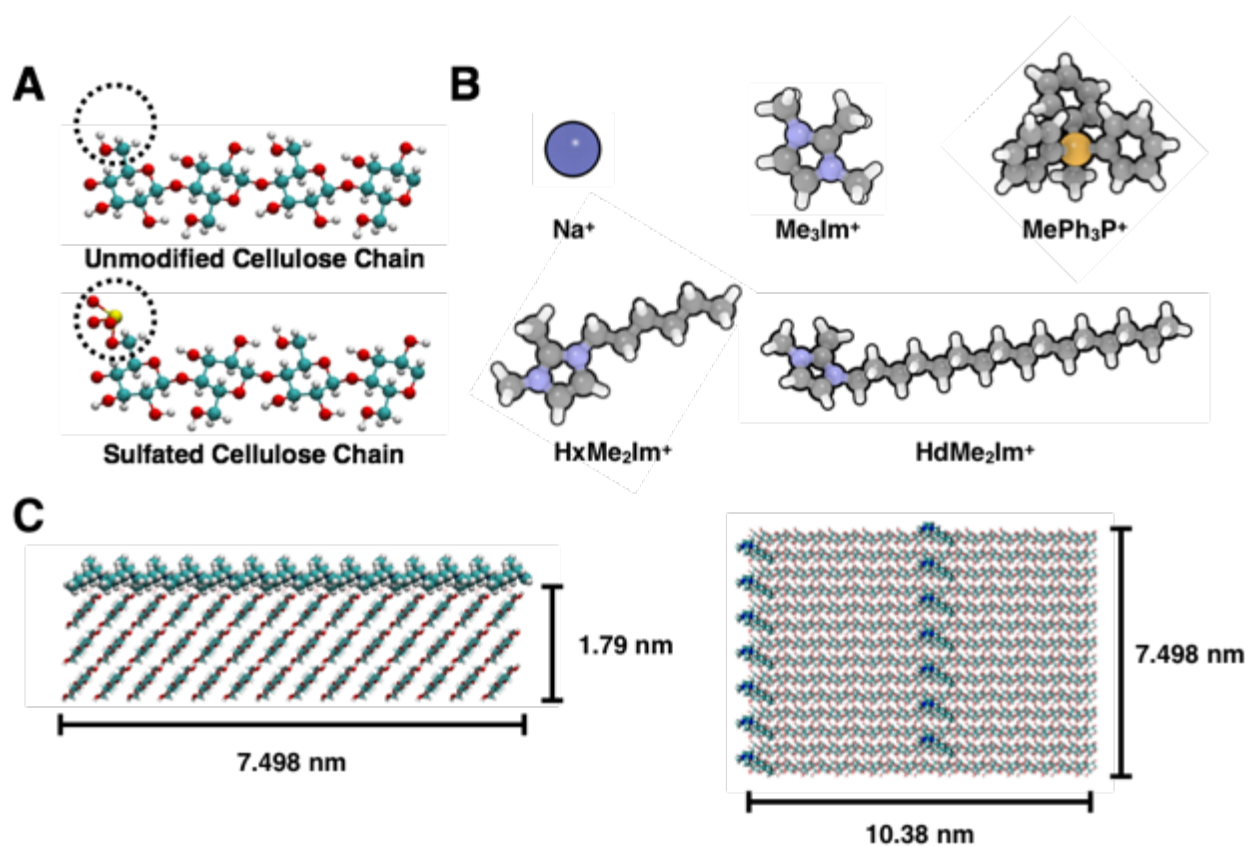


Figure 8-1: Illustration of ion exchange surface modifications. (A) Illustration of the replacement of hydroxyl groups on CNC surfaces by sulfate groups upon extraction from natural sources using acid hydrolysis with sulfuric acid. (B) Illustrations of the four different cations used to replace sodium with an ion exchange technique. The ions are methyltriphenylphosphonium (MePh_3P^+), 1-Hexyl-2,3dimethyl imidazolium (HxMe_2Im^+), 1- Hexadecyl-2,3-dimethyl imidazolium (HdMe_2Im^+), and 1,2,3-trimethylimidazolium (Me_3Im^+). (C) Image of surface modified CNCs showing the 10% modification density and the physical arrangement of surface modifications used in this study along with the CNC dimensions from a side view (left image) and a top view (right image).

Beyond these CNC-CNC interactions that are representative of filler-filler cohesive interactions in a polymer nanocomposite, we are also interested in studying the behavior of CNC-polymer interfaces. In the previous chapter, we simulated the behavior of these interfaces by modelling a CNC fully embedded within a polymer matrix. However, these interfaces, illustrated in Figure 8-2(A), can also be more simply simulated by using a thin film geometry in which a CNC is placed on top of a polymer thin film. We are again interested in quantifying how the surface chemistry of CNCs influences the interfacial filler-matrix adhesion, but are also interested in the effect of polymer chemistry on this interaction energy. To characterize the influence of polymer chemistry and utilize available experimental data, we conduct simulations using three matrix polymers: polystyrene (PS), poly(methyl methacrylate) (PMMA), and a bisphenol A diglycidyl ether (DGEBA) polydietheramine (PEDA) epoxy. The chemical structures of these polymers are illustrated in Figure 8-2(B). By studying these three specific polymers we can consider the effect of hydrophobicity (PS being very hydrophobic, PMMA and epoxy being relatively hydrophilic and capable of forming hydrogen bonds) and cross-linking (epoxy being inherently cross-linked through curing, PS and PMMA being non-cross-linked) in addition to the effects of CNC surface chemistry.

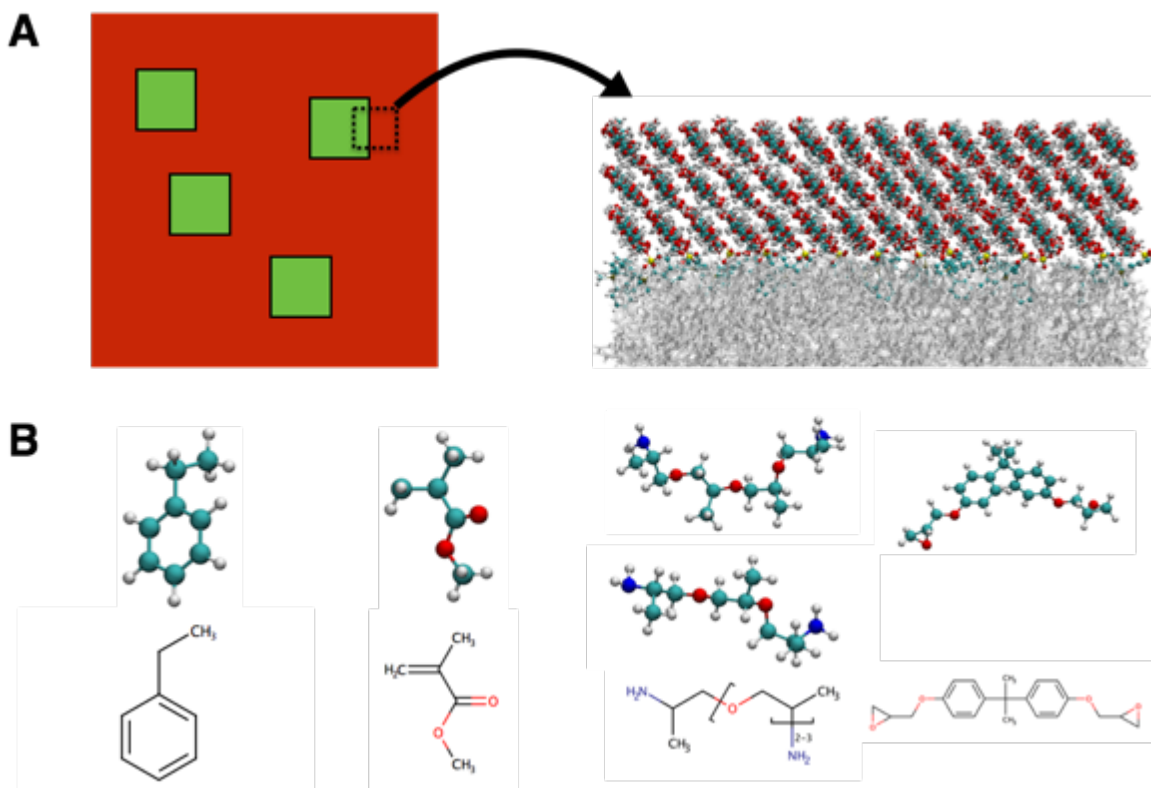


Figure 8-2: Illustration of CNC-polymer interfaces and matrix polymers studied. (A) Illustration of a polymer nanocomposite showing the interface between fillers and matrix. We utilize a CNC placed on top of a thin film to model this interface and calculate the polymer-CNC adhesion energy. (B) Molecular representations and chemical structures of the three polymers considered in this work: polystyrene (PS), poly(methyl methacrylate), and bisphenol A diglycidyl ether (DGEBA) polydietheramine (PEDA) epoxy.

Before conducting simulations to obtain the interfacial energies, we must generate polymer thin films. The process of generating these films is independent of the polymer chemistry, except for the epoxy where some additional steps are necessary. For the PS and PMMA, 100-mer chains are generated in a relaxed conformation using Materials Studio. Using packmol²⁰⁰ and the experimental density of PMMA (1.18 g/cm³) or PS (g/cm³), 60 chains are packed into a film having a cross-section of 7.498 nm x 10.38 nm to match the cross-sectional area of the surface-modified CNCs. This results in a PMMA film having a thickness of 11.3 nm and a PS film having a thickness of 12.8 nm. While this film has the appropriate geometry, additional steps need to be taken to fully

relax and equilibrate the polymer chains within the film. To do so, a simple annealing process is utilized. Using NAMD, simulations are conducted under an NVT ensemble in which the temperature of the system is ramped up to 750 K from 300 K in increments of 50 K. The system is then held at 750 K for 2 ns before the temperature is lowered back to 300 K in increments of 50 K. This annealing process is repeated 3 times to ensure that the system is fully equilibrated before introducing the CNC to create the CNC-polymer interface as discussed in the following section.

For the epoxy system, additional steps must be taken. The epoxy used in experiments to which the simulations will be compared utilizes a 2:1 stoichiometric ratio of DGEBA to PEDA. Additionally, it was noted that the PEDA in experiment had an average degree of polymerization of 2.6 indicating a 3:2 ratio of DP = 3 to DP = 2 PEDA macromolecules. Based on these ratios, an epoxy film is generated with 120 DGEBA monomers and 60 PEDA monomers (36 with a DP = 3 and 24 with a DP = 2). Rather than generate monomers that have the structures exactly as pictured in Figure 8-2(B), we utilize DGEBA that have the epoxide ring open and PEDA with the terminal hydrogens removed to prepare them for cross-linking. These monomers are then packed into a film geometry using packmol²⁰⁰ and having a cross-section of 7.496 nm x 10.38 nm and a resulting film thickness of nm. Once the monomers have been packed into a film, they are annealed using the procedure discussed in the previous paragraph. However, the process of film generation differs for the epoxy since the monomers must be crosslinked. After the initial equilibration, a protocol is utilized to crosslink monomers in LAMMPS in which the degree of crosslinking is specified. Here, the degree of crosslinking is defined as the number of DGEBA-PEDA crosslinked epoxide bonds divided by the maximum number of these bonds possible in the system. For this study, we will present results for a degree of crosslinking of 50%.

To quantify the CNC-CNC or CNC-polymer interfacial energy a simple equilibration simulation is conducted. The two structures of interest are placed near each other in the simulation box to form an initial interface. The structures are then constrained such that the two materials can only move normal to the interface that is to be developed. Simulations are conducted under an NVT ensemble and temperature of 300 K for an overall duration of 5 ns to completely form the nanoscale interface. To ensure that the interface has come into an equilibrium configuration, we ensure that the energy of the system has reached a constant value over the final portion of the simulation.

8.2 Direct Energy Summation Method for Quantifying Interfacial Energies

During equilibration simulations for these interfaces, the energy of the system will change as the two materials (either multiple CNCs or the CNC and polymer thin film) form a complete interface. Here, we discuss the direct energy summation (DES) method for calculating the adhesion energy between materials across the interface. In the DES method, we simply track the non-bonded interaction energy between materials across the interface by summing up all pairwise thermodynamic interactions across the interface. An alternative method that was employed in our previous studies was to use SMD simulations to separate an equilibrated interface and measure changes in the free energy. Compared to SMD, DES offers several advantages. First, we can determine the relative magnitude of both electrostatic interactions and van der Waals interactions. Second, this calculation is less computationally intensive as we can conduct a single equilibration simulation rather than an equilibration followed by multiple SMD runs. The key difference between SMD and DES approaches is that SMD values for the interfacial energy are slightly lower than those obtained from the DES approach because of the entropic contribution to the adhesion energy. A plot of the interfacial energy as a function of simulation time is plotted in Figure 8-3

for a CNC-polymer interface. To quantify the interfacial adhesion energy, we average the interaction energy over the final 2 ns of simulation. Figure 8-3 also shows how the interfacial energy converges to a constant value and once it does so we can consider the two materials to be in equilibrium.

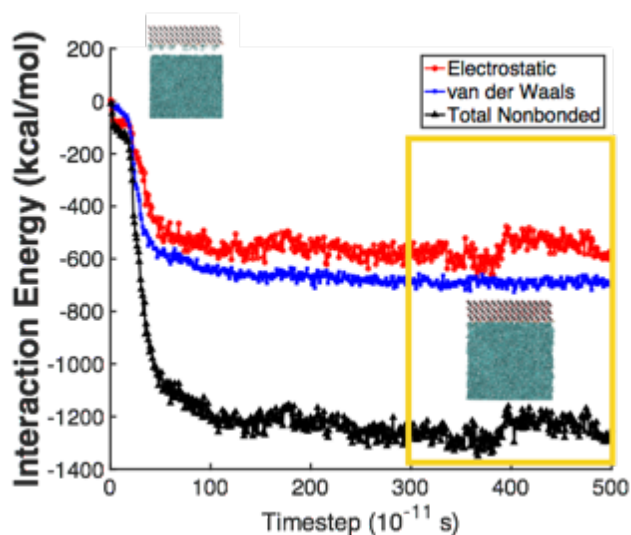


Figure 8-3: Direct energy summation (DES) method for quantifying interfacial adhesion. Plot of the interaction energy across the interface as a function of simulation time. The DES technique allows us to determine the contributions to the total interfacial energy (black line) from electrostatic interactions (red line) and non-bonded van der Waals interaction (blue line). Initially, the system has a high energy as the two materials are relatively far apart and the energy decreases as the interface is fully developed. To quantify the interaction energy, the energy values are averaged over the final 2 ns.

The calculated interfacial adhesion energies for each of the CNC-polymer interfaces are shown in Figure 8-4(A). There are several interesting trends we observe. First, we notice that by replacing sodium ions on the CNC surface we greatly reduce the polymer-CNC interaction energy for all modifications and all polymers. Additionally, we find that in all cases the surface modifications decrease the interaction energy by reducing electrostatic interactions while vdW interactions remain largely unchanged. Second, we observe that the relative contributions of

electrostatic and vdW interactions is highly dependent on the polymer chemistry. For the hydrophilic polymers that can form hydrogen bonds (epoxy and PMMA), the electrostatic contributions account for more than 50% of the total interaction energy. However, for hydrophobic polymers (PS) that do not form any hydrogen bonds, the vdW interactions account for greater than 80% of the total interaction energy. Finally, we notice that the magnitude of interfacial energies is largely dependent on polymer chemistry. We find that CNCs interact the strongest with epoxy, followed by PMMA, and weakest with PS. This again is explained by electrostatic interactions and hydrogen bonding. As shown in Figure 8-2(B), the epoxy has a higher number of hydrogen bond donors and acceptors than PMMA that directly explains the higher interaction energy as CNCs themselves can form a high number of hydrogen bonds. Further, PS has the lowest energy as it cannot form any hydrogen bonds. Altogether, the results presented in Figure 8-4(A) demonstrate the importance of both CNC surface chemistry and polymer chemistry on matrix-filler interfacial adhesion energy.

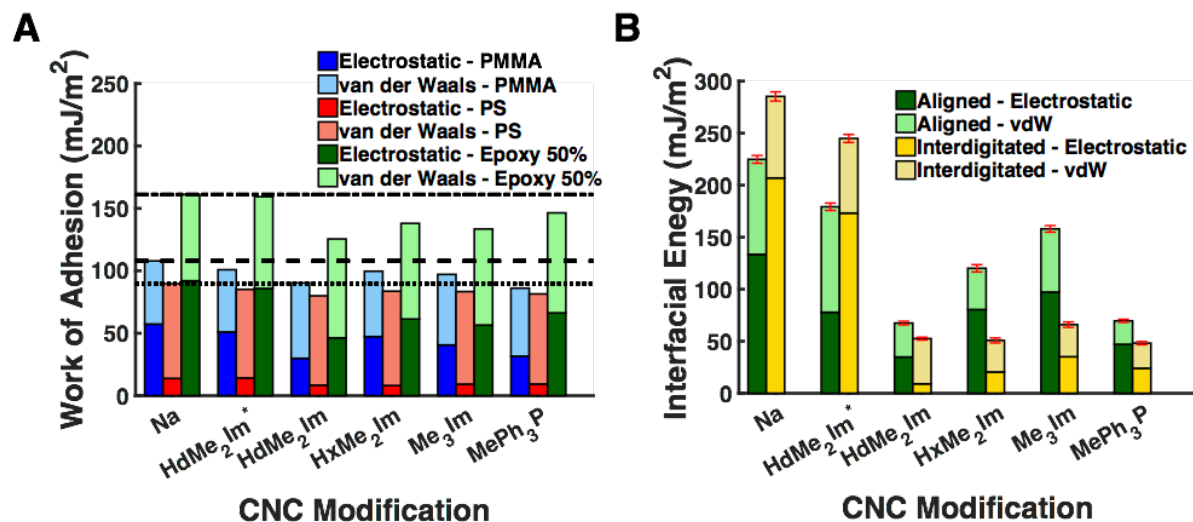


Figure 8-4: Interfacial adhesion energies for CNC-polymer and CNC-CNC interfaces. (A) Interfacial adhesion energy (i.e. work of adhesion) for CNC-polymer interfaces and all the different CNC surface modifications of interest. Blue bars correspond to CNC-PMMA interfaces, red bars correspond to CNC-PS interfaces, and green bars correspond to CNC-epoxy interfaces. The darker portions of the bars correspond to the electrostatic interactions and the light portions of the bars correspond to the vdW contributions. (B) Interfacial adhesion energy for CNC-CNC interfaces for each of the different surface modifications. Green bars correspond to the aligned conformation of CNC interfaces and yellow bars correspond to the interdigitated conformation. The darker portions of the bars correspond to the electrostatic contribution while the lighter portions of the bars correspond to the vdW contribution. Red bars indicate the standard deviation of the interfacial energy measured over the 2 ns of calculation.

To obtain CNC-CNC interfacial energies, two CNCs having the same dimensions as the CNC placed on top of the polymer film were arranged, as shown in Figure 8-5. Here, two cases of interfacial alignment are considered. The first case is referred to as an aligned interface (aCNC-CNC) where the exchanged ions are directly aligned across the interface and interact directly with one another. The second case is referred to as an interdigitated interface (iCNC-CNC) where the exchanged ions are offset from one another and the ions interact with the opposing CNC surface. It should again be noted that in all cases, 10% of the total exposed hydroxyl groups on the CNC

surfaces are replaced by sulfate groups and sodium ions with the arrangement of modifications on the CNC surface pictured in Figure 8-1(C).

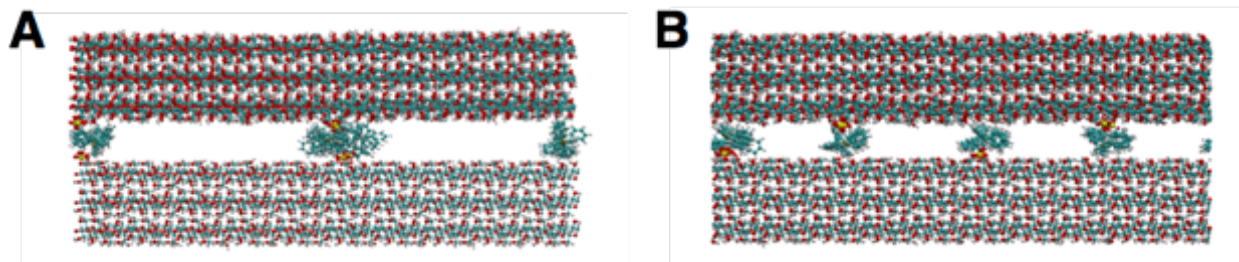


Figure 8-5: Aligned and interdigitated conformation of CNC interfaces. (A) Aligned conformation of CNCs where the surface modifications interact directly with each other across the interface. (B) Interdigitated conformation of CNCs where the surface modifications interact directly with the opposing CNC surface.

Compared to the CNC-polymer interfacial energy, CNC-CNC interfacial interactions show a much more dramatic change as the ion-exchanged modifications reduced interfacial energies from 65 to 80% with the MePh3P-CNCs exhibiting the largest reduction as shown in Figure 8-4(B). This reduction can be attributed to two factors, with the degree of importance for each depending on the specific surface modification. First, van der Waals interactions are reduced as the ions physically increase the distance between CNC surfaces at equilibrium, thus reducing non-bonded interactions that scale with the square of inverse distance. Second, electrostatic interactions are greatly reduced due to the increased distance between surfaces that prevents the formation of hydrogen bonds across the interface. Additionally, at interfacial locations where ions are present, hydrogen bonds cannot be formed as the ions act as a physical barrier or shield and prevent the CNC surfaces from interacting electrostatically (i.e., hydrogen bonding). Additionally, we notice that the conformation of CNCs (aligned vs. interdigitated) also plays a role in the CNC-CNC adhesion energy. For all cases except the sodium, the aligned conformation has a higher interfacial energy as cation-cation interactions have a larger interaction energy than CNC-cation interactions.

The results shown in Figure 8-4 lead us to examine the effect of exchange percentage on the interfacial adhesion energy. In Figure 8-4(B) we begin to examine this effect by comparing the adhesion energy for the case of 100% exchanged HdMe₂Im surfaces with 14% exchanged HdMe₂Im surfaces (denoted by HdMe₂Im* in Figure 8-4(B)). We find that exchanging only a fraction of the sodium cations with the larger HdMe₂Im ions only has a mild effect compared to exchanging 100% of the sodium cations. Based on this observation, we aim to confirm this trend by conducting a set of simulations in which we measure the interfacial adhesion energy for 25%, 50%, and 75% exchange of sodium ions. These results are presented in Figure 8-6 and demonstrate that there is a clear correlation between the exchange percentage and the interfacial adhesion energy. However, it is also important to note that the adhesion energy is not linearly related to the degree of exchange. Rather, there seems to be some critical exchange percentage at which the surface acts more like a fully sodium covered surface or a fully HdMe₂Im covered surface – estimated to be between 25% and 50% for this specific chemistry and ion arrangement. This is an important result for experimentalists as it suggests that 100% exchange, something that is difficult to achieve experimentally, is not necessary to obtain the benefits of surface modification. Rather, ensuring the exchange is above this critical value will be adequate. Computational simulations can aid in determining these critical values by rapidly exploring the available design space.

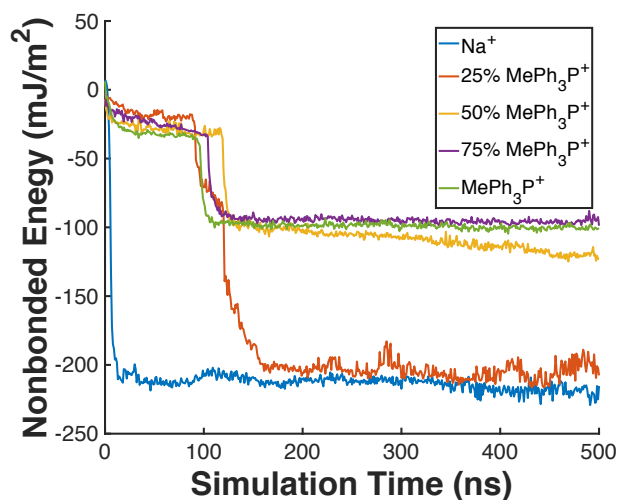


Figure 8-6: Effect of partial ion exchange on interfacial filler adhesion. Interfacial non-bonded energy as a function of simulation time for different percentages of sodium cations exchanged by HdMe₂Im. As the number of sodium ions exchanged with HdMe₂Im is increased, the interfacial adhesion energy decreases suggesting the exchange percentage is a major design parameter in CNC-polymer nanocomposites.

8.3 Predicting Dispersion of CNCs in Nanocomposites

While quantifying the nanoscale adhesion energies provides some insight into the molecular level behavior of interfaces in CNC-polymer nanocomposites, our aim in computational materials-by-design is to utilize this information to predict bulk material properties. Here we present a multiscale model developed to predict the macroscale dispersion state of nanoparticles in these composites based on nanoscale interfacial energy measurements. The observed dispersion of modified CNCs in polymers can be explained by quantifying the so-called dispersion factor of different surface modifications. This dispersion factor D , explained previously by Khoshkava and Kamal²⁰⁸, is a ratio of the filler–matrix adhesion energy (W_{FM}) to the filler–filler adhesion energy (W_{FF}) defined by Eq. (8-1).

$$D = \frac{W_{FM}}{W_{FF}} \quad (8-1)$$

A large value of the dispersion factor indicates a well-dispersed nanocomposite, while a low value of the dispersion factor indicates poor dispersion and the formation of larger microaggregates. Using values of the CNC-polymer interfacial energy and the CNC-CNC interfacial energy (taken as the average of interdigitated and aligned cases), the dispersion factor is calculated for each CNC-polymer system and plotted in Figure 8-7. According to this calculation, one would expect the Na-CNCs to exhibit poor dispersion in all the polymers studied here in comparison to each of the other surface modifications. Additionally, one can also conclude that MePh₃P ions should exhibit the best dispersion out of all the cases examined here. The results also suggest that CNCs with 100% exchange of HdMe₂Im would exhibit improved dispersion, but up to this point that degree of exchange has not been achieved experimentally. Notably, these predictions agree well with the experimentally observed dispersion pictured in Figure 8-8¹⁷⁴, thereby suggesting that tailoring surface energies, specifically the CNC-CNC adhesion, is a key strategy for controlling dispersion of CNCs in polymer nanocomposites.

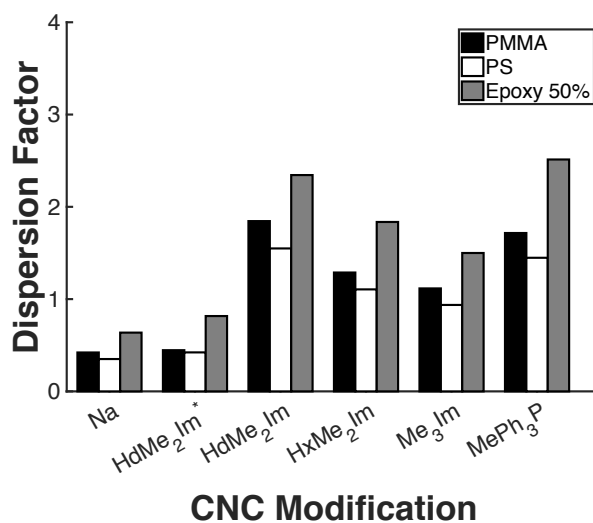


Figure 8-7: Predicted dispersion factor of CNC-based nanocomposites. Dispersion factor calculated from Eq. (8-1) using the previously obtained CNC-polymer and CNC-CNC interfacial adhesion energy for PMMA (black bars), PS (white bars), and 50% cross-linked epoxy (gray bars). We find that replacing sodium cations with any of the larger cations improves dispersion of CNCs within the material by greatly reducing CNC-CNC interaction energies.

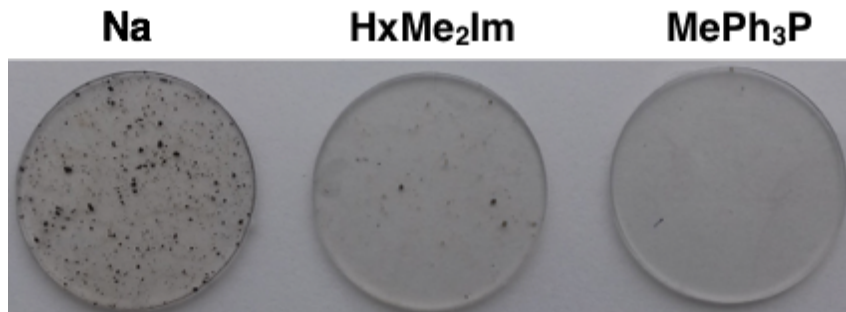


Figure 8-8: Experimentally observed dispersion of CNCs in nanocomposites. Photographs of experimental samples PS + 1% Na-CNC, PS + 1% HdMe₂Im-CNC, and PS + 1% MePh₃P-CNC showing the change in dispersion with CNC surface modification. Black spots in the photographs correspond to thermally degraded CNC aggregates with larger black spots corresponding to larger aggregation of CNCs. These photos provide experimental evidence that replacing sodium cations with other larger cations can improve CNC dispersion in these materials.

8.4 Predicting Nanocomposite Glass Transition Temperature from Interfacial Adhesion Energies

As a second application of this multiscale modeling approach to optimizing the properties of CNC-polymer nanocomposites, here we present a multiscale modeling approach that combines

the benefits of AA-MD and CG-MD simulations. Using CNC–PMMA nanocomposites as a model system, we demonstrate that the glass transition temperature (T_g) of a nanocomposite can be predicted directly from atomistic inputs including interfacial adhesion energies, interphase thickness and properties, along with average microstructural features of the material. The first component of this multiscale model is to utilize fully atomistic simulations to quantify the interfacial adhesion energy between CNCs and PMMA (Section 8.3). Then, we employ CG-MD simulations of polymer thin films to determine the relationship between interfacial adhesion energy and nanoconfinement effects that alter the T_g of the film. Finally, by drawing upon the quantitative analogy between thin films and nanocomposites¹⁹⁰, we establish a multiscale, predictive modeling approach to link nanoscale interfacial properties and size effects to the nanocomposite T_g . The synthesis of these three elements, summarized in Figure 8-9, allows us to create a comprehensive, computational framework that captures the important physics of polymer nanocomposites with a minimal need for experimental inputs.

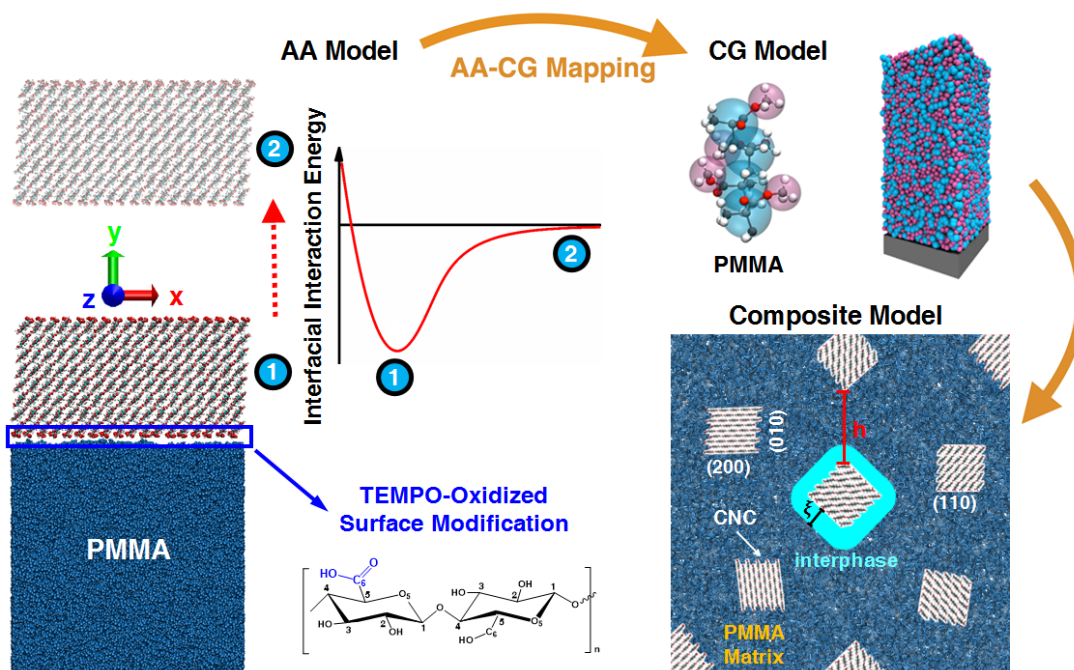


Figure 8-9: Multiscale modeling approach to predicting T_g in nanocomposites. In this multiscale approach, we aim to link nanoscale interfacial adhesion energies to the bulk glass transition temperature (T_g) of polymer nanocomposites. First, we calculate interfacial adhesion energies using fully atomistic molecular dynamics simulations using the direct energy summation technique. Second, we utilize a coarse-grained model to understand how the interfacial energy between a thin film and substrate changes the T_g of the film. Finally, we utilize a continuum model to explain how changes in the T_g of a nanocomposite are related to changes in thin film thermomechanical properties and quantitatively link the nanoscale interfacial adhesion energy to the macroscopic T_g .

To determine the effects of the interfacial adhesion energy on the T_g of polymer thin films, coarse-grained PMMA thin film simulations are carried out using the LAMMPS molecular dynamics package. We use a two-bead-per-monomer CG mapping scheme including backbone and side-chain beads as described in further detail in previous studies by members of our research group²⁰⁹. The supported CG thin film systems, chosen over capped film systems to ensure proper equilibration and relaxation dynamics, consist of 52 to 115 chains with 200 monomers per chain, resulting in film thicknesses ranging from ~ 11 to 42 nm (along the y-axis) with a bulk

computational T_g of 397 K. Periodic boundary conditions are applied in the x-z plane and non-periodic boundary conditions are applied in the y-direction. To simulate the interaction of the polymer film with a cellulose nanocrystal, we utilize a perfectly smooth implicit wall, captured by a 12-6 Lennard-Jones potential function with interaction energy ϵ_{sp} . To estimate the interfacial adhesion energy, the DES approach is used to calculate all pairwise interactions between the CG polymer chains and the implicit wall. By varying ϵ_{sp} from 1.5 to 30.0 kcal/mol, we obtain simulation data for adhesion energies ranging from 47 to 1456 mJ/m². Calculations of T_g for these systems were performed by evaluating the polymer segmental relaxation from the self-part intermediate scattering function²¹⁰⁻²¹¹. These calculation details are not essential to the development of this multiscale model, so the reader is simply referred to the Supporting Information of the original reference²¹².

The overall multiscale framework can be briefly summarized by Figure 8-9. A representative nanocomposite structure is shown, where a PMMA matrix is reinforced with well-dispersed CNCs. Using the thin film-nanocomposite analogy, the average interparticle spacing h is equivalent to the film thickness as specified in the CG model. The interphase developed within the PMMA due to the presence of the CNCs has a thickness ξ and is highlighted in Figure 8-9. This analogy between a thin film and nanocomposite is used to relate the interfacial adhesion energy to the nanocomposite T_g and is discussed in greater detail in the remaining text.

While it has been previously established that macroscopic thermomechanical properties of nanocomposites are greatly influenced by filler-matrix interactions due to the formation of interphase regions^{202, 207, 213}, a direct link between the adhesion energy and the properties of this interphase region has not been quantified. As mentioned previously, to determine these effects we utilize the thin film geometry in lieu of a representative volume model of nanocomposites as these

are less computationally intensive models and experiments have shown equivalency between interphase thickness and local T_g in thin films and nanocomposites. Using the CG PMMA model, we quantify how thin film T_g depends on interfacial adhesion energy as shown in Figure 8-10(A). This figure shows a clear dependence of ΔT_g^{film} , defined by Eq. (8-2) and a function of the glass transition temperature of the film T_g^{film} and that of the bulk polymer T_g^{bulk} , on the interfacial adhesion energy.

$$\Delta T_g^{film} = T_g^{film} - T_g^{bulk} \quad (8-2)$$

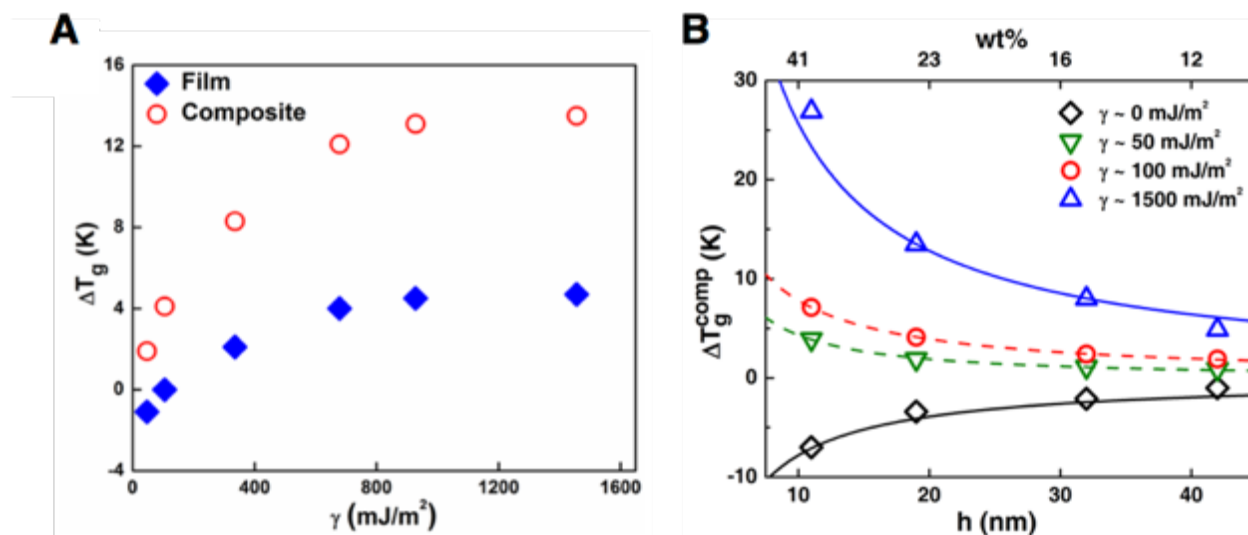


Figure 8-10: Effect of interfacial adhesion and dispersion on T_g of thin films and composites. (A) Change in T_g with respect to the bulk value as a function of interfacial adhesion energy γ for the supported thin film with a thickness of 19 nm and the corresponding composite calculated using the continuum layered model. γ is measured using the DES approach in the CG simulations. (B) Change in T_g of the composite (ΔT_g^{comp}) with different interparticle spacing h (corresponding film thickness) and weight fraction (wt. %) of CNCs for different adhesion energy. The markers and dashed lines correspond to data points obtained directly from MD simulations.

Specifically, we find that for a low interfacial adhesion energy, there is a depression in the glass transition temperature (i.e. negative value of ΔT_g^{film}), but as the adhesion energy increases

there is an appreciation of this value (i.e. positive value of ΔT_g^{film}). However, at some point any additional increase in the adhesion energy is negligible as the change in glass transition temperature saturates to a constant value. While these results are interesting for thin films, we are further interested in extending the results to predicting behavior of nanocomposites. In a supported thin film, there are influences on the T_g both from the free surface as well as the substrate-film interface (equivalent to the matrix-filler interface in nanocomposites). In nanocomposites, however, there are no free surfaces, so it is necessary to decouple these effects and only consider the influence of the substrate. We have developed a layered composite model²¹⁴⁻²¹⁶ to predict the change in T_g of a nanocomposite, ΔT_g^{comp} as a function of ΔT_g^{film} given by Eq. (8-3)

$$\Delta T_g^{comp} = 2\Delta T_g^{film} - \left(\frac{2\xi}{h}\right)\Delta T_g^{surf} \quad (8-3)$$

where h is the film thickness (equivalent to the interparticle spacing in a nanocomposite) and ξ is the interphase thickness. From simulations, we determine the free surface effect (ΔT_g^{surf}) to be approximately -13 K for the specific CG model assuming an interphase thickness of 3 nm. Using this model, the dependence of ΔT_g^{comp} on the interfacial adhesion energy is shown in Figure 8-10(A) and shows a qualitatively similar relationship to the thin film results. Figure 8-10(B) shows how ΔT_g^{comp} changes with interparticle spacing. This plot demonstrates that as the interparticle spacing is decreased, or equivalently the weight/volume fraction of CNCs is reduced, changes in the T_g converge to zero. These results agree quite well with recent experiments on CNC-PMMA nanocomposites that examined the effect of surface modifications on T_g . In these experiments, where the CNCs are extracted with acid hydrolysis that introduces some extent of surface modification, the enhancement in T_g is about 6.4 K for a nanocomposite with 33 wt. % CNC that corresponds to an effective interparticle spacing of 10.9 nm⁵⁹. Based on our simulations,

the predicted adhesion energy for this modification is between 50 and 100 mJ/m², thereby indicating this multiscale model is capable of accurately capturing changes in thermomechanical properties of nanocomposites.

Beyond the specific multiscale models presented here, the first used to predict dispersion and the second used to predict changes in T_g , our computational materials-by-design approach to developing multiscale models could easily be extended to develop other structure–property relationships that arise from nanoscale interfaces such as elastic response, fracture behavior, or even stimuli-responsive behavior. Additionally, our approach is general enough that it can be implemented for a wide range of material systems beyond CNC-polymer nanocomposites, while only requiring calculations of a few thermodynamic quantities. Finally, our results provide fundamental insight into the nanoconfinement effect within these materials through the formation of interphases and property variation near filler particles. Through the developed structure–property relationship, we demonstrate that strong interfacial energies are crucial to fully leverage the confinement features facilitated by the nanoscale proximity of particles. This multiscale approach to modeling and understanding emergent properties of nanocomposites is a key first step towards developing a comprehensive, computational materials-by-design approach for new materials. Predicting diverse structure–property relationships computationally from the nanoscale to the macroscale will be essential for fast and accurate exploration of the vast materials design space of nanocomposites.

Chapter 9 – Nanoscale Origins of Drying Creep

In the final research chapter of this work, we move away from the specific case of cellulose-based nanocomposites and demonstrate the broader applicability of computational materials-by-design. Here, we focus on utilizing nanoscale simulation to explain an existing phenomenon known as the Pickett effect for nanoporous solids. My interest in this material behavior was piqued by the fact that this effect is observed for cellulosic-based materials such as wood and paper, as well as more traditionally for concrete. Previously this effect had only been explained using macroscale experiments and micromechanical models, but using molecular simulation has allowed us to provide new insight into the nanoscale origins of this effect. We utilize coarse-grained molecular dynamics (CGMD) simulations to study the behavior of water confined in a nanopore and demonstrate the effect of nanoconfinement on water viscosity, mobility, and underlying energy barriers. We utilize these results in a computational materials-by-design framework to link results at the nanoscale to macroscale drying creep behavior of nanoporous solids and further, provide guidance for how to optimize material properties and response under drying creep conditions. Portions of the text and figures within this chapter are reprinted or adapted with permission from Sinko et al., *Proc. Royal. Soc. A* 2016. Copyright 2016 The Royal Society Publishing.

9.1 The Pickett Effect

Nanoporous solids²¹⁷⁻²¹⁸ contain many internal cavities (pores, channels, or both) that are predominantly nanoscale in terms of their average width. These materials are used commonly in applications ranging from chemical separations (zeolites and metal-organic frameworks²¹⁹) to structural materials (concrete²²⁰ and cellulose-based materials²²¹⁻²²²) in which there exists a tremendous amount of internal surface area through which the solid can interact with fluids

confined in the nanoscale cavities. For hydrophilic materials, pore water retained from processing in the form of moisture is always present in these nanopores, even after long periods of drying.

An intriguing aspect of nanoporous solids is the way they respond to changes in their internal moisture content, specifically in terms of their creep behavior. The so-called “Pickett effect”²²³ is one specific phenomenon that is of particular interest for these materials as it has yet to be fully explained²²³⁻²²⁵. This effect is based on the observations of Pickett²²³ who noted that the strain of concrete specimens undergoing drying and mechanical loading simultaneously is much greater than the sum of the strains from pure creep (i.e., observed under mechanical loading but in absence of any drying) and drying shrinkage (i.e., observed upon drying in absence of any mechanical loading). This concept is illustrated schematically in Figure 9-1(A).

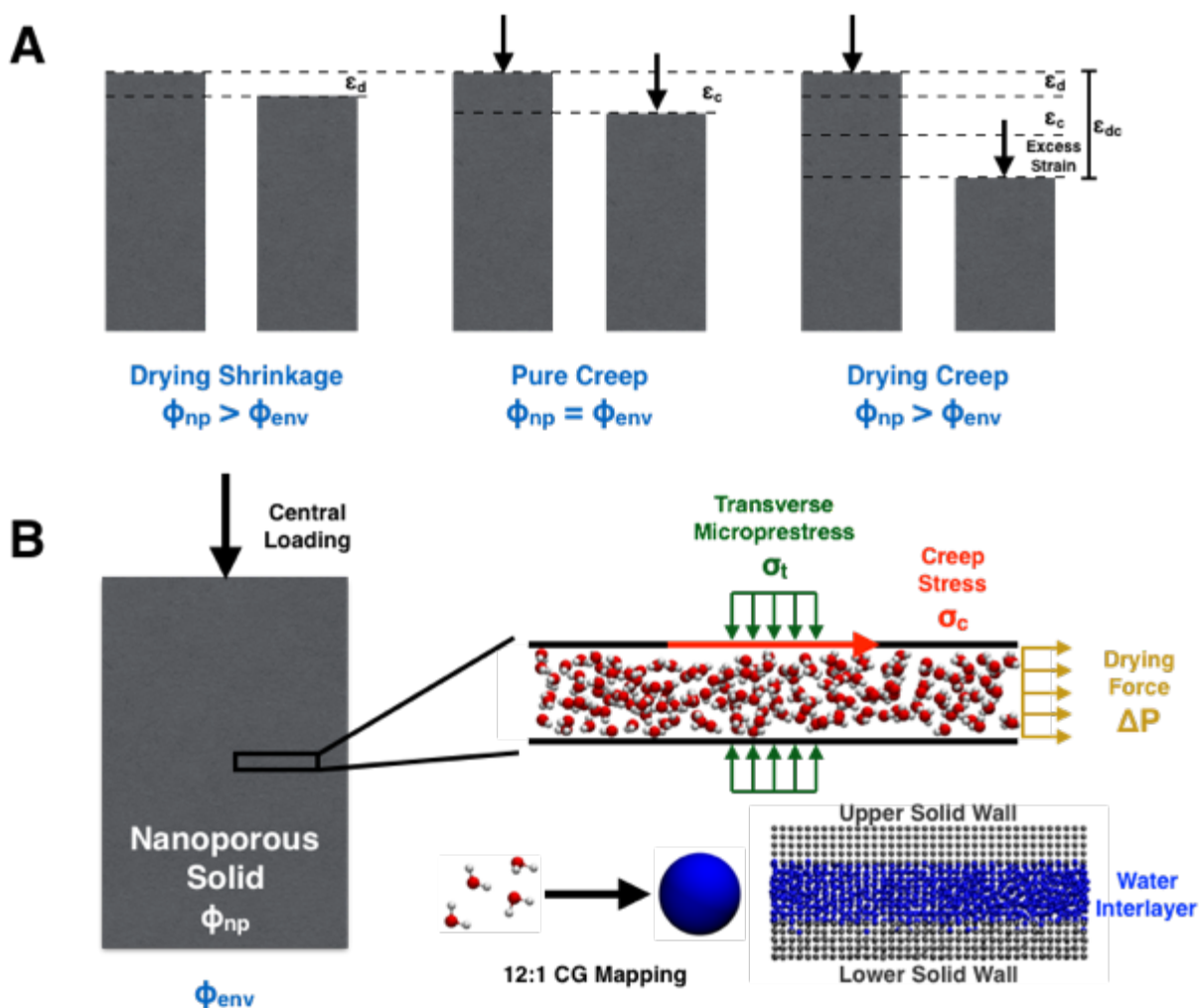


Figure 9-1: Illustration of the Pickett effect for nanoporous solids. (A) The Pickett effect states that the strain experienced by a specimen undergoing drying creep (i.e. simultaneous mechanical creep and drying shrinkage) is greater than the sum of strains due to pure drying shrinkage (no load, humidity driven moisture loss) and pure creep (applied mechanical load, no moisture loss). (B) Illustration of a nanopore within these specimens showing the three external forces considered in this study: 1) transverse microstress due to hindered adsorption of water, 2) shear creep stress caused by the macroscopically applied mechanical load, and 3) drying force or pressure caused by differences in the relative humidity of the specimen (ϕ_{np}) and the environment (ϕ_{env}).

The Pickett effect, while being central and initially discovered in terms of the creep deformation of concrete²²⁶⁻²²⁸ and thus the life-cycle performance of most structural and infrastructural systems, remains to be fully explained. Since the discovery of the Pickett effect

nearly 80 years ago, there has been continued experimentation²²⁹ to quantify this behavior. In addition to observations of the Pickett effect for cement paste²³⁰ and concrete²³¹, this drying creep phenomenon has also been observed for a number of other nanoporous solid materials²³² including cellulose-based materials such as wood²³³⁻²³⁶ and paper²³⁷⁻²³⁸, keratin fibers²³⁹⁻²⁴⁰, and synthetic polymers including Kevlar²⁴¹ and nylon²⁴². The existence of the Pickett effect for cellulosic materials is of particular interest for this work as the response of cellulose of moisture is a key concern to designing and understanding cellulose-based hierarchical materials.

Several theories have been proposed to explain the root causes of the Pickett effect. While these theories have typically been developed with concrete as the system of interest, they can easily be extended to cellulosic materials. Initially, the Pickett effect was widely thought to be explained by a difference in microcracking caused by non-uniform moisture distributions. In a companion load-free shrinkage specimen, the microcracks remain open during drying, thus reducing the observed overall shrinkage compared to that in the compressed creep specimen in which, despite drying, there is almost no microcracking. However, later tests under sustained compressive forces of different eccentricities²²⁵ showed that the differences in microcracking explain only a minor part of Pickett effect in concrete. Currently, the most widely accepted theories^{225, 243-246} are based on micromechanical models of concrete that are easily extendable to other material systems as they focus on inherent nanostructure as opposed to specific chemistry. These theories attribute the increased strain observed under drying creep to a combination of both microcracking and microprestress developed during concrete formation or during drying. In the microstructure of hardened cement gel, the hindered adsorbed water completely filling the nanopores (of width < 3 nm) exerts enormous disjoining pressure²⁴⁷⁻²⁴⁸ on the pore walls, which introduces tensile microprestress into the solid skeleton of the material. Especially, the solid bridges across the nanopores

must have highly stressed atomic bonds. As these bonds gradually break, the micro-prestress progressively relaxes, which gradually reduces the rate of creep due to external loads²⁴³⁻²⁴⁴. Extended to the transitional thermal creep²⁴⁹ (an effect similar to the Pickett effect), and combined with the solidification theory for the cement hydration process, the microprestress-solidification theory allowed close enough fits of test data.

Nevertheless, the existing theory has some limitations. It is not deep enough. Particularly, the connection of the microprestress increase to the increased creep is not explained in terms of nanomechanics. The water transport along the filled nanopores is not considered. Yet, the viscosity of nanopore water must be expected to play a role. Because of the effect of surface forces at nanopore walls, it is surely not Newtonian, i.e., depends on the shear deformation rate. The non-Newtonian behavior is supported by a number of recent studies focused on the behavior of water confined in nanotubes²⁵⁰⁻²⁵² or nanochannels^{112, 253-254}. In these studies, nanoconfined water exhibits interesting characteristics that vary significantly from its macroscopic behavior including non-Newtonian fluid behavior and glassy or ice-like structure and mobility near hydrophilic surfaces. Therefore, it is plausible that the behavior of nanoconfined water under combined creep and drying forces may lead to physical phenomena that may be an important contributor to the creep enhancement during drying. Some have proposed that the Pickett effect originates at the scale of this nanoconfined water¹⁶.

In this study, we aim to investigate and quantify these nanoscale effects to further explain the origin of the Pickett effect in nanoporous solids. To examine the notion that nanoscale effects may play a key role in the macroscopic Pickett effect, here we conduct coarse-grained molecular dynamics simulations (CGMD) of the flow of water in a nanochannel as illustrated in Figure 9-1(B). We utilize a generalized model of water interacting with a hydrophilic solid surface, such

that our results could be extended to any nanoporous solid and would not be limited to any specific material chemistry. In addition to understanding the drying creep behavior, we are interested in how the magnitude of the transverse microstress developed on the walls of the nanopore during solidification and drying²⁴³⁻²⁴⁶ influences the intensity of the Pickett effect (Sections 9.7 and 9.8). In our simulations, we focus on quantifying the relative creep displacement or relative creep velocity of the solid boundaries of the nanopore under an applied creep force and further characterize how these values change when drying occurs (i.e. flow of water within the nanopore).

9.2 Coarse-Grained (CG) Model and Simulation Parameters

As mentioned previously, we aim to examine the Pickett effect from a nanoscale perspective using CGMD simulations of water flow through a nanopore/nanochannel. Here, we use a slit pore geometry to simulate the flow of water at the nanoscale under drying creep conditions. The nanochannel, illustrated in the context of the nanoporous material in Figure 9-1(B) and more explicitly in Figure 9-2, consists of water confined between two solid, hydrophilic, walls that are analogous to the semi-crystalline solid phase in nanoporous solids such as cellulose in wood or a calcium silica hydrate (C-S-H) phase in concrete. Generally speaking, the surface chemistry of the walls will vary from one system to another, but for materials exhibiting the Pickett effect, the walls are expected to be strongly hydrophilic, fully wetting surfaces where macroscopically the contact angle of a water droplet on the surfaces should be much less than 90° , in fact virtually 0. Thus, rather than using chemistry-specific systematic coarse-graining techniques^{209, 255-256}, here we use a generic coarse-grained (CG) model²⁵⁷ that captures the essential aspects of the problem such as the bulk properties of the fluid and the contact angle of the fluid with the walls.

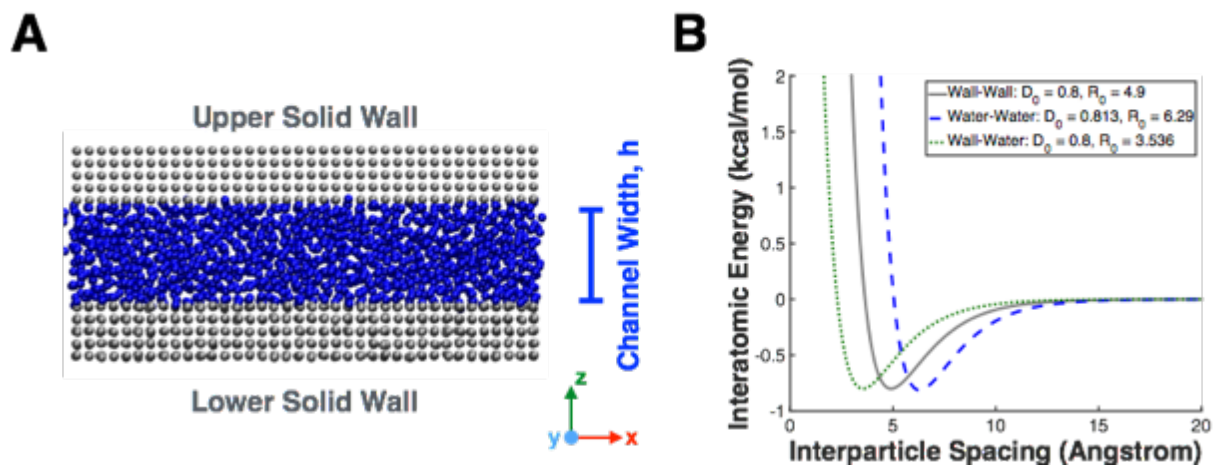


Figure 9-2: Coarse-grained model of water in nanopore and interatomic potentials. (A) Snapshot of our chemistry independent, coarse-grained (CG) model of a nanopore/nanochannel within a solid material that exhibits the Pickett effect. The nanochannel is periodic in the x and y directions and has a finite dimension in the z -dimension with a channel width of h . The gray beads represent the solid walls of the nanochannel (e.g. C-S-H phase in concrete or crystalline cellulose in wood) while the blue beads represent water molecules. (B) The plot shows the Morse interatomic potential used to model the energetic interactions between particles in our system with the gray, solid curve representing interactions between atoms in the solid wall ($D_0 = 0.8$ kcal/mol, $\alpha = 0.5500 \text{ \AA}^{-1}$, $R_0 = 4.9 \text{ \AA}$), the blue, dashed curve representing water-water interactions ($D_0 = 0.813$ kcal/mol, $\alpha = 0.5552 \text{ \AA}^{-1}$, $R_0 = 6.29 \text{ \AA}$), and the green, dotted curve representing the cross-interactions ($D_0 = 0.8$ kcal/mol, $\alpha = 0.5552 \text{ \AA}^{-1}$, $R_0 = 3.536 \text{ \AA}$).

To ensure that the parameter space studied be relevant for realistic systems, we use a previously developed model²⁵⁷ that accurately captures the bulk viscosity, surface tension, density of water, and wall interactions that represent a fully wetting hydrophilic surface¹¹². This (CG) model employs the Morse interatomic potential to represent interactions between CG particles (also referred to as beads). The Morse interatomic potential energy U is given by Eq. (9-1) below as a function of the interatomic distance between particles, r , where D_0 is the depth of the energy well, r_0 is the equilibrium distance between particles, and α governs the decay characteristics and curvature of the interaction potential.

$$U(r) = D_0[e^{-2\alpha(r-r_0)} - 2e^{-\alpha(r-r_0)}] \quad (9-1)$$

The parameters in Eq. (9-1) are determined for a 4:1 mapping for water, indicating that each coarse-grained water bead represents 4 water molecules (12 total atoms). Parameters for the solid wall material are chosen such that the water-wall interaction be hydrophilic – something that is accomplished by setting the D_0 parameter of water-wall interactions to be the same as that for water-water interactions. The specific parameters and Morse interatomic potentials for different pairs of interactions are plotted as a function of interatomic distance r in Figure 9-2(B).

Using this model, CGMD simulations are conducted using the Large-scale Atomic/Molecular Massively Parallel Simulator (LAMMPS) molecular dynamics package⁸⁶. Periodic boundary conditions (PBCs) are applied in the x and y directions, with the system having a finite thickness in the z -direction (for reference to Cartesian directions see Figure 9-2(A)). The simulation box has dimensions of 15 nm by 3 nm by 6 nm and the nanochannel width is chosen to be 4 nm – an intermediate nanopore size in many nanoporous solids²⁵⁸. In concrete, such width is characteristic of the size of the pores in the C-S-H gel. During simulations, the bottom solid layer is fixed by tethering the atoms to their initial position using virtual springs having a spring constant of 10.0 kcal/mol-Å². Here, we chose a harmonic constraint over a complete fix/freeze in order to prevent distinct differences between water-wall interactions at the top and bottom surfaces that may arise if the bottom layer is frozen. Additionally, we have verified that changing the value of this spring constant does not significantly change the results of our simulation (e.g., ~10 - 15% change in the measured velocities when the spring constant is varied from 5.0 kcal/mol-Å² to 50.0 kcal/mol-Å², at given creep stress of 9.5 MPa and drying pressure of 100 MPa). To simulate the effect of basic (or pure) creep, individual forces are added to the atoms in the top layer having a

magnitude denoted by f_{ic} . To simulate drying, individual forces, of magnitude f_{id} , are added to the water beads within the channel.

After constructing the nanopore using a predefined face-centered cubic (FCC) lattice with an edge length of 8.33 Å, the system is equilibrated for 0.5 ns in order to reach a minimum energy configuration. Simulations are run under the microcanonical ensemble (constant number of particles, volume, and energy) with a dissipative particle dynamics (DPD) thermostat. A DPD thermostat is employed in simulations to accurately capture the hydrodynamics of the system by preserving momentum of the particles – something that is often neglected by other global thermostats¹¹². The DPD potential is overlaid on the interatomic Morse potential and thermostats the system temperature to 300 K and utilizes a damping coefficient of 2875 kcal-fs/mol-Å². This damping coefficient has been previously calibrated to match the bulk viscosity of water of 9.0×10^{-4} Pa-s¹¹². The calibration conducted in our previous study¹¹² was performed by inducing Couette flow in a 25 nm width channel and measuring the shear stress as a function of the shear rate. By calculating the slope of the shear stress vs. shear rate curve, a viscosity was obtained and the DPD damping coefficient was tuned until the viscosity matched that of bulk water. During equilibration, the top layer is free to move up and down in the z-direction, but is constrained to move as a rigid body and remain parallel to the bottom layer.

Once the system is equilibrated, forces are applied individually to beads in the top wall and/or the water layer to simulate pure creep, pure drying, drying creep, and transverse microstress. In our simplified geometry, the basic creep is simulated by applying forces to the beads only in the top layer in the x-direction, pure drying is simulated by applying forces to only the water beads in the x-direction, and drying creep is simulated by applying forces to both the water beads and those in the top solid layer in the x-direction. To account for transverse

microprestress (considered in Section 9.7 and 9.8), individual forces are applied to beads in the top layer in the z-direction. Flow simulations are run for 40 ns (2,000,000 time steps of 20 fs) to ensure that the system has reached a steady-state condition. The primary output from these simulations is the average, steady-state velocity of the top wall. This velocity, which we will refer to as the creep velocity of the nanochannel from this point onward, is directly related to the total creep displacement and strain that is of interest in the context of the Pickett effect.

9.3 Behavior of Nanoconfined Water

A good starting point for our discussions is the behavior of water under nanoconfinement. Specifically, we first investigate how the dynamics, specifically the apparent viscosity, of the water change as a function of both the creep force F_c and the drying force F_d . As shown in Figure 9-1(A), on a macroscopic specimen, a uniaxial compressive load is applied to cause creep. This macroscopic compressive creep force is translated to shear stress between various molecular components (e.g. C-S-H colloidal particles in concrete or cellulose microfibrils in wood) at interfaces within the material. Recent models have been proposed for hydrated matrix-interface composites that have further quantified the translation of these forces across length scales and support shear displacement of these nanopores due to the applied macroscopic stresses²⁵⁹⁻²⁶². Therefore, the creep stress F_c can be understood in our simulations as the shear stresses applied to the solid pore walls because of the uniaxially applied compressive loads that cause shear displacement across the pore walls. This creep force, or alternatively creep stress τ_c (here denoted by a shear stress symbol to highlight shear deformation of the nanopores), can be calculated from the forces applied to individual atoms in the top layer, f_{ic} , by Eq. (9-2)

$$\tau_c = \frac{F_c}{A_s} = \frac{\sum_i f_{ic}}{A_s} \quad (9-2)$$

where A_s is the cross-sectional area of the solid wall in the pulling direction (xy plane). The drying forces applied to the water beads in our system are the result of a pressure differential that exists across the nanopore, denoted as P . This pressure differential is caused by differences in the relative humidity of the nanopore and the ambient environment. Differences in the relative humidity create a chemical potential and vapor pressure gradient that induces water flow (i.e. drying) along the nanochannel²⁶³. The pressure differential, ΔP , across the nanopore can be calculated from the individual forces applied to the water beads, f_{id} , by Eq. (9-3), where A_w is the cross-sectional area of the water within the nanochannel. In Eq. (9-3), we also show a direct relation between this driving pressure and the difference in vapor pressure within the nanopore, $P_{v,np}$, at a relative humidity of ϕ_{np} and the vapor pressure of the ambient environment, $P_{v,env}$, at a relative humidity of ϕ_{env} . Note that $P_{sat}|_T$ is the saturation pressure at a given temperature;

$$\Delta P = \frac{F_d}{A_w} = \frac{\sum_i f_{id}}{A_w} = P_{v,np} - P_{v,env} = (\phi_{np} - \phi_{env})P_{sat}|_T \quad (9-3)$$

In our simulations, we are interested in the mobility of the water in the nanochannel under these external forces of the pressure difference (drying force) and the applied creep stress. However, what really matters for deformations is the apparent viscous behavior of the water, which provides the shear resistance between the two walls as a significant source of resistance to creep deformation. This effective viscosity, capturing all aspects governing the total displacement of the top wall with respect to the fixed bottom, will depend on the external stress boundary conditions. To measure changes in water behavior as a function of pressure differential across the channel that causes drying and creep stress, we define an effective viscosity η as given by Eq. (9-4) where F_c is the applied creep force and $v_{c,mean}$ is the creep velocity of the top plate;

$$\eta = \frac{F_c}{v_{c,mean}} \quad (9-4)$$

Here, we use the quantity $v_{c,mean}$ since we do not know in which direction the water will flow within the pore relative to the creep force *a-priori*. During drying, water will flow out of the pore, but would be equally likely to flow “forwards” or “backwards” relative to the creep force. Therefore, we must calculate the creep velocity both in the case where water flow is in the same direction as creep (v_{c+}) and in the case where it is in the opposite direction (v_{c-}). Rather than look at these cases individually, we simply can estimate a mean velocity that is given by Eq. (9-5) and is used in all of our calculations by noting that the two cases are equally likely and there is no net directional preference.

$$v_{c,mean} = \frac{v_{c+} + v_{c-}}{2} \quad (9-5)$$

From our simulations, we can then measure the effective viscosity of water as a function of both the applied creep stress and the applied water pressure differential. The results of our simulations are presented in Figure 9-3, with the viscosity calculated from Eq. (9-4) plotted as a function of the applied creep stress in Figure 9-3(A) and as a function of the applied water pressure in Figure 9-3(B). In Figure 9-3(A), the different symbols correspond to a range of the quantity $r = f_{id}/f_{ic}$ which covers a wide range of drying conditions from relatively little drying (low r values) to larger amounts of drying (high r values). In Figure 9-3(B), the different line colors and symbols correspond to varying magnitudes of the creep stress applied to the top wall.

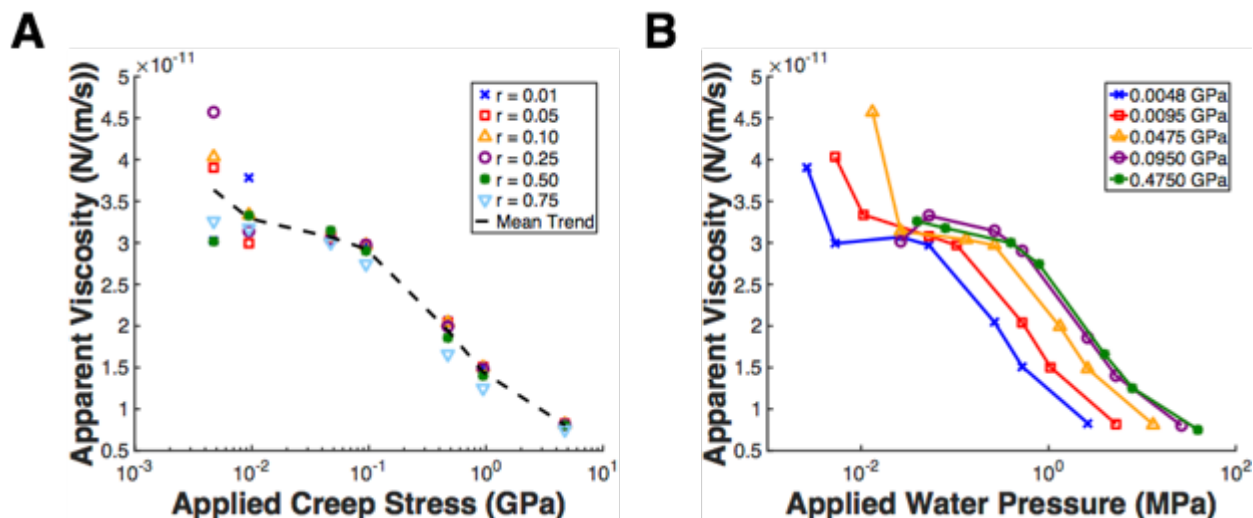


Figure 9-3: Shear thinning behavior of nanoconfined water. (A) Effective viscosity of water measured in simulation as a function of the applied creep stress. Symbols in the plot correspond to different values of the drying force as defined by the variable $r = F_d/F_c$. The dashed, black line shows the mean trend by averaging over all value of r at a given applied creep stress. (B) Effective viscosity as a function of the pressure differential applied across the nanochannel to the water beads. Each symbol and corresponding line represents a different value of the applied creep stress. Both of these plots suggest that water exhibits shear thinning behavior under nanoconfinement as the viscosity decreases with increasing shear deformation rate.

When examining these figures, we notice that the viscosity of water is not constant as a function of either the drying force or creep force, indicating that water confined in the nanochannel is exhibiting non-Newtonian behavior. Under bulk conditions, and since water is a Newtonian fluid at the macroscale, we would expect the viscosity to remain constant and be independent of the shear rate and, indeed, CGMD simulations carried out in large enough channels without any nanoconfinement reproduce the linearity of the shear response. This linearity of the shear response has been verified in a previous study using this model¹¹², and has also been verified for a larger 25 nm channel in this work. However, from our simulations we see that the effective viscosity decreases with both increasing drying force and increasing creep force. Specifically, we conclude that water exhibits shear thinning, non-Newtonian behavior with increasing shear rates.

These findings are consistent with previous experimental and computational studies that have shown similar shear thinning behavior of water²⁶⁴⁻²⁶⁷ and other fluids²⁶⁸ under nanoconfinement. Additionally, this shear thinning behavior has been observed for a wide range of values of the DPD damping coefficient. This illustrates two important facts. First, the shear thinning effect is not an artifact of the DPD thermostat and, second, this shear thinning behavior is not limited to only water but can be extended to any fluid under nanoconfinement since changing the DPD thermostat damping parameter is equivalent to modeling fluids with a different bulk viscosity.

This is distinctly different from water behavior in the bulk state and is believed to be a result of the glass-like nature of water under nanoconfinement²⁶⁹. We hypothesize that this behavior is related to the Pickett effect since the drying pressure on the fluid introduces this shear thinning behavior and consequently accelerates the creep of the material. Further, although we are using relatively high shear rates (10^{-2} to 10^2 s⁻¹) in MD simulations, a recent study has shown that a similar shear thinning behavior of collagen observed in MD can be extended to the low shear regime (10^{-6} to 10^2 s⁻¹) using a number of different extrapolation methods²⁷⁰. This provides further evidence that our results for the flow of water at unrealistically large flow rates in a system submitted to unrealistically large shear rates can be extended to nanoporous solids submitted to realistic creep and drying rates.

As mentioned above, this glass-like nature of water under nanoconfinement has been observed for numerous systems. Typically, this glass-like behavior is attributed to the molecular ordering of fluid near solid surfaces²⁷¹ due to either non-bonded interactions²⁷¹ or the local electrical environment through electrostatic interactions²⁷². In our system, we do not explicitly include any electrostatic effects, however, we still observe this glass-like behavior through reduced mobility

and the relative water-water and water-wall interactions. In order to quantify this reduced mobility and increased molecular ordering, we calculate two quantities. First, we calculate the local mean-squared displacement (MSD) of the water beads as defined by Eq. (9-6) for a single particle

$$MSD(n) = \frac{1}{n} \sum_{t=1}^n (r(t) - r_0)^2 \quad (9-6)$$

where n is the number of time steps, $\vec{r}(t)$ is the position of the particle at time t , and \vec{r}_0 is some reference position of the particle which is taken to be the average position of the particle for the previous $n - 1$ time steps. We calculate the local MSD by binning the water molecules based on their position along the width of the nanochannel (i.e. z-dimension in Figure 9-2(A)) and averaging over all particles in each bin. For the local MSD calculation, we use a spatial resolution (i.e. bin size) of 1 Å. Because the water beads are relatively mobile and able to move between bins over the course of the whole simulation (40 ns), we focus on the results of the initial 2 ns when the beads have not yet moved out of their initial spatial bins. Using these relatively short time scales (picoseconds or nanoseconds) to assess the mobility of binned particles has also been employed in Debye-Waller Factor calculations for polymer thin films in previous studies²⁷³⁻²⁷⁴.

Secondly, we calculate the radial distribution function (RDF), $g(r)$, that describes how the water beads in our system are radially packed around one another. The RDF is calculated using the appropriate plugin in VMD²⁷⁵, and is given by Eq. (9-7)

$$g(r) = \lim_{dr \rightarrow 0} \frac{p(r)}{4\pi(N_{pairs}/V)r^2 dr} \quad (9-7)$$

where $p(r)$ is the average number of atom pairs found within a certain spherical shell extending from r to $r + dr$ over a specified simulation time, V is the selection volume, and N_{pairs} is the total of number of atom pairs in the selection. To determine how the molecular ordering changes throughout the nanochannel, the RDF is calculated for three regions of water along the width of

the nanochannel: water beads within 0.75 nm of the lower water-solid interface ($y = 0.00$ nm to $y = 0.75$ nm), water beads within 0.75 nm of the upper water-solid interface ($y = 3.25$ nm to $y = 4.00$ nm), and the remaining water beads in the middle of the channel ($y = 0.75$ nm to $y = 3.25$ nm).

The local MSD as a function of location within the nanochannel is shown in Figure 9-4(A) and the local MSD as a function of simulation time for each of the different bins is shown in Figure 9-4(B). The RDFs for each of the three different regions within the nanochannel are shown in Figure 9-4(C). The spatial profile of the local MSD is averaged from time $t = 0$ to time $t = 2$ ns and is overlaid over an illustration of the nanochannel. This plot demonstrates that the mobility of the water beads, as measured by the magnitude of the local MSD, is greatly decreased near the walls of the nanochannel. These nanoconfined layers (illustrated as red beads in Figure 9-4(A)) near the walls exhibit vastly decreased mobility compared to the water beads in the middle of the nanochannel (blue beads in Figure 9-4(B)) due to increased molecular ordering.

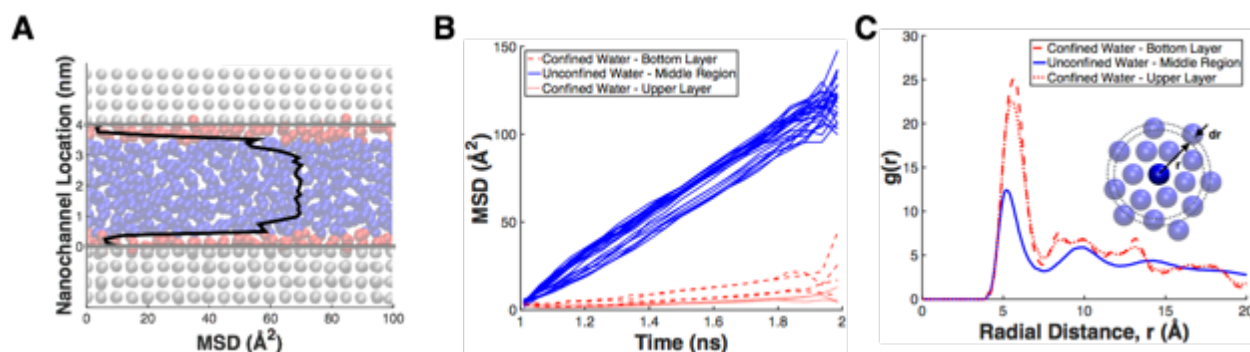


Figure 9-4: Nanoconfinement of water near solid surfaces. (A) Local mean-squared displacement (MSD) as a function of position along the width of the nanochannel, with $y = 0$ nm corresponding to the bottom surface and $y = 4$ nm corresponding to the top surface. The local MSD is averaged over the first 2 nanoseconds of the simulation. This plot is overlaid on an illustration of the nanochannel where the gray beads are the solid layer, the red beads are the confined water layers, and the blue beads are the unconfined water. (B) Local MSD as a function of simulation time. The local MSD is calculated by assigning water beads to spatial bins (bin size of 1 \AA) along the width of the nanochannel. Three distinct regions are observed: a confined region of water near the bottom water-solid interface ($0.00 - 0.75$ nm and red, dashed lines), an unconfined region of water in the middle of the nanochannel ($0.75 - 3.25$ nm and blue, solid lines), and a confined region of water near the upper water-solid interface ($3.25 - 4.00$ nm and red, dotted lines). (C) Radial distribution function $g(r)$ of the water molecules for each of the three different regions observed from local MSD calculations. We observe that the water beads are more densely packed near the top and bottom surfaces compared to the middle of the nanochannel and exhibit greater molecular ordering (i.e. nanoconfinement).

The increased molecular ordering is confirmed by the RDFs in Figure 9-4(C) which show larger peaks for beads close to the solid-liquid interface and indicate a more densely packed fluid. Further, when examining the MSD vs. time plot in Figure 9-4(B), we see that the MSD is lower for the layers of water near the solid surfaces (red curves). From these plots, we conclude that the confined layers extend approximately $0.50 - 0.75$ nm from both the top and bottom surfaces. These dimensions correspond to 2 or 3 atomic layers of water that are considered to be confined at the liquid-solid interface. Together, these plots help to demonstrate that our relatively simple model

can capture the glass-like behavior of water due to nanoconfinement. Specifically, our model, using only Morse non-bonded interactions, captures the decreased mobility near solid surfaces due to higher molecular ordering of the fluid.

9.4 Analytical Model for Drying Creep at the Nanoscale

After observing the change in water properties as a function of the applied creep force and drying force, a model was developed to try and describe these changes. The central issue we wish to address is: How does the creep velocity change as a function of the applied drying force and the applied creep force? One way to explain creep deformation is to invoke concepts such as energy landscapes and kinetics to describe the breaking and reformation of chemical bonds, in which deformation can be seen to proceed by hopping over energy barriers at the nanoscale. Each hopping event represents the breaking and reformation of weak interactions that resist the relative displacement of the walls. These reorganization events may occur at the wall-fluid interface (slip), and also within the fluid phase.

Traditionally, these concepts are employed to describe the failure of materials or interfaces at the nanoscale, as in the works of Bell¹²⁸ and Zhurkov²⁷⁶. The common feature of the kinetic models is that they employ an Arrhenius relationship that describes the lifetime of nanoscale bonds (or equivalently the probability of a bond breaking) using a single energy barrier and distance to the transition state, regardless of the specific chemistry of the bonds involved. This simplifying assumption works, at least phenomenologically, reasonably well for many types of chemical bonds, including those involved in fracture of glasses, polymers, and metals, in cell adhesion¹²⁸ and protein unfolding²⁷⁷⁻²⁷⁸, and in many other nanoscale phenomena governed by the underlying energy barriers⁷⁹. Where these models fall short and are often incorrect, however, is for processes that involve overcoming multiple energy barriers in succession (i.e. multiple bond breaking events

in the context of Zhurkov's model). In this case, if the difference between the successive potential troughs is small, both the forward and backward rates must be considered.

In the context of creep of nanoporous solids, we now use this idea to describe how the two solid walls move past one another and overcome nanoscale energy barriers to sliding motion. Overcoming the underlying energy barrier to sliding, E_b , as is the case in these creep simulations, is analogous to the rupture of atomic bonds as they both require some force or energy input into the system to encourage relative deformation or displacement. For our specific system, we can further relate this probability to the total creep displacement or creep velocity (the quantity measured in simulation) as a function of the applied creep force and drying force. Since these systems are under steady state conditions, the creep velocity is more or less constant and the creep displacement could be calculated by multiplying this value by the simulation time. The probability of overcoming some underlying energy barrier is given by Eq. (8) where E_b is the underlying energy barrier to shear displacement, k_b is Boltzmann's constant (1.38×10^{-23} J/K), T is the temperature of the system, f is the total force applied to the particle, and x_b is the distance between energy barriers that is a measure of the atomic roughness of the underlying energy landscape.

$$p = \exp\left(-\frac{E_b - fx_b}{k_b T}\right) \quad (9-8)$$

From a molecular perspective, our system contains a slit pore filled with water molecules between two solid walls interacting with Morse interatomic potentials (Figure 9-2). From a modeling perspective, however, we treat the beads in the top wall as a single object that interacts with the bottom wall with some periodic interatomic potential having an energy barrier E_b and a period of $2x_b$. Further, although creep forces (f_{ic}) and drying forces (f_{id}) are applied to individual beads in our simulation, we can resolve these forces to net forces acting on the top wall as

illustrated in Figure 9-5(A). The net creep force, F_c , is simply a sum of the individual creep forces applied directly to each of the beads in the top wall. The net drying force, F_d , is applied directly to the water beads, but also imparts some force on the top wall through viscous shear transfer. Therefore, the force imparted on the top wall by the water through shear transfer is denoted as cF_d , where c denotes the ratio of the shear force transfer and is a fitting parameter in our current study. Although this is currently a fitting parameter, c can be thought of as a measure of the drag coefficient or slip length between the fluid and the top wall. This is a physical quantity that could be measured experimentally.

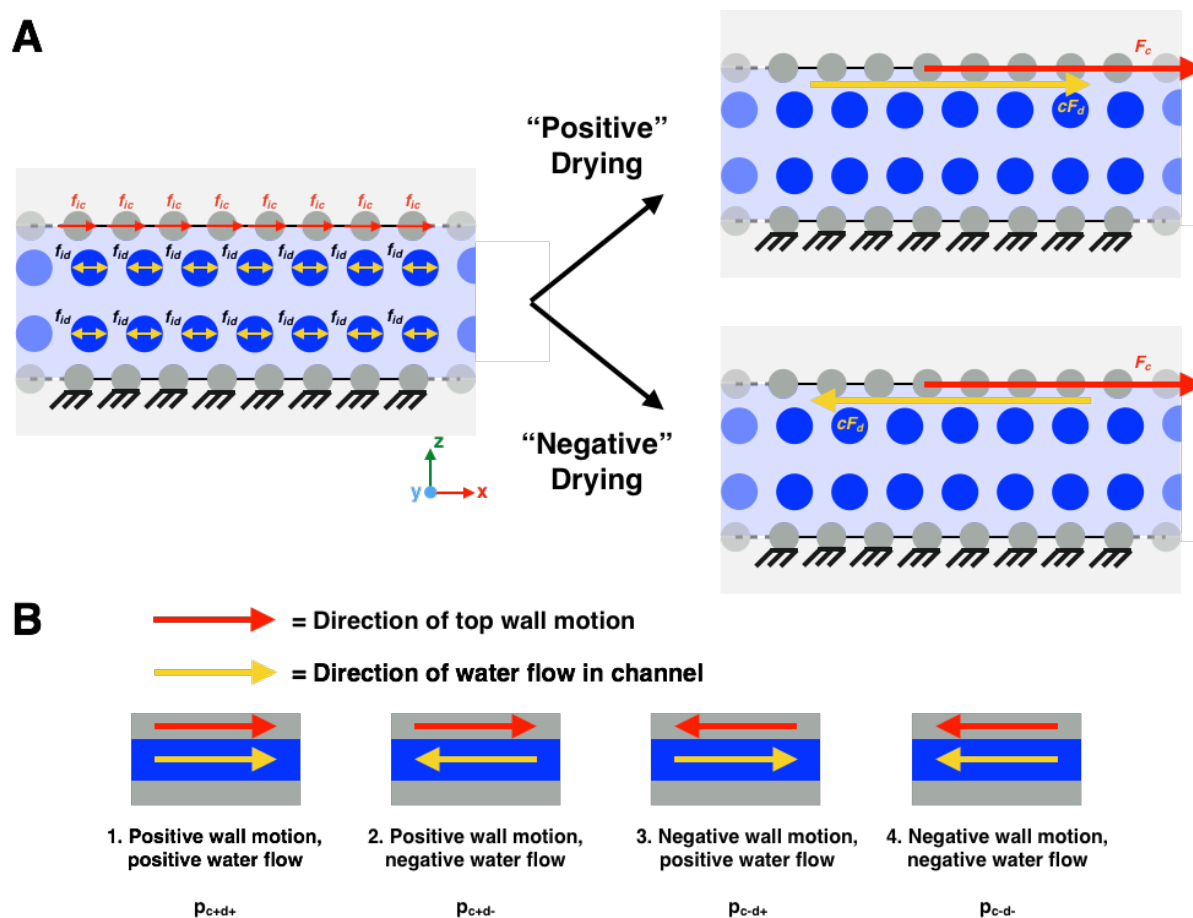


Figure 9-5: CGMD simulation methodology for analytical model of drying creep. (A) Illustration of the boundary conditions applied to the CGMD systems to simulate the effects of drying creep on a nanopore/nanochannel. Drying is simulated by adding an individual force (f_{id}) to each water atom while creep is simulated by adding an individual force (f_{ic}) to each atom in the top solid wall (while keeping the bottom solid wall fixed). Although forces are applied to atoms individually, we can resolve these into a net creep force applied to the top plate, F_c , and a net drying force applied to the top plate, cF_d , through viscous shear transfer. In our model, we consider “positive” drying to be the case where the net drying force and creep force are in the same direction and “negative” drying to be the case where the net drying force opposes the creep force. (B) In the development of our analytical model, we must consider 4 different cases of drying creep. In cases 1 and 2, the top wall moves in the positive x-direction and in cases 3 and 4, the top wall moves in the negative x-direction. In all of these cases, the creep force is applied in the positive x-direction.

Although we can directly define the probability of overcoming an energy barrier, the novelty of this model is to relate this probability to the net displacement or velocity of the top wall

as a function of the applied creep and drying (i.e. motion of the water within the nanochannel). To calculate the net displacement, we must consider the probabilities of four cases as illustrated in Figure 9-5(B): (1) the top layer moves forward with positive water flow (p_{c+d+}), (2) the top layer moves forward with negative water flow (p_{c+d-}), (3) the top layer moves backward with positive water flow (p_{c-d+}), and (4) the top layer moves backward with negative water flow (p_{c-d-}). Even though the creep force is always in the positive x-direction and will assist the top wall in moving forward, the top wall still has some probability (although it is admittedly small) to move backwards due to thermal fluctuations. In this formulation, we improve upon Zhurkov's classical model by considering both the forward (cases 1 and 2) and backward (cases 3 and 4) motion of the solid walls to overcoming the underlying energy barriers. Further, the cases of both positive and negative water flow must be considered since there is no *a-priori* knowledge of the drying directionality. Therefore, the probabilities of overcoming an energy barrier E_b for these four cases are given by Eq. (9-9) – Eq. (9-12).

$$p_{c+d+} = \exp\left(-\frac{E_b - F_c x_b - cF_d x_b}{k_b T}\right) \quad (9-9)$$

$$p_{c+d-} = \exp\left(-\frac{E_b - F_c x_b + cF_d x_b}{k_b T}\right) \quad (9-10)$$

$$p_{c-d+} = \exp\left(-\frac{E_b + F_c x_b - cF_d x_b}{k_b T}\right) \quad (9-11)$$

$$p_{c-d-} = \exp\left(-\frac{E_b + F_c x_b + cF_d x_b}{k_b T}\right) \quad (9-12)$$

The total displacement, Δx_c , or creep velocity, v_c , of the top layer can be computed using Eq. (9-13), which is derived from Bell's model¹²⁸ and also includes the frequency of molecular vibrations ω . Although we include the frequency term in our model, we can assume this to be a constant since the frequency of molecular vibrations will not vary greatly between systems.

$$\Delta x_{dc} = v_c t = \frac{(p_{c+d+} + p_{c+d-} - p_{c-d+} - p_{c-d-})}{2} x_b \omega \quad (9-13)$$

It is also important to consider and derive expressions for the cases of pure creep, that is, the creep in the absence of the drying force on the water molecules, and of pure drying in the absence in any creep force applied to top wall. For pure creep, the probability of forward motion is given by Eq. (9-14), the probability of backward motion is given by Eq. (9-15), and the total displacement for pure creep is given by Eq. (9-16).

$$p_{c+} = \exp\left(-\frac{E_b - F_c x_b}{k_b T}\right) \quad (9-14)$$

$$p_{c-} = \exp\left(-\frac{E_b + F_c x_b}{k_b T}\right) \quad (9-15)$$

$$\Delta x_c = v_c t = (p_{c+} - p_{c-}) x_b \omega \quad (9-16)$$

Similarly, for pure drying, the analogous probabilities and displacement are given by Eq. (9-17) – (9-19).

$$p_{d+} = \exp\left(-\frac{E_b - cF_d x_b}{k_b T}\right) \quad (9-17)$$

$$p_{d-} = \exp\left(-\frac{E_b + cF_d x_b}{k_b T}\right) \quad (9-18)$$

$$\Delta x_d = v_d t = (p_{d+} - p_{d-}) x_b \omega \quad (9-19)$$

To determine whether or not the Pickett effect is informed by these nanoscale “bond-breaking” events where an underlying energy barrier is overcome, we compare the net displacements predicted for the case of drying creep and the summation of displacements due to pure creep and pure drying shrinkage. It is important to note that although the Pickett effect deals with the

summation of creep and drying strains, it is equivalent to compare displacement and/or velocities that are simple scalar multiples of these strain values.

These results are presented in Figure 9-6 and show the predicted displacement for the cases of basic (pure) creep (black, dotted lines) and pure drying shrinkage (green, dashed lines), the summation of these displacement (red, dot-dash lines) and the predicted displacement for the case of drying creep (blue, solid lines) for underlying energy barriers of $4k_bT$ and $8k_bT$. These values are representative of the underlying energy barriers calculated for nanochannels with a width of 4 nm and 3 nm, respectively, as discussed in Section 3(d). In Figure 9-6, we define a ratio of $r = F_d/F_c$ and show results for the case of $r = 0.5$. We also note that the case of basic creep corresponds to $r = 0$ and the case of pure drying corresponds to $r = \infty$. In these specific iterations of the model, the variable c is assumed to have a value of 1 for simplicity. Finally, we note that both the creep force and the relative creep displacement are presented as dimensionless quantities to evaluate the model and potential importance of underlying energy barriers more easily.

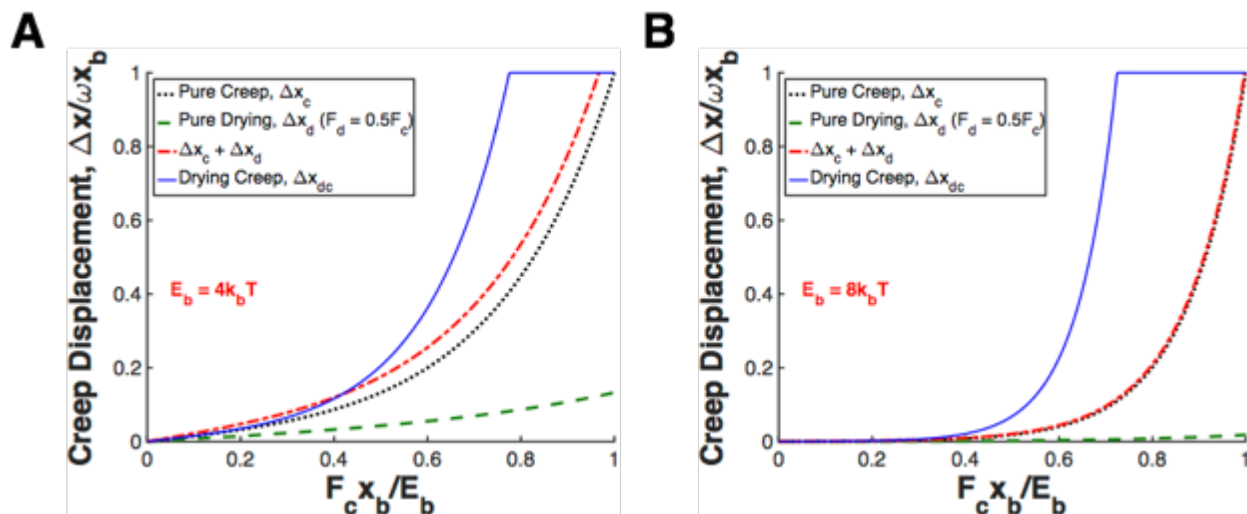


Figure 9-6: Analytical predictions from Bell's model. These panels show the predicted displacement of the top wall as a function of the creep force for underlying energy barriers of (A) $4k_b T$ (2.372 kcal/mol) and (B) $8k_b T$ (4.744 kcal/mol). The black, dashed lines correspond to pure creep (Δx_c), the green, dashed lines correspond to pure drying (Δx_d), the red, dot-dash lines are the summation of pure creep and pure drying displacements ($\Delta x_c + \Delta x_d$), and the blue, solid lines correspond to drying creep (Δx_{dc}). Our model demonstrates that the displacement due to drying creep is greater than the summation of pure creep and pure drying for a wide range of applied creep and drying forces. These results provide some evidence that the extent of the Pickett effect is dependent on the drying rate and the magnitude of the underlying energy barriers.

The results presented in Figure 9-6 demonstrate consistent and interesting trends that help to further explain the Pickett effect. First, Figure 9-6 indicates that our model clearly captures the main finding of the Pickett effect – the relative displacement (or equivalently strain) due to drying creep is greater than the sum of the displacement due to basic creep and pure drying. For high underlying energy barriers (Figure 9-6(B)), this relationship holds for the entire range of the applied creep and drying forces. For lower energy barriers (Figure 9-6(A)), we see a small region for low applied creep and drying forces where the summation is marginally greater (at most 0.01) than the relative displacement due to drying creep. This indicates there may be some range of loading conditions for which the Pickett effect is observed. However, for larger applied creep

forces with higher creep displacement and probabilities, we see that the Pickett effect is still observed.

Together these results demonstrate the importance of energy barriers and the nanoscale dimensions of pores within materials that exhibit the Pickett effect. The nanoscale size of these pores leads to higher underlying energy barriers that exhibit excess strain due to drying creep. From our simulations, we see that the systems with a drying force would be expected to exhibit accelerated creep due to a disproportionate tilt of the underlying energy landscape that results from the shear thinning behavior of the fluid. As the fluid shear thins and effectively tilts the energy landscape, the walls are able to move past one another more easily, because of reduced energy barriers to motion, thereby accelerating the creep of the material beyond an additive effect.

Understanding the importance of energy barriers in this context also lends us theoretical understanding of how the system were to behave if the creep force was perpendicular to the nanochannel, while the drying force would still act along the nanochannel. In that case, the creep force would serve to compress or expand the nanochannel, which would cause an effective increase or decrease, respectively, in the energy barrier to relative plate motion²⁷⁹. Therefore, although our model does not explicitly include the cases where creep forces act perpendicular to the nanochannel, our model can adequately capture this scenario by understanding that this will only change the energy barrier to shear motion. The effect of changing the energy barrier, shown in Figure 6, qualitatively explains how the results would be different in the presence of a perpendicular component of stress.

The more interesting result of our model is that this increase in the drying creep displacement compared to the creep and drying displacement summation is clearly nonlinear as a function of both creep force and drying force. It is important to note that even though we consider

drying forces in both directions and assume them to be equally likely, their net effect does not cancel out because of the exponential terms in our model. This net effect is the reason we observe the distinct non-linearity. Additionally, the results shown in Figure 6 suggest that, for larger energy barriers, these non-linearity effects are even more pronounced. In this context, these results suggest that characterizing the activation energy of key interfacial sliding mechanisms that govern creep deformation may be an important factor in describing the degree of the Pickett effect. Specifically, greater confinement and also more strongly hydrophilic interfaces should lead to rougher landscapes that accentuate the Pickett effect due to the drying force which induces shear thinning behavior of the fluid within the nanopores.

9.5 Estimation of Underlying Energy Barriers to Shear Displacement

The model developed in the previous section clearly demonstrates the importance of nanoscale energy barriers in the context of the Pickett effect. These energy barriers between the two walls dictate the relative sliding motion of the nanochannel and are ultimately related to the energy barrier governing the relative motion of the confined water molecules to move past one another under shear deformation. These barriers are further related to the molecular mobility of the water beads, whose temperature-dependent viscosity follows a simple Arrhenius relationship. The relationship, presented in Eq. (9-20) relates the measured viscosity η to the system temperature T and the underlying energy barrier E_b .

$$\eta = \eta_0 \exp \frac{E_b}{k_b T} \quad (9-20)$$

We can algebraically manipulate Eq. (9-20) to the form shown in Eq. (9-21), which clearly shows that the natural logarithm of viscosity is linearly related to the inverse of temperature;

$$\ln \eta = \frac{1}{T} \frac{E_b}{k_b} - \ln \eta_0 = a \frac{1}{T} + b \quad (9-21)$$

At low temperatures, measuring the viscosity, and thus the energy barriers from MD simulations, becomes problematic due to poor sampling. However, by measuring the viscosity of nanoconfined water at different temperatures in simulations, we can estimate the energy barrier by taking a linear fit of the natural log of viscosity versus inverse temperature curve. These data are plotted for a 4 nm width channel in Figure 9-7(A) for a number of different applied creep stresses. The plot shows a clear linear relationship between the natural log of viscosity and inverse temperature as predicted by Eq. (21). By taking a linear fit of this data, we can estimate the underlying energy barrier to shear displacement of the walls to be approximately 2.67 kcal/mol.

By itself, the estimation of this energy barrier is just a number that describes the ease with which two solid walls can move past another. Greater energy barriers get manifested in a greater resistance by the pore water to creep deformation and to sliding. However, more interesting is how the value of this energy barrier changes when we change the size of our nanochannel, or equivalently, the nanoconfinement effect.

To elucidate this issue, here we carried out additional temperature-dependent viscosity simulations for channels having widths of 3 nm, 6 nm, and 8 nm. The calculated energy barriers are plotted as a function of the channel width in Figure 9-7(B). Here, we see that the underlying energy barrier is a function of the channel width, with the energy barrier increasing with decreasing channel/pore size in a clearly non-linear fashion. This indicates that these nanochannels exhibit nanoconfinement effects; namely, as the water becomes more confined due to decreasing channel size, it becomes more difficult for the channels to slide past one another, due to increased energy barriers. For example, this nanoconfinement effect is shown in Figure 9-7(B) where we see that

the fluid in the 4 nm channel exhibits greater viscosity than the fluid in the larger 10 nm channel, as measured by a doubling of the energy barrier to flow. When examined in the context of our analytical model, these results also suggest that nanoporous solids with smaller nanopores under the same drying conditions would exhibit the Pickett effect to a varying extent as measured by the degree of non-linearity in the relationship between drying creep strain and the summation of load-induced creep strain and drying shrinkage. These differences are attributed to the relationship between nanopore size and underlying energy barriers between solid walls that are increased due to water under nanoconfinement.

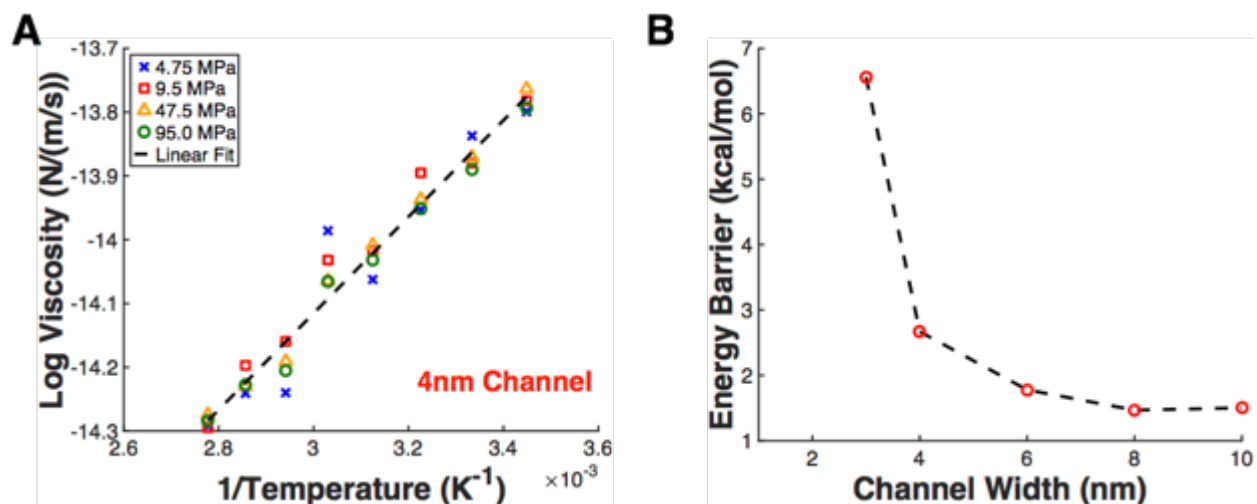


Figure 9-7: Estimating energy barrier to shear from an Arrhenius model for the temperature dependence of viscosity. (A) In order to estimate the underlying energy barrier to shear displacement of the nanochannel, we use an Arrhenius model to describe the viscosity as a function of temperature. The energy barrier is estimated by plotting the log of viscosity as a function of the inverse temperature for a range of applied creep stresses (4.75 – 95.0 MPa), as indicated by different symbols in the plot. The slope of the linear fit can be related to the underlying energy barrier by Eq. (21), with the results of a $h = 4$ nm width channel shown here. (B) The estimated energy barrier calculated using this technique as a function of channel width shows an inverse relationship between the two quantities. As the channel width decreases, the energy barrier gets larger, showing a clear nanoconfinement effect and suggesting that there are differences in the extent of the Pickett effect for materials with different pore sizes.

9.6 Comparison of Analytical Model and CGMD Simulations

To verify the results of the analytical model that describes the Pickett effect in nanoporous solids, the results of our CGMD simulations were compared directly to the analytical model derived in the previous section by CGMD simulations conducted under an applied drying creep condition while the total relative displacement velocity of the top solid wall of atoms was recorded during simulation. To compare our model to the measured creep velocity, we must develop an expression for the applied creep velocity as a function of the applied creep force and applied drying force. To determine this function, Eqs. (9-9) – (9-12) are substituted into Eq. (9-13). The final result is presented in Eq. (9-22) where A is a fitting constant that is a function of the system temperature, underlying energy barrier, and energy landscape roughness given by Eq. (9-23);

$$v_c = A \sinh\left(\frac{F_c x_b}{k_b T}\right) \cosh\left(\frac{c F_d x_b}{k_b T}\right) \quad (9-22)$$

$$A = 2x_b \omega \exp\left(\frac{-E_b}{k_b T}\right) \quad (9-23)$$

Upon simplifying this analytical function, we see the emergence of a hyperbolic sine term that is consistent with previous work on activation-energy-controlled propagation of nanocracks²⁸⁰. In both of these studies, an improvement upon Zhurkov's classical model (that solely takes into account the rate of forward motion) is provided. Using this analytical function, the simulation data can be directly fitted to our model (using the fitting parameters A , x_b , and c) to predict the creep velocity as a function of the applied creep force. After obtaining the fitting parameters A , c , and x_b , and using a least-squares regression, we estimate the underlying energy barrier to be $E_b = 2.04$ kcal/mol, which is in relatively good agreement with our prediction from the temperature-dependent viscosity simulations (2.67 kcal/mol). A plot comparing the simulation results and model prediction is presented in Figure 9-8(A). It demonstrates good agreement between the

simulations and our model, with a coefficient of determination of $r^2 = 0.98$ for the case of $F_d/F_c = 0.75$. A more detailed explanation of our calculation of the coefficient of the determination is included in the Supplemental Information. Although not shown, we have also found good agreement between the simulation and the model for values of F_d/F_c ranging from 0.01 to 0.75. The agreement between simulations and our model suggests that the drying creep behavior of a nanopore is clearly a non-linear function of the applied creep force – something that has been commonly neglected when considering drying creep and the Pickett effect.

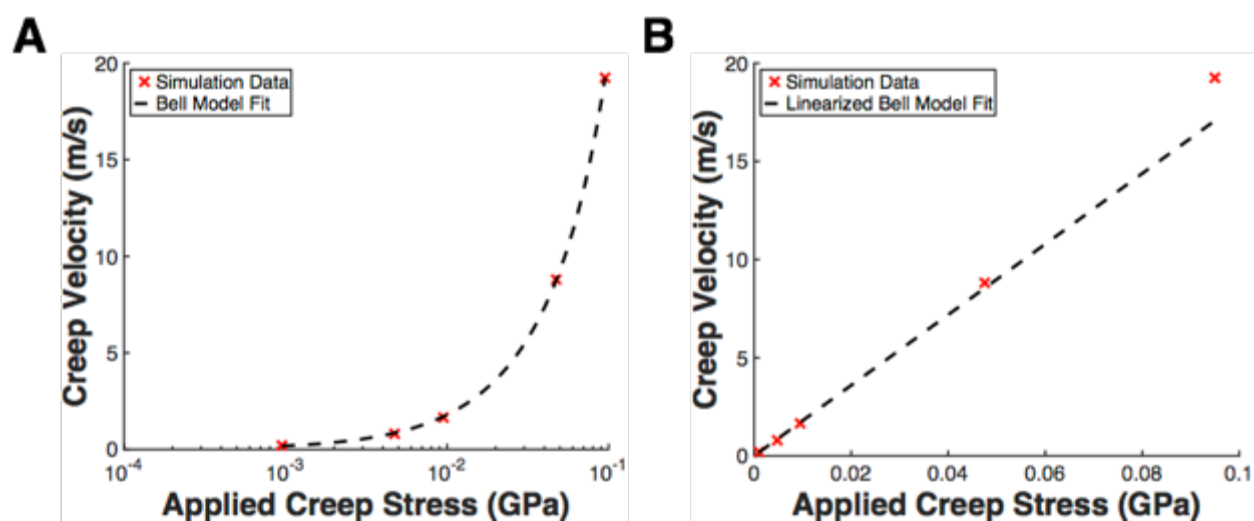


Figure 9-8: Comparison of simulation results with analytical model. (A) Using the function derived from Bell's model for the creep velocity as a function of applied creep force/stress in Eq. (22), we fit the CGMD simulation data using least-squares regression techniques. The model and simulation show good agreement and have a coefficient of determination of $r^2 = 0.99$. (B) Using a Taylor series expansion of our analytical model around $F_c = 0$, we derive a linear approximation of the model and fit it to the simulation data. Although our model and simulation data suggest clear non-linear behavior, the linear approximation still fits quite well with the simulation data ($r^2 = 0.94$). This suggests that assuming a linear relationship between applied creep and drying creep velocity (or equivalently drying creep strain) might be adequate for most practical applications.

Although there may be other models that fit the data, ours provides an exceptionally good fit while also having the advantage that our fitting parameters are all physically informed and could

be directly extracted from actual experiments or additional simulations. Further, although we only use statistical fitting to obtain values of these parameters in this work, it is promising that their calibrated values are realistic. The parameter x_b is related to the surface roughness of the solid wall, A is related primarily to the underlying energy barrier against relative shear displacement, as well as to the surface roughness of the channel, and c is related to the shear transfer capability of the fluid and the associated slip length governed by the specific solid-liquid interaction. It should be noted that the fitting parameters for the energy barrier E_b and surface roughness x_b (2.04 kcal/mol and 7.88 Å) are in good agreement with the energy barrier measured from the temperature-dependent viscosity of the water beads (2.67 kcal/mol) and the FCC lattice parameter used in system generation that defines the solid wall's surface roughness (8.33 Å). Although we have not directly measured the parameter c (fit value of 1.32), this parameter could be obtained from experiments in the future that measure the slip length or drag force/coefficient of a specific solid-liquid interface. The physical basis for these fitting parameters, coupled with the high correlation coefficient ($r^2 = 0.98$) of the analytical model, and the fact that the calibrated values of those parameters are realistic, verifies that our model can explain the non-linear relation between the applied creep force and the magnitude of drying creep.

Traditionally, scientists and engineers working on materials that exhibit a Pickett effect have assumed that there exists an approximately linear relationship between the drying creep magnitude and the applied creep force²⁸¹. Although we have demonstrated clear non-linearities associated with drying creep, it is of interest to assess the validity of this linearity assumption (i.e., the drying creep strain and velocity being a linear function of the applied creep force). Beyond these conventional assumptions, the functional form of the model given by Eq. (9-22) itself suggests a range for which this linear relationship between applied creep force and the drying creep

strain would be observed. This linear behavior is also anticipated because of the presence of the hyperbolic sine term and the fact that $\sinh(x) \approx x$ for $x \ll 1$. In Eq. (9-22), the argument of the hyperbolic sine function is $F_c x_b / k_b T$. Therefore, we expect that for small values of F_c , and a constant drying force F_d , there should be an approximately linear relationship between the drying creep strain (or relative displacement) and the applied creep force.

To mathematically assess this assumption, we linearize our analytical model by taking a Taylor series expansion around $F_c = 0$ of the analytical function given by Eq. (9-22). The first derivative of Eq. (9-22) is given by Eq. (9-24) below, in which we define $q = x_b / k_b T$ as a collection of constants, for simplicity. The Taylor series expansion and linearization of our model is then shown in Eq. (9-25);

$$f'(F_c) = \frac{x_b}{2} \exp \frac{-E_b}{k_b T} [crq \sinh qF_c \sinh cqF_d + q \cosh qF_c \cosh cqF_d] \quad (9-24)$$

$$f(F_c) \approx f(0) + f'(0)F_c \approx \frac{x_b}{2} \exp \frac{-E_b}{k_b T} qF_c = A \frac{x_b}{k_b T} F_c \quad (9-25)$$

Using the values of A and x_b calculated from our previous least squares regression, we plot this linear fit against the simulation data in Figure 9-8(B). This linear fit is calculated to have a coefficient of determination of $r^2 = 0.94$ over the entire range of creep forces applied to the top solid wall. Despite the r^2 value being lower than that for the non-linear model in Eq. (9-22), this value is still quite high and indicates that the linear fit still agrees well with the simulation data. However, upon visual inspection, as well as a detailed look at the residuals between the model and simulation data, we see that it neglects the non-linearity created by shear thinning of nanoconfined water for high values of the creep stress. However, for low values of the creep stress applied to the pore walls ($\sim 20 - 50$ MPa), this linearization fits quite well with the simulation data and indicates that a linear relationship is appropriate for a certain range of loading conditions.

Even though the linear model does not fully account for nanoscale behaviors, we can conclude that this commonly used linear approximation is adequate for most practical applications. We believe that the range of the creep stresses applied to the pore walls for which the linearization is applicable (less than or equal to ~ 20 MPa) is on the same order of magnitude of internal shear stresses in real nanoporous solids, and that it is well below the failure strength of pore wall materials (e.g. $\sim 0.8 - 2.0$ GPa for both C-S-H²⁸² and nanocrystalline cellulose¹⁵). Additionally, the linearization is found to be applicable for drying pressures ranging from $\sim 10 - 100$ MPa, which are also representative of real nanoporous solid materials²⁸³. Therefore, our study not only elucidates the clear role of underlying nanoscale energy barriers in drying creep, for the first time, but also agrees with the conventionally employed linearity in the small creep stress regime.

9.7 Effect of Transverse Microprestress on Pure Creep Behavior

While we have provided a fundamental explanation of the Pickett effect for the first time using nanoscale simulations, this model does not consider the influence of transverse microprestress. This transverse microprestress, σ_t , developed within the solid layers is explained by the microprestress-solidification theory for concrete²⁴³⁻²⁴⁴, and can easily be extended to other nanoporous solid materials. Due to the small size of the nanopores, the full thickness of the adsorption layer for water molecules cannot develop completely. This “hindered adsorption” of water molecules therefore exerts some disjoining pressure on the pore walls and results in this so-called transverse microprestress. It is important to note that this transverse microprestress cannot be changed by changing the internal load, but rather is an internally developed material property that is only changed when the local chemical environment of the sample is changed through drying, temperature, or the hydration process. Rather than hold the nanochannel spacing constant and overfill or underfill the nanochannel to develop a reactionary transverse microprestress, we

simulate this transverse force by applying individual forces to all solid beads in the top layer normal to the direction of pore displacement. In our model, the net transverse microprestress, or alternatively transverse force F_t , is the sum of the individual transverse forces applied to each atom in the top layer, f_{it} , normalized by the cross-sectional area of the solid layer along the width and is given by Eq. (9-26).

$$\sigma_t = \frac{F_t}{A_t} = \frac{\sum_i f_{it}}{A_t} \quad (9-26)$$

Taking into account the existence of this transverse microprestress by applying individual forces to the beads in the top layer in the z -direction (see Figure 9-2), the first set of simulations we conduct are for the case of pure creep in which no external drying pressure/force is applied to the interlayer water beads (i.e., $f_{id} = 0$). These simulations are used to understand the effect of the transverse microprestress on the relative motion of the solid pore walls without considering the influence of drying. The results of our simulations are summarized in Figure 9-9 which show the creep velocity (i.e. measured velocity of the top solid layer) in panel A and the effective viscosity of the water interlayer in panel B, as a function of the applied creep force. Results are shown for both tensile and compressive transverse microprestress ranging from 0 to 50 MPa with the tensile cases shown in blue and the compressive cases shown in red. For comparison, results from our previous study and the case of $\sigma_t = 0$ are shown in black in both panels.

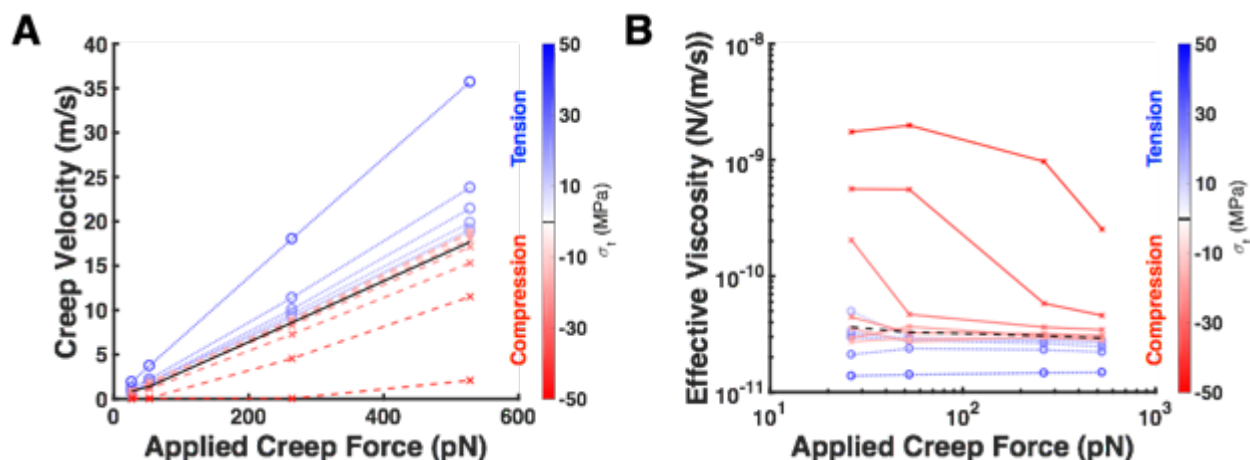


Figure 9-9: Effect of transverse microprestress on pure creep behavior. (A) Measured velocity of the top solid plate from simulation as a function of both the applied creep force and the transverse microprestress σ_t in tension (blue, dotted lines with circle markers) or compression (red, dashed lines with cross markers). A tensile microprestress accelerates the creep velocity of the solid layers while a compressive microprestress decreases the creep velocity. (B) Effective viscosity measured as the ratio of the applied creep force to the velocity of the top plate ($\eta = F_c/v_c$). For all transverse loadings, the water interlayer exhibits shear thinning behavior as the applied creep force increases. A tensile microprestress reduces the effective viscosity of the water interlayer while a compressive microprestress increases this viscosity. Each data point is obtained by averaging the system output over 1.5 ns of simulation.

For a given applied creep force, we note that a compressive microprestress decreases the creep velocity, while a tensile microprestress increases the creep velocity. These changes in the creep velocity are coupled with changes in the effective viscosity of the water interlayer where compressive microprestress increases the viscosity of the fluid and a tensile microprestress decreases the viscosity of the fluid. In compression, the transverse microprestress serves to reduce the width of the nanopore ($\sim -4.7\%$ for $\sigma_t = -50$ MPa) and increases the degree of confinement between particles – thereby increasing the viscosity of the fluid. On the other hand, a tensile microprestress increases the width of the nanopore ($\sim 9.5\%$ for $\sigma_t = 50$ MPa) which effectively reduces the viscosity of the water beads as it allows for increased mobility between particles. The

water beads in our simulation exhibit clear compressibility on the order of $\sim 9.4 \times 10^{-10} \text{ Pa}^{-1}$ which is in line with the bulk compressibility of water of $4.4 \times 10^{-10} \text{ Pa}^{-1}$ at 300 K²⁸⁴.

9.8 Modification of Analytical Model for Pure Creep and Calculation of Underlying Energy Barriers

In sections 9.3–9.6, we developed an analytical model to describe the deformation of nanopores under creep or drying creep conditions as the successive “hopping” of underlying energy barriers at the nanoscale. Each of these hopping events corresponds to the breaking and reformation of molecular interactions that serve to resist deformation of the solid layers. While simple thermal fluctuations may cause the solid layers to move relative to one another and overcome these inherent energy barriers, the key driving force is external forces, such as the applied creep force, that effectively tilt the energy landscape and encourage successive hopping events that lead to macroscale deformation of the material. While we have shown this model to work well to explain simulation results, this model does not consider the magnitude of the transverse microstress applied to the system, so we must determine the impact of transverse microstress – specifically the effect of transverse microstress on the underlying energy barriers to sliding motion of the nanopores.

Intuitively, a compressive microstress should increase the energy barrier to sliding motion as the water particles are more compressed. A tensile microstress should have the opposite effects. To verify these assumptions and better understand the effect of microstress on nanoscale energy barriers, we conduct a set of simulations to quantify these underlying energy barriers. The energy barrier to sliding motion is closely related to the molecular mobility (i.e. diffusivity and viscosity) of water beads that governs how they move past one another under some external deformation. To quantify the molecular mobility on confined water molecules and

compute the associated effective energy barrier to molecular rearrangements, we simulate the temperature-dependent viscosity of the water interlayer for temperatures ranging for $T = 280\text{ K}$ to $T = 370\text{ K}$ and utilize the Arrhenius relationship between viscosity and temperature described in Section 9.5 and Eq. (9-20) and (9-21).

The results of these simulations as well as the linear fit are shown in Figure 9-10(A) for a compressive microprestress and in Figure 9-10(B) for a tensile microprestress. Figure 9-10(C) summarizes these results by plotting the calculated underlying energy barrier ($E_b = ak_b$) as a function of the transverse microprestress. As expected, the energy barrier to shear deformation is increased for a compressive microprestress as it serves to decrease the relative mobility of the particles. A tensile microprestress decreases the energy barrier due to increases in particle mobility. Further, we find that there exists an exponential relationship between the transverse microprestress and the additional contribution to the underlying energy barrier, E_{ba} , of the form given by Eq. (9-27) where σ_t is the transverse microprestress and c_1 and c_2 are fitting constants. Based on the form of Eq. (9-27), if there is a tensile microprestress ($\sigma_t > 0$) the contribution is negative but if there is a compressive microprestress ($\sigma_t < 0$) the contribution is positive.

$$E_{ba}(\sigma_t) = c_1(\exp(-c_2\sigma_t) - 1) \quad (9-27)$$

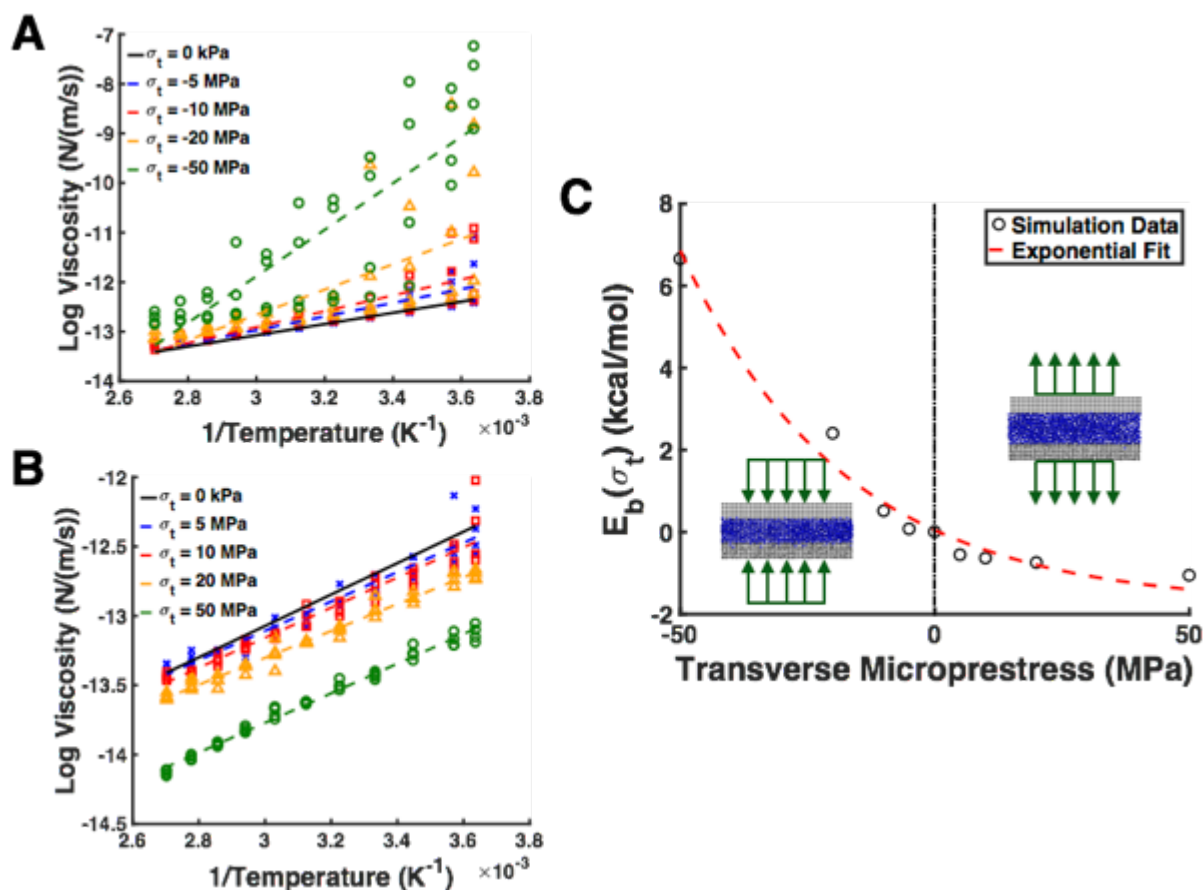


Figure 9-10: Transverse microstress changes the underlying energy barrier to shear displacement. Effective viscosity of the water interlayer as a function of temperature for (A) compressive microstress and (B) tensile microstress. Each different color and symbol type represent a different magnitude of the microstress, while the black lines reference the case of no microstress. Assuming an Arrhenius viscosity-temperature relationship, we determine the activation energy barrier by taking a linear fit of our simulation data. The energy barrier, $E_b = ak_b$ where a is the slope of the linear fit and k_b is Boltzmann's constant. (C) Added activation energy barrier as a function of microstress shows that there is an exponential relationship between the added activation energy barrier and the microstress.

Physically, these fitting constants are related to the compressibility of the fluid and the strength of intermolecular interactions that govern molecular mobility (i.e. viscosity). After quantifying the effect of transverse microstress on the underlying energy barrier, we propose a simple modification to our existing analytical model that predicts the creep behavior of nanoporous

solids. To account for the transverse microstress, an additional energy barrier component must be added to the numerator of Eq. (9-7) that describes how the energy barrier changes as a function of the transverse microstress. Assuming this function to be a simple exponential as suggested by Figure 9-10(C), we propose the following modification given by Eq. (9-28) that considers the presence of some transverse microstress in our system.

$$\begin{aligned}
 p_t &= \exp\left(-\frac{E_b + E_{ba}(\sigma_t) - F_c x_b}{k_b T}\right) - \exp\left(-\frac{E_b + E_{ba}(\sigma_t) + F_c x_b}{k_b T}\right) \\
 &= \exp\left(-\frac{E_b + c_1(\exp(-c_2 \sigma_t) - 1) - F_c x_b}{k_b T}\right) \\
 &\quad - \exp\left(-\frac{E_b + c_1(\exp(-c_2 \sigma_t) - 1) + F_c x_b}{k_b T}\right)
 \end{aligned} \tag{9-28}$$

Here, we note that when $\sigma_t = 0$, we recover the initial form of our model with an underlying energy barrier to shear displacement of E_b . To evaluate this modification to our model, we use the calculated energy barriers from our simulations to plot the predicted creep displacement as a function of creep force shown in Figure 9-11(A). Qualitatively, we see that the trends of the analytical model in Figure 9-11(A) agree quite well with our simulation data presented in Figure 9-9(A). However, a more quantitative comparison is desired. Here, we define a ratio between the probability of shear displacement in the case of no transverse microstress, p_{pc} , (for which our model has been shown to work well in our previous study) to the case of transverse microstress included here, p_t . Taking the ratio of these two quantities, we find the following relationship given by Eq. (9-29)

$$\frac{p_{pc}}{p_t} = \frac{v_{pc}}{v_t} = A_0 \exp\left(\frac{E_{ba}(\sigma_t)}{k_b T}\right) \tag{9-29}$$

where $E_b(\sigma_t)$ is the additional energy barrier contribution introduced by the transverse microprestress given by Eq. (9-27) and A_0 is a fitting constant. Physically, A_0 indicates how the distance between energy barriers x_b changes with transverse microprestress. Although the surface roughness of the solid layers largely governs this parameter, changing the density of the water interlayer can also change the energy landscape to shear displacement.

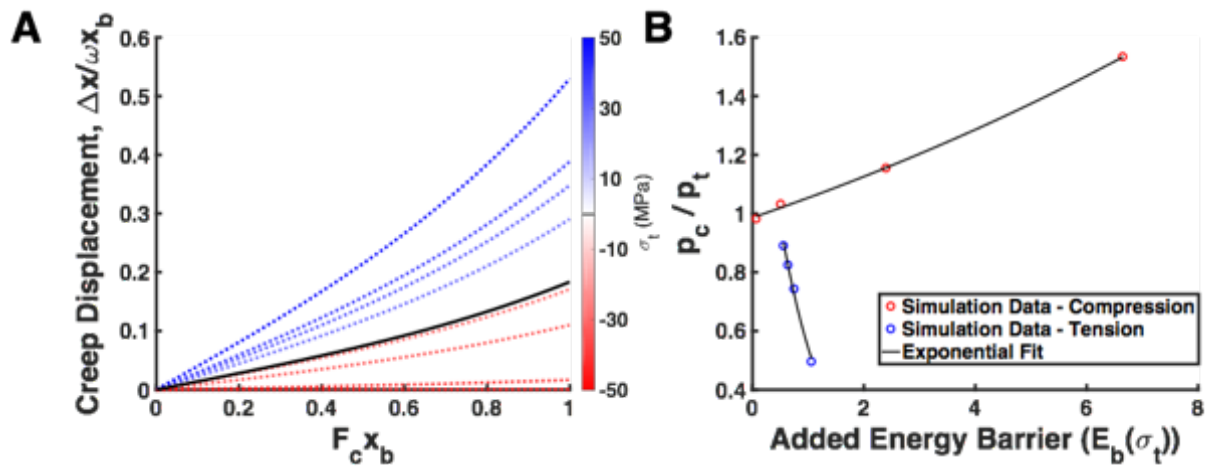


Figure 9-11: Modification of analytical model and comparison to CGMD simulations. (A) Using the analytical model described in the text and in our previous study, we predict similar trends to those obtained from CGMD simulations (Figure 9-9). Increasing the energy barrier (red curves) serves to decrease creep displacement while decreasing the energy barrier (blue curves) serves to increase creep displacement. (B) Ratio of the probability of creep displacement under no transverse microprestress (p_c) to that of the creep displacement with a transverse microprestress (p_t). Simulation data is shown as colored points (red – compression, blue – tension) and the black lines are the predicted exponential fit.

Using our simulation data, we plot this ratio for both tensile and compressive transverse microprestress as shown in Figure 9-11(B). An exponential fit is shown in addition to the simulation data and shows good agreement between our simulation data and model prediction. For a compressive microprestress, we note the value of A_0 is close to 1, indicating the distance between energy barriers does not change. However, for a tensile microprestress, A_0 has a value greater than

one, indicating the distance between energy barriers is decreased due to the increased mobility of water molecules. This quantitative evidence helps justify the simple addition to our model that under pure creep conditions a transverse microprestress serves to effectively change the underlying shear energy barrier to slip deformation of nanopores.

9.9 Effect of Transverse Microprestress on Drying Creep Behavior

Our initial simulations of pure creep behavior provided insight into the nanoscale effects of transverse microprestress and how it changes the underlying energy barriers to shear deformation. However, of more importance to understanding these forces in the context of the Pickett effect are simulations that consider drying creep behavior of the nanopore in which the creep force applied to the top solid layer is coupled with external forces applied to the water interlayer. While the drying force is independent of the applied creep force, we define the ratio $r = F_d/F_c$ in our simulations to characterize the relative magnitude of these two forces and determine how this influences the drying creep behavior. Our simulations consider the cases of $r = 0.25, 0.50,$ and 0.75 . Figure 9-12 shows the creep velocity as a function of the transverse microprestress for each of the different drying conditions separated by compressive microprestress (panel A) and tensile microprestress (panel B).

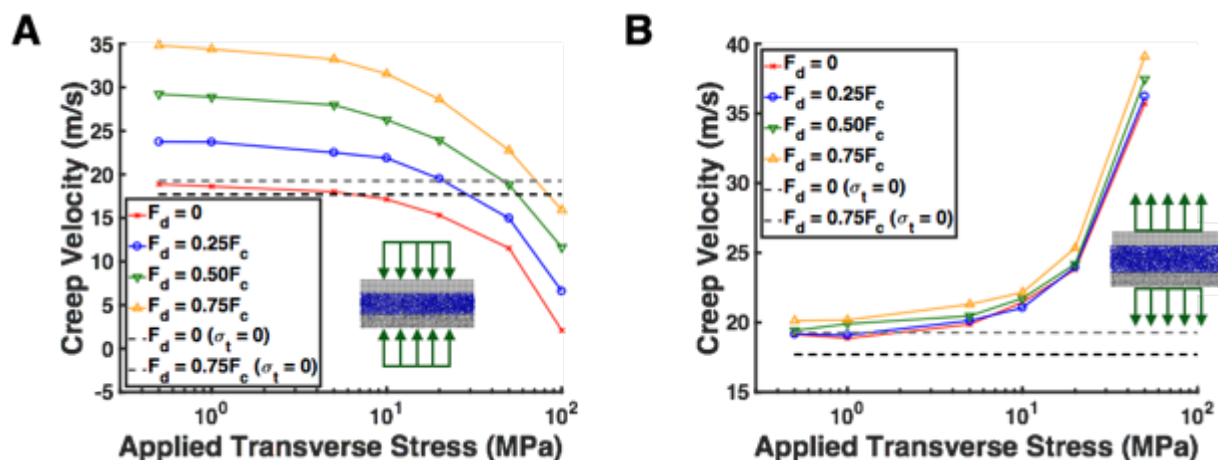


Figure 9-12: Effect of transverse microstress on drying creep behavior. Creep velocity as a function of the applied transverse microstress σ_t for (A) compressive microstress and (B) tensile microstress. Colored lines and symbols represent different magnitudes of the drying force F_d (given in terms of a fraction of the creep force F_c) while the black and grey lines correspond to cases of no microstress. For a compressive microstress, increasing the drying force F_d significantly accelerates motion of the nanopore. Nanopores subject to a tensile microstress only exhibit a slight increase in motion as the drying force is increased.

Figure 9-12 reveals a few interesting trends. First, we note that increasing the magnitude of the drying force applied to the water beads serves to accelerate the creep behavior independent of the direction (i.e. tension or compression) of the microstress. This parallels the results of our previous study that showed increasing the drying force in the absence of any microstress also accelerates the creep behavior as increased motion of the water interlayer encourages additional sliding displacement of the top solid layer. However, the key difference between tension and compression is the degree to which the creep behavior is accelerated by increasing the drying force. As the drying force is increased from $F_d = 0$ to $F_d = 0.75F_c$ (the largest drying force examined in this study), the creep is accelerated by $\sim 84\%$ in the case of compressive microstress but only by $\sim 7.9\%$ in the case of tensile microstress. This behavior is more clearly illustrated in Figure 9-13(A), which shows the creep velocity as a function of an applied creep force and an applied

transverse microstress. Here, the difference between pure creep (red curves) and the highest drying rate (golden curves) is significantly larger for a compressive microstress compared to the tensile microstress.

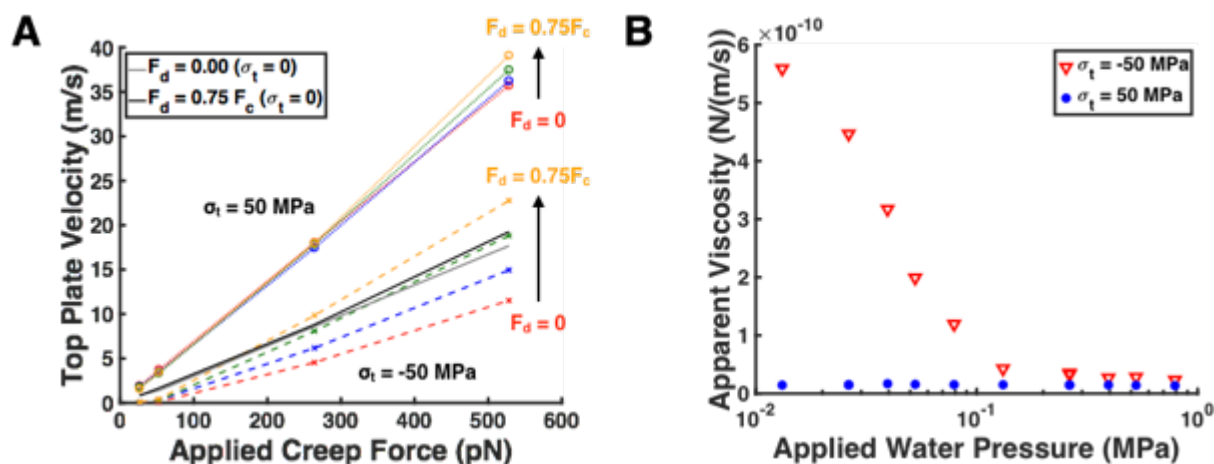


Figure 9-13: Differences in effects of transverse microstress with increasing drying force for tension and compression. (A) The top plate velocity of the nanopore increases with increasing water force. If the magnitude of the drying force is large enough, even nanopores with a compressive microstress can exhibit accelerated creep compared to the case of no microstress. Different color lines indicate different magnitude of the drying force. (B) The effective viscosity of the water interlayer exhibits significant shear thinning behavior for a compressive microstress (red lines) and little to no change for a tensile microstress (blue lines). These results help explain the trends observed in panel (A).

An explanation for this behavior is provided by Figure 9-13(B) which shows the effective viscosity of the water interlayer as a function of drying force for transverse compression (red) and tension (blue). In tension, the viscosity of the fluid does not change significantly with the drying force and only exhibits slight shear thinning behavior (less than an order of magnitude). In contrast, under compression, the water interlayer exhibits significant shear thinning behavior of almost a full order of magnitude with increasing drying force. This quantitatively large shear thinning behavior explains why for a system at constant compressive microstress, creep is significantly

accelerated with increasing drying force. These differences in the shear thinning behavior for different directions of the transverse microstress help explain the clear differences exhibited in Figure 9-13(A). It is also interesting to note that for a high compressive microstress and high drying force, the creep velocity exceeds that of the system under no microstress, indicating that the microstress can cause increased creep under the appropriate drying conditions. Physically, although the activation energy barrier to shearing is higher under compression, motion of the water interlayer during drying effectively tilts the energy landscape such that the effective energy barrier is lowered.

The results presented here for the cases of drying creep help provide a more comprehensive understanding of the Pickett effect and further validate some of the existing micromechanical theories. First, our results confirm that the intensity of the Pickett effect (i.e. the magnitude of drying creep) depends on the magnitude of the transverse microstress, which is usually compressive in real systems as described by the microstress-solidification theory. Based on our results, we find that higher compression leads to a milder Pickett effect and as the compression is decreased, creep is accelerated in a non-linear fashion. In real systems, the transverse microstress is relaxed (i.e. decreased) due to drying and a change of the relative humidity within nanopores. As the microstress is relaxed, the viscosity of the fluid interlayer is decreased (see Figure 9-9(B)) and shearing effects become more energetically favorable – thereby increasing the creep rate. Therefore, our simulations verify that as the system dries and the compressive microstress is relaxed, creep is accelerated and a stronger Pickett effect is observed – thereby confirming the assumed mechanisms of the Pickett effect proposed by existing micromechanical theories.

9.10 Modification of Analytical Model for Drying Creep

We have shown that our model can be easily modified for the case of pure creep to capture the effects of changing transverse microprestress. Here we discuss modifications that must be considered for the case of drying creep with an applied transverse microprestress. Like the case of pure creep, we know that for drying creep, the transverse microprestress serves to change the underlying energy barrier to shear deformation of the nanopore. However, it is unclear whether it has effects on other physical parameters within our model. In addition to changing the underlying energy barrier, the transverse microprestress also significantly changes the viscosity of the water interlayer. Due to this change in viscosity, the force imparted on the top solid layer by the water interlayer may also change. This material property, captured in our model through some shear transfer capability constant c , was assumed constant in our previous work. However, here, the extent of shear thinning behavior with increasing drying force is more pronounced and changes by over an order of magnitude (see Figure 9-13(B)). We hypothesize instead that this value should change depending on the transverse loading condition (tension or compression) as well as with the magnitude of the drying force. Therefore, our modified model describes the drying creep displacement under an applied transverse stress σ_t as:

$$\Delta x_{dct} = B \sinh\left(\frac{F_c x_{bdct}}{k_b T}\right) \cosh\left(\frac{c(\sigma_t, F_d) F_d x_{bdct}}{k_b T}\right) \quad (9-30)$$

$$B = 2x_b \omega \exp\left(-\frac{E_b + E_{ba}(\sigma_t)}{k_b T}\right) \quad (9-31)$$

To verify our hypothesis that the shear transfer coefficient changes in addition to the underlying energy barrier, we calculate the ratio of the displacements of drying creep with no transverse stress to that with an applied transverse stress. This ratio, $\Delta x_{dc}/\Delta x_{dct}$, is given by Eq. (9-32)

$$\frac{\Delta x_{dc}}{\Delta x_{dct}} = B_0 \exp\left(\frac{E_{ba}(\sigma_t)}{k_b T}\right) \quad (9-32)$$

where B_0 is a fitting constant that describes differences between the cases of drying creep with no microprestress compared to a finite value of this stress. The exact value of B_0 depends on the shear transfer capability and the distance between energy barriers for the two cases. Based on Eq. (9-32) we predict an exponential relationship for the ratio of creep displacements for these two cases. The ratios for these cases calculated from our simulations are presented in Figure 9-14(A) for a compressive microprestress and Figure 9-14(B) for a tensile microprestress. For the case of compression, we see clear differences for each of the different values of the drying force. Notably, when fitting the simulation data with an exponential fit, we find that the scaling constant in front of the exponential term decreases with increasing drying force. This suggests that the shear transfer coefficient increases with the drying force (~20% based on fitting parameters). For the case of tension on the other hand, the scaling constant in front of the exponential fitting equation remains essentially unchanged with increasing drying force.

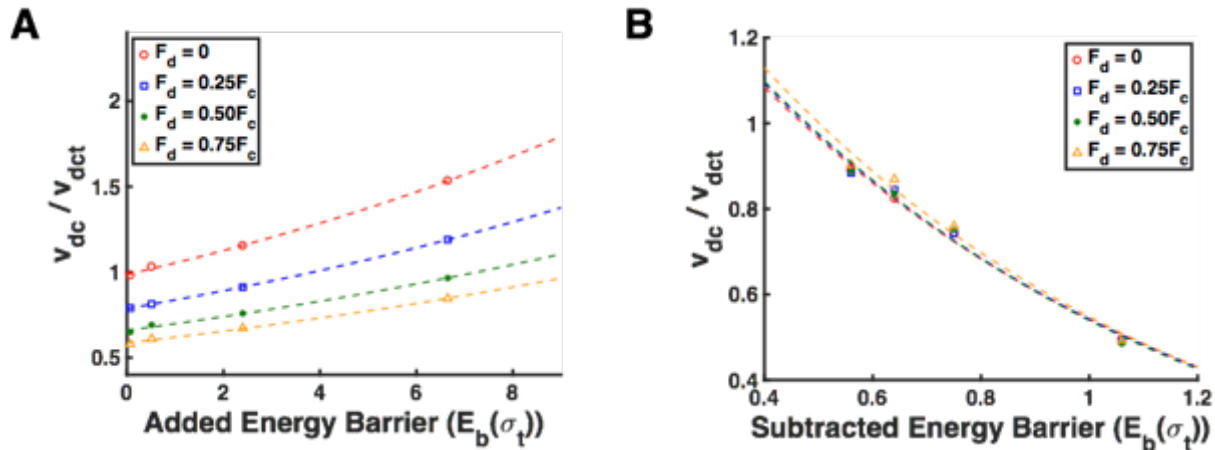


Figure 9-14: Modification of existing analytical model of drying creep. Our modification for Bell's model presented in the text considers the added (compressive microprestress) or subtracted (tensile microprestress) energy barrier to shear displacement. Here we present the ratio of the top plate velocity under no microprestress (v_{dc}) to that under microprestress (v_{dct}) for (A) compression and (B) tension. We find that the predicted exponential relationship between this ratio and the added or subtracted energy contribution to the shear activation energy barrier agrees well with our simulation data.

Although the constant B_0 contains contributions from both the distance between energy barriers and the shear transfer coefficient, we can deconvolute these effects based on the results of pure creep simulations. For pure creep under compression, we know that distance between energy barriers is unchanged (i.e. $x_{bdc} = x_{bdct}$). Therefore, B_0 is solely a measure of how the shear transfer capability of the water interlayer changes. Based on the fitting of our simulation data, we find that the shear transfer capability increases with increasing water force. Under compression, low drying forces cause the water beads to impart a low amount of their momentum to the top solid layer due to their decreased mobility. As the drying pressure is increased, the mobility of the water particles also increases – thereby enhancing the shear transfer capability.

The case of tensile transverse microprestress is a bit more involved. From the cases of drying creep, our model predicts that the distance between energy barriers decreases and B_0 should

have a value greater than 1. If there was any change in the shear transfer capability of the fluid, then the value of B_0 should change with the drying force. However, we find that this fitting constant does not change appreciably as evidenced by the curves shown in Figure 7B, thereby indicating the shear transfer capability does not change with drying force. This can be explained by the fact that the mobility of water molecules is high under a transverse tensile stress and increasing the applied pressure does not greatly enhance the mobility of water molecules.

Our simulation data also supports these conclusions. Figure 9-15 shows the mean water velocity of the interlayer plotted as a function of the applied water pressure. For a tensile microprestress, we find that the water velocity increases only slightly with increasing drying force as the mobility is not enhanced. However, for a compressive microprestress, increasing the drying force increases the water velocity significantly as the mobility of particles in the interlayer is increased and consequently transfers more force to the top solid layer – thereby accelerating creep. Despite the differences in physical mechanisms, we show that our existing analytical model can be easily modified to describe the drying creep behavior of nanopores with an applied transverse microprestress - for both tensile and compressive stresses.

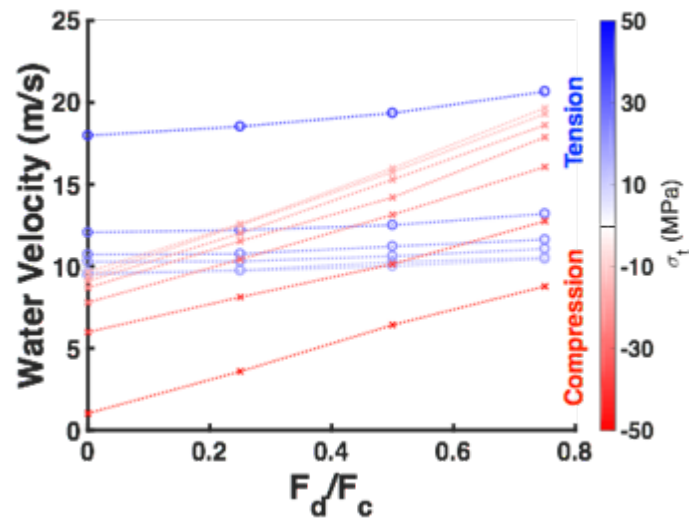


Figure 9-15: Water interlayer velocity as a function of drying force. Average velocity of the water interlayer is extracted from simulation and plotted against the magnitude of the drying force applied. Results here are shown for a constant creep force of 528 pN. Each curve corresponds to a different value of the transverse microstress and are colored by their magnitude (light colors are low magnitude and dark colors are high magnitude) and direction (blue for tension and red for compression). For a compressive microstress, we find that increasing the drying force increases the water velocity which promotes greater momentum transfer to the solid upper layer that accelerates creep. For a tensile microstress, there is a weak linear relationship, helping to explain that mobility is not significantly change and there is only a slight acceleration of creep with increasing drying force.

Chapter 10 – Conclusions and Outlook

Throughout this dissertation, I have described a novel computational materials-by-design approach for the development of cellulose-based nanocomposites. After identifying current shortcomings in these materials at the start of my time as a graduate student, we have identified strategies and methods towards improving their material performance – specifically their thermomechanical properties – throughout the entirety of my graduate work. Our approach has systematically advanced through the computational materials-by-design process by first focusing on materials discovery, moving on to materials development, and finally focusing on property optimization. Our research has clearly identified the benefits of this computational approach including a high capacity for iteration and the development of new computational methods and approaches to accelerate the materials-by-design process. Through collaborations with experimental researchers, we have further verified the results of our models and produced tangible materials that have begun to improve the properties of these CNC-based nanocomposites. In the following paragraphs, I will provide a summary of the major contributions from each study.

In materials discovery, we utilized this approach to reveal interesting underlying mechanofunctionality of CNCs. By simulating the fracture behavior of individual CNCs, we revealed the importance of underlying molecular interactions that give rise to the impressive mechanical properties (elastic modulus and strength) of these biomolecules. Further, we have illustrated key size-dependent fracture behavior of these materials and developed theoretical models to explain the scaling of these mechanical properties with crystal size. Ultimately, this work demonstrated the utility of molecular simulation in exploring biomaterials and illuminating natural design principles, herein related to the reason CNCs themselves are nanoscale in size in natural systems. Keeping with materials discovery, we then shifted to probing the interfacial

traction-separation behavior of CNC-CNC interfaces, as well as investigating the response of these interfaces moisture. These simulations allowed us to simulate material behaviors that are very difficult to probe experimentally, and have provided fundamental insight into the interfacial behaviors of CNCs that govern hierarchical material performance.

With an understanding of unmodified CNCs as a promising biomolecule to be incorporated into polymer nanocomposites, our focus then shifted towards materials development. Here, we primarily focused on two methods towards improving the performance of polymer nanocomposites – chemical surface modification and polymer grafting. After building models of the specific chemical surface modifications of interest, simulations have revealed how these surface modifications can be used to effectively change the water adsorption behavior and interfacial mechanics of CNCs. Through these simulations, we have been able to provide a molecular level explanation for the observed experimental trends and further developed a methodology that can be used to rapidly evaluate new surface modifications in the future. Moving beyond chemical modifications, we investigated the effects of directly grafting polymers to the surface of CNCs. By studying the relaxation dynamics of polymer chains, we have shown how polymer grafts can effectively change interfaces within the matrix and alter nanoconfinement effects while further providing additional compatibility between the nanofiller and matrix.

Finally, my work shifted towards further optimizing the properties of CNC-nanocomposites through the development of predictive multiscale models. We began by developing multiscale models that link nanoscale quantities obtained directly from simulation (i.e. interfacial adhesion energy) to macroscale material properties (filler dispersion and glass transition temperature). In the future, these tools can be used by experimentalists to reduce the amount of “trial and error” experiments needed to create materials with optimized properties. Rather they can

utilize models such as these in a predictive fashion to determine what system parameters are worth exploring more directly through experiments. Finally, we utilized nanoscale simulations to explain a longstanding phenomenon of nanoporous solids, thus highlighting the importance of considering nanoscale effects in the design of materials and the broad transferability of our approach.

Throughout the course of my graduate work I have applied this computational materials-by-design approach to a single system. However, I believe its broad applicability will allow myself and other researchers to study many diverse systems in the future. Through the materials discovery process we can effectively evaluate new materials and their capability to be incorporated in new bioinspired materials. Specifically, biomolecules such as chitin, keratin, etc. could be evaluated in this framework in the hope of being incorporated into new bioinspired architectures. Materials development will allow us to develop tools to rapidly evaluate the vast design space for these new materials and beyond examining chemical surface modifications, could be used to evaluate system architecture, geometry, and size-dependence of the material systems. Finally, property optimization approaches will be especially important to the acceleration of the materials design process. By developing new and improved multiscale methods, we can utilize relatively cheap and effective nanoscale simulations to effectively predict material properties. Ultimately this computational materials-by-design approach is designed to be an effective complement to traditional experiments and theory development by replacing the need for repeated “trial and error” design. Instead, this symbiotic relationship between simulation and experiment will ultimately help achieve the goals of the Materials Genome Initiative and accelerate the materials design process and improve the overall efficiency/effectiveness of materials design.

Chapter 11 – References

1. Hashin, Z., ANALYSIS OF PROPERTIES OF FIBER COMPOSITES WITH ANISOTROPIC CONSTITUENTS. *Journal of Applied Mechanics-Transactions of the Asme* **1979**, *46* (3), 543-550.
2. Hajji, P.; Cavaille, J. Y.; Favier, V.; Gauthier, C.; Vigier, G., Tensile behavior of nanocomposites from latex and cellulose whiskers. *Polymer Composites* **1996**, *17* (4), 612-619.
3. Ohji, T.; Jeong, Y.-K.; Choa, Y.-H.; Niihara, K., Strengthening and Toughening Mechanisms of Ceramic Nanocomposites. *Journal of the American Ceramic Society* **1998**, *81* (6), 1453-1460.
4. Leary, M.; Schiavone, F.; Subic, A., Lagging for control of shape memory alloy actuator response time. *Materials & Design* **2010**, *31* (4), 2124-2128.
5. Saralegi, A.; Fernandes, S. C. M.; Alonso-Varona, A.; Palomares, T.; Foster, E. J.; Weder, C.; Eceiza, A.; Corcuera, M. A., Shape-Memory Bionanocomposites Based on Chitin Nanocrystals and Thermoplastic Polyurethane with a Highly Crystalline Soft Segment. *Biomacromolecules* **2013**, *14* (12), 4475-4482.
6. Carpi, F.; Smela, E., *Biomedical applications of electroactive polymer actuators*. John Wiley & Sons: Chichester, West Sussex, 2009; p xx, 476 p.
7. Dastjerdi, A.; Pagano, M.; Kaartinen, M.; McKee, M.; Barthelat, F., Direct Measurements of the Cohesive Behavior of Soft Biological Interfaces. In *Mechanics of Biological Systems and Materials, Volume 5*, Prorok, B. C.; Barthelat, F.; Korach, C. S.; Grande-Allen, K. J.; Lipke, E.; Lykofatitits, G.; Zavattieri, P., Eds. Springer New York: 2013; pp 207-215.
8. Wang, C.-a.; Huang, Y.; Zan, Q.; Guo, H.; Cai, S., Biomimetic structure design — a possible approach to change the brittleness of ceramics in nature. *Materials Science and Engineering: C* **2000**, *11* (1), 9-12.
9. Okubo, K.; Fujii, T.; Yamashita, N., Improvement of Interfacial Adhesion in Bamboo Polymer Composite Enhanced with Micro-Fibrillated Cellulose. *JSME International Journal Series A Solid Mechanics and Material Engineering* **2005**, *48* (4), 199-204.
10. Okubo, K.; Fujii, T.; Thostenson, E. T., Multi-scale hybrid biocomposite: Processing and mechanical characterization of bamboo fiber reinforced PLA with microfibrillated cellulose. *Composites Part a-Applied Science and Manufacturing* **2009**, *40* (4), 469-475.
11. Mushi, N. E.; Utsel, S.; Berglund, L. A., Nanostructured biocomposite films of high toughness based on native chitin nanofibers and chitosan. *Frontiers in Chemistry* **2014**, *2*, 99.
12. Egan, P.; Sinko, R.; LeDuc, P. R.; Keten, S., The role of mechanics in biological and bio-inspired systems. *Nat Commun* **2015**, *6*.
13. Jain, A.; Ong, S. P.; Hautier, G.; Chen, W.; Richards, W. D.; Dacek, S.; Cholia, S.; Gunter, D.; Skinner, D.; Ceder, G.; Persson, K. A., Commentary: The Materials Project: A materials genome approach to accelerating materials innovation. *APL Materials* **2013**, *1* (1), 011002.
14. Fratzl, P., Biomimetic materials research: what can we really learn from nature's structural materials? *Journal of the Royal Society Interface* **2007**, *4* (15), 637-642.
15. Moon, R. J.; Martini, A.; Nairn, J.; Simonsen, J.; Youngblood, J., Cellulose nanomaterials review: structure, properties and nanocomposites. *Chemical Society Reviews* **2011**, *40* (7), 3941-3994.
16. Iguchi, M.; Yamanaka, S.; Budhiono, A., Bacterial cellulose - a masterpiece of nature's arts. *Journal of Materials Science* **2000**, *35* (2), 261-270.

17. Fratzl, P.; Elbaum, R.; Burgert, I., Cellulose fibrils direct plant organ movements. *Faraday Discussions* **2008**, *139*, 275-282.
18. Goswami, L.; Dunlop, J. W. C.; Jungnikl, K.; Eder, M.; Gierlinger, N.; Coutand, C.; Jeronimidis, G.; Fratzl, P.; Burgert, I., Stress generation in the tension wood of poplar is based on the lateral swelling power of the G-layer. *Plant Journal* **2008**, *56* (4), 531-538.
19. Burgert, I.; Fratzl, P., Actuation systems in plants as prototypes for bioinspired devices. *Philosophical Transactions of the Royal Society a-Mathematical Physical and Engineering Sciences* **2009**, *367* (1893), 1541-1557.
20. Fratzl, P.; Barth, F. G., Biomaterial systems for mechanosensing and actuation. *Nature* **2009**, *462* (7272), 442-448.
21. Sinko, R.; Qin, X.; Keten, S., Interfacial mechanics of cellulose nanocrystals. *MRS Bulletin* **2015**, *40* (04), 340-348.
22. Eichhorn, S. J., Stiff as a Board: Perspectives on the Crystalline Modulus of Cellulose. *Acs Macro Letters* **2012**, *1* (11), 1237-1239.
23. Matthews, J. F.; Skopec, C. E.; Mason, P. E.; Zuccato, P.; Torget, R. W.; Sugiyama, J.; Himmel, M. E.; Brady, J. W., Computer simulation studies of microcrystalline cellulose I beta. *Carbohydrate Research* **2006**, *341* (1), 138-152.
24. Diddens, I.; Murphy, B.; Krisch, M.; Mueller, M., Anisotropic Elastic Properties of Cellulose Measured Using Inelastic X-ray Scattering. *Macromolecules* **2008**, *41* (24), 9755-9759.
25. Tanaka, F.; Iwata, T., Estimation of the elastic modulus of cellulose crystal by molecular mechanics simulation. *Cellulose* **2006**, *13* (5), 509-517.
26. Šturcová, A.; Davies, G. R.; Eichhorn, S. J., Elastic Modulus and Stress-Transfer Properties of Tunicate Cellulose Whiskers. *Biomacromolecules* **2005**, *6* (2), 1055-1061.
27. W.D. Callister, J., *Materials Science and Engineering: An Introduction*. John Wiley & Sons, Inc.: New York, 1994.
28. Jarvis, M., Chemistry: Cellulose stacks up. *Nature* **2003**, *426* (6967), 611-612.
29. Nishiyama, Y.; Johnson, G. P.; French, A. D.; Forsyth, V. T.; Langan, P., Neutron Crystallography, Molecular Dynamics, and Quantum Mechanics Studies of the Nature of Hydrogen Bonding in Cellulose I β . *Biomacromolecules* **2008**, *9* (11), 3133-3140.
30. Nishiyama, Y.; Langan, P.; Chanzy, H., Crystal structure and hydrogen-bonding system in cellulose I β from synchrotron X-ray and neutron fiber diffraction. *Journal of the American Chemical Society* **2002**, *124* (31), 9074-9082.
31. Habibi, Y.; Lucia, L. A.; Rojas, O. J., Cellulose Nanocrystals: Chemistry, Self-Assembly, and Applications. *Chemical Reviews* **2010**, *110* (6), 3479-3500.
32. Ishikawa, A.; Okano, T.; Sugiyama, J., Fine structure and tensile properties of ramie fibres in the crystalline form of cellulose I, II, III and IVI. *Polymer* **1997**, *38* (2), 463-468.
33. Li, Q.; Rennekar, S., Supramolecular Structure Characterization of Molecularly Thin Cellulose I Nanoparticles. *Biomacromolecules* **2011**, *12* (3), 650-659.
34. Eichhorn, S. J.; Davies, G. R., Modelling the crystalline deformation of native and regenerated cellulose. *Cellulose* **2006**, *13* (3), 291-307.
35. Zhao, Z.; Shklyaev, O. E.; Nili, A.; Mohamed, M. N. A.; Kubicki, J. D.; Crespi, V. H.; Zhong, L., Cellulose Microfibril Twist, Mechanics, and Implication for Cellulose Biosynthesis. *Journal of Physical Chemistry A* **2013**, *117* (12), 2580-2589.
36. Siqueira, G.; Bras, J.; Dufresne, A., Cellulosic Bionanocomposites: A Review of Preparation, Properties and Applications. *Polymers* **2010**, *2* (4), 728-765.

37. Roy, D.; Semsarilar, M.; Guthrie, J. T.; Perrier, S., Cellulose modification by polymer grafting: a review. *Chemical Society Reviews* **2009**, *38* (7), 2046-2064.
38. Siro, I.; Plackett, D., Microfibrillated cellulose and new nanocomposite materials: a review. *Cellulose* **2010**, *17* (3), 459-494.
39. Johnson, R. K.; Zink-Sharp, A.; Renneckar, S. H.; Glasser, W. G., A new bio-based nanocomposite: fibrillated TEMPO-oxidized celluloses in hydroxypropylcellulose matrix. *Cellulose* **2009**, *16* (2), 227-238.
40. Ifuku, S.; Nogi, M.; Abe, K.; Handa, K.; Nakatsubo, F.; Yano, H., Surface modification of bacterial cellulose nanofibers for property enhancement of optically transparent composites: Dependence on acetyl-group DS. *Biomacromolecules* **2007**, *8* (6), 1973-1978.
41. Lu, J.; Askeland, P.; Drzal, L. T., Surface modification of microfibrillated cellulose for epoxy composite applications. *Polymer* **2008**, *49* (5), 1285-1296.
42. Stenstad, P.; Andresen, M.; Tanem, B. S.; Stenius, P., Chemical surface modifications of microfibrillated cellulose. *Cellulose* **2008**, *15* (1), 35-45.
43. Yamanaka, S.; Ishihara, M.; Sugiyama, J., Structural modification of bacterial cellulose. *Cellulose* **2000**, *7* (3), 213-225.
44. Lasseguette, E.; Roux, D.; Nishiyama, Y., Rheological properties of microfibrillar suspension of TEMPO-oxidized pulp. *Cellulose* **2008**, *15* (3), 425-433.
45. Montanari, S.; Rountani, M.; Heux, L.; Vignon, M. R., Topochemistry of carboxylated cellulose nanocrystals resulting from TEMPO-mediated oxidation. *Macromolecules* **2005**, *38* (5), 1665-1671.
46. Saito, T.; Kimura, S.; Nishiyama, Y.; Isogai, A., Cellulose nanofibers prepared by TEMPO-mediated oxidation of native cellulose. *Biomacromolecules* **2007**, *8* (8), 2485-2491.
47. Eichhorn, S. J.; Dufresne, A.; Aranguren, M.; Marcovich, N. E.; Capadona, J. R.; Rowan, S. J.; Weder, C.; Thielemans, W.; Roman, M.; Renneckar, S.; Gindl, W.; Veigel, S.; Keckes, J.; Yano, H.; Abe, K.; Nogi, M.; Nakagaito, A. N.; Mangalam, A.; Simonsen, J.; Benight, A. S.; Bismarck, A.; Berglund, L. A.; Peijs, T., Review: current international research into cellulose nanofibres and nanocomposites. *Journal of Materials Science* **2010**, *45* (1), 1-33.
48. Nogi, M.; Iwamoto, S.; Nakagaito, A. N.; Yano, H., Optically Transparent Nanofiber Paper. *Advanced Materials* **2009**, *21* (16), 1595-+.
49. Nogi, M.; Yano, H., Transparent nanocomposites based on cellulose produced by bacteria offer potential innovation in the electronics device industry. *Advanced Materials* **2008**, *20* (10), 1849-+.
50. Okahisa, Y.; Yoshida, A.; Miyaguchi, S.; Yano, H., Optically transparent wood-cellulose nanocomposite as a base substrate for flexible organic light-emitting diode displays. *Composites Science and Technology* **2009**, *69* (11-12), 1958-1961.
51. Eichhorn, S. J., Cellulose nanowhiskers: promising materials for advanced applications. *Soft Matter* **2011**, *7* (2), 303-315.
52. Klemm, D.; Heublein, B.; Fink, H. P.; Bohn, A., Cellulose: Fascinating biopolymer and sustainable raw material. *Angewandte Chemie-International Edition* **2005**, *44* (22), 3358-3393.
53. Lee, K.-Y.; Tammelin, T.; Schultfer, K.; Kiiskinen, H.; Samela, J.; Bismarck, A., High Performance Cellulose Nanocomposites: Comparing the Reinforcing Ability of Bacterial Cellulose and Nanofibrillated Cellulose. *Acs Applied Materials & Interfaces* **2012**, *4* (8), 4078-4086.

54. Samir, M.; Alloin, F.; Paillet, M.; Dufresne, A., Tangling effect in fibrillated cellulose reinforced nanocomposites. *Macromolecules* **2004**, *37* (11), 4313-4316.
55. Alemdar, A.; Sain, M., Isolation and characterization of nanofibers from agricultural residues - Wheat straw and soy hulls. *Bioresource Technology* **2008**, *99* (6), 1664-1671.
56. Banerjee, M.; Sain, S.; Mukhopadhyay, A.; Sengupta, S.; Kar, T.; Ray, D., Surface treatment of cellulose fibers with methylmethacrylate for enhanced properties of in situ polymerized PMMA/cellulose composites. *Journal of Applied Polymer Science* **2014**, *131* (2), n/a-n/a.
57. Cao, X.; Dong, H.; Li, C. M., New nanocomposite materials reinforced with flax cellulose nanocrystals in waterborne polyurethane. *Biomacromolecules* **2007**, *8* (3), 899-904.
58. Cheng, Q.; Wang, S.; Rials, T. G., Poly(vinyl alcohol) nanocomposites reinforced with cellulose fibrils isolated by high intensity ultrasonication. *Composites Part a-Applied Science and Manufacturing* **2009**, *40* (2), 218-224.
59. Dong, H.; Strawhecker, K. E.; Snyder, J. F.; Orlicki, J. A.; Reiner, R. S.; Rudie, A. W., Cellulose nanocrystals as a reinforcing material for electrospun poly(methyl methacrylate) fibers: Formation, properties and nanomechanical characterization. *Carbohydrate Polymers* **2012**, *87* (4), 2488-2495.
60. Habibi, Y.; Dufresne, A., Highly filled bionanocomposites from functionalized polysaccharide nanocrystals. *Biomacromolecules* **2008**, *9* (7), 1974-1980.
61. Jonoobi, M.; Harun, J.; Mathew, A.; Hussein, M.; Oksman, K., Preparation of cellulose nanofibers with hydrophobic surface characteristics. *Cellulose* **2010**, *17* (2), 299-307.
62. Seydibeyoglu, M. O.; Oksman, K., Novel nanocomposites based on polyurethane and micro fibrillated cellulose. *Composites Science and Technology* **2008**, *68* (3-4), 908-914.
63. Siqueira, G.; Bras, J.; Dufresne, A., Cellulose Whiskers versus Microfibrils: Influence of the Nature of the Nanoparticle and its Surface Functionalization on the Thermal and Mechanical Properties of Nanocomposites. *Biomacromolecules* **2009**, *10* (2), 425-432.
64. Suryanegara, L.; Nakagaito, A. N.; Yano, H., The effect of crystallization of PLA on the thermal and mechanical properties of microfibrillated cellulose-reinforced PLA composites. *Composites Science and Technology* **2009**, *69* (7-8), 1187-1192.
65. Sinko, R.; Mishra, S.; Ruiz, L.; Brandis, N.; Keten, S., Dimensions of Biological Cellulose Nanocrystals Maximize Fracture Strength. *ACS Macro Letters* **2014**, *3* (1), 64-69.
66. Mizuno, C.; John, B.; Okamoto, M., Percolated Network Structure Formation and Rheological Properties in Nylon 6/Clay Nanocomposites. *Macromolecular Materials and Engineering* **2013**, *298* (4), 400-411.
67. Capadona, J. R.; Shanmuganathan, K.; Trittschuh, S.; Seidel, S.; Rowan, S. J.; Weder, C., Polymer nanocomposites with nanowhiskers isolated from microcrystalline cellulose. *Biomacromolecules* **2009**, *10* (4), 712-716.
68. Capadona, J. R.; Shanmuganathan, K.; Tyler, D. J.; Rowan, S. J.; Weder, C., Stimuli-responsive polymer nanocomposites inspired by the sea cucumber dermis. *Science* **2008**, *319* (5868), 1370-1374.
69. Capadona, J. R.; Van Den Berg, O.; Capadona, L. A.; Schroeter, M.; Rowan, S. J.; Tyler, D. J.; Weder, C., A versatile approach for the processing of polymer nanocomposites with self-assembled nanofibre templates. *Nature Nanotechnology* **2007**, *2* (12), 765-769.

70. Dagnon, K. L.; Shanmuganathan, K.; Weder, C.; Rowan, S. J., Water-Triggered Modulus Changes of Cellulose Nanofiber Nanocomposites with Hydrophobic Polymer Matrices. *Macromolecules* **2012**, *45* (11), 4707-4715.
71. Shanmuganathan, K.; Capadona, J. R.; Rowan, S. J.; Weder, C., Bio-inspired mechanically-adaptive nanocomposites derived from cotton cellulose whiskers. *Journal of Materials Chemistry* **2010**, *20* (1), 180-186.
72. Rahman, A., Correlations in the Motion of Atoms in Liquid Argon. *Physical Review* **1964**, *136* (2A), A405-A411.
73. Alder, B. J.; Wainwright, T. E., Studies in Molecular Dynamics. I. General Method. *The Journal of Chemical Physics* **1959**, *31* (2), 459-466.
74. Kulasinski, K.; Keten, S.; Churakov, S.; Derome, D.; Carmeliet, J., A comparative molecular dynamics study of crystalline, paracrystalline and amorphous states of cellulose. *Cellulose* **2014**, 1-14.
75. Kulasinski, K.; Keten, S.; Churakov, S. V.; Guyer, R.; Carmeliet, J.; Derome, D., Molecular Mechanism of Moisture-Induced Transition in Amorphous Cellulose. *ACS Macro Letters* **2014**, *3* (10), 1037-1040.
76. Dri, F. L.; Hector, L. G.; Moon, R. J.; Zavattieri, P. D., Anisotropy of the elastic properties of crystalline cellulose I-beta from first principles density functional theory with Van der Waals interactions. *Cellulose* **2013**, *20* (6), 2703-2718.
77. Wu, X.; Moon, R.; Martini, A., Atomistic Simulation of Frictional Sliding Between Cellulose I β Nanocrystals. *Tribol Lett* **2013**, *52* (3), 395-405.
78. Sinko, R.; Keten, S., Effect of moisture on the traction-separation behavior of cellulose nanocrystal interfaces. *Appl Phys Lett* **2014**, *105* (24), 243702.
79. Sinko, R.; Keten, S., Traction-separation laws and stick-slip shear phenomenon of interfaces between cellulose nanocrystals. *Journal of the Mechanics and Physics of Solids* **2015**, *78* (0), 526-539.
80. Bergenstrahle, M.; Berglund, L. A.; Mazeau, K., Thermal response in crystalline I beta cellulose: A molecular dynamics study. *Journal of Physical Chemistry B* **2007**, *111* (30), 9138-9145.
81. Bergenstrahle, M.; Mazeau, K.; Berglund, L. A., Molecular modeling of interfaces between cellulose crystals and surrounding molecules: Effects of caprolactone surface grafting. *European Polymer Journal* **2008**, *44* (11), 3662-3669.
82. Bergensträhle, M.; Thormann, E.; Nordgren, N.; Berglund, L. A., Force Pulling of Single Cellulose Chains at the Crystalline Cellulose-Liquid Interface: A Molecular Dynamics Study. *Langmuir* **2009**, *25* (8), 4635-4642.
83. Bergenstrahle, M.; Wohlert, J.; Larsson, P. T.; Mazeau, K.; Berglund, L. A., Dynamics of cellulose-water interfaces: NMR spin-lattice relaxation times calculated from atomistic computer simulations. *Journal of Physical Chemistry B* **2008**, *112* (9), 2590-2595.
84. Tuckerman, M.; Berne, B. J.; Martyna, G. J., Reversible multiple time scale molecular dynamics. *The Journal of Chemical Physics* **1992**, *97* (3), 1990-2001.
85. Gibbs, J. W., *Elementary principles in statistical mechanics*. Courier Corporation: 2014.
86. Plimpton, S., Fast Parallel Algorithms for Short-Range Molecular Dynamics. *Journal of Computational Physics* **1995**, *117* (1), 1-19.

87. Phillips, J. C.; Braun, R.; Wang, W.; Gumbart, J.; Tajkhorshid, E.; Villa, E.; Chipot, C.; Skeel, R. D.; Kale, L.; Schulten, K., Scalable molecular dynamics with NAMD. *Journal of Computational Chemistry* **2005**, *26* (16), 1781-1802.
88. Berendsen, H. J. C.; van der Spoel, D.; van Drunen, R., GROMACS: A message-passing parallel molecular dynamics implementation. *Computer Physics Communications* **1995**, *91* (1-3), 43-56.
89. Case, D. A.; Cheatham, T. E.; Darden, T.; Gohlke, H.; Luo, R.; Merz, K. M.; Onufriev, A.; Simmerling, C.; Wang, B.; Woods, R. J., The Amber biomolecular simulation programs. *Journal of Computational Chemistry* **2005**, *26* (16), 1668-1688.
90. Brooks, B. R.; Bruccoleri, R. E.; Olafson, B. D.; States, D. J.; Swaminathan, S.; Karplus, M., CHARMM: A program for macromolecular energy, minimization, and dynamics calculations. *Journal of Computational Chemistry* **1983**, *4* (2), 187-217.
91. Brooks, B. R.; Bruccoleri, R. E.; Olafson, B. D.; States, D. J.; Swaminathan, S.; Karplus, M., CHARMM - A PROGRAM FOR MACROMOLECULAR ENERGY, MINIMIZATION, AND DYNAMICS CALCULATIONS. *Journal of Computational Chemistry* **1983**, *4* (2), 187-217.
92. Brooks, B. R.; Bruccoleri, R. E.; Olafson, B. D.; Swaminathan, S.; Karplus, M., CHARMM: A program for macromolecular energy, minimization, and dynamics calculations. *Journal of computational chemistry* **2004**, *4* (2), 187-217.
93. Brooks, B. R.; III, C. L. B.; Jr, A. D. M.; Nilsson, L.; Petrella, R. J.; Roux, B.; Won, Y.; Archontis, G.; Bartels, C.; Boresch, S.; Caflisch, A.; Caves, L.; Cui, Q.; Dinner, A. R.; Feig, M.; Fischer, S.; Gao, J.; Hodoseck, M.; Im, W.; Kuczera, K.; Lazaridis, T.; Ma, J.; Ovchinnikov, V.; Paci, E.; Pastor, R. W.; Post, C. B.; Pu, J. Z.; Schaefer, M.; Tidor, B.; Venable, R. M.; Woodcock, H. L.; Wu, X.; Yang, W.; York, D. M.; Karplus, M., CHARMM: The biomolecular simulation program. *Journal of Computational Chemistry* **2009**, *30* (10), 1545-1614.
94. Raman, E. P.; Guvench, O.; MacKerell, A. D., CHARMM Additive All-Atom Force Field for Glycosidic Linkages in Carbohydrates Involving Furanoses. *The Journal of Physical Chemistry B* **2010**, *114* (40), 12981-12994.
95. Dri, F. L.; Wu, X.; Moon, R. J.; Martini, A.; Zavattieri, P. D., Evaluation of reactive force fields for prediction of the thermo-mechanical properties of cellulose I β . *Computational Materials Science* **2015**, *109*, 330-340.
96. Grootenhuys, P. D. J.; Haasnoot, C. A. G., A CHARMM Based Force Field for Carbohydrates Using the CHEAT Approach: Carbohydrate Hydroxyl Groups Represented by Extended Atoms. *Molecular Simulation* **1993**, *10* (2-6), 75-95.
97. Ha, S. N.; Giammona, A.; Field, M.; Brady, J. W., A revised potential-energy surface for molecular mechanics studies of carbohydrates. *Carbohydrate Research* **1988**, *180* (2), 207-221.
98. Vanommeslaeghe, K.; Hatcher, E.; Acharya, C.; Kundu, S.; Zhong, S.; Shim, J.; Darian, E.; Guvench, O.; Lopes, P.; Vorobyov, I.; MacKerell, A. D., CHARMM General Force Field (CGenFF): A force field for drug-like molecules compatible with the CHARMM all-atom additive biological force fields. *Journal of computational chemistry* **2010**, *31* (4), 671-690.
99. Mayne, C. G.; Saam, J.; Schulten, K.; Tajkhorshid, E.; Gumbart, J. C., Rapid Parameterization of Small Molecules Using the Force Field Toolkit. *J Comput Chem* **2013**, *34* (32), 2757-2770.
100. Humphrey, W.; Dalke, A.; Schulten, K., VMD: visual molecular dynamics. *J Mol Graph* **1996**, *14* (1), 33-8, 27-8.

101. Frisch, M. J., G. W. Trucks, H. B. Schlegel, G. E. Scuseria, M. A. Robb, J. R. Cheeseman, G. Scalmani, V. Barone, B. Mennucci, G. A. Petersson, H. Nakatsuji, M. Caricato, X. Li, H. P. Hratchian, A. F. Izmaylov, J. Bloino, G. Zheng, J. L. Sonnenberg, M. Hada, M. Ehara, K. Toyota, R. Fukuda, J. Hasegawa, M. Ishida, T. Nakajima, Y. Honda, O. Kitao, H. Nakai, T. Vreven, J. A. Montgomery, Jr., J. E. Peralta, F. Ogliaro, M. Bearpark, J. J. Heyd, E. Brothers, K. N. Kudin, V. N. Staroverov, R. Kobayashi, J. Normand, K. Raghavachari, A. Rendell, J. C. Burant, S. S. Iyengar, J. Tomasi, M. Cossi, N. Rega, J. M. Millam, M. Klene, J. E. Knox, J. B. Cross, V. Bakken, C. Adamo, J. Jaramillo, R. Gomperts, R. E. Stratmann, O. Yazyev, A. J. Austin, R. Cammi, C. Pomelli, J. W. Ochterski, R. L. Martin, K. Morokuma, V. G. Zakrzewski, G. A. Voth, P. Salvador, J. J. Dannenberg, S. Dapprich, A. D. Daniels, Ö. Farkas, J. B. Foresman, J. V. Ortiz, J. Cioslowski, and D. J. Fox, Gaussian 09, Revision D.01, Gaussian, Inc., Wallingford CT (2009).
102. Park, S.; Khalili-Araghi, F.; Tajkhorshid, E.; Schulten, K., Free energy calculation from steered molecular dynamics simulations using Jarzynski's equality. *Journal of Chemical Physics* **2003**, *119* (6), 3559-3566.
103. Cappella, B.; Dietler, G., Force-distance curves by atomic force microscopy. *Surface science reports* **1999**, *34* (1), 1-104.
104. Zhong, Q.; Inniss, D.; Kjoller, K.; Elings, V., Fractured polymer/silica fiber surface studied by tapping mode atomic force microscopy. *Surface Science Letters* **1993**, *290* (1), L688-L692.
105. Siedlecki, C. A.; Marchant, R. E., Atomic force microscopy for characterization of the biomaterial interface. *Biomaterials* **1998**, *19* (4), 441-454.
106. Jarzynski, C., Nonequilibrium Equality for Free Energy Differences. *Physical Review Letters* **1997**, *78* (14), 2690-2693.
107. Kulasinski, K.; Guyer, R.; Keten, S.; Derome, D.; Carmeliet, J., Impact of moisture adsorption on structure and physical properties of amorphous biopolymers. *Macromolecules* **2015**, *48* (8), 2793-2800.
108. Allen, M. P. Tildesley., D. J. , *Computer Simulation of Liquids*. Clarendon Press: Oxford: 1987.
109. Warren, P. B., Dissipative particle dynamics. *Current Opinion in Colloid & Interface Science* **1998**, *3* (6), 620-624.
110. Groot, R. D.; Warren, P. B., Dissipative particle dynamics: Bridging the gap between atomistic and mesoscopic simulation. *The Journal of Chemical Physics* **1997**, *107* (11), 4423-4435.
111. Pastorino, C.; Kreer, T.; Müller, M.; Binder, K., Comparison of dissipative particle dynamics and Langevin thermostats for out-of-equilibrium simulations of polymeric systems. *Physical Review E* **2007**, *76* (2), 026706.
112. Stroberg, W.; Keten, S.; Liu, W. K., Hydrodynamics of Capillary Imbibition under Nanoconfinement. *Langmuir* **2012**, *28* (40), 14488-14495.
113. Fedosov, D. A.; Caswell, B.; Karniadakis, G. E., A multiscale red blood cell model with accurate mechanics, rheology, and dynamics. *Biophysical journal* **2010**, *98* (10), 2215-2225.
114. Pons-Siepermann, I. C.; Glotzer, S. C., Design of Patchy Particles Using Quaternary Self-Assembled Monolayers. *ACS Nano* **2012**, *6* (5), 3919-3924.
115. Li, Q.; Renneckar, S., Molecularly thin nanoparticles from cellulose: isolation of sub-microfibrillar structures. *Cellulose* **2009**, *16* (6), 1025-1032.
116. Gomes, T. C. F.; Skaf, M. S., Cellulose-Builder: A toolkit for building crystalline structures of cellulose. *Journal of Computational Chemistry* **2012**, *33* (14), 1338-1346.

117. Wiederhorn, S. *Strength of Glass--A Fracture Mechanics Approach*; DTIC Document: 1974.
118. Weiner, J. H., *Statistical Mechanics of Elasticity*. Dover Publications: 2002.
119. Lahiji, R. R.; Xu, X.; Reifengerger, R.; Raman, A.; Rudie, A.; Moon, R. J., Atomic Force Microscopy Characterization of Cellulose Nanocrystals. *Langmuir* **2010**, *26* (6), 4480-4488.
120. Azizi Samir, M. A. S.; Alloin, F.; Dufresne, A., Review of Recent Research into Cellulosic Whiskers, Their Properties and Their Application in Nanocomposite Field. *Biomacromolecules* **2005**, *6* (2), 612-626.
121. Dufresne, A., Comparing the mechanical properties of high performances polymer nanocomposites from biological sources. *Journal of Nanoscience and Nanotechnology* **2006**, *6* (2), 322-330.
122. Kong, K.; Eichhorn, S. J., The influence of hydrogen bonding on the deformation micromechanics of cellulose fibers. *Journal of Macromolecular Science-Physics* **2005**, *B44* (6), 1123-1136.
123. Nishiyama, Y.; Johnson, G. P.; French, A. D.; Forsyth, V. T.; Langan, P., Neutron Crystallography, Molecular Dynamics, and Quantum Mechanics Studies of the Nature of Hydrogen Bonding in Cellulose I-beta. *Biomacromolecules* **2008**, *9* (11), 3133-3140.
124. Nishiyama, Y.; Sugiyama, J.; Chanzy, H.; Langan, P., Crystal structure and hydrogen bonding system in cellulose I α from synchrotron X-ray and neutron fiber diffraction. *Journal of the American Chemical Society* **2003**, *125* (47), 14300-14306.
125. Bodvik, R.; Dedinaite, A.; Karlson, L.; Bergström, M.; Bäverbäck, P.; Pedersen, J. S.; Edwards, K.; Karlsson, G.; Varga, I.; Claesson, P. M., Aggregation and network formation of aqueous methylcellulose and hydroxypropylmethylcellulose solutions. *Colloids and Surfaces A: Physicochemical and Engineering Aspects* **2010**, *354* (1), 162-171.
126. Biermann, O.; Hädicke, E.; Koltzenburg, S.; Müller-Plathe, F., Hydrophilicity and Lipophilicity of Cellulose Crystal Surfaces. *Angewandte Chemie International Edition* **2001**, *40* (20), 3822-3825.
127. Lindman, B.; Karlstrom, G.; Stigsson, L., On the mechanism of dissolution of cellulose. *Journal of Molecular Liquids* **2010**, *156* (1), 76-81.
128. Bell, G., Models for the specific adhesion of cells to cells. *Science* **1978**, *200* (4342), 618-627.
129. Ruiz, L.; VonAchen, P.; Lazzara, T. D.; Xu, T.; Keten, S., Persistence length and stochastic fragmentation of supramolecular nanotubes under mechanical force. *Nanotechnology* **2013**, *24* (19).
130. Desiraju, G. R., The C-H \cdots O Hydrogen Bond: Structural Implications and Supramolecular Design. *Accounts of Chemical Research* **1996**, *29* (9), 441-449.
131. Yamane, C.; Aoyagi, T.; Ago, M.; Sato, K.; Okajima, K.; Takahashi, T., Two Different Surface Properties of Regenerated Cellulose due to Structural Anisotropy. *Polym. J* **2006**, *38* (8), 819-826.
132. Keten, S.; Xu, Z.; Ihle, B.; Buehler, M. J., Nanoconfinement controls stiffness, strength and mechanical toughness of beta-sheet crystals in silk. *Nature Materials* **2010**, *9* (4), 359-367.
133. Nova, A.; Keten, S.; Pugno, N. M.; Redaelli, A.; Buehler, M. J., Molecular and Nanostructural Mechanisms of Deformation, Strength and Toughness of Spider Silk Fibrils. *Nano Letters* **2010**, *10* (7), 2626-2634.
134. Israelachvili, J., *Intermolecular and Surface Forces, Third Edition*. Academic Press: 2010.

135. Bergström, L.; Stemme, S.; Dahlfors, T.; Arwin, H.; Ödberg, L., Spectroscopic Ellipsometry Characterisation and Estimation of the Hamaker Constant of Cellulose. *Cellulose* **1999**, *6* (1), 1-13.
136. Derocco, A. G.; Hoover, W. G., On the Interaction of Colloidal Particles. *Proceedings of the National Academy of Sciences of the United States of America* **1960**, *46* (8), 1057-1065.
137. Van Oss, C. J.; Chaudhury, M. K.; Good, R. J., Interfacial Lifshitz-van der Waals and polar interactions in macroscopic systems. *Chemical reviews* **1988**, *88* (6), 927-941.
138. Kim, H.; Shi, F., Refractive index of polycrystalline submicrometer polymer thin films: thickness dependence. *Journal of Materials Science: Materials in Electronics* **2001**, *12* (7), 361-364.
139. Ackbarow, T.; Chen, X.; Keten, S.; Buehler, M. J., Hierarchies, multiple energy barriers, and robustness govern the fracture mechanics of alpha-helical and beta-sheet protein domains. *Proceedings of the National Academy of Sciences of the United States of America* **2007**, *104* (42), 16410-16415.
140. Buehler, M. J.; Yao, H. M.; Ji, B. H.; Gao, H. J., Atomistic and continuum studies of flaw tolerant nanostructures in biological systems. In *Mechanical Properties of Bioinspired and Biological Materials*, Viney, C.; Katti, K.; Ulm, F. J.; Hellmich, C., Eds. 2005; Vol. 844, pp 207-212.
141. Gao, H.; Ji, B.; Buehler, M. J.; Yao, H., Flaw tolerant bulk and surface nanostructures of biological systems. *Mechanics & chemistry of biosystems : MCB* **2004**, *1* (1), 37-52.
142. Gao, H. J.; Ji, B. H.; Jager, I. L.; Arzt, E.; Fratzl, P., Materials become insensitive to flaws at nanoscale: Lessons from nature. *Proceedings of the National Academy of Sciences of the United States of America* **2003**, *100* (10), 5597-5600.
143. Mu, X.; Gray, D. G., Formation of Chiral Nematic Films from Cellulose Nanocrystal Suspensions Is a Two-Stage Process. *Langmuir* **2014**, *30* (31), 9256-9260.
144. Park, K.; Paulino, G. H., Cohesive Zone Models: A Critical Review of Traction-Separation Relationships Across Fracture Surfaces. *Applied Mechanics Reviews* **2013**, *64* (6), 060802-060802.
145. Humphrey, W.; Dalke, A.; Schulten, K., VMD: Visual molecular dynamics. *Journal of Molecular Graphics & Modelling* **1996**, *14* (1), 33-38.
146. Nishiyama, Y.; Langan, P.; Chanzy, H., Crystal structure and hydrogen-bonding system in cellulose 1 beta from synchrotron X-ray and neutron fiber diffraction. *Journal of the American Chemical Society* **2002**, *124* (31), 9074-9082.
147. Keten, S.; Buehler, M. J., Nanostructure and molecular mechanics of spider dragline silk protein assemblies. *Journal of The Royal Society Interface* **2010**, *7* (53), 1709-1721.
148. Reising, A. B.; Moon, R. J.; Youngblood, J. P., Effect of particle Alignment on mechanical properties of neat cellulose nanocrystal films. *J. Sci. Technol. For. Prod. Process* **2013**, *2*, 32-41.
149. Imai, T.; Putaux, J.-L.; Sugiyama, J., Geometric phase analysis of lattice images from algal cellulose microfibrils. *Polymer* **2003**, *44* (6), 1871-1879.
150. Karnopp, D., Computer Simulation of Stick-Slip Friction in Mechanical Dynamic Systems. *Journal of Dynamic Systems, Measurement, and Control* **1985**, *107* (1), 100-103.
151. Yoshizawa, H.; Israelachvili, J., Fundamental mechanisms of interfacial friction. 2. Stick-slip friction of spherical and chain molecules. *The Journal of Physical Chemistry* **1993**, *97* (43), 11300-11313.

152. Nasuno, S.; Kudrolli, A.; Bak, A.; Gollub, J. P., Time-resolved studies of stick-slip friction in sheared granular layers. *Physical Review E* **1998**, *58* (2), 2161-2171.
153. Socoliuc, A.; Bennewitz, R.; Gnecco, E.; Meyer, E., Transition from Stick-Slip to Continuous Sliding in Atomic Friction: Entering a New Regime of Ultralow Friction. *Physical Review Letters* **2004**, *92* (13), 134301.
154. Popov, V., The Prandtl-Tomlinson Model for Dry Friction. In *Contact Mechanics and Friction*, Springer Berlin Heidelberg: 2010; pp 155-174.
155. Verhoeven, G. S.; Dienwiebel, M.; Frenken, J. W. M., Model calculations of superlubricity of graphite. *Physical Review B* **2004**, *70* (16), 165418.
156. Henriksson, M.; Berglund, L. A.; Isaksson, P.; Lindström, T.; Nishino, T., Cellulose Nanopaper Structures of High Toughness. *Biomacromolecules* **2008**, *9* (6), 1579-1585.
157. Liu, Y.; Xie, B.; Zhang, Z.; Zheng, Q.; Xu, Z., Mechanical properties of graphene papers. *Journal of the Mechanics and Physics of Solids* **2012**, *60* (4), 591-605.
158. Liu, Y.; Xu, Z., Multimodal and self-healable interfaces enable strong and tough graphene-derived materials. *Journal of the Mechanics and Physics of Solids* **2014**, *70* (0), 30-41.
159. Wei, X.; Naraghi, M.; Espinosa, H. D., Optimal Length Scales Emerging from Shear Load Transfer in Natural Materials: Application to Carbon-Based Nanocomposite Design. *ACS Nano* **2012**, *6* (3), 2333-2344.
160. Jeffrey, G. A., *An Introduction to Hydrogen Bonding*. Oxford University Press: 1997.
161. Dörmann, M.; Schmid, H.-J., Simulation of Capillary Bridges between Nanoscale Particles. *Langmuir* **2014**, *30* (4), 1055-1062.
162. Rabinovich, Y. I.; Esayanur, M. S.; Moudgil, B. M., Capillary Forces between Two Spheres with a Fixed Volume Liquid Bridge: Theory and Experiment. *Langmuir* **2005**, *21* (24), 10992-10997.
163. Yang, S. H.; Nosonovsky, M.; Zhang, H.; Chung, K.-H., Nanoscale water capillary bridges under deeply negative pressure. *Chemical Physics Letters* **2008**, *451* (1-3), 88-92.
164. Scatena, L. F.; Brown, M. G.; Richmond, G. L., Water at Hydrophobic Surfaces: Weak Hydrogen Bonding and Strong Orientation Effects. *Science* **2001**, *292* (5518), 908-912.
165. Kumar, A.; Park, B. J.; Tu, F.; Lee, D., Amphiphilic Janus particles at fluid interfaces. *Soft Matter* **2013**, *9* (29), 6604-6617.
166. Walther, A.; Müller, A. H. E., Janus Particles: Synthesis, Self-Assembly, Physical Properties, and Applications. *Chemical Reviews* **2013**, *113* (7), 5194-5261.
167. and wet interfaces., S. s. m. a. U. w. i. b. A. f. f. e. o. t. c. o. S. p. a. c. o. t. e. l. a. f.-d. c. f. d.
168. Sotres, J.; Arnebrant, T., Experimental Investigations of Biological Lubrication at the Nanoscale: The Cases of Synovial Joints and the Oral Cavity. *Lubricants* **2013**, *1* (4), 102-131.
169. Ifuku, S.; Nogi, M.; Abe, K.; Handa, K.; Nakatsubo, F.; Yano, H., Surface Modification of Bacterial Cellulose Nanofibers for Property Enhancement of Optically Transparent Composites: Dependence on Acetyl-Group DS. *Biomacromolecules* **2007**, *8* (6), 1973-1978.
170. Lee, K.-Y.; Blaker, J. J.; Bismarck, A., Surface functionalisation of bacterial cellulose as the route to produce green polylactide nanocomposites with improved properties. *Composites Science and Technology* **2009**, *69* (15-16), 2724-2733.
171. Reising, A. B.; Moon, R. J.; Youngblood, J. P., EFFECT OF PARTICLE ALIGNMENT ON MECHANICAL PROPERTIES OF NEAT CELLULOSE NANOCRYSTAL FILMS. *J-for-Journal of Science & Technology for Forest Products and Processes* **2012**, *2* (6), 32-41.

172. Lu, P.; Hsieh, Y.-L., Preparation and properties of cellulose nanocrystals: Rods, spheres, and network. *Carbohydrate Polymers* **2010**, *82* (2), 329-336.
173. Camarero Espinosa, S.; Kuhnt, T.; Foster, E. J.; Weder, C., Isolation of Thermally Stable Cellulose Nanocrystals by Phosphoric Acid Hydrolysis. *Biomacromolecules* **2013**, *14* (4), 1223-1230.
174. Fox, D. M.; Rodriguez, R. S.; Devilbiss, M. N.; Woodcock, J.; Davis, C. S.; Sinko, R.; Keten, S.; Gilman, J. W., Simultaneously Tailoring Surface Energies and Thermal Stabilities of Cellulose Nanocrystals Using Ion Exchange: Effects on Polymer Composite Properties for Transportation, Infrastructure, and Renewable Energy Applications. *ACS Applied Materials & Interfaces* **2016**, *8* (40), 27270-27281.
175. Habibi, Y.; Lucia, L. A.; Rojas, O. J., Cellulose Nanocrystals: Chemistry, Self-Assembly, and Applications. *Chem Rev* **2010**, *110* (6), 3479-3500.
176. Fox, D. M.; Rodriguez, R. S.; Devilbiss, M. N.; Woodcock, J.; Davis, C. S.; Sinko, R.; Keten, S.; Gilman, J. W., Simultaneously Tailoring Surface Energies and Thermal Stabilities of Cellulose Nanocrystals Using Ion Exchange: Effects on Polymer Composite Properties for Transportation, Infrastructure, and Renewable Energy Applications. *Acs Appl Mater Inter* **2016**, *8* (40), 27270-27281.
177. Vanommeslaeghe, K.; Hatcher, E.; Acharya, C.; Kundu, S.; Zhong, S.; Shim, J.; Darian, E.; Guvench, O.; Lopes, P.; Vorobyov, I.; MacKerell, A. D., CHARMM General Force Field: A Force Field for Drug-Like Molecules Compatible with the CHARMM All-Atom Additive Biological Force Fields. *J Comput Chem* **2010**, *31* (4), 671-690.
178. Grootenhuys, P. D. J.; Haasnoot, C. A. G., A Charmm Based Force-Field for Carbohydrates Using the Cheat Approach - Carbohydrate Hydroxyl-Groups Represented by Extended Atoms. *Mol Simulat* **1993**, *10* (2-6), 75-95.
179. Ha, S. N.; Giammona, A.; Field, M.; Brady, J. W., A revised potential-energy surface for molecular mechanics studies of carbohydrates. *Carbohyd Res* **1988**, *180* (2), 207-221.
180. Raman, E. P.; Guvench, O.; MacKerell, A. D., CHARMM Additive All-Atom Force Field for Glycosidic Linkages in Carbohydrates Involving Furanoses. *Journal of Physical Chemistry B* **2010**, *114* (40), 12981-12994.
181. Gomes, T. C. F.; Skaf, M. S., Cellulose-Builder: A toolkit for building crystalline structures of cellulose. *J Comput Chem* **2012**, *33* (14), 1338-1346.
182. Martinez, L.; Andrade, R.; Birgin, E. G.; Martinez, J. M., PACKMOL: A Package for Building Initial Configurations for Molecular Dynamics Simulations. *J Comput Chem* **2009**, *30* (13), 2157-2164.
183. Sinko, R.; Keten, S., Traction-separation laws and stick-slip shear phenomenon of interfaces between cellulose nanocrystals. *J Mech Phys Solids* **2015**, *78*, 526-539.
184. Wierchowski, S. J.; Kofke, D. A., Fugacity coefficients of saturated water from molecular simulation. *Journal of Physical Chemistry B* **2003**, *107* (46), 12808-12813.
185. Rabinovich, Y. I.; Esayanur, M. S.; Moudgil, B. M., Capillary forces between two spheres with a fixed volume liquid bridge: Theory and experiment. *Langmuir* **2005**, *21* (24), 10992-10997.
186. Dormann, M.; Schmid, H. J., Simulation of Capillary Bridges between Nanoscale Particles. *Langmuir* **2014**, *30* (4), 1055-1062.
187. Sinko, R.; Keten, S., Effect of moisture on the traction-separation behavior of cellulose nanocrystal interfaces. *Appl Phys Lett* **2014**, *105* (24).

188. Desiraju, G. R., The C-H center dot center dot center dot O hydrogen bond: Structural implications and supramolecular design. *Accounts Chem Res* **1996**, *29* (9), 441–449.
189. Kobayashi, R.; Chappellear, P.; Deans, H., PHYSICOCHEMICAL MEASUREMENTS BY GAS CHROMATOGRAPHY. *Industrial & Engineering Chemistry* **1967**, *59* (10), 63-82.
190. Bansal, A.; Yang, H.; Li, C.; Benicewicz, B. C.; Kumar, S. K.; Schadler, L. S., Controlling the thermomechanical properties of polymer nanocomposites by tailoring the polymer–particle interface. *Journal of Polymer Science Part B: Polymer Physics* **2006**, *44* (20), 2944-2950.
191. Akcora, P.; Liu, H.; Kumar, S. K.; Moll, J.; Li, Y.; Benicewicz, B. C.; Schadler, L. S.; Acehan, D.; Panagiotopoulos, A. Z.; Pryamitsyn, V.; Ganesan, V.; Ilavsky, J.; Thiyagarajan, P.; Colby, R. H.; Douglas, J. F., Anisotropic self-assembly of spherical polymer-grafted nanoparticles. *Nat Mater* **2009**, *8* (4), 354-359.
192. Fernandes, N. J.; Koerner, H.; Giannelis, E. P.; Vaia, R. A., Hairy nanoparticle assemblies as one-component functional polymer nanocomposites: opportunities and challenges. *MRS Communications* **2013**, *3* (01), 13-29.
193. Goffin, A. L.; Raquez, J. M.; Duquesne, E.; Siqueira, G.; Habibi, Y.; Dufresne, A.; Dubois, P., Poly(ϵ -caprolactone) based nanocomposites reinforced by surface-grafted cellulose nanowhiskers via extrusion processing: Morphology, rheology, and thermo-mechanical properties. *Polymer* **2011**, *52* (7), 1532-1538.
194. Habibi, Y.; Goffin, A.-L.; Schiltz, N.; Duquesne, E.; Dubois, P.; Dufresne, A., Bionanocomposites based on poly (ϵ -caprolactone)-grafted cellulose nanocrystals by ring-opening polymerization. *Journal of Materials Chemistry* **2008**, *18* (41), 5002-5010.
195. Coskun, M.; Temüz, M. M., Grafting studies onto cellulose by atom-transfer radical polymerization. *Polymer International* **2005**, *54* (2), 342-347.
196. Morandi, G.; Heath, L.; Thielemans, W., Cellulose Nanocrystals Grafted with Polystyrene Chains through Surface-Initiated Atom Transfer Radical Polymerization (SI-ATRP). *Langmuir* **2009**, *25* (14), 8280-8286.
197. Carlmark, A.; Malmström, E., Atom Transfer Radical Polymerization from Cellulose Fibers at Ambient Temperature. *Journal of the American Chemical Society* **2002**, *124* (6), 900-901.
198. Meng, T.; Gao, X.; Zhang, J.; Yuan, J.; Zhang, Y.; He, J., Graft copolymers prepared by atom transfer radical polymerization (ATRP) from cellulose. *Polymer* **2009**, *50* (2), 447-454.
199. Hansson, S.; Tischer, T.; Goldmann, A. S.; Carlmark, A.; Barner-Kowollik, C.; Malmstrom, E., Visualization of poly(methyl methacrylate) (PMMA) grafts on cellulose via high-resolution FT-IR microscopy imaging. *Polymer Chemistry* **2012**, *3* (2), 307-309.
200. Martínez, L.; Andrade, R.; Birgin, E. G.; Martínez, J. M., PACKMOL: a package for building initial configurations for molecular dynamics simulations. *Journal of computational chemistry* **2009**, *30* (13), 2157-2164.
201. Xia, W.; Song, J.; Hsu, D. D.; Keten, S., Understanding the Interfacial Mechanical Response of Nanoscale Polymer Thin Films via Nanoindentation. *Macromolecules* **2016**.
202. Xia, W.; Hsu, D.; Keten, S. In *Predicting Thermomechanical Responses of Polymer Thin Films and Nanocomposites via an Innovative Coarse-grained Approach*, APS Meeting Abstracts, 2016.
203. Cook, M.; Watts, D. C.; Williams, G., Correlation function approach to the dielectric behaviour of amorphous polymers. *Transactions of the Faraday Society* **1970**, *66* (0), 2503-2511.

204. Lang, R. J.; Simmons, D. S., Interfacial Dynamic Length Scales in the Glass Transition of a Model Freestanding Polymer Film and Their Connection to Cooperative Motion. *Macromolecules* **2013**, *46* (24), 9818-9825.
205. Lin, Y.; Liu, L.; Zhang, D.; Liu, Y.; Guan, A.; Wu, G., Unexpected segmental dynamics in polystyrene-grafted silica nanocomposites. *Soft Matter* **2016**, *12* (41), 8542-8553.
206. Rissanou, A. N.; Harmandaris, V., Structural and Dynamical Properties of Polystyrene Thin Films Supported by Multiple Graphene Layers. *Macromolecules* **2015**, *48* (8), 2761-2772.
207. Xia, W.; Mishra, S.; Keten, S., Substrate vs. free surface: Competing effects on the glass transition of polymer thin films. *Polymer* **2013**, *54* (21), 5942-5951.
208. Khoshkava, V.; Kamal, M. R., Effect of Surface Energy on Dispersion and Mechanical Properties of Polymer/Nanocrystalline Cellulose Nanocomposites. *Biomacromolecules* **2013**, *14* (9), 3155-3163.
209. Hsu, D. D.; Xia, W.; Arturo, S. G.; Keten, S., Systematic Method for Thermomechanically Consistent Coarse-Graining: A Universal Model for Methacrylate-Based Polymers. *Journal of Chemical Theory and Computation* **2014**, *10* (6), 2514-2527.
210. Ruan, D.; Simmons, D. S., Glass Formation near Covalently Grafted Interfaces: Ionomers as a Model Case. *Macromolecules* **2015**, *48* (7), 2313-2323.
211. Marvin, M. D.; Lang, R. J.; Simmons, D. S., Nanoconfinement effects on the fragility of glass formation of a model freestanding polymer film. *Soft Matter* **2014**, *10* (18), 3166-3170.
212. Qin, X.; Xia, W.; Sinko, R.; Keten, S., Tuning Glass Transition in Polymer Nanocomposites with Functionalized Cellulose Nanocrystals through Nanoconfinement. *Nano Letters* **2015**, *15* (10), 6738-6744.
213. Xia, W.; Keten, S., Coupled Effects of Substrate Adhesion and Intermolecular Forces on Polymer Thin Film Glass-Transition Behavior. *Langmuir* **2013**, *29* (41), 12730-12736.
214. Ellison, C. J.; Torkelson, J. M., The distribution of glass-transition temperatures in nanoscopically confined glass formers. *Nat Mater* **2003**, *2* (10), 695-700.
215. Forrest, J. A.; Mattsson, J., Reductions of the glass transition temperature in thin polymer films: Probing the length scale of cooperative dynamics. *Physical Review E* **2000**, *61* (1), R53-R56.
216. Kawana, S.; Jones, R. A. L., Character of the glass transition in thin supported polymer films. *Physical Review E* **2001**, *63* (2), 021501.
217. Férey, G.; Haouas, M.; Loiseau, T.; Taulelle, F., Nanoporous Solids: How Do They Form? An In Situ Approach. *Chemistry of Materials* **2014**, *26* (1), 299-309.
218. Jeffroy, M.; Fuchs, A. H.; Boutin, A., Structural changes in nanoporous solids due to fluid adsorption: thermodynamic analysis and Monte Carlo simulations. *Chemical Communications* **2008**, (28), 3275-3277.
219. Farha, O. K.; Eryazici, I.; Jeong, N. C.; Hauser, B. G.; Wilmer, C. E.; Sarjeant, A. A.; Snurr, R. Q.; Nguyen, S. T.; Yazaydin, A. O. z. r.; Hupp, J. T., Metal-organic framework materials with ultrahigh surface areas: is the sky the limit? *Journal of the American Chemical Society* **2012**, *134* (36), 15016-15021.
220. Sercombe, J.; Ulm, F.-J.; Toutlemonde, F., Viscous hardening plasticity for concrete in high-rate dynamics. *Journal of engineering mechanics* **1998**, *124* (9), 1050-1057.
221. Chun, S.-J.; Choi, E.-S.; Lee, E.-H.; Kim, J. H.; Lee, S.-Y.; Lee, S.-Y., Eco-friendly cellulose nanofiber paper-derived separator membranes featuring tunable nanoporous network channels for lithium-ion batteries. *Journal of Materials Chemistry* **2012**, *22* (32), 16618-16626.

222. Cai, J.; Kimura, S.; Wada, M.; Kuga, S., Nanoporous cellulose as metal nanoparticles support. *Biomacromolecules* **2008**, *10* (1), 87-94.
223. Pickett, G. In *The Effect of Change in Moisture-Content on the Crepe of Concrete Under a Sustained Load*, ACI Journal Proceedings, ACI: 1942.
224. Pickett, G. In *Effect of aggregate on shrinkage of concrete and a hypothesis concerning shrinkage*, ACI Journal Proceedings, ACI: 1956.
225. Bažant, Z. P.; Yunping, X., Drying creep of concrete: constitutive model and new experiments separating its mechanisms. *Materials and structures* **1994**, *27* (1), 3-14.
226. Lea, F. M., The chemistry of cement and concrete. **1970**.
227. Recommendation, R. D.; DE LA RILEM, P. D. R., Creep and shrinkage prediction model for analysis and design of concrete structures-model B3. *Mater. Struct* **1995**, *28*, 357-365.
228. Wittmann, F.; Roelfstra, P., Total deformation of loaded drying concrete. *Cement and Concrete Research* **1980**, *10* (5), 601-610.
229. Altoubat, S. A.; Lange, D. A., The Pickett effect at early age and experiment separating its mechanisms in tension. *Materials and Structures* **2002**, *35* (4), 211-218.
230. Bažant, Z. P.; Asghari, A. A.; Schmidt, J., Experimental study of creep of hardened Portland cement paste at variable water content. *Mat. Constr.* **1976**, *9* (4), 279-290.
231. Vandamme, M.; Ulm, F.-J., Nanogranular origin of concrete creep. *Proceedings of the National Academy of Sciences* **2009**, *106* (26), 10552-10557.
232. Vlahinić, I.; Thomas, J. J.; Jennings, H. M.; Andrade, J. E., Transient creep effects and the lubricating power of water in materials ranging from paper to concrete and Kevlar. *Journal of the Mechanics and Physics of Solids* **2012**, *60* (7), 1350-1362.
233. Armstrong, L.; Kingston, R., The effect of moisture content changes on the deformation of wood under stress. *Australian journal of applied science* **1962**, *13* (4), 257-276.
234. Armstrong, L.; Kingston, R., Effect of moisture changes on creep in wood. *Nature, London* **1960**, *185* (4716), 862-3.
235. Armstrong, L.; Christensen, G., Influence of moisture changes on deformation of wood under stress. *Nature* **1961**, *191*, 869-870.
236. Olsson, A.-M.; Salmén, L.; Eder, M.; Burgert, I., Mechano-sorptive creep in wood fibres. *Wood Science and Technology* **2007**, *41* (1), 59-67.
237. Alifhan, J., The effect of humidity cycle amplitude on accelerated tensile creep of paper. *Mechanics of Time-Dependent Materials* **2004**, *8* (4), 289-302.
238. Byrd, V. L., Effect of relative humidity changes during creep on handsheet paper properties. *Tappi* **1972**, *55* (2), 247-&.
239. Danilatos, G.; Postle, R., Low-strain dynamic mechanical properties of keratin fibers during water absorption. *Journal of Macromolecular Science, Part B: Physics* **1981**, *19* (1), 153-165.
240. Mackay, B.; Downes, J., The effect of the sorption process on the dynamic rigidity modulus of the wool fiber. *Journal of Applied Polymer Science* **1959**, *2* (4), 32-38.
241. Wang, J. Z.; Dillard, D. A.; Wolcott, M. P.; Kamke, F. A.; Wilkes, G. L., Transient moisture effects in fibers and composite materials. *Journal of Composite Materials* **1990**, *24* (9), 994-1009.
242. Habeger, C.; Coffin, D.; Hojjatie, B., Influence of humidity cycling parameters on the moisture-accelerated creep of polymeric fibers. *Journal of Polymer Science Part B: Polymer Physics* **2001**, *39* (17), 2048-2062.

243. Bažant, Z. P.; Hauggaard, A. B.; Baweja, S., Microprestress-solidification theory for concrete creep. II: Algorithm and verification. *Journal of Engineering Mechanics* **1997**, *123* (11), 1195-1201.
244. Bažant, Z. P.; Hauggaard, A. B.; Baweja, S.; Ulm, F.-J., Microprestress-solidification theory for concrete creep. I: Aging and drying effects. *Journal of Engineering Mechanics* **1997**, *123* (11), 1188-1194.
245. Bažant, Z. P.; Prasanna, S., Solidification theory for concrete creep. II: Verification and application. *Journal of Engineering mechanics* **1989**, *115* (8), 1704-1725.
246. Bažant, Z. P.; Prasanna, S., Solidification theory for concrete creep. I: Formulation. *Journal of engineering mechanics* **1989**, *115* (8), 1691-1703.
247. Bažant, Z. P., Thermodynamics of interacting continua with surfaces and creep analysis of concrete structures. *Nuclear Engineering and Design* **1972**, *20* (2), 477-505.
248. Bažant, Z. P.; Bazant, M. Z., Theory of sorption hysteresis in nanoporous solids: Part I: Snap-through instabilities. *Journal of the Mechanics and Physics of Solids* **2012**, *60* (9), 1644-1659.
249. Bažant, Z.; Cusatis, G.; Cedolin, L., Temperature Effect on Concrete Creep Modeled by Microprestress-Solidification Theory. *Journal of Engineering Mechanics* **2004**, *130* (6), 691-699.
250. Pascal, T. A.; Goddard, W. A.; Jung, Y., Entropy and the driving force for the filling of carbon nanotubes with water. *Proceedings of the National Academy of Sciences* **2011**, *108* (29), 11794-11798.
251. Hummer, G.; Rasaiah, J. C.; Noworyta, J. P., Water conduction through the hydrophobic channel of a carbon nanotube. *Nature* **2001**, *414* (6860), 188-190.
252. Ruiz, L.; Wu, Y.; Keten, S., Tailoring the water structure and transport in nanotubes with tunable interiors. *Nanoscale* **2015**, *7* (1), 121-132.
253. Bonnaud, P.; Coasne, B.; Pellenq, R. J., Molecular simulation of water confined in nanoporous silica. *Journal of Physics: Condensed Matter* **2010**, *22* (28), 284110.
254. Puibasset, J.; Pellenq, R. J.-M., Grand canonical Monte Carlo simulation study of water adsorption in silicalite at 300 K. *The Journal of Physical Chemistry B* **2008**, *112* (20), 6390-6397.
255. Ruiz, L.; Xia, W.; Meng, Z.; Keten, S., A coarse-grained model for the mechanical behavior of multi-layer graphene. *Carbon* **2015**, *82*, 103-115.
256. Hsu, D. D.; Xia, W.; Arturo, S. G.; Keten, S., Thermomechanically Consistent and Temperature Transferable Coarse-Graining of Atactic Polystyrene. *Macromolecules* **2015**, *48* (9), 3057-3068.
257. Chiu, S.-W.; Scott, H. L.; Jakobsson, E., A Coarse-Grained Model Based on Morse Potential for Water and n-Alkanes. *Journal of Chemical Theory and Computation* **2010**, *6* (3), 851-863.
258. Adolphs, J.; Setzer, M.; Auberg, R.; Keck, H. In *The role of nanopores in concrete*, International RILEM Workshop on Frost Resistance of Concrete, RILEM Publications SARL: 2002; pp 45-52.
259. Shahidi, M.; Pichler, B.; Hellmich, C., Viscous interfaces as source for material creep: A continuum micromechanics approach. *European Journal of Mechanics - A/Solids* **2014**, *45*, 41-58.
260. Shahidi, M.; Pichler, B.; Hellmich, C., How interface size, density, and viscosity affect creep and relaxation functions of matrix-interface composites: a micromechanical study. *Acta Mechanica* **2015**, *227* (1), 229-252.

261. Shahidi, M.; Pichler, B.; Hellmich, C., Interfacial Micromechanics Assessment of Classical Rheological Models. II: Multiple Interface Sizes and Viscosities. *Journal of Engineering Mechanics* **2015**, *142* (3), 04015093.
262. Shahidi, M.; Pichler, B.; Hellmich, C., Interfacial Micromechanics Assessment of Classical Rheological Models. I: Single Interface Size and Viscosity. *Journal of Engineering Mechanics* **2015**, *142* (3), 04015092.
263. Siau, J. F., *Transport Processes in Wood*. Springer Berlin Heidelberg: 2012.
264. Gao, J.; Szoszkiewicz, R.; Landman, U.; Riedo, E., Structured and viscous water in subnanometer gaps. *Physical Review B* **2007**, *75* (11), 115415.
265. Riedo, E., Water behaves like a viscous fluid on the nano-scale. *Membrane Technology* **2007**, *2007* (8), 8.
266. Sendner, C.; Horinek, D.; Bocquet, L.; Netz, R. R., Interfacial water at hydrophobic and hydrophilic surfaces: Slip, viscosity, and diffusion. *Langmuir* **2009**, *25* (18), 10768-10781.
267. Leng, Y.; Cummings, P. T., Fluidity of hydration layers nanoconfined between mica surfaces. *Physical review letters* **2005**, *94* (2), 026101.
268. Manias, E.; Bitsanis, I.; Hadziioannou, G.; Ten Brinke, G., On the nature of shear thinning in nanoscopically confined films. *EPL (Europhysics Letters)* **1996**, *33* (5), 371.
269. Angell, C. A., Insights into Phases of Liquid Water from Study of Its Unusual Glass-Forming Properties. *Science* **2008**, *319* (5863), 582-587.
270. Qu, T.; Verma, D.; Shahidi, M.; Pichler, B.; Hellmich, C.; Tomar, V., Mechanics of organic-inorganic biointerfaces—Implications for strength and creep properties. *MRS Bulletin* **2015**, *40* (04), 349-358.
271. Pivonka, P.; Hellmich, C.; Smith, D., Microscopic effects on chloride diffusivity of cement pastes—a scale-transition analysis. *Cement and Concrete Research* **2004**, *34* (12), 2251-2260.
272. Abdalrahman, T.; Scheiner, S.; Hellmich, C., Is trabecular bone permeability governed by molecular ordering-induced fluid viscosity gain? Arguments from re-evaluation of experimental data in the framework of homogenization theory. *Journal of Theoretical Biology* **2015**, *365*, 433-444.
273. Xia, W.; Hsu, D. D.; Keten, S., Molecular Weight Effects on the Glass Transition and Confinement Behavior of Polymer Thin Films. *Macromolecular Rapid Communications* **2015**, *36* (15), 1422-1427.
274. Xia, W.; Keten, S., Interfacial stiffening of polymer thin films under nanoconfinement. *Extreme Mechanics Letters* **2015**, *4*, 89-95.
275. Levine, B. G.; Stone, J. E.; Kohlmeyer, A., Fast analysis of molecular dynamics trajectories with graphics processing units—Radial distribution function histogramming. *Journal of Computational Physics* **2011**, *230* (9), 3556-3569.
276. Zhurkov, S. N., Kinetic concept of the strength of solids. *International Journal of Fracture* **1984**, *26* (4), 295-307.
277. Walton, E. B.; Lee, S.; Van Vliet, K. J., Extending Bell's Model: How Force Transducer Stiffness Alters Measured Unbinding Forces and Kinetics of Molecular Complexes. *Biophysical Journal* **2008**, *94* (7), 2621-2630.
278. Schlierf, M.; Rief, M., Single-Molecule Unfolding Force Distributions Reveal a Funnel-Shaped Energy Landscape. *Biophysical Journal* **2006**, *90* (4), L33-L35.

279. Vandamme, M.; Bažant, Z.; Keten, S., Creep of Lubricated Layered Nano-Porous Solids and Application To Cementitious Materials. *Journal of Nanomechanics and Micromechanics* **2015**, *5* (4), 04015002.
280. Bažant, Z. P.; Le, J.-L.; Bazant, M. Z., Scaling of strength and lifetime probability distributions of quasibrittle structures based on atomistic fracture mechanics. *Proceedings of the National Academy of Sciences* **2009**, *106* (28), 11484-11489.
281. Day, R. L.; Cuffaro, P.; Illston, J. M., The effect of rate of drying on the drying creep of hardened cement paste. *Cement and Concrete Research* **1984**, *14* (3), 329-338.
282. Hou, D.; Zhu, Y.; Lu, Y.; Li, Z., Mechanical properties of calcium silicate hydrate (C-S-H) at nano-scale: A molecular dynamics study. *Materials Chemistry and Physics* **2014**, *146* (3), 503-511.
283. Kalifa, P.; Menneteau, F.-D.; Quenard, D., Spalling and pore pressure in HPC at high temperatures. *Cement and Concrete Research* **2000**, *30* (12), 1915-1927.
284. Fine, R. A.; Millero, F. J., Compressibility of water as a function of temperature and pressure. *The Journal of Chemical Physics* **1973**, *59* (10), 5529-5536.

Chapter 12 – Appendix: CHARMM Force Field Parameters

12.1 CHARMM Force Field for Carbohydrates

CHARMM force field parameters for CNCs are obtained directly from the previously parameterized CHARMM force field for carbohydrates. As mentioned in the text, cellulose chains found within CNCs are polysaccharides that are a linear chain of $\beta(1 \rightarrow 4)$ linked glucose units. Within the CHARMM force field for carbohydrates, this corresponds to two BGLC residues bonded together as illustrated in Figure 12-1 along with the associated CHARMM carbohydrate atom types. To link multiple repeat units, a 14bb patch is employed in which the terminal hydrogen and oxygen from each repeat unit are deleted and replaced by a single oxygen atom of type OC301 that links together the two units. The specific bond, angle, and dihedral parameters for these combinations of atom types are found in the CHARMM force field for carbohydrates and is readily available from: http://mackerell.umaryland.edu/charmm_ff.shtml#charmm

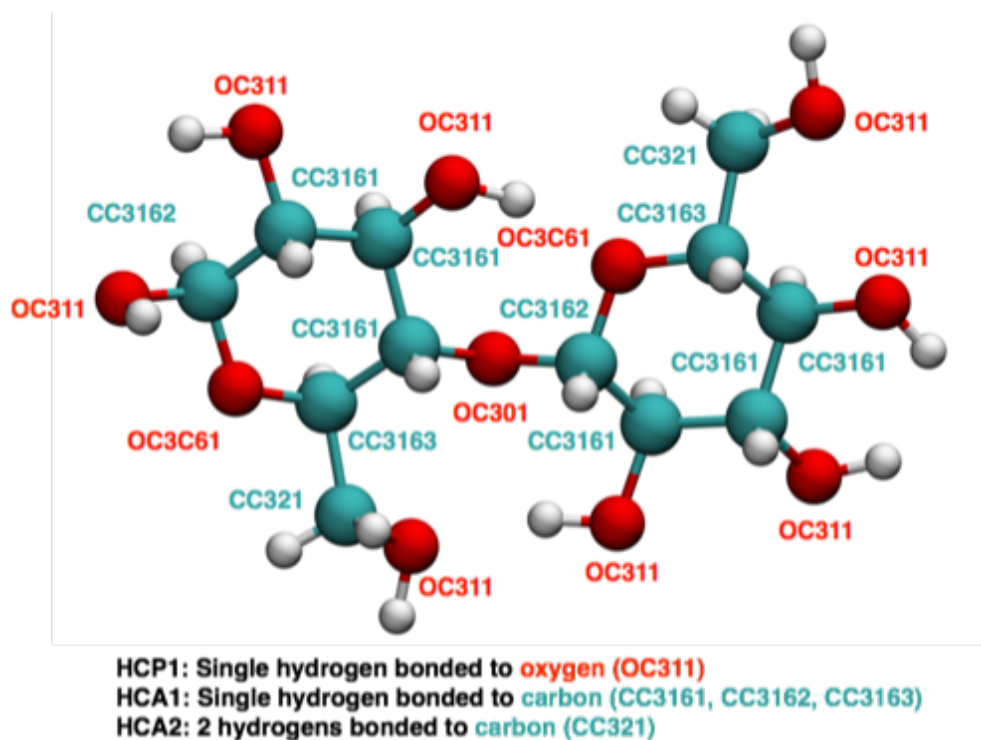


Figure 12-1: Cellulose repeat unit atom types. Illustration of a single cellulose repeat unit that consists of two BGLC CHARMM carbohydrate residues bonded together through the $\beta(1 \rightarrow 4)$ linkage. Atom types for carbon and oxygen atoms are indicated directly in the figure, with the hydrogen atom types specified by the legend.

12.2 *cgenff* Force Field Parameters for Synthetic Polymers

To obtain the CHARMM force field parameters for the synthetic polymers used in this work, the generalized CHARMM force field (*cgenff*) is employed. Here we focus on three synthetic polymers: poly(methyl methacrylate) (PMMA), polystyrene (PS), and epoxy (DGEBA and polyetherdiamine blend). First, for PMMA, the atom types, names, and partial charges are shown in Figure 12-2. Here, we utilize three residues where MMAB and MMAE are the beginning and ending residues for a single chain that include extra hydrogen atoms to cap the chains and MMAM are the middle residues. The bond, angle, and dihedral parameters for PMMA are obtained using the *cgenff* program.

was necessary. Therefore, the bond, angle, and dihedral parameters can be obtained by using the atom types indicated in Figure 12-3 at: http://mackerell.umaryland.edu/charmm_ff.shtml#charmm

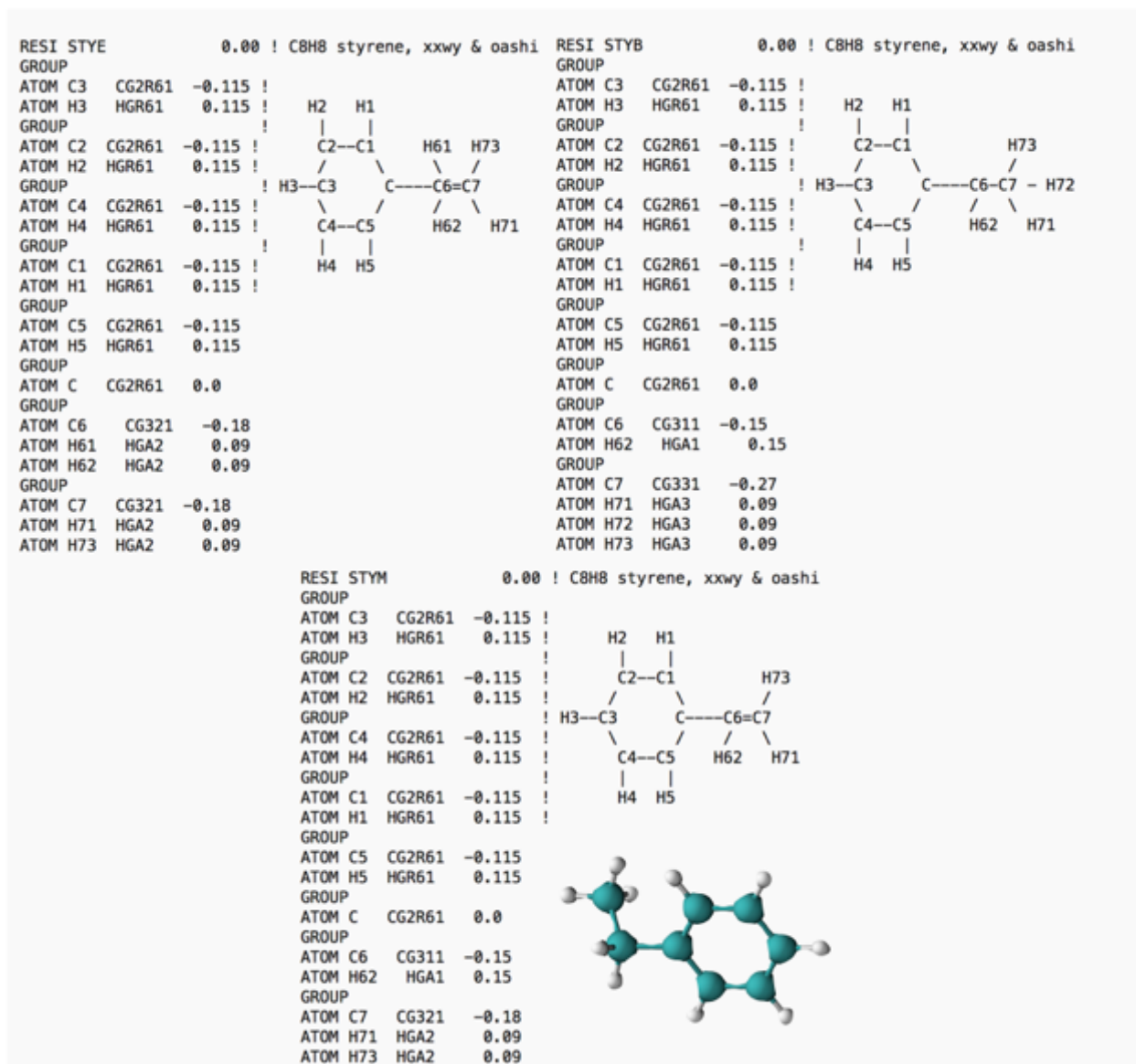


Figure 12-3: PS atom names, types, and partial charges. Images from the topology file used to generate PS structures indicating the atom name, CHARMM type, and partial charge on each line as well as an indication of the residue structure. For PS, we consider three residues: STYE and STYB are the end residues on a chain that contain an extra hydrogen atom (H61 or H72) that caps the chain and STYM residues that are in the middle of the chain and are bonded together to form the polymer. These topology files are obtained directly from the cgenff topology file as the

styrene monomer is already explicitly included as a residue type and modifications are made to accommodate polymerization of this molecule.

Finally, for the epoxy system we consider three different residue types. The first, bisphenol A diglycidyl ether (DGEBA), is shown in Figure 12-4 with the appropriate atom names, types, and partial charges. For the polyetherdiamine (PEDA), we consider molecules with a degree of polymerization of 2 and 3, with these structures and relevant force field information (names, types, and partial charges) shown in Figure 12-5 and Figure 12-6. In all cases, the penalty values for the partial charges were low enough such that no further verification was necessary. For the epoxy structures, estimates of the parameters by analogy were necessary for certain bonds, angles, and dihedrals and those estimates are shown in Table 12-1, Table 12-2, and Table 12-3. Specific bonds, angles, and dihedrals that are not shown are obtained directly from the CHARMM generalized force field and are available at: http://mackerell.umaryland.edu/charmm_ff.shtml#charmm

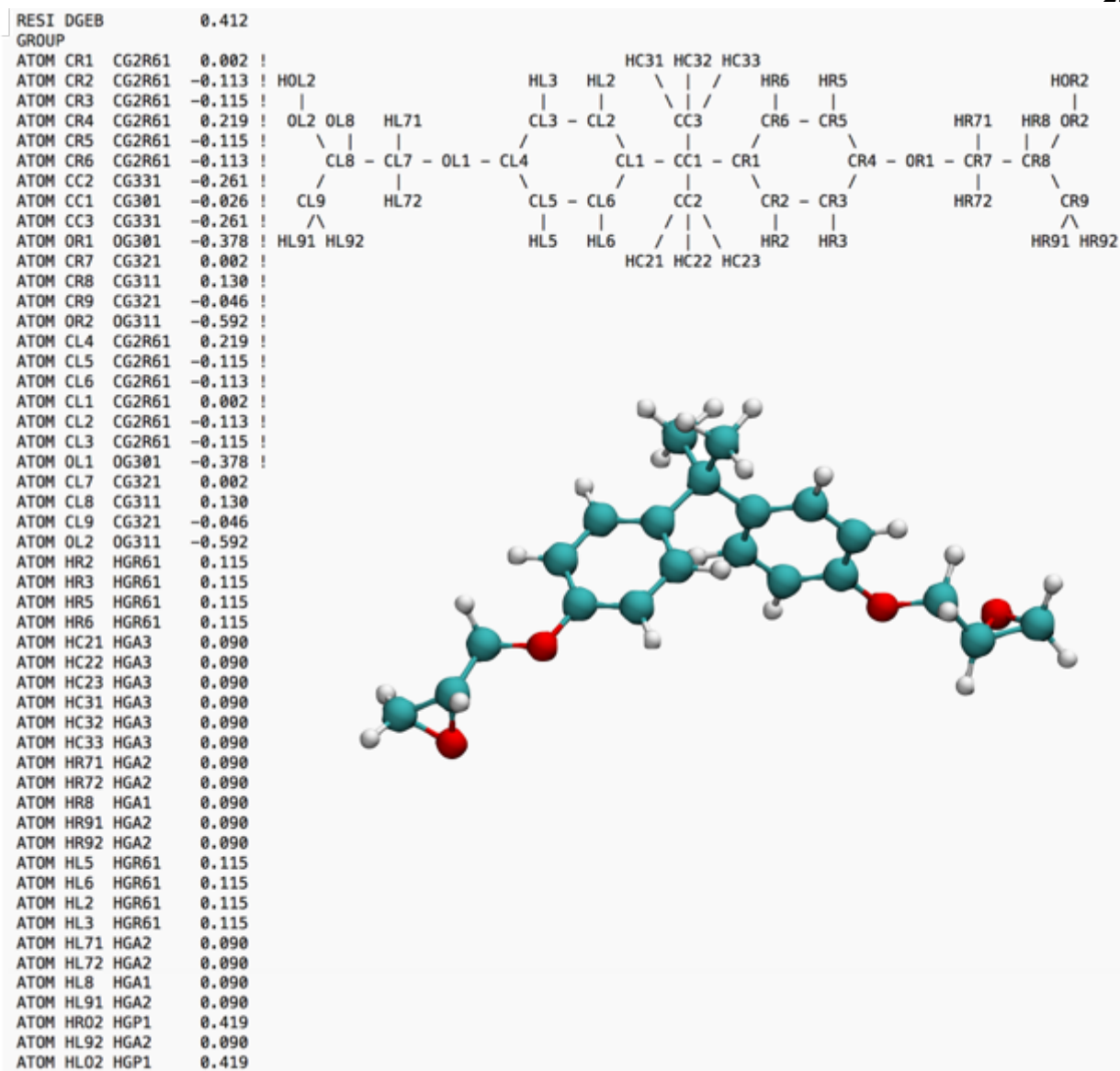


Figure 12-4: DGEBA atom names, types, and partial charges. Images from the topology file used to generate DGEBA component of the epoxy structures indicating the atom name, CHARMM type, and partial charge on each line as well as an indication of the residue structure.

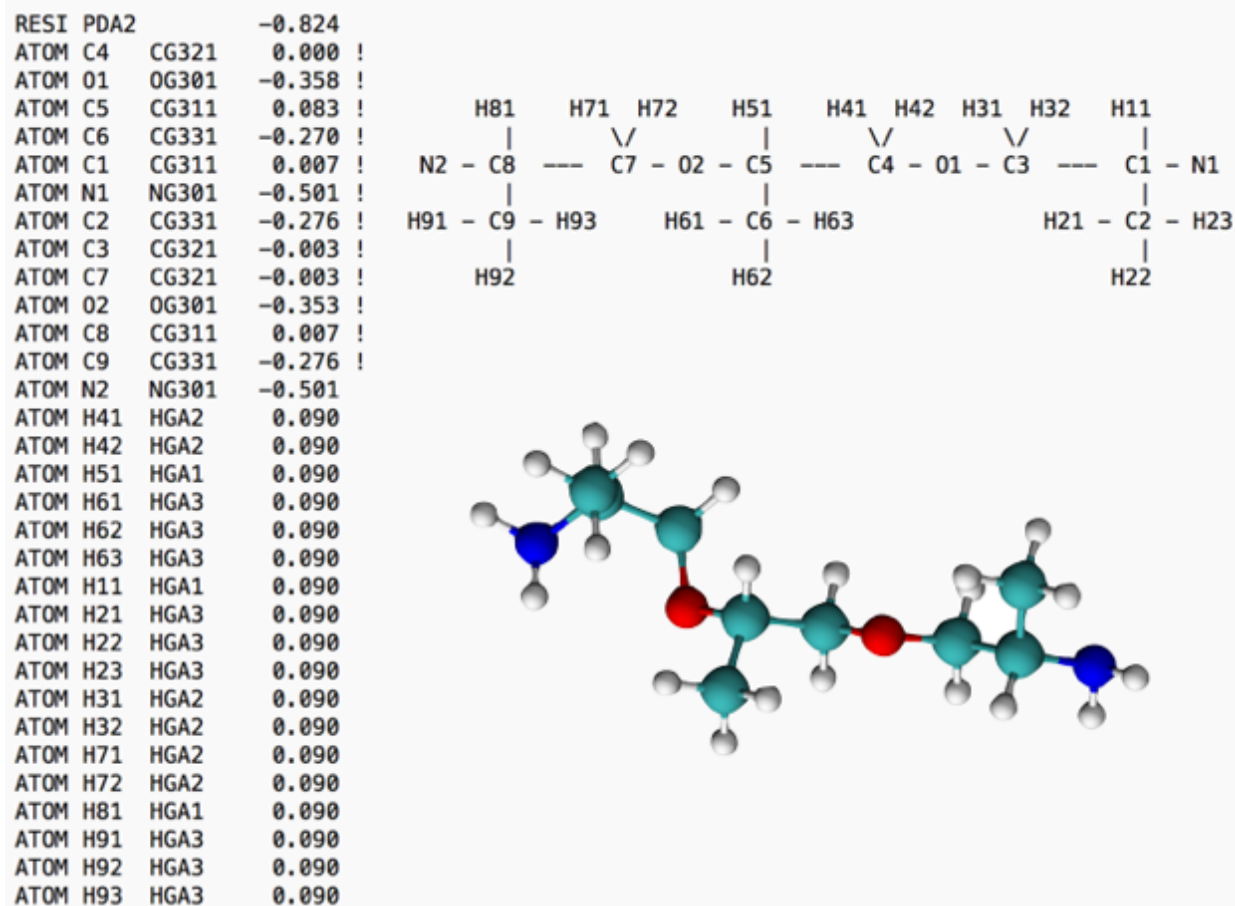


Figure 12-5: PEDDA (DP = 2) atom names, types, and partial charges. Images from the topology file used to generate PEDDA component of the epoxy structures indicating the atom name, CHARMM type, and partial charge on each line as well as an indication of the residue structure. Here, PEDDA is shown with a degree of polymerization of two.

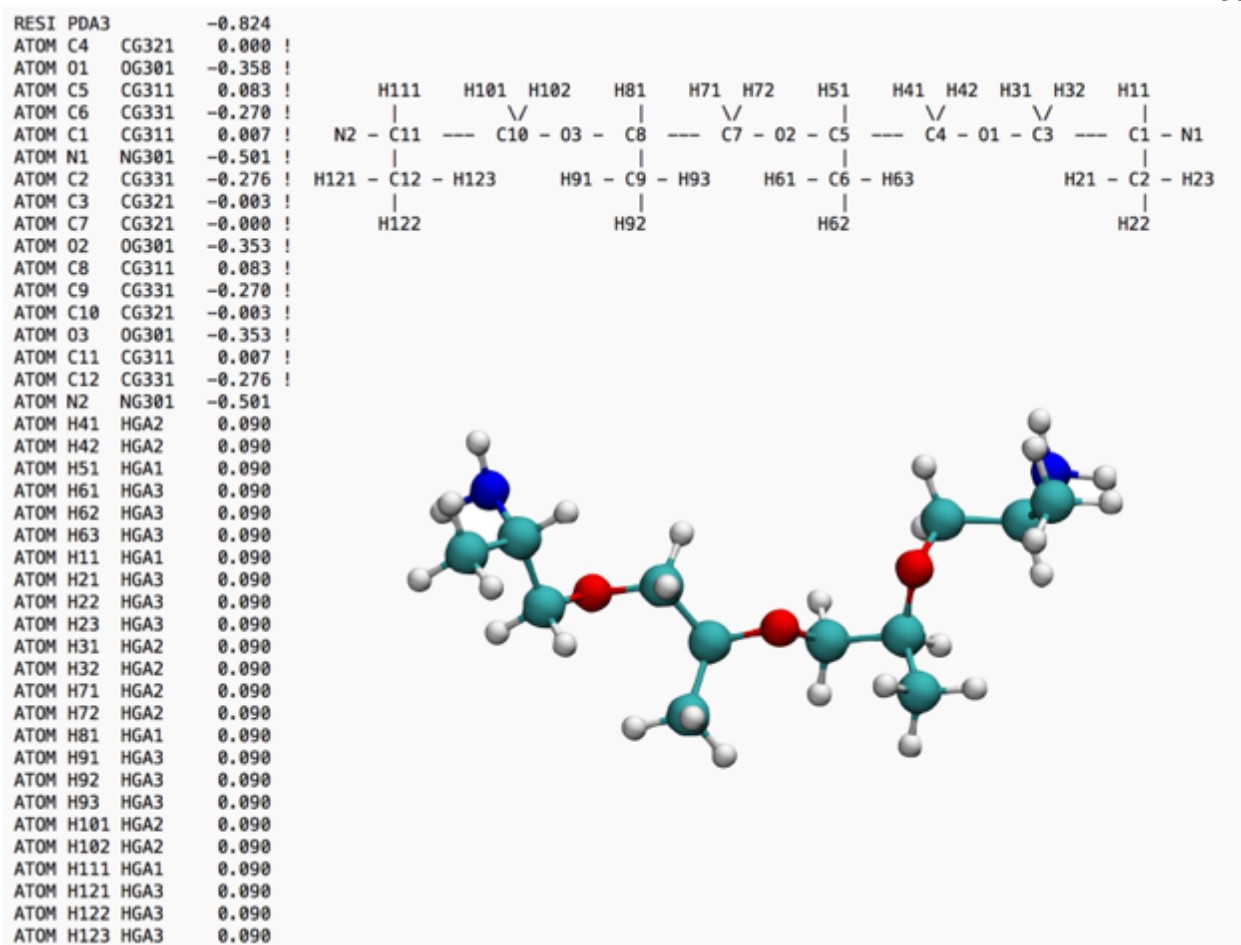


Figure 12-6: PEDA (DP = 3) atom names, types, and partial charges. Images from the topology file used to generate PEDA component of the epoxy structures indicating the atom name, CHARMM type, and partial charge on each line as well as an indication of the residue structure. Here, PEDA is shown with a degree of polymerization of three.

Table 12-1: Bond parameters for epoxy systems. List of the bond parameters determined from the cgenff program through analogy. The remaining bond parameters are determined directly from the generalized CHARMM force field.

Bond	k_b	b_0
CG2R61 CG301	230	1.49
CG321 NG301	263	1.474
CG331 NG301	255	1.463
CG311 NG301	263	1.474

Table 12-2: Angle parameters for epoxy systems. List of the angle parameters determined from the cgenff program through analogy. The remaining angle parameters are determined directly from the generalized CHARMM force field.

Angle			k_{θ}	θ_0
CG2R61	CG2R61	CG301	45.8	120
CG2R61	CG301	CG2R61	51.8	107.5
CG2R61	CG301	CG331	51.8	107.5
CG321	CG311	NG301	43.7	112.2
CG331	CG311	NG301	43.7	112.2
NG301	CG311	HGA1	32.4	109.5
OG301	CG311	OG301	70.49	107
CG311	CG321	NG301	43.7	112.2
CG311	CG321	OG301	75.7	110.1
NG301	CG321	HGA2	32.4	109.5
NG301	CG331	HGA3	30.5	109.7
CG311	NG301	CG311	53	110.9
CG311	NG301	CG321	53	110.9
CG321	NG301	CG321	53	110.9
CG321	NG301	CG331	53	110.9
CG331	NG301	CG331	53	110.9
CG311	OG301	CG321	95	109.7
CG321	CG311	OG301	115	109.7
CG311	CG321	OG301	75.7	110.1
CG311	OG301	CG321	95	109.7

Table 12-3: Dihedral parameters for epoxy systems. List of the dihedral parameters determined from the cgenff program through analogy. The remaining dihedral parameters are determined directly from the generalized CHARMM force field.

Dihedrals				k_{ϕ}	n	δ
CG331	CG311	CG321	OG301	0.2	3	0
OG301	CG311	CG321	OG301	0.2	3	0
OG301	CG311	CG321	HGA2	0.195	3	0
HGA1	CG311	CG321	OG301	0.195	3	0
CG321	CG311	OG301	CG321	0.4	1	0
CG321	CG311	OG301	CG321	0.49	3	0

CG331	CG311	OG301	CG321	0.4	1	0
CG331	CG311	OG301	CG321	0.49	3	0
HGA1	CG311	OG301	CG321	0.284	3	0
CG311	CG321	OG301	CG311	0.57	1	0
CG311	CG321	OG301	CG311	0.29	2	0
CG311	CG321	OG301	CG311	0.43	3	0
CG311	CG321	OG301	CG321	0.57	1	0
CG311	CG321	OG301	CG321	0.29	2	0
CG311	CG321	OG301	CG321	0.43	3	0
HGA2	CG321	OG301	CG311	0.284	3	0
CG2R61	CG2R61	CG2R61	CG301	3.1	2	180
CG301	CG2R61	CG2R61	HGR61	2.4	2	180
CG2R61	CG2R61	CG301	CG2R61	0.23	2	180
CG2R61	CG2R61	CG301	CG331	0.23	2	180
CG2R61	CG301	CG331	HGA3	0.04	3	0
CG321	CG311	CG321	NG301	0.2	3	180
CG321	CG311	CG321	OG301	0.2	3	180
CG331	CG311	CG321	OG301	0.2	3	0
NG301	CG311	CG321	OG301	0.2	3	0
NG301	CG311	CG321	HGA2	0.16	3	0
OG311	CG311	CG321	NG301	0.2	3	0
OG311	CG311	CG321	OG301	0.2	3	0
HGA1	CG311	CG321	NG301	0.16	3	0
HGA1	CG311	CG321	OG301	0.195	3	0
NG301	CG311	CG331	HGA3	0.16	3	0
CG321	CG311	NG301	CG311	0.1	3	0
CG321	CG311	NG301	CG321	0.1	3	0
CG331	CG311	NG301	CG311	2.5	1	180
CG331	CG311	NG301	CG311	1.5	2	0
CG331	CG311	NG301	CG311	0.5	3	0
CG331	CG311	NG301	CG321	2.5	1	180
CG331	CG311	NG301	CG321	1.5	2	0
CG311	CG321	NG301	CG321	2.5	1	180
CG331	CG311	NG301	CG321	0.5	3	0
HGA1	CG311	NG301	CG311	0	3	180
HGA1	CG311	NG301	CG321	0	3	180
CG331	CG311	OG301	CG321	0.4	1	0
CG331	CG311	OG301	CG321	0.49	3	0
OG301	CG311	OG301	CG321	0.51	1	0

OG301	CG311	OG301	CG321	0.67	2	0
OG301	CG311	OG301	CG321	0.26	3	0
OG301	CG311	OG301	CG331	0.51	1	0
OG301	CG311	OG301	CG331	0.67	2	0
OG301	CG311	OG301	CG331	0.26	3	0
HGA1	CG311	OG301	CG321	0.284	3	0
CG311	CG321	NG301	CG311	2.5	1	180
CG311	CG321	NG301	CG311	1.5	2	0
CG311	CG321	NG301	CG311	0.5	3	0
CG311	CG321	NG301	CG331	2.5	1	180
CG311	CG321	NG301	CG331	1.5	2	0
CG311	CG321	NG301	CG331	0.5	3	0
HGA2	CG321	NG301	CG311	0	3	180
HGA2	CG321	NG301	CG331	0	3	180
CG311	CG321	OG301	CG2R61	0.24	1	0
CG311	CG321	OG301	CG2R61	0.29	2	0
CG311	CG321	OG301	CG2R61	0.02	3	0
CG311	CG321	OG301	CG311	0.57	1	0
CG311	CG321	OG301	CG311	0.29	2	0
CG311	CG321	OG301	CG311	0.43	3	0
HGA2	CG321	OG301	CG311	0.284	3	0
HGA3	CG331	NG301	CG321	0	3	180
HGA3	CG331	NG301	CG331	0	3	180
HGA2	CG321	NG301	CG321	0	3	180

12.3 FFTK Parameters for CNC Surface Modifications

Initially, parameterization for the surface modifications of CNCs studied in this work was attempted through the cgenff program. This procedure worked well for the covalently bonded sulfate group studied in Chapters 6 and 8 (page 102 and page 135, respectively) as well as the atom transfer radical polymerization ATRP compound studied in Chapter 7 (page 122). The atom types, names, and partial charges for these two surface modifications are shown in Figure 12-7. The force field parameters that are assigned by analogy are included in Table 12-4 for the sulfate group and in Table 12-5 for the ATRP compound. For the ATRP compound, we include parameters for

Table 12-5: ATRP compound bond, angle and dihedral parameters. Bond, angle, and dihedral parameters for the ATRP compound that are obtained from the cgenff program through analogy. This table includes bond, angle, and dihedral parameters necessary for covalently bonding this compound to the CNC and polymer graft. Additional parameters are available from the generalized CHARMM force field parameter file.

Atom Name (Type)	Partial Charge	Angle	k_θ, θ_0
C1 (CG202)	0.791	CG301-CT2-CT1	58.35, 113.50
O1 (OG2D1)	-0.650	CG202-CG301-CT2	52.00, 108.00
C2 (CG301)	-0.141	CG331-CG301-CT2	58.35, 113.50
C3 (CG331)	-0.270	CG301-CT2-HA	26.50, 110.10
H1, H2, H3 (HGA3)	0.090		
C4 (CG331)	-0.270		
H4, H5, H6 (HGA3)	0.090		
Bond	k_b, b_0	Dihedral	k_ϕ, n, δ
CG301-CT2 (ATRP – PMMA Bond)	222.50, 1.538	CG301-CT2-CT1-CT3	0.2000, 3, 0
CG202 – OC311 (ATRP-CNC Bond)	150.0, 1.334	CG202-CG301-CT2-CT1	0.2000, 3, 0
		CG301-CT2-CT1-CC	0.2000, 3, 0
		OG2D1-CG202-CG301-CT2	0.0500, 6, 180
		CT2-CG301-CG331-HGA3	0.1600, 3, 0

When trying to assign parameters for the larger cations that replace sodium ions in several of our studies, we found that the cgenff program resulted in partial charges and parameters with extremely high penalty values. As discussed in Chapter 2 (page 27), we decided to use the force field toolkit (FFTK) parameterization procedure to determine new values of these parameters. In the following subsections, we present results of the FFTK parameterization for four different cations: methyltriphenylphosphonium (MePh^3P^+), 1-Hexyl-2,3dimethyl imidazolium (HxMe_2Im^+), 1-Hexadecyl-2,3-dimethyl imidazolium (HdMe_2Im^+), and 1,2,3-trimethylimidazolium (Me_3Im^+). First, we present an illustration of each cation with the atom names used. Second, we present a table that shows the CHARMM atom types, an initial estimation of the partial charges and the resulting partial charges after refinement using FFTK. Finally, we

include a table of bond, angle, and dihedral parameters that have been determined using FFTK and in addition to terms from the generalized CHARMM force field, allows us to simulate the behavior of these cations. For HdMe_2Im^+ we do not include a table of the parameters as they are identical to those for HxMe_2Im^+ as the only difference is an extended hydrocarbon chain.

12.3.A Methyltriphenylphosphonium (MePh_3P^+) Parameters

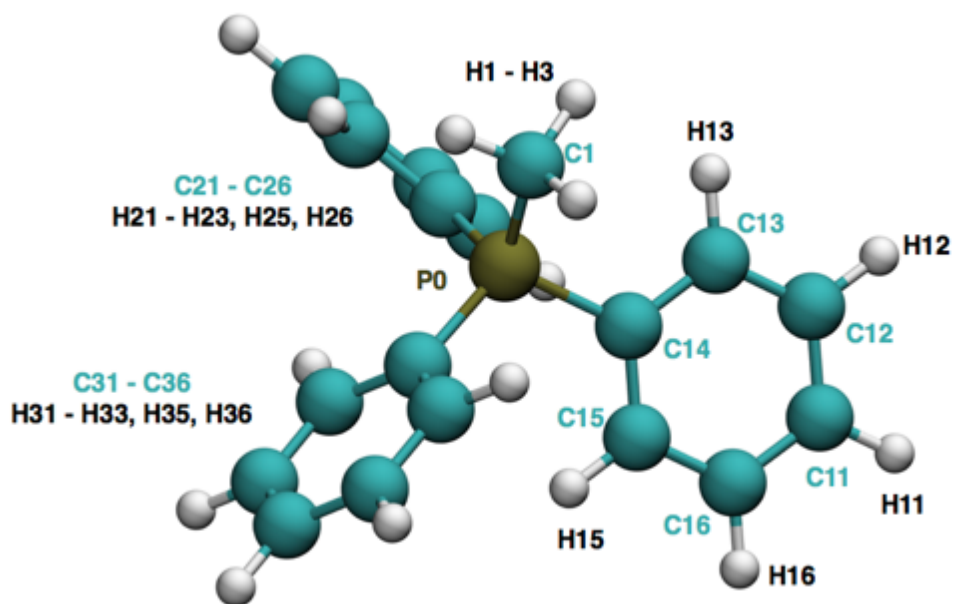


Figure 12-8: MePh_3P^+ cation atom names.

Table 12-6: MePh₃P⁺ atom types and partial charges. CHARMM atom types and partial charges calculated for each atom in the cation. We show initial estimates for the partial charges provided by cgenff and the refined values obtained using FFTK. Additionally, for hydrogen bond donors and acceptors, we show the interaction energy with water molecules calculated using QM that are used to determine the partial charges.

Atom Name	Atom Type	cgenff Partial Charge	cgenff Penalty	FFTK Partial Charge	QM Energy (kcal/mol)	MM Energy (kcal/mol)	QMD Delta (Å)
C11, C21, C31	CG2R61	-0.115	0.000	-0.115			
C12, C16, C22, C26, C36	CG2R61	-0.115	6.325	-0.115			
C13, C15, C23, C25, C33, C35	CG2R61	-0.249	19.992	-0.243			
C14, C24, C34	CG2R61	-0.446	187.222	0.041			
C1	CG331	-0.703	80.842	-0.519			
H11, H21, H31	HGR61	0.115	0.000	0.115	-17.807	-9.6	0.40
H12, H16, H22, H26, H32, H36	HGR61	0.115	0.000	0.115	-34.784	-23.351	0.40
H13, H15, H23, H25, H33, H35	HGR61	0.210	13.510	0.250	34.326	34.9	0.25–0.40
H1, H2, H3	HGA3	0.090	4.365	0.090	-25.95	-22.119	0.40
P0	PG0	2.005	326.244	1.084			
Total		0.000	N/A	1.000	-44.215	-20.17	Accept

Table 12-7: MePh₃P⁺ bond, angle, and dihedral parameters. Bond, angle, and dihedral parameters for the cation determined using the FFTK protocol. The remaining force field parameters are obtained from the generalized force field using the specified atom types.

Bond	k_b, b_0
CG2R61-PG0	217.766, 1.754
CG331-PG0	210.076, 1.805
Angle	k_θ, θ_0
CG2R61-CG2R61-PG0	23.547, 125.939
CG2R61-PG0-CG2R61	34.996, 111.069
CG2R61-PG0-CG331	42.808, 110.108
PG0-CG331-HGA3	46.946, 110.118
Dihedral	k_ϕ, n, δ
HGR61-CG2R61-CG2R61-PG0	2.5300, 4, 180.00
HGR61-CG2R61-CG2R61-PG0	18.6970, 2, 180.00
HGR61-CG2R61-CG2R61-PG0	12.1320, 3, 0.00
CG2R61-CG2R61-PG0-CG331	0.2720, 6, 180.00
CG2R61-CG2R61-PG0-CG331	6.1010, 3, 0.00
CG2R61-CG2R61-CG2R61-PG0	10.3110, 2, 180.00
CG2R61-CG2R61-CG2R61-PG0	2.1940, 4, 0.00
CG2R61-CG2R61-PG0-CG2R61	2.3590, 3, 0.00
CG2R61-CG2R61-PG0-CG2R61	0.3520, 6, 0.00
CG2R61-CG2R61-PG0-CG2R61	1.2470, 4, 180.00
CG2R61-CG2R61-PG0-CG2R61	2.0720, 2, 0.00
HGA3-CG331-PG0-CG2R61	0.0710, 6, 0.00
HGA3-CG331-PG0-CG2R61	0.1020, 3, 180.00

12.3.B 1-Hexyl-2,3-dimethyl imidazolium (HxMe₂Im⁺) Parameters

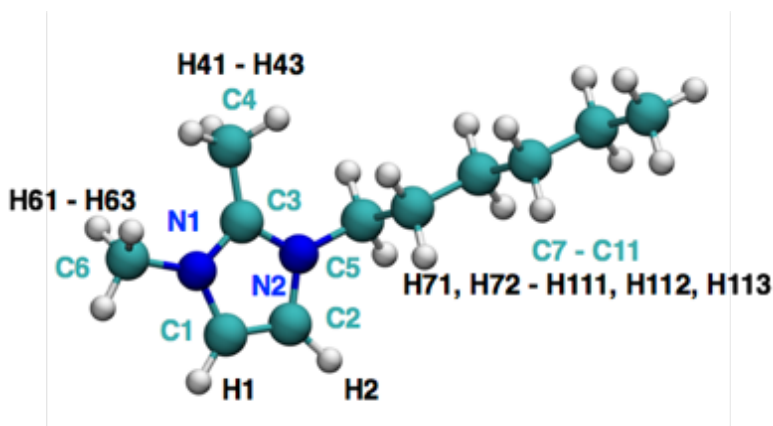


Figure 12-9: HxMe₂Im⁺ cation atom names.

Table 12-8: HxMe₂Im⁺ atom types and partial charges. CHARMM atom types and partial charges calculated for each atom in the cation. We show initial estimates for the partial charges provided by cgenff and the refined values obtained using FFTK. Additionally, for hydrogen bond donors and acceptors, we show the interaction energy with water molecules calculated using QM that are used to determine the partial charges.

Atom Name	Atom Type	cgenff Partial Charge	cgenff Penalty	FFTK Partial Charge	QM Energy (kcal/mol)	MM Energy (kcal/mol)	QMD Delta (Å)
N1	NG2R52	-0.524	80.157	0.258	0.088	0.079	0.40
N2	NG2R52	-0.491	80.114	-0.467	0.087	0.077	0.40
C1	CG2R51	0.209	31.451	-0.419			
C2	CG2R51	0.209	31.451	-0.186			
C3	CG2R53	0.363	47.235	0.404			
C4	CG331	-0.101	43.622	-0.178			
C5	CG324	0.211	79.443	0.277			
C6	CG334	0.156	79.682	-0.052			
C7	CG321	-0.173	3.949	-0.173			
C8	CG321	-0.184	0.000	-0.184			
C9	CG321	-0.181	0.000	-0.181			
C10	CG321	-0.180	0.000	-0.180			
C11	CG331	-0.270	0.000	-0.270			
H1	HGR52	0.123	21.198	0.332	-10.277	-9.808	0.20
H2	HGR52	0.123	21.198	0.309	-9.891	-9.204	0.20
All Other Hydrogens	HGA2 or HGA3	0.090	2.407 - 3.537	0.090	-108.226	-88.15	0.20 - 0.40
Total		1.000	N/A	1.000	-128.219	-107.006	Accept

Table 12-9: HxMe₂Im⁺ bond, angle, and dihedral parameters. Bond, angle, and dihedral parameters for the cation determined using the FFTK protocol. The remaining force field parameters are obtained from the generalized force field using the specified atom types.

Bond	k_b, b_0
NG2R52-CG324	294.923, 1.471
NG2R52-CG334	295.687, 1.385
CG2R53-CG331	334.175, 1.466
Angle	k_θ, θ_0
NG2R52-CG334-HGA3	90.013, 107.091
NG2R52-CG324-CG321	63.337, 111.796
NG2R52-CG2R53-CG331	60.232, 131.497
CG2R51-NG2R52-CG324	92.955, 127.525
CG2R51-NG2R52-CG334	47.316, 125.455
NG2R52-CG334-HGA3	51.209, 107.334
CG2R53-CG331-HGA3	55.383, 110.745
CG2R53-NG2R52-CG334	41.961, 122.269
CG2R53-NG2R52-CG324	43.691, 127.760
Dihedral	k_ϕ, n, δ
CG2R53-NG2R53-CG324-CG321	7.0970, 6, 0
NG2R52-CG2R53-CG331-HGA3	0.1860, 6, 180
NG2R52-CG324-CG321-CG321	2.2720, 3, 180
CG334-NG2R52-CG2R53-CG331	2.1360, 2, 0
CG2R51-NG2R52-CG2R53-CG331	1.3020, 2, 180
CG324-NG2R52-CG2R51-CG2R51	7.7120, 2, 0
CG2R51-CG2R51-NG2R52-CG334	14.9740, 2, 180
HGR52-CG2R51-NG2R52-CG334	9.9520, 2, 180
CG2R51-NG2R52-CG324-HGA2	2.2260, 6, 180
CG324-NG2R52-CG2R53-NG2R52	1.7720, 2, 180
CG334-NG2R52-CG2R53-NG2R52	10.730, 2, 0
CG324-NG2R52-CG2R53-CG331	10.6850, 2, 180
CG2R53-NG2R52-CG324-HGA2	5.2110, 6, 180
CG2R51-NG2R52-CG334-HGA3	0.9940, 6, 180
CG2R53-NG2R52-CG334-HGA3	2.1420, 6, 0
NG2R52-CG324-CG321-HGA2	3.5450, 3, 0
CG324-NG2R52-CG2R51-HGR52	14.9960, 2, 180
CG2R51-NG2R52-CG324-CG321	8.4490, 6, 0

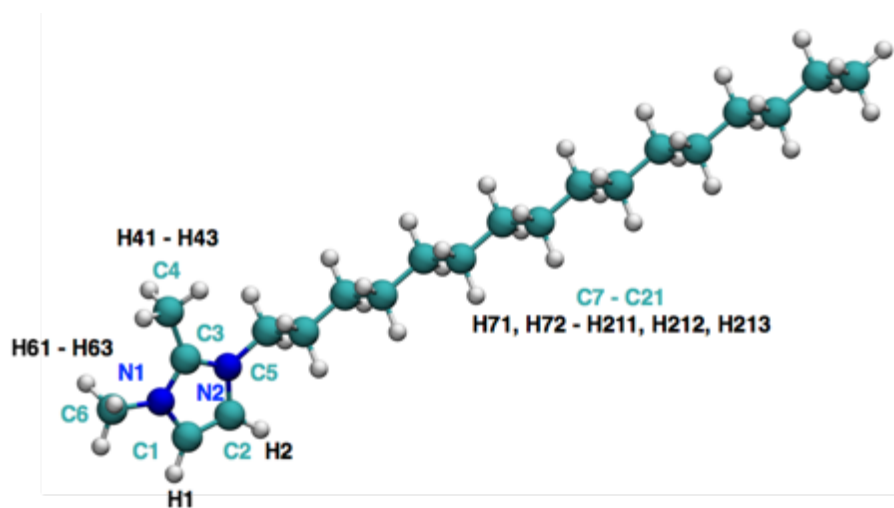
12.3.C 1-Hexadecyl-2,3-dimethyl imidazolium (HdMe₂Im⁺) ParametersFigure 12-10: HdMe₂Im⁺ cation atom names.

Table 12-10: HdMe₂Im⁺ atom types and partial charges. CHARMM atom types and partial charges calculated for each atom in the cation. We show initial estimates for the partial charges provided by cgenff and the refined values obtained using FFTK. Additionally, for hydrogen bond donors and acceptors, we show the interaction energy with water molecules calculated using QM that are used to determine the partial charges.

Atom Name	Atom Type	cgenff Partial Charge	cgenff Penalty	FFTK Partial Charge	QM Energy (kcal/mol)	MM Energy (kcal/mol)	QMD Delta (Å)
N1	NG2R52	-0.524	80.157	0.258	0.088	0.079	0.40
N2	NG2R52	-0.491	80.114	-0.467	0.087	0.077	0.40
C1	CG2R51	0.209	31.451	-0.419			
C2	CG2R51	0.209	31.451	-0.186			
C3	CG2R53	0.363	47.235	0.404			
C4	CG331	-0.101	43.622	-0.178			
C5	CG324	0.211	79.443	0.277			
C6	CG334	0.156	79.682	-0.052			
C7	CG321	-0.173	3.949	-0.173			
C8	CG321	-0.184	0.000	-0.184			
C9	CG321	-0.181	0.000	-0.181			
C10	CG321	-0.180	0.000	-0.180			
C11	CG321	-0.180	0.000	-0.180			
C12	CG321	-0.180	0.000	-0.180			
C13	CG321	-0.180	0.000	-0.180			
C14	CG321	-0.180	0.000	-0.180			
C15	CG321	-0.180	0.000	-0.180			
C16	CG321	-0.180	0.000	-0.180			
C17	CG321	-0.180	0.000	-0.180			
C18	CG321	-0.180	0.000	-0.180			
C19	CG321	-0.180	0.000	-0.180			
C20	CG321	-0.180	0.000	-0.180			
C21	CG331	-0.270	0.000	-0.270			
H1	HGR52	0.123	21.198	0.332	-10.277	-9.808	0.20
H2	HGR52	0.123	21.198	0.309	-9.891	-9.204	0.20
All Other Hydrogens	HGA2 or HGA3	0.090	2.407 - 3.537	0.090	-108.226	-88.15	0.20 - 0.40
Total		1.000	N/A	1.000	-128.219	-107.006	Accept

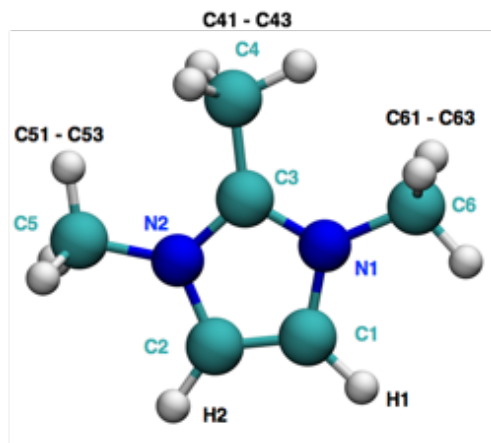
12.3.D 1,2,3-trimethylimidazolium (Me_3Im^+) ParametersFigure 12-11: Me_3Im^+ cation atom names.

Table 12-11: Me_3Im^+ atom types and partial charges. CHARMM atom types and partial charges calculated for each atom in the cation. We show initial estimates for the partial charges provided by cgenff and the refined values obtained using FFTK. Additionally, for hydrogen bond donors and acceptors, we show the interaction energy with water molecules calculated using QM that are used to determine the partial charges.

Atom Name	Atom Type	cgenff Partial Charge	cgenff Penalty	FFTK Partial Charge	QM Energy (kcal/mol)	MM Energy (kcal/mol)	QMD Delta (Å)
N1	NG2R52	-0.524	80.158	0.427	0.079	0.070	0.400
N2	NG2R52	-0.524	80.158	-0.336	0.0650	0.058	0.400
C1	CG2R51	0.209	32.099	-0.549			
C2	CG2R51	0.209	32.099	-0.486			
C3	CG2R53	0.363	47.237	-0.011			
C4	CG331	-0.101	43.622	-0.155			
C5	CG334	0.156	79.682	0.343			
C6	CG334	0.156	79.682	0.065			
H1	HGR52	0.123	21.198	0.413	-10.160	-10.479	0.150
H2	HGR52	0.123	21.198	0.479	-10.633	-11.113	0.150
H41, H42, H43, H51, H52, H53, H61, H62, H63	HGA3	0.090	2.407 - 3.537	0.090	-78.411	-63.57	0.150 - 0.400
Total		1.000	N/A	1.000	-99.1311	-85.034	Accept

Table 12-12: Me₃Im⁺ bond, angle, and dihedral parameters. Bond, angle, and dihedral parameters for the cation determined using the FFTK protocol. The remaining force field parameters are obtained from the generalized force field using the specified atom types.

Bond	k_b, b_0
CG2R61-PG0	217.766, 1.754
CG331-PG0	210.076, 1.805
Angle	k_θ, θ_0
CG2R61-CG2R61-PG0	23.547, 125.939
CG2R61-PG0-CG2R61	34.996, 111.069
CG2R61-PG0-CG331	42.808, 110.108
PG0-CG331-HGA3	46.946, 110.118
Dihedral	k_ϕ, n, δ
HGR52-CG2R51-NG2R52-CG334	2.9990, 3, 180
CG2R51-CG2R51-NG2R52-CG334	0.1910, 3, 180
CG2R53-NG2R52-CG334-HGA3	0.1320, 3, 0
NG2R52-CG2R53-CG331-HGA3	1.3170, 3, 0
CG334-NG2R52-CG2R53-NG2R52	1.5980, 3, 0
CG334-NG2R52-CG2R53-CG331	2.6050, 3, 180
CG2R51-NG2R52-CG334-HGA3	0.2410, 3, 0
CG2R51-NG2R52-CG2R53-CG331	2.8150, 3, 0

Chapter 13 – Appendix: Interfacial Mechanics Results for Additional CNC Lengths

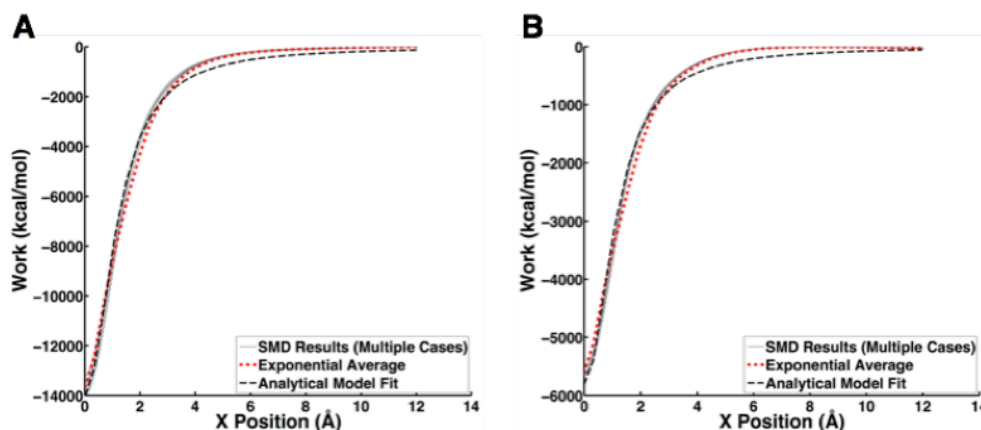


Figure 13-1: Energy landscapes of CNC-CNC interfacial separation (10.38 nm length). Additional work vs displacement curves obtained for SMD simulations of separating the (A) (110)–(110) interface and (B) (200)–(200) interface for a CNC having a length of 10.38 nm. In both plots the gray, solid curves represent energy landscapes for 10 individual simulations, the red, dotted curves represent the exponential average of these different cases, and the blue, dashed curves represent the analytical model discussed in Section 4.4.

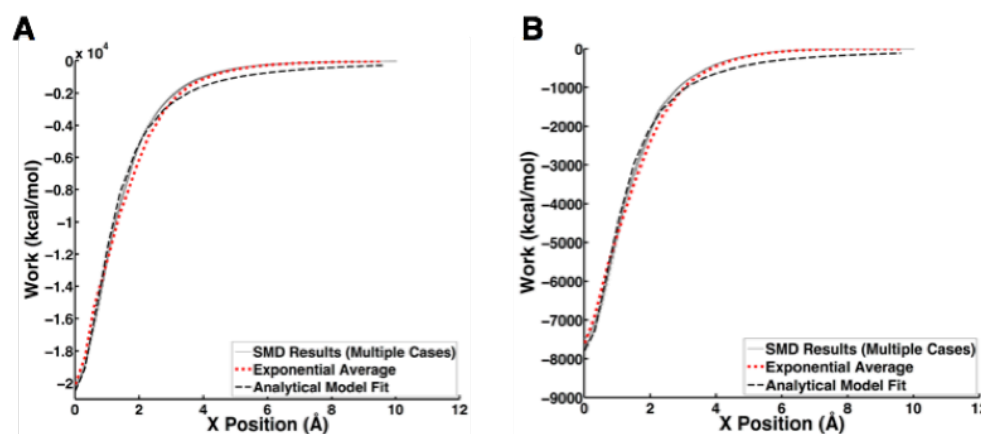


Figure 13-2: Energy landscapes of CNC-CNC interfacial separation (15.57 nm length). Additional work vs displacement curves obtained for SMD simulations of separating the (A) (110)–(110) interface and (B) (200)–(200) interface for a CNC having a length of 15.57 nm. In both plots the gray, solid curves represent energy landscapes for 10 individual simulations, the red, dotted curves represent the exponential average of these different cases, and the blue, dashed curves represent the analytical model discussed in Section 4.4.

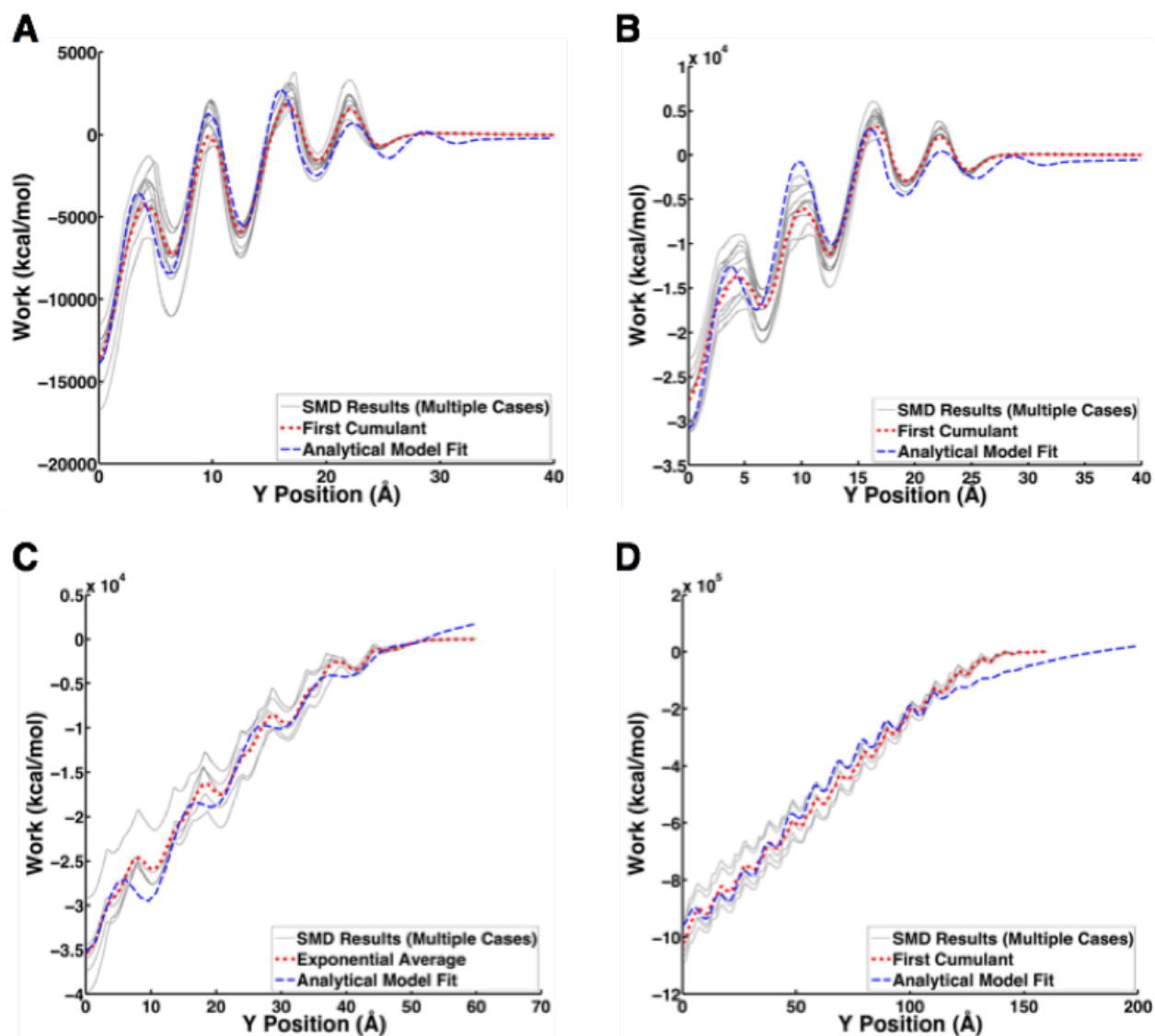


Figure 13-3: Energy landscapes of (110)–(110) interfacial shear (additional lengths). Additional work vs displacement curves obtained for SMD simulations of shearing the (110)–(110) interface (A) along the width for a 10.38 nm CNC, (B) along the width for the 15.57 nm CNC, (C) along the length for a 5.19 nm CNC, and (D) along the length for a 15.57 nm CNC. In all plots the gray, solid curves represent energy landscapes for 10 individual simulations, the red, dotted curves represent the exponential average of these different cases, and the blue, dashed curves represent the analytical model discussed in Section 4.4.

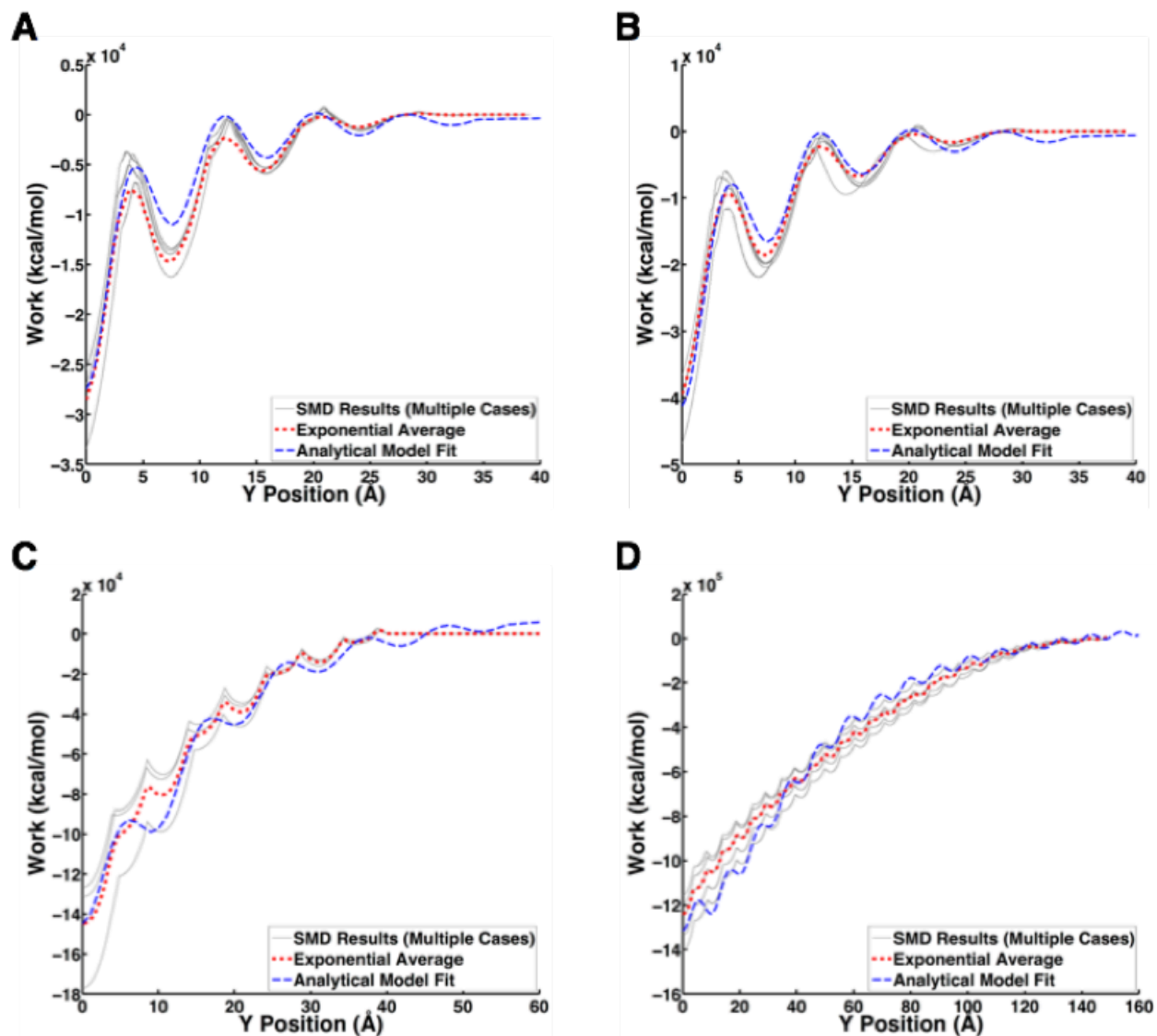


Figure 13-4: Energy landscapes of (200)-(200) interfacial shear (additional lengths). Additional work vs displacement curves obtained for SMD simulations of shearing the (200)-(200) interface (A) along the width for a 10.38 nm CNC, (B) along the width for the 15.57 nm CNC, (C) along the length for a 5.19 nm CNC, and (D) along the length for a 15.57 nm CNC. In all plots the gray, solid curves represent energy landscapes for 10 individual simulations, the red, dotted curves represent the exponential average of these different cases, and the blue, dashed curves represent the analytical model discussed in Section 4.4.

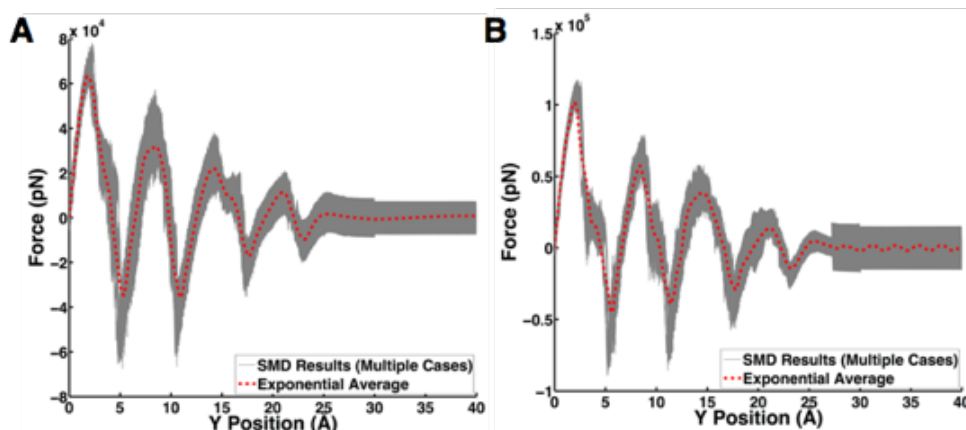


Figure 13-5: Force-displacement curves for (110)–(110) interfacial shear (additional lengths). The force-displacement curves for shearing of the (110)–(110) interface along the width for a (A) 10.38 nm length CNC and (B) 15.57 nm length CNC. The gray curves represent force-displacement curves from all of the individual SMD simulations while the red, dashed line represents the exponential average of these simulations. These results again shows that the (110)–(110) interface exhibits a smooth, sinusoidal shape in the force-displacement curve indicative of continuous interfacial sliding.

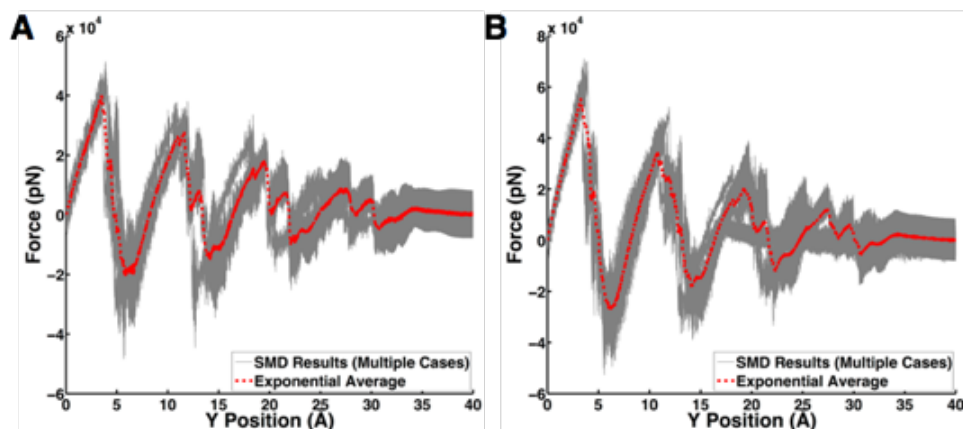


Figure 13-6: Force-displacement curves for (200)–(200) interfacial shear (additional lengths). The force-displacement curves for shearing of the (200)–(200) interface along the width for a (A) 10.38 nm length CNC and (B) 15.57 nm length CNC. The gray curves represent force-displacement curves from all of the individual SMD simulations while the red, dashed line represents the exponential average of these simulations. These results again shows that the (200)–(200) interface exhibits a sharp, zigzag shape in the force-displacement curve indicative of stick-slip interfacial friction.

Chapter 14 – Curriculum Vitae

4144 N Sheridan Rd, APT 508
Chicago, IL 60613

Robert Sinko

robertsinko2012@u.northwestern.edu
Cell: (440) 829-4518

EDUCATION

Northwestern University Evanston, IL
Ph.D in Mechanical Engineering, GPA 4.0/4.0 *September 2017*

- Developed expertise in computational materials science and applied mechanics with an emphasis on biological and bioinspired materials.
- Provisional thesis title: “A computational materials-by-design approach for cellulose-based nanocomposites”. Advisor: Sinan Keten.
- Thesis committee: Sinan Keten, Catherine Brinson, Randall Snurr.

Northwestern University Evanston, IL
M.S. in Mechanical Engineering, GPA 4.0/4.0 *December 2015*

- Thesis title: “A Molecular Dynamics Approach to Understanding Size Effects and Interfacial Mechanics of Cellulose Nanocrystals”. Advisor: Sinan Keten.

Miami University Oxford, OH
B.S. in Mechanical Engineering and B.S. in Statistics, GPA 4.0/4.0 *May 2012*

- University Honors with Distinction and Mechanical Engineering Departmental Honors
- Undergraduate thesis title: “Characterization, Modeling, and Applications of Novel Magneto-Rheological Elastomers”. Advisor: Jeong-Hoi Koo.

AWARDS

National Defense Science & Engineering Graduate (NDSEG) Fellowship *2013-2016*
Northwestern ME Department Graduate Leadership and Service Award *2014*
Northwestern University Walter P. Murphy Fellowship *2012-2013*
Tau Beta Pi Fellowship *2012-2013*

RESEARCH EXPERIENCE

Northwestern University *September 2012 – August 2017*
Advisor: Sinan Keten

- Conducted a wide variety of molecular dynamics simulations focused on the interfacial mechanics of cellulose nanocrystals (CNCs) to determine their nanoscale interfacial properties.
- Explained why CNCs found in nature are nanoscale in size by studying how the fracture energy of these materials is related to their size using both simulation results and theoretical derivations.
- Demonstrated the effect of water and surface hydrophilicity on CNC-CNC interfacial properties and showed how these quantities can be used to predict the mechanical properties of CNC thin films.
- Developed multiscale models of CNC-polymer nanocomposites that are able to predict bulk macroscale properties (glass transition temperature and dispersion) from nanoscale interfacial adhesion energies.
- Explained the nanoscale origins of the Pickett effect in cementitious materials using coarse-grained MD simulations of water flow in a nanopore coupled with analytical models of nanoscale energy barriers.
- Research resulted in five first author publications, two additional co-authored publications, three review articles, and six conference presentations.

Miami University *September 2010 – May 2012*
Advisor: Jeong-Hoi Koo

- Prepared samples of hard magnetorheological elastomers (H-MRE) with magnetic particles embedded in rubbery polymers for use as actuators and vibration absorbers.
- Designed and conducted experiments to assess the feasibility of H-MRE materials to be utilized in active vibration absorbers that change their natural frequency in response to an applied magnetic field.
- Developed models to predict the displacement and blocking force of H-MRE actuators and obtained experimental results to verify these models.
- Traveled abroad in support of project research at Korea Advanced Institute of Science and Technology (KAIST) from May – July 2011.
- Research resulted in one first author publication and two conference presentations.

TEACHING EXPERIENCE

Northwestern Searle Center for Advancing Learning & Teaching *September 2016 – May 2017*
Teaching Certificate Program

- Participating in the graduate student teaching certificate program aimed at helping students develop reflective teaching practices and designing learner-centered courses.
- Program includes eight seminars, two teaching workshops, as well as discussions with peer and faculty

mentors to gain feedback on teaching methods and course design.

- Completing a course-design project focused on the Computational Nanodynamics (ME 416-1) graduate course at Northwestern and will develop course objectives, lesson plans, assessments, and evaluations.
- Co-teaching ME 416-1 in Spring 2017.

ME 416-1 Computational Nanodynamics

May 2014 – June 2017

ME 418-1 Multiscale Modeling & Simulation in Mechanics II

Guest Lecturer (Instructor: Sinan Keten)

- Delivered guest lectures that combined components of research with fundamental principles in support of the course curriculum such as steered molecular dynamics, coarse-graining methods, dissipative particle dynamics, etc.
- Lectures delivered were:
 - “Atomistic Modeling of Nanoscale Creep and Cellulosic Materials” (Feb. 2016)
 - “Interfacial Mechanics of Cellulose Nanocrystal-Based Nanocomposites” (May 2015)
 - “Interfacial Mechanics of Cellulose Nanocrystals” (May 2014)
- Designed homework problems based on research to illustrate the concepts of steered molecular dynamics and interfacial energy calculations.

GEN_ENG 206-3 Engineering Analysis III Honors

March 2013 – June 2013

Teaching Assistant (Instructor: Sridhar Krishnaswamy)

- First-year undergraduate course focused on dynamics of particles, friction, energy and momentum conservation, spring-block-damper mechanical oscillators, electrical oscillators, and computational methods with MATLAB.
- Graded homework/quizzes and conducted a weekly recitation section to review homework solutions with students and prepare them for quizzes.
- Assisted students with a final project in which they had to apply concepts of dynamic systems learned in class to a project of their own choosing. Assisted students in identifying real-world dynamic systems and developing codes to analyze problems using MATLAB.
- 5.5/6.0 average CTEC rating

Rinella Learning Center, Miami University

January 2011 – May 2012

Student Tutor

- Tutored students in engineering courses through weekly one-on-one appointments.
- Developed learning plans for students based on their individual needs in an attempt to improve study habits, problem-solving skills, and performance on exams/quizzes/homework.

**ADVISING &
LEADERSHIP
EXPERIENCE**

Northwestern University

May 2015 – August 2015

Graduate Research Mentor

March 2016 – August 2016

- Advised two undergraduate students working in our research group during the summer through the SROP program on research related to cellulose nanocrystals.
- Taught the students the basics of molecular dynamics simulations and advised them on conducting and analyzing simulations focused on understanding the interactions of cellulose with other materials including silica/concrete and gases.

United States Association of Computational Mechanics Student Chapter

October 2015 – August 2017

Treasurer and Founding Member

- Founding member of the Northwestern student chapter of USACM.
- Focused on securing funding sources to start holding events for the chapter including social events and student-led seminar series and journal clubs.

Mechanical Engineering Graduate Student Society (MEGSS)

March 2013 – January 2015

President, Recruitment Chair, and Social Chair

- Served as president of MEGSS for one year (January 2014 – 2015) and oversaw all the associated programs including social and professional development events as well as the recruiting weekend. Managed the organizations finances and obtaining appropriate funding throughout the year.
- Served as a social chair and recruitment chair for MEGSS and was responsible for planning social events for students in the department as well as planning recruiting for prospective students.

PUBLICATIONS

- [1] Sinko, R., Bažant, Z. P. , & Keten, S. “ A nanoscale perspective on the effects of transverse microprestress on drying creep of nanoporous solids ” (In submission).
- [2] Sinko, R. & Keten, S. “Effects of water at CNC-epoxy interfaces.” (In preparation).
- [3] Wei, Z. *, Sinko, R. *, Keten, S., Luijten, E. “Effect of surface modification on the water adsorption and interfacial mechanics of cellulose nanocrystals” (*Indicates co-first authorship) (In preparation)
- [4] Sinko, R., Xia, W., Keten, S. “Local polymer dynamics of poly(methyl methacrylate) in cellulose nanocrystal-polymer nanocomposites” (In preparation)
- [5] Fox, D., Rodriguez, R., Devilbiss, M., Davis, C., Woodcock, J., Sinko, R., Keten, S., Gilman, J. “Simultaneously Tailoring Surface Energies and Thermal Stabilities of Cellulose Nanocrystals Using Ion Exchange: Effects on Polymer Composite Properties for Transportation, Infrastructure, and Renewable Energy Applications” *ACS Applied Materials & Interfaces* 8, 27270-27281, doi:10.1021/acsami.6b06083 (2016).
- [6] Sinko, R., Vandamme, M., Bažant, Z. P. & Keten, S. Transient effects of drying creep in nanoporous solids: understanding the effects of nanoscale energy barriers. *Proceedings of the Royal Society A: Mathematical, Physical and Engineering Science* 472, doi:10.1098/rspa.2016.0490 (2016).
- [7] Qin, X., Xia, W., Sinko, R. & Keten, S. Tuning Glass Transition in Polymer Nanocomposites with Functionalized Cellulose Nanocrystals through Nanoconfinement. *Nano Letters* 15, 6738-6744, doi:10.1021/acs.nanolett.5b02588 (2015).
- [8] Sinko, R. & Keten, S. Understanding emergent functions in self-assembled fibrous networks. *Nanotechnology* 26, 352501 (2015).
- [9] Egan, P., Sinko, R., LeDuc, P. R. & Keten, S. The role of mechanics in biological and bio-inspired systems. *Nat Commun* 6, doi:10.1038/ncomms8418 (2015).
- [10] Sinko, R., Qin, X. & Keten, S. Interfacial mechanics of cellulose nanocrystals. *MRS Bulletin* 40, 340-348 (2015).
- [11] Sinko, R. & Keten, S. Traction–separation laws and stick–slip shear phenomenon of interfaces between cellulose nanocrystals. *Journal of the Mechanics and Physics of Solids* 78, 526-539, doi:http://dx.doi.org/10.1016/j.jmps.2015.02.012 (2015).
- [12] Sinko, R. & Keten, S. Effect of moisture on the traction-separation behavior of cellulose nanocrystal interfaces. *Applied Physics Letters* 105, 243702, doi:doi:http://dx.doi.org/10.1063/1.4904708 (2014).
- [13] Sinko, R., Mishra, S., Ruiz, L., Brandis, N. & Keten, S. Dimensions of Biological Cellulose Nanocrystals Maximize Fracture Strength. *ACS Macro Letters* 3, 64-69, doi:10.1021/mz400471y (2014).
- [14] Sinko, R., Karnes, M., Koo, J.-H., Kim, Y.-K. & Kim, K.-S. Design and test of an adaptive vibration absorber based on magnetorheological elastomers and a hybrid electromagnet. *Journal of Intelligent Material Systems and Structures* 24, 803-812, doi:10.1177/1045389x12463461 (2013).

PRESENTATIONS

- [1] Sinko, R. Improving Dispersion in Cellulose Nanocrystal-Polymer Composites through Ion-Exchange Surface Modifications . 2nd Midwest Workshop on Mechanics of Materials and Structures August 15, 2016, Northwestern University, Evanston, IL, USA (poster presentation)
- [2] Keten, S.; Designing Better Structural Materials by Understanding Nanoconfinement and Nanoscale Interfaces. 2016 Engineering Mechanics Institute (EMI) Conference May 22-25, 2016, Vanderbilt University, Nashville, TN, USA (Presented by Sinko, R.)
- [3] Sinko, R.; Vandamme, M.; Bažant, Z.; Keten, S.; Transient Effects of Drying Creep in Nanoporous Solids: Understanding the Effects of Nanoscale Energy Barriers. 2016 Engineering Mechanics Institute (EMI) Conference May 22-25, 2016, Vanderbilt University, Nashville, TN, USA
- [4] Sinko, R; Keten, S.; Atomistic simulation and modeling of the interface between cellulose nanocrystal elementary fibrils. Society of Engineering Science 51st Annual Technical Meeting October 1-3, 2014, Purdue University, West Lafayette, IN, USA
- [5] Sinko, R.; Keten, S.; Atomistic Simulations on the Fracture Strength of Cellulose Nanocrystals (CNCs) and CNC-CNC Interfaces. 17th U.S. National Congress on Theoretical & Applied Mechanics (USNCTAM) June 15-20, 2014, Michigan State University, East Lansing, MI, USA
- [6] Sinko, R.; Keten, S.; Development of a computational model to study nanoscale interactions in new generations of nanocomposites. 2013 Engineering Mechanics Institute (EMI) Conference August 4-7, 2013, Northwestern University, Evanston, IL, USA (poster presentation)
- [7] Sinko, R.; Koo, J.-H.; Kim, Y.-K.; Kim, K.-S.; Characterization and Modeling of Bending Behavior of a New Generation of Magnetorheological Elastomers. 12th Joint Intermag/MMM Conference, January 20-24, 2013, Chicago, IL, USA
- [8] Sinko, R.; Karnes, M.; Koo, J.-H.; Kim, Y.-K.; Kim, K.-S.; ASME, Design and Test of an Adaptive Tuned Vibration Absorber for Reducing Cryogenic Cooler Vibrations. 2012; p 325-331. (Technical Paper and Presentation at 2011 ASME Smart Materials, Adaptive Structures and Intelligent Systems (SMASIS) Conference – Phoenix, AZ)

INVITED TALKS

- [1] Sinko, R. (January 2014) “ME 512 Quick Tech Talk: Atomistic simulations of the fracture strength of

- cellulose nanocrystals” *Mechanical Engineering Departmental Seminar, Northwestern University*.
- [2] **Sinko, R.** (February 2017) “Transient effects of drying creep in nanoporous solids: understanding the effect of nanoscale energy barriers” *United States Association of Computational Mechanics Student Seminar Series, Northwestern University*.

REFERENCES

Professor Sinan Keten
 Departments of Mechanical Engineering and Civil &
 Environmental Engineering
 Northwestern University
 2145 Sheridan Road
 Tech A133
 Evanston, IL 60208-3109
 (847) 491-5282
s-keten@northwestern.edu

Professor Zdeněk Bažant
 Departments of Civil & Environmental Engineering,
 Mechanical Engineering, and Material Science and
 Engineering
 Northwestern University
 2145 Sheridan Road
 Tech A135
 Evanston, IL 60208-3109
 (847) 491-4025
z-bazant@northwestern.edu

Professor Catherine Brinson
 Department of Mechanical Engineering
 Northwestern University
 2145 Sheridan Road
 Tech A214
 Evanston, IL 60208-3109
 (847) 467-2347
cbrinson@northwestern.edu

Dr. Jeffrey Gilman
 Materials Science and Engineering Division, Material
 Measurement Laboratory
 National Institute of Standards and Technology
 Gaithersburg, Maryland 20899-8664
 (301) 975-6573
jeffrey.gilman@nist.gov